# Towards a computer-assisted global linear stability analysis of fluid particles

Vom Fachbereich Maschinenbau
an der Technischen Universität Darmstadt
zur
Erlangung des Grades eines Doktor-Ingenieurs (Dr.-Ing.)
genehmigte

**Dissertation**

vorgelegt von

**Johannes Richard Kromer**

aus Würzburg

| | |
|---|---|
| Referent: | Prof. Dr. rer. nat. Dieter Bothe |
| Korreferent: | Prof. Dr.-Ing. Cameron Tropea |
| Tag der Einreichung: | 15. Oktober 2019 |
| Tag der mündlichen Prüfung: | 18. Dezember 2019 |

Darmstadt 2019

D 17

Meinen Eltern

Carola und Eckhard Kromer

## Acknowledgements

While working on this thesis, I have received a great deal of support in different ways and from various sources. First and foremost, my heartfelt appreciation belongs to my thesis supervisor Prof. Dr. Dieter Bothe. Besides giving me the chance to work on a fascinating topic, I have learned a lot from discussing with you.
Furthermore, I would like to thank Prof. Dr. Cameron Tropea for agreeing to be my second supervisor.
The time at the research group *Mathematical Modeling and Analysis* was instructive, both to a scientific and non-scientific extent. I have had the unique pleasure of discussing with keen and passionate minds, which more than once proved to be a beacon. This work was made possible through the financial support by the Excellence Initiative of the German Federal and State Governments, within the scope of the Graduate School of Computational Engineering (GSC CE 233) and the SFB-TRR 75 (#84292822).

The last, but by no means least, expression of gratitude I address to my wife: *Amelie, this work would not have been possible without you! Your patience and unconditional support provided an inexhaustible source of motivation during the last six years.*

No words of mine could measure up to the esteem and gratitude I owe to my parents.

Johannes Kromer Frankfurt am Main, October 2019

## Affidavit

I hereby warrant that the content of this thesis is the direct result of my own work and that any use made in it of published or unpublished material is fully and correctly referenced.

Johannes Richard Kromer

Frankfurt am Main, February 20, 2020

# Abstract

For many technical processes, the dynamics of rising or falling liquid particles are of paramount importance. Their paths and forms show a complex spectrum of physical phenomena, involving instabilities and bifurcations. Despite numerous numerical and experimental investigations, many of these phenomena remain to be understood. While experimental access to local quantities is often not feasible without interfering with the flow, numerical studies allow their extraction without disturbance.

The present work, therefore, is concerned with the development and implementation of an algorithm capable of global linear stability analysis of deformable fluid particles. In mathematical terms, stability is assessed by eigenvalues, which are calculated by a combination of a numerical flow solver and linear algebra. For this purpose, a stationary state of the system is superimposed with a small perturbation and numerically integrated to obtain the evolution of the perturbation. In the context of two-phase flows, the presence of dynamic interfaces requires a transformation onto a reference configuration, whose mathematical foundations are derived. The stability of two relevant prototypical configurations – spherical particles in zero gravity and droplets freely rising in an ambient fluid – is investigated, whereby the modes belonging to the unstable eigenvalues are described both quantitatively and qualitatively.

For small perturbations, initialization of the numerical flow solver requires highly accurate volume fractions, whose computation in three spatial dimensions is mathematically demanding and resorts to a novel method developed in the context of this work. Exploiting the appropriate divergence theorems for hypersurfaces, in combination with an approximation motivated by differential geometry, allows transforming the integrals in three spatial dimensions to line integrals, implying a considerable reduction of complexity for their numerical quadrature. The consideration of topological configurations of the intersected computational cells allows for a robust implementation, that is numerically tested for spheres, ellipsoids, and disturbed spheres. The global errors of the volume approximation show up to fourth–order convergence with spatial resolution.

Employing numerical methods for stability analysis of physical systems implies that the spectra found contain both numerical and physical elements. Surface tension is crucial for the flows considered here, the numerical treatment of which requires the calculation of mean curvatures from discrete volume fractions. A substantiated interpretation of the results of stability analysis, therefore, requires accurate knowledge of the properties of the implemented numerical schemes. A theoretical and numerical investigation of the height function method is conducted for several technically relevant hypersurfaces, with statistical processing flanking the interpretation. Provided sufficiently accurate volume fractions, the theoretical errors exhibit second-order convergence for smooth hypersurfaces. However, numerical experiments show that the quality of the volume fractions (in terms of global volume conservation) is not sufficient for the expected convergence. This is directly related to the unstable eigenvalues found.

## Zusammenfassung

Für viele technische Prozesse ist die Dynamik aufsteigender oder fallender Flüssigkeitspartikel von großer Bedeutung. Deren Pfade und Formen zeigen ein komplexes Spektrum physikalischer Phänomene, das Instabilitäten und Bifurkationen beinhaltet. Trotz zahlreicher numerischer und experimenteller Untersuchungen sind viele dieser Phänomene noch nicht verstanden. Während der experimentelle Zugang zu lokalen Größen häufig nicht möglich ist, erlauben numerische Untersuchungen deren Extraktion ohne Störung der zugrundeliegenden Strömung.

Die vorliegende Arbeit beschäftigt sich daher mit der Entwicklung und Implementierung eines Algorithmus zur globalen linearen Stabilitätsanalyse verformbarer fluider Partikel. Die mathematische Beschreibung der Stabilität erfolgt durch Eigenwerte, deren Berechnung durch eine Kombination aus numerischer Strömungslösung und linearer Algebra erfolgt. Dazu wird ein stationärer Zustand des Systems mit einer kleinen Störung überlagert und numerisch integriert, um die Evolution der Störung zu erhalten. Die Präsenz dynamischer Grenzflächen erfordert eine Transformation in eine Referenzkonfiguration, deren mathematische Grundlagen hergeleitet werden. Die Stabilität von zwei relevanten prototypischen Konfigurationen – sphärische Partikel in Schwerelosigkeit und frei aufsteigende Tropfen – wird untersucht, wobei die zu den instabilen Eigenwerten gehörenden Moden quantitativ und qualitativ beschrieben werden.

Eine Initialisierung des numerischen Strömungslösers erfordert für kleine Störungen sehr genaue Volumenfraktionen, deren Berechnung in drei Raumdimensionen mathematisch anspruchsvoll ist und mittels einer im Rahmen dieser Arbeit neu entwickelten Methode erfolgt. Die Verwendung entsprecheder Divergenztheoreme für Hyperflächen erlaubt, in Kombination mit einer differentialgeometrisch motivierten Approximation, die Transformation von Integralen in drei Raumdimensionen in Linienintegrale, die einer numerischen Quadratur wesentlich einfacher zugänglich sind. Die Berücksichtigung topologischer Konfigurationen der geschnittenen Zellen erlaubt eine robuste Implementierung, die für Sphären, Ellipsoide und gestörte Sphären numerisch getestet wird. Die globalen Fehler der Volumenapproximation zeigen Konvergenz bis zu vierter Ordnung mit räumlicher Auflösung.

Die Verwendung numerischer Methoden zur Stabilitätsanalyse physikalischer Systeme impliziert, dass die gefundenen Spektren sowohl numerische als auch physikalische Elemente enthalten. Für die hier untersuchten Strömungen spielt Oberflächenspannung eine zentrale Rolle, deren numerische Behandlung die Berechnung von mittleren Krümmungen aus Volumenfraktionen erfordert. Die substantiierte Interpretation der Ergebnisse einer Stabilitätsanalyse setzt daher genaue Kenntnis der Eigenschaften der implementierten numerischen Schemata voraus. Diese werden für die Methode der Höhenfunktionen theoretisch und numerisch für eine Reihe technisch relevanter Hyperflächen untersucht, wobei eine statistische Aufbereitung die Interpretation flankiert. Während für genügend genaue Volumenfraktionen die theoretischen Fehler für glatte Hyperflächen von zweiter Ordnung konvergieren, zeigt sich in numerischen Experimenten, dass die Qualität der Volumenfraktionen (im Sinne der globalen Volumenerhaltung) für die erwartete Konvergenz nicht hinreichend ist. Dies steht in direktem Zusammenhang mit den gefundenen instabilen Eigenwerten.

# Publications

Some of the results presented in this thesis have previously appeared in the following publications:

## Journal papers

[5] Christoph Albert, **Johannes Kromer**, A. M. Robertson, and Dieter Bothe. Dynamic behaviour of buoyant high viscosity droplets rising in a quiescent liquid. *Journal of Fluid Mechanics*, 778: 485–533, 2015.

[78] **Johannes Kromer** and Dieter Bothe. Highly accurate computation of volume fractions using differential geometry. *Journal of Computational Physics*, 396:761–784, 2019.

## Conference contributions

- **Dynamics of buoyant high viscosity droplets rising in a quiescent liquid**
  $14^{\text{th}}$ Workshop on Two-Phase Flow Predictions
  September $7^{\text{th}}$ to $10^{\text{th}}$ 2015, Halle (Germany)
- **Towards a 3D global linear stability analysis for buoyant fluid particles**
  $9^{\text{th}}$ International Conference on Multiphase Flow
  May $22^{\text{nd}}$ to $27^{\text{th}}$ 2016, Florence (Italy)
- **Numerical quadrature of surface integrals using the surface Laplace-Beltrami operator**
  $3^{\text{rd}}$ International Conference on Numerical Methods in Multiphase Flows
  June $26^{\text{th}}$ to $29^{\text{th}}$ 2017, Tokyo (Japan)

# List of Symbols

## Physical units

| | | | |
|---|---|---|---|
| $L$ | length | – | m |
| $M$ | mass | – | kg |
| $T$ | time | – | s |

## Latin

| Symbol | Description | Dimensions | Units |
|---|---|---|---|
| $L_\Sigma$ | order of spherical harmonics | – | 1 |
| $N_\mathcal{S}$ | number of points (shape extraction; section 3.2) | – | 1 |
| $N_\Sigma$ | number of intersected cells | – | 1 |
| $U_t$ | terminal rise velocity | $\frac{L}{T}$ | $\frac{\mathrm{m}}{\mathrm{s}}$ |
| $\boldsymbol{f}$ | flow solver | – | 1 |
| $\boldsymbol{P}_\Sigma$ | tangential projection; see eq. (4.15) | – | 1 |
| $\boldsymbol{n}_\Sigma$ | interface outer unit normal | – | 1 |
| $\boldsymbol{u}$ | velocity | $\frac{L}{T}$ | $\frac{\mathrm{m}}{\mathrm{s}}$ |
| $\boldsymbol{u}^\Sigma$ | interface velocity | $\frac{L}{T}$ | $\frac{\mathrm{m}}{\mathrm{s}}$ |
| $f$ | volume fraction | – | 1 |
| $t$ | time | $T$ | s |
| $p$ | pressure | $\frac{M}{LT^2}$ | $\frac{\mathrm{kg}}{\mathrm{m\,s^2}}$ |

## Greek

| Symbol | Description | Dimensions | Units |
|---|---|---|---|
| $\Delta t$ | time step size | $T$ | s |
| $\Omega$ | simulation domain | – | 1 |
| $\theta$ | polar angle | – | 1 |
| $\varphi$ | azimuthal angle | – | 1 |

| | | | |
|---|---|---|---|
| $\Sigma$ | hypersurface | – | – |
| $\Gamma$ | hypersurface (approximated) | – | 1 |
| $\rho$ | density | $\frac{M}{L^3}$ | $\frac{\mathrm{kg}}{\mathrm{m}^3}$ |
| $\mu$ | dyn. viscosity | $\frac{M}{LT}$ | $\frac{\mathrm{kg}}{\mathrm{m\,s}}$ |
| $\nu$ | kin. viscosity | $\frac{L^2}{T}$ | $\frac{\mathrm{m}^2}{\mathrm{s}}$ |
| $\sigma$ | surface tension coefficient | $\frac{M}{T^2}$ | $\frac{\mathrm{kg}}{\mathrm{s}^2}$ |
| $\kappa_\Sigma$ | mean curvature | $\frac{1}{L}$ | $\frac{1}{\mathrm{m}}$ |
| $\kappa_i$ | $i$-th principal curvature | $\frac{1}{L}$ | $\frac{1}{\mathrm{m}}$ |

## Other

| | |
|---|---|
| $\mathcal{E}_2^\kappa$ | $L_2$-error of curvature ($L_\infty$ analogous); see eq. (5.19) |
| $\mathcal{E}_2^\mathcal{S}$ | $L_2$-error of shape extraction ($L_\infty$ analogous); see eq. (3.12) |
| $\mathbb{S}^2$ | parameter domain of the unit sphere |
| $\mathcal{K}$ | computational cell |
| $\mathcal{E}_k$ | edge of computational cell |
| $\mathcal{F}_k$ | face of computational cell |
| $\mathfrak{S}()$ | status of entity |
| $\boldsymbol{\nu}_k$ | vertex of computational |
| $\mathcal{E}_2^f$ | $L_2$-error of volume fractions ($L_\infty$ analogous); see eq. (4.62) |
| $\mathcal{E}^V$ | global volume error; see eq. (4.59) |

## Stability analysis

| | |
|---|---|
| $\boldsymbol{\chi}$ | state vector |
| $N$ | number of time steps |
| $\boldsymbol{\zeta}$ | state perturbation |
| $\gamma_M^k$ | ARNOLDI convergence measure |
| $\boldsymbol{\chi}_0$ | steady state |
| $\epsilon$ | perturbation magnitude |
| $\alpha_T$ | relative radial extension of transformation domain; see eq. (6.36) |
| $R_\pm$ | radial boundaries of transformation domain |
| $\Omega_\mathbf{1}$ | identity domain |
| $\Omega_\boldsymbol{T}$ | transformation domain |

# List of Figures

# Contents

# 1. Introduction

In contrast to solid objects, fluid particles, such as liquid drops or gas bubbles, may strongly and dynamically deform while they move through ambient media. The shape deformation is mainly induced by pressure differences resulting from local flow caused by, e.g., the buoyancy-driven particle motion. Of course, other mechanisms of excitation may occur as well. Depending on the nondimensional flow parameters, such as, e.g., the REYNOLDS or EÖTVÖS number, the respective trajectories of the particle motion may display linear, spherical and helical behavior as well as irregular curves. Simultaneously – especially for liquid drops and gas bubbles – the shape of the fluid particle oscillates due to the feedback of the ambient flow, which crucially reaffects the dynamics of motion. While restrictive assumptions concerning the dynamics allow for an analytical treatment, more realistic formulations of the respective equations of motion feature highly nonlinear characteristics, producing nonlinear oscillations of both the path and shape of the fluid particle. The physical effects behind the dynamics exhibit complex bifurcations as well as instabilities.

There is a wide variety of industrial processes for which the motion of fluid particles in ambient media is decisive, in particular in the chemical industry, but also in atmospheric science or human medicine. In technical applications, the sizes of the particles range from the cm (cloud formation, Pinsky et al. [106]) over the mm (spray cooling, Cheng et al. [28]) to the µm (printing, Wu et al. [156]) and nm (pharmaceutical industry, Rodríguez-Abreu and Pena [121]) scale, thereby admitting a rich spectrum of physical phenomena. Despite their importance, both in a scientific and practical view, there still is little understanding of many of the phenomena mentioned above, especially regarding the characteristics of nonlinear shape and path oscillations. The range of experimental investigations focussing on the effect of nondimensional numbers on integral quantities, such as, e.g., terminal rise velocities, is wide. For example, de Vries [37] conducts a series of experiments focussing on the path and wake of rising bubbles, whereas Lunde and Perkins [87] and Elligsen and Risso [41] investigate the corresponding shape oscillations. For a thorough overview, the reader is referred to the seminal book of Clift et al. [32]. Experimental scrutinizing of the bifurcations or regime transitions in terms of local quantities, however, remains notoriously difficult, due to the sensitivity of the flows with respect to probing. On the other hand, numerical simulations inherently allow for the extraction of local and instantaneous quantities without interfering with the physics of the flow. Thus, a detailed investigation of the aforementioned dynamical systems concerning their stability properties calls for computer-aided analysis, constituting the **motivation** of this thesis. To establish a fundamental understanding of the underlying hydrodynamics, the present work examines a single viscous particle embedded in a viscous ambient fluid. Flows of this type are governed by the conservation of mass and linear momentum, where a deformable interface of zero thickness separates the fluids. Within each of the respective fluid phases, the well-known NAVIER-STOKES equations hold, accompanied by appropriate material models and transmission conditions for mass and momentum exchange across the interface. Within this thesis, only NEWTONIAN fluids are considered.

In mathematical terms, the linear stability of a (state of a) dynamical system is determined by the

eigenvalues of its JACOBIAN. If all eigenvalues admit a negative real part, the state is said to be *stable*, whereas a single eigenvalue with a positive real part renders the state *unstable*. Tezuka and Suzuki [140] first proposed an algorithm for the linear stability analysis of flows around a spheroid, thereby extending the method of Chiba [29]. The concept combines the linearization of a viscous flow problem around a steady state $\boldsymbol{\chi}_0$, consisting of the discrete velocities stored at the nodes of the computational grid. The eigenvalues of the associated JACOBIAN are approximated by the method of Arnoldi [7], where the latter requires performing linear algebra. The action of the JACOBIAN is inferred from a FRECHET-type derivative, resorting to the numerically computed evolutions of a small perturbation $\boldsymbol{\zeta}$ of the steady state, i.e. $\boldsymbol{\chi}_0 \pm \epsilon\boldsymbol{\zeta}$. The flows under consideration in Tezuka and Suzuki [140] comprise a single phase, implying that the state space is also a vector space, which is convenient from a mathematical point of view. For two-phase flows, however, this property is lost. To see why this is the case, consider two different states of a perturbed spherical droplet (material A) immersed in material B, corresponding to two different occupations of the respective phases.


While phase A of state 1 corresponds to phase A of state 2 in the green region, the correspondence is respectively inverted in the red region. In other words, the states cannot be meaningfully compared, i.e. superposed, to each other, which is required for the application of linear algebra. Albert et al. [4] resolved this obstacle by introducing a divergence-preserving domain transformation, which maps the evolved states to a common referential domain, on which linear algebra can be safely performed. By investigating falling films in two spatial dimensions, they were able to prove that the global linear stability analysis concept of Tezuka and Suzuki [140] is applicable to flows with a deformable interface.

Hence, the **first goal of this thesis** is to lay the methodological foundation for a computer-aided global linear stability analysis of fluid particles by extending the work of Albert et al. [4] to three spatial dimensions. For various reasons of theoretical and numerical provenience, however, this task is highly demanding and features a zoo of hidden obstacles and sub-problems, which shall be addressed in detail within this thesis. The **second goal** comprises the application of the aforementioned algorithm to two prototypical configurations of fluid particles, namely spherical droplets in zero gravity and droplets freely rising in an ambient fluid due to buoyancy. The rationale behind the choice of the first configuration is motivated by the concept of the algorithm itself. While the NAVIER-STOKES equations admit a (trivial) solution for spherical particles in zero gravity, recall that the flow solver employed for the numerical integration does not necessarily sustain such a state. In other words, the spectrum of the JACOBIAN is enriched by numerical artifacts, where an appropriate discretization should not exhibit amplifying mechanisms. The motivation behind the second configuration (freely rising droplets) is to identify the mechanisms behind the transition from steady vertical to oblique rise.

After section 1.1 outlines the structure of the present work in detail, we find it crucial to establish a

consistent notation and provide basic definitions, which is the subject of section 1.2. The implementation of the algorithms presented within this thesis frequently resorts to some libraries and software, for which we offer a consolidated description in section 1.3.

## 1.1. Outline of this thesis

Chapter 2 commences by stating the continuum mechanical conservation laws in their appropriate form. Furthermore, since this thesis is concerned with fluid particles, a comprehensive collection of remarks on the representation of hypersurfaces embedded in $\mathbb{R}^3$ is provided, along with some basic facts of differential geometry.

The numerical solutions of the NAVIER-STOKES equations for two-phase flows are computed using the flow solver FS3D, which was originally developed by Rieber [120] and resorts to the Volume-of-Fluid (VOF) approach of Hirt and Nichols [64], allowing to numerically represent the different phases. A detailed description of the underlying concepts as well as the implementation is the subject of chapter 3.

To provide accurate initial conditions for the phases occupying the simulation domain, chapter 4 introduces a numerical algorithm for the computation of volume fractions from implicitly defined hypersurfaces. The novelty of the presented approach consists in exploiting differential geometry both for the approximation of the hypersurface and the evaluation of the resulting integral expressions. Numerical experiments are conducted for some classes of technically relevant hypersurfaces.

Subsequently, chapter 5 is devoted to an in-depth analysis of the height function method, which is employed for the numerical computation of mean curvature from volume fractions. After recalling the basic concept of the method, along with some implementation details, a theoretical reference is established by combining a local TAYLOR expansion of the hypersurface with a second-order approximation of the error.

In chapter 6, an algorithm for computer-assisted global linear stability analysis of fluid particles is presented. After a detailed mathematical formulation of the problem, we shed some light on the so-called *eigenvalue problem* of non-symmetric matrices. The algorithm is applied to stagnant and freely rising particles.

Chapter 7 gathers and highlights the main findings, puts them into perspective and draws a conclusion.

## 1.2. Notation and basic definitions

The present section introduces some basic definitions as well as the notation, which will be applied consistently throughout this thesis. Unless stated otherwise, all quantities in this work are assumed to be real. Appendix A assembles a mathematical supplement containing extensive definitions. A comprehensive list of symbols can be found on page I.

### Notation

**Scalar** quantities/funtions are denoted by Greek and Roman letters, e.g., $\phi, f$.

**Vector** quantities/functions are denoted by bold Greek and Roman letters, e.g., $\boldsymbol{\phi}, \boldsymbol{f}$. Their elements are addressed with the respective non-bold indexed letter, e.g., $\boldsymbol{\phi} = \sum_{k=1}^{N} \phi_k \boldsymbol{e}_k$, where $\{\boldsymbol{e}_k\}$ are the standard unit basis vectors.

**Tensor** quantities/functions are denoted by bold captial Greek and Roman letters, e.g., $\boldsymbol{A}, \boldsymbol{\Phi}$. Within this work, only tensors of rank two are considered, where the addressing of the elements is analogous to the vector case, i.e. $\boldsymbol{A} = \sum_{i=1}^{N} \sum_{j=1}^{M} A_{ij} \boldsymbol{e}_i \otimes \boldsymbol{e}_j$. Here, $\otimes$ denotes the standard dyadic product, allowing to express the identity matrix as $\boldsymbol{I} = \sum_{i=1}^{N} \boldsymbol{e}_i \otimes \boldsymbol{e}_i$.

**Summation:** In order to achieve notational brevity, the present work makes use of the EINSTEIN convention, implying summation over two common indices, e.g., the matrix-vector product $\boldsymbol{Ab}$ becomes $A_{ij} b_j \boldsymbol{e}_i$.

**Differentiability** The set of functions which are $k$ times continuously differentiable on some domain $\Omega$ is denoted by $\mathcal{C}^k(\Omega)$.

**Partial derivatives:** For a continuously differentiable scalar (vector) function $\phi(\boldsymbol{x})$ ($\boldsymbol{\phi}(\boldsymbol{x})$), the partial derivative is denoted by $\phi_k := \frac{\partial \phi}{\partial x_k}$ ($\boldsymbol{\phi}_k := \frac{\partial \boldsymbol{\phi}}{\partial x_k}$). To avoid misinterpretation, partial derivatives of indexed functions are denoted by $\partial$, e.g., $\boldsymbol{\phi}_k = \partial_k \phi_m \boldsymbol{e}_m$. The concept analogously applies to partial derivatives of higher order.

**Spherical coordinates:** Let $r \in \mathbb{R}^+$, $\varphi \in [0, 2\pi)$ and $\theta \in [0, \pi]$ denote the radius, azimuthal and polar angle, respectively. With the standard basis

$$\boldsymbol{e}_r = \begin{bmatrix} \cos\varphi \sin\theta \\ \sin\varphi \sin\theta \\ \cos\theta \end{bmatrix}, \quad \boldsymbol{e}_\varphi = \begin{bmatrix} -\sin\varphi \\ \cos\varphi \\ 0 \end{bmatrix} \quad \text{and} \quad \boldsymbol{e}_\theta = \begin{bmatrix} \cos\varphi \cos\theta \\ \sin\varphi \cos\theta \\ -\sin\theta \end{bmatrix}$$

and some origin $\boldsymbol{x}_0 = x_{0,i} \boldsymbol{e}_i$, one obtains $\boldsymbol{x} = \boldsymbol{x}_0 + r\boldsymbol{e}_r$. The JACOBIAN of the forward and backward transformation, respectively, reads

$$\boldsymbol{J}_{\boldsymbol{x}} := \frac{\mathrm{d}\boldsymbol{x}}{\mathrm{d}(r, \varphi, \theta)} = \begin{bmatrix} \cos\varphi \sin\theta & -r \sin\varphi \sin\theta & r \cos\varphi \cos\theta \\ \sin\varphi \sin\theta & r \cos\varphi \sin\theta & r \sin\varphi \cos\theta \\ \cos\theta & 0 & -r \sin\theta \end{bmatrix}, \tag{1.1}$$

$$\boldsymbol{J}_{\boldsymbol{r}} := \frac{\mathrm{d}(r, \varphi, \theta)}{\mathrm{d}\boldsymbol{x}} = \begin{bmatrix} \cos\varphi \sin\theta & \sin\varphi \sin\theta & \cos\theta \\ -\frac{\sin\varphi}{r \sin\theta} & \frac{\cos\varphi}{r \sin\theta} & 0 \\ \frac{\cos\varphi \sin\theta}{r} & \frac{\sin\varphi \cos\theta}{r} & \frac{-\sin\theta}{r} \end{bmatrix} = \boldsymbol{J}_{\boldsymbol{x}}^{-1}, \tag{1.2}$$

where spherical coordinates are computed from their CARTESIAN correspondent via

$$r = \sqrt{(x_i - x_{0,i})^2}, \quad \tan\varphi = \frac{x_2 - x_{0,2}}{x_1 - x_{0,1}} \quad \text{and} \quad \cos\theta = \frac{x_3 - x_{0,3}}{r}. \tag{1.3}$$

Due to $\arctan : \mathbb{R} \mapsto (-\frac{\pi}{2}, \frac{\pi}{2})$, the numerical computation of the azimuthal angle $\varphi$ from CARTESIAN coordinates is carried out using $\arctan_2 : (\mathbb{R} \times \mathbb{R}) \setminus (0,0) \mapsto (-\pi, \pi]$ with

$$\arctan_2(y, x) = \begin{cases} \arctan(\frac{y}{x}) + \operatorname{sign}(y)\, \pi & x < 0, y \neq 0 \\ \arctan(\frac{y}{x}) & x > 0, y \neq 0 \\ \operatorname{sign}(y)\, \frac{\pi}{2} & x = 0, y \neq 0 \\ \frac{\pi}{2}(1 - \operatorname{sign}(x)) & y = 0 \end{cases}.$$

Henceforth, the parameter domain $\mathbb{S}^2 := [0, 2\pi) \times [0, \pi]$ is referred to as unit sphere. The partial derivatives are denoted by the respective subscripts, cf. above.

### Definitions

**Inner product:** For two vectors $\{\boldsymbol{a}, \boldsymbol{b}\} \subset \mathbb{R}^N$ and symmetric $\boldsymbol{A}$, the inner product is $\langle \boldsymbol{a}, \boldsymbol{b} \rangle_{\boldsymbol{A}} = \boldsymbol{a}^\mathsf{T} \boldsymbol{A} \boldsymbol{b} = a_i A_{ij} b_j$. The standard inner product employs the identity and reads $\langle \boldsymbol{a}, \boldsymbol{b} \rangle := \langle \boldsymbol{a}, \boldsymbol{b} \rangle_{\boldsymbol{I}}$.

**Outer product:** For two vectors $\{\boldsymbol{a}, \boldsymbol{b}\} \subset \mathbb{R}^N$, the outer or dyadic product is $\boldsymbol{a} \otimes \boldsymbol{b} = \boldsymbol{a}\boldsymbol{b}^\mathsf{T}$.

**Contraction:** Two tensors of rank two are contracted by $\boldsymbol{A} : \boldsymbol{B} := \operatorname{tr}\left(\boldsymbol{A}^\mathsf{T} \boldsymbol{B}\right) = A_{ki} B_{ik}$.

**Gradient:** For a scalar function $\phi(\boldsymbol{x})$, the gradient is denoted by $\nabla \phi(\boldsymbol{x}) = \partial_k \phi(\boldsymbol{x}) \boldsymbol{e}_k$, the corresponding operator for a vector $\boldsymbol{\phi}(\boldsymbol{x})$ reads $\nabla \boldsymbol{\phi} = \partial_j \phi_i \boldsymbol{e}_i \otimes \boldsymbol{e}_j$.

**Hessian:** For a twice continuously differentiable function $\phi : \mathbb{R}^M \mapsto \mathbb{R}$, the Hessian matrix is denoted by $\Delta \phi(\boldsymbol{x}) = \phi_{ij}(\boldsymbol{x}) \boldsymbol{e}_i \otimes \boldsymbol{e}_j$.

## 1.3. Software and libraries

### Software development

The numerical algorithms employed within this thesis are implemented in `Fortran` 2008 using an 8-byte (4-byte) representation for real numbers (integers), where object-oriented implementation was used where possible. The binaries are compiled from the source code via `gfortran` from the GNU Compiler Collection (GCC, version 8.2.0), where parallel execution is made possible by exploiting the wrappers from openMPI (version 4.0.1). The output of field data resorts to the MPI parallel output routines, which allow creating a single binary file per field, irrespective of the number of processes used for the execution. Furthermore, some of the standard tasks from the field of linear algebra are carried out using subroutines from the seminal library `LAPACK` (version 3.8.0); cf. Anderson et al. [6]. Table (1.1) gathers some frequently used routines, which are applied unless explicitly specified otherwise.

Table 1.1.: Default `LAPACK` routines for numerical linear algebra.

| **task** | **routine** | |
|---|---|---|
| | (symmetric) | (non-symmetric) |
| eigen decomposition | `dsyev` | `dgeev` |
| linear solver | `dsysv` | `dgesv` |

### Figures and diagrams

The vector graphics depicted within this thesis were produced employing the library `pstricks`, where details of its implementation can be found in the book of Voß [148]. The employed page description language `postscript` allows performing arithmetic operations within graphics at compile time, where potentially underlying data is stored as text with at least 6 significant figures. The final figures are produced using `ghostscript` (version 9.26) with the workflow

`latex` → `dvi2ps` → `gs`.

The rendered three-dimensional figures are produced using `ParaView` (version 5.4.1), where the Xdmf format was used for the description of the organization of the binary data; cf. Ahrens et al. [2] and Ayachit [9].

## Comparison of real numbers

Most of the algorithms employed within this thesis require at one point or another the equality comparison of real numbers to obtain boolean expressions, e.g., if one seeks to check whether a number is zero. Despite the fact that `Fortran` offers an operator for the equality comparison of reals, it is preferable to resort to a numerically robust comparison with a prescribed tolerance $\epsilon_{\text{zero}} = 10^{-14}$, i.e. for $x, y \in \mathbb{R}$ let

$$x \overset{?}{=} y := \begin{cases} \text{true} & |x - y| < \epsilon_{\text{zero}} \\ \text{false} & |x - y| \geq \epsilon_{\text{zero}} \end{cases} . \tag{1.4}$$

## Numerical computation of roots

Algorithm (1) describes Newtons algorithm, which is employed for the numerical computation of roots of continuously differentiable functions $f : \mathbb{R} \mapsto \mathbb{R}$. Note that the choice of the tolerance $\epsilon_{\text{zero}}$ must be in accordance with the real comparison described above. For reasons of numerical robustness, the evaluation of polynomial functions and their derivatives resorts to the scheme of Horner.

**Algorithm 1:** Newtons method for numerical computation of roots of smooth function $f$.

**Data:** function $f(x)$, derivative $f_x(x)$, initial value $x_0$, max. number of iterations $N_{\max}$
**Result:** $x_0$ such that $|f(x_0)| \leq \epsilon_{\text{zero}}$

```
n := 1;
while |f(x_0)| ≥ ε_zero ∧ n ≤ N_max do
    n := n + 1;
    if |f_x(x_0)| ≥ ε_zero then
        /* update root                                   */
        x_0 := x_0 − f(x_0)/f_x(x_0);
    else
        /* degenerate case                               */
        break;
    end
end
```

## Random numbers

Whenever *random numbers* $X$ are required within the numerical computations, they are assumed to be normally distributed with average $\hat{\mu}$ and variance $\hat{\sigma}^2$, denoted by $X \sim \mathcal{N}(\hat{\mu}, \hat{\sigma}^2)$. The numerical evaluation is carried out by alg. (2), employing the transformation introduced by Box and Muller [22]. Figure (1.1) exemplifies the algorithm for varying sample sizes, indicating good agreement with the desired normal distribution.

**Algorithm 2:** Random generation of real numbers $X$. The random seed $s$ is obtained from reading an 8-byte real from `/dev/urandom` once per program run.

**Data:** mean $\hat{\mu}$, variance $\hat{\sigma}^2 > 0$

**Result:** pseudo-random number $X$.

1 call `random_seed`$(s)$;

`/* obtain pseudo-random numbers` $u_1, u_2$ `uniformly distributed in` $(0, 1)$ `*/`

2 call `random_number`$(u_i)$;

`/* apply Box-Muller transformation */`

3 $X = \hat{\mu} + \hat{\sigma}\sqrt{-2 \ln u_1} \cos 2\pi u_2$;

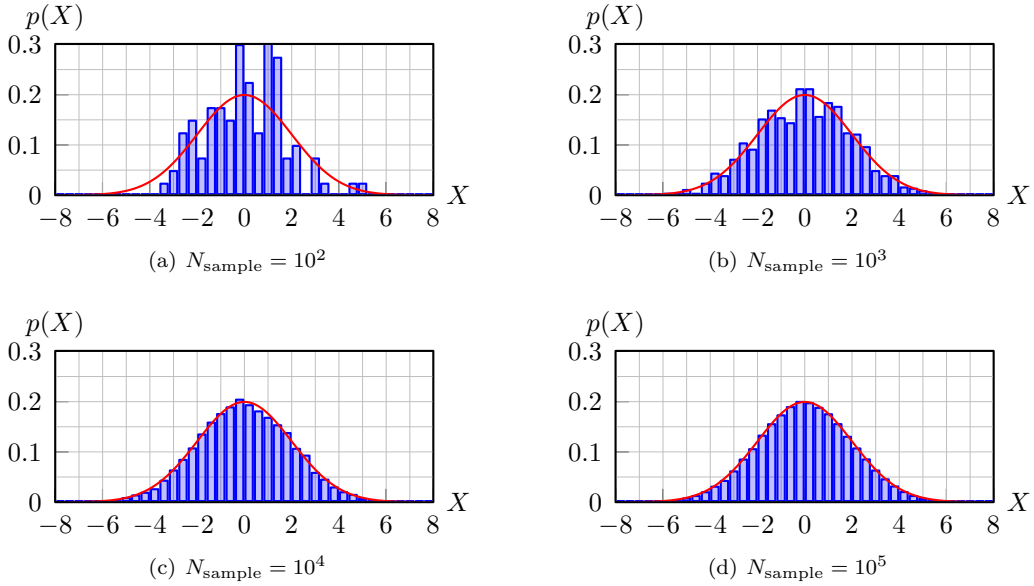


(a) $N_{\text{sample}} = 10^2$ (b) $N_{\text{sample}} = 10^3$

(c) $N_{\text{sample}} = 10^4$ (d) $N_{\text{sample}} = 10^5$

Figure 1.1.: Pseudo-random normal distribution obtained from alg. (2) (bars) and normal distribution (curve) for $\hat{\sigma}^2 = 4$, $\hat{\mu} = 0$ and varying sample size.

# 2. Mathematical model

This chapter provides the fundamental equations of motion for a flow consisting of two phases, where the *phases* are constituted of fluids that do not mix on a molecular level, e.g., tap water and oil. Despite this seemingly strong restriction within the field of fluid flows, the scope of physical phenomena which may occur is extremely rich. The variable flow parameters are, besides others, involved materials parameters (e.g., mass density/viscosity), rheological material models (e.g., NEWTON's law/viscoelasticity), chemical reactions, transfer of mass and species across the interface, and many others. Furthermore, the topology of the flow may cover falling films, bubbles and droplets rising or falling due to buoyancy, liquid bridges, etc., which all feature a rich and diverse spectrum of phenomena on their own.

Section 2.1 introduces the basic equations for the balance of mass and linear momentum. Since this thesis is concerned with fluid particles, section 2.2 provides some basic concepts of hypersurface representation.

## 2.1. Continuum mechanical model

This thesis is concerned with two-phase flows of incompressible NEWTONIAN fluids. The respective phases are separated by a sharp interface, which is passively advected by the flow and, from a mathematical point of view, admits zero thickness. Since the present work focusses on the basic hydrodynamics of pure fluids, we shall henceforth consider iso-thermal flows without phase change, where the interface is inviscid and holds no mass. Therefore, the involved material parameters are the densities, viscosities, and surface tension coefficient, which are assumed to be (phase-wise) constant. Under the aforementioned assumptions, the flow is governed by the NAVIER-STOKES equations, corresponding to the conservation of mass and linear momentum. Figure (2.1) illustrates the geometrical quantities that are relevant for fixing the notation.

Let $\Omega \subset \mathbb{R}^3$ be some spatially fixed domain, intersected by the deformable interface $\Sigma(t)$, inducing the dynamic disjoint decomposition

$$\Omega = \Omega^-(t) \cup \Omega^+(t) \cup \Sigma_\Omega(t) \quad \text{with} \quad \Sigma_\Omega(t) := \Omega \cap \Sigma(t), \tag{2.1}$$

where, henceforth, the superscripts denote quantities belonging to the *exterior* $(+)$ and *interior* $(-)$ subdomain, respectively. Throughout this work, the interior phase shall be synonymously referred to as *disperse*, whereas the exterior phase shall be referred to as *continuous* or *ambient*. Note that a generic physical quantity $\phi$ may assume different values in the respective phases, i.e.

$$\phi(t, \boldsymbol{x}) = \begin{cases} \phi^+(t, \boldsymbol{x}) & \boldsymbol{x} \in \Omega^+(t) \\ \phi^-(t, \boldsymbol{x}) & \boldsymbol{x} \in \Omega^-(t) \end{cases}. \tag{2.2}$$

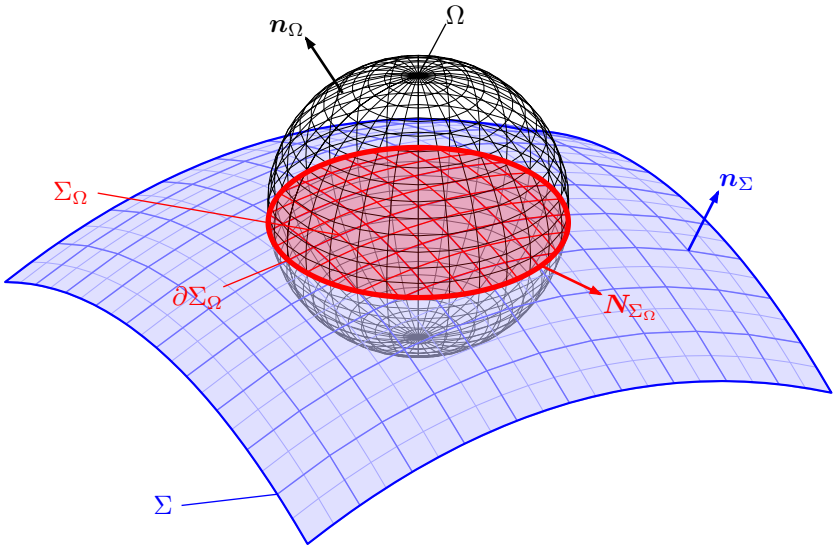


Figure 2.1.: Spatially fixed control volume $\Omega$ intersected by deformable interface $\Sigma(t)$.

With phase-wise constant densities $\rho^{\pm}$, conservation of mass becomes conservation of volume, i.e.

$$\nabla \cdot \boldsymbol{u} = 0 \quad \text{for} \quad \boldsymbol{x} \in \Omega \setminus \Sigma(t), \tag{2.3}$$

where $\boldsymbol{u}(t, \boldsymbol{x})$ denotes the local and instantaneous velocity. In the bulk phases, i.e. for $\boldsymbol{x} \in \Omega \setminus \Sigma(t)$, the conservation of linear momemtum is governed by

$$\partial_t(\rho \boldsymbol{u}) + \nabla \cdot (\rho \boldsymbol{u} \otimes \boldsymbol{u}) = -\nabla p + \nabla \cdot \boldsymbol{S} + \rho \boldsymbol{g}, \tag{2.4}$$

with $\boldsymbol{g}$ and $p(t, \boldsymbol{x})$ denoting the acceleration due to gravity and pressure, respectively. The viscous stress tensor reads

$$\boldsymbol{S} = \mu \left( \nabla \boldsymbol{u} + \nabla \boldsymbol{u}^{\mathsf{T}} \right), \tag{2.5}$$

where $\mu$ denotes the phase-wise constant dynamical viscosity. The discontinous character of the interface induces jumps in the physical quantities, which are captured by the *jump brackets*

$$[\![\phi]\!](t, \boldsymbol{x}) := \lim_{\epsilon \to 0^+} \left[ \phi(t, \boldsymbol{x} + \epsilon \boldsymbol{n}_\Sigma) - \phi(t, \boldsymbol{x} - \epsilon \boldsymbol{n}_\Sigma) \right] \quad \text{for} \quad \boldsymbol{x} \in \Sigma(t). \tag{2.6}$$

With $\boldsymbol{u}^\Sigma(t, \boldsymbol{x})$ denoting the velocity of $\Sigma(t)$, the momentum transmission condition can be written as

$$\left[\!\left[ \rho \boldsymbol{u} \otimes \left( \boldsymbol{u} - \boldsymbol{u}^\Sigma \right) + p \boldsymbol{I} - \boldsymbol{S} \right]\!\right] \boldsymbol{n}_\Sigma = \sigma \kappa_\Sigma \boldsymbol{n}_\Sigma + \nabla_\Sigma \sigma \quad \text{for} \quad \boldsymbol{x} \in \Sigma(t), \tag{2.7}$$

where $\nabla_\Sigma \sigma$, $\boldsymbol{n}_\Sigma$ and $\kappa_\Sigma$ respectively denote the surface gradient of the surface tension coefficient $\sigma$, the unit outer normal and mean curvature; cf. fig. (2.1). In the absence of phase change, the normal component of the interface velocity $V_\Sigma := \langle \boldsymbol{u}^\Sigma, \boldsymbol{n}_\Sigma \rangle$ coincides with the respective components of the velocity of the adjacent phases. Since both fluids admit a positive viscosity, we further assume that there is no tangential slip at the interface. In combination, this implies that $\Sigma(t)$ is advected passively by the

flow, resulting in $\boldsymbol{u}^\Sigma = \boldsymbol{u}^+ = \boldsymbol{u}^-$. Recalling that the surface tension coefficient $\sigma$ is considered constant allows simplifying the transmission condition in eq. (2.7) and yields

$$[\![p\boldsymbol{I} - \boldsymbol{S}]\!]\,\boldsymbol{n}_\Sigma = \sigma\kappa_\Sigma \boldsymbol{n}_\Sigma \qquad \text{and} \qquad [\![\boldsymbol{u}]\!] = \boldsymbol{0} \quad \text{for} \quad \boldsymbol{x} \in \Sigma. \tag{2.8}$$

A detailed discussion on the continuum mechanical modelling of two-phase flows can be found, e.g., in the book of Slattery [130].

## 2.2. On the representation of fluid interfaces

The present work is concerned with fluid particles, admitting closed interfaces. Of those, particles resembling moderately deformed spheres are of special interest and are so-called star domains. A domain $\Omega \subset \mathbb{R}^3$ is said to be *star-shaped* iff

$$\exists \boldsymbol{x}_0 \in \Omega \quad \text{such that} \quad \boldsymbol{x}_0 + \lambda(\boldsymbol{x} - \boldsymbol{x}_0) \in \Omega \qquad \forall (\lambda, \boldsymbol{x}) \in [0,1] \times \Omega, \tag{2.9}$$

where $\boldsymbol{x}_0$ is called a *star point* of $\Omega$. Figure (2.2) provides an illustration.

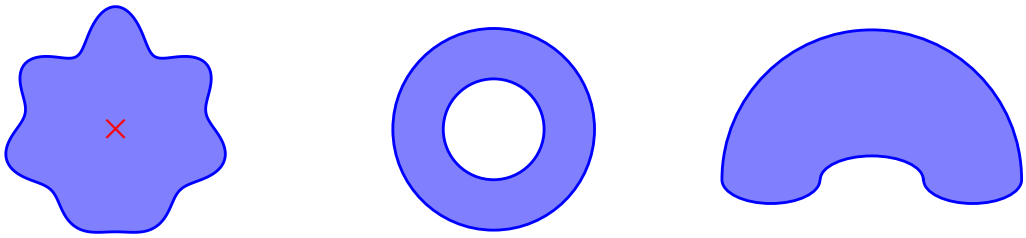

Figure 2.2.: Domains in two spatial dimensions with (left) and without (center, right) star point $\boldsymbol{x}_0$ (×).

Hypersurfaces $\Sigma \subset \mathbb{R}^3$, which are the boundary of a star-shaped domain, can be represented in spherical coordinates as

$$\Sigma = \{\boldsymbol{R}(\varphi,\theta) : [\varphi,\theta] \in \mathbb{S}^2\} \quad \text{with} \quad \boldsymbol{R}(\varphi,\theta) = \boldsymbol{x}_0 + R(\varphi,\theta)\boldsymbol{e}_r, \tag{2.10}$$

where the radius $R(\varphi,\theta) : \mathbb{S}^2 \mapsto \mathbb{R}^+$ is assumed to be sufficiently smooth on $\mathbb{S}^2$. Henceforth, let $\boldsymbol{x}_0 \equiv \boldsymbol{0}$ without loss of generality. The outer unit normal reads

$$\boldsymbol{n}_\Sigma = \frac{\boldsymbol{R}_\theta \times \boldsymbol{R}_\varphi}{\|\boldsymbol{R}_\theta \times \boldsymbol{R}_\varphi\|} = \frac{R\boldsymbol{e}_r - R_\theta \boldsymbol{e}_\theta - \frac{R_\varphi}{\sin\theta}\boldsymbol{e}_\varphi}{\sqrt{R^2 + R_\theta^2 + \frac{R_\varphi^2}{\sin^2\theta}}}. \tag{2.11}$$

The above expression obviously features a singularity at the poles, i.e. for $\theta \in \{0, \pi\}$, whose treatment is postponed to subsection 2.2.1; cf. eq. (2.41). For $\Sigma$ to be $K$ times continuously differentiable, the azimuthal periodicity conditions

$$\left.\frac{\mathrm{d}^{u+v}R}{\mathrm{d}\varphi^u \mathrm{d}\theta^v}\right|_{\varphi=0} = \left.\frac{\mathrm{d}^{u+v}R}{\mathrm{d}\varphi^u \mathrm{d}\theta^v}\right|_{\varphi=2\pi} \quad \text{for} \quad u + v \leq K \tag{2.12}$$

must hold. In fact, due to the degeneration at the poles, i.e. for $\theta \in \{0, \pi\}$, one additionally requires

$$\left.\frac{\mathrm{d}^k R}{\mathrm{d}\varphi^k}\right|_{\theta\in\{0,\pi\}} = 0 \quad \text{and} \quad \left.\frac{\mathrm{d}^k R}{\mathrm{d}\theta^k}(\varphi,\theta)\right|_{\theta\in\{0,\pi\}} = (-1)^k \left.\frac{\mathrm{d}^k R}{\mathrm{d}\theta^k}(\varphi+\pi,\theta)\right|_{\theta\in\{0,\pi\}} \quad \text{for} \quad k \leq K. \tag{2.13}$$

implying

$$\left.\frac{\mathrm{d}^k R}{\mathrm{d}\theta^k}\right|_{\theta\in\{0,\pi\}} = \begin{cases} \sum_{m=0}^{\infty} \alpha_{2m+1}^k \cos(2m+1)\varphi + \beta_{2m+1}^k \sin(2m+1)\varphi & k \text{ odd} \\ \sum_{m=0}^{\infty} \alpha_m^k \cos m\varphi + \beta_m^k \sin m\varphi & k \text{ even} \end{cases}. \tag{2.14}$$

The volume of the ball enclosed by $\Sigma$ is

$$\mathrm{vol}(\Sigma) := \frac{1}{3}\int_{\mathbb{S}^2} R^3 \sin\theta \,\mathrm{d}\theta\mathrm{d}\varphi, \tag{2.15}$$

while the integral of some function $f$ over the hypersurface itself can be obtained via

$$\mathrm{area}(f) := \int_\Sigma f(\boldsymbol{x})\mathrm{d}o = \int_{\mathbb{S}^2} f(\boldsymbol{R}(\varphi,\theta)) R \sqrt{(R^2 + R_\theta^2)\sin^2\theta + R_\varphi^2}\,\mathrm{d}\varphi\mathrm{d}\theta. \tag{2.16}$$

It is advantageous to express the radius $R$ in terms of spherical harmonics $Y_l^m$, since they (i) by definition fulfill the above requirements, (ii) form an orthonormal basis on $\mathbb{S}^2$ and (iii) allow for the expansion of any function which is square-integrable on the unit sphere $\mathbb{S}^2$; cf. appendix A.1 for a definition. Statement (iii) implies

$$R(\varphi,\theta;\boldsymbol{c}_\Sigma) = \sum_{l=0}^{\infty}\sum_{m=-l}^{l} c_{\Sigma,l,m} Y_l^m(\varphi,\theta) \quad \text{with} \quad \boldsymbol{c}_\Sigma := \{c_{\Sigma,l,m}\}, \tag{2.17}$$

where, within the scope of this thesis, the expansion is truncated above some order $L_\Sigma$. The choice of a suitable $L_\Sigma$ is made on a case-by-case basis. Henceforth, let $\boldsymbol{c}_\Sigma \in \mathbb{R}^{(L_\Sigma+1)^2}$ be the vector of coefficients describing $\Sigma$. Then, the volume operator given in eq. (2.15) becomes

$$\mathrm{vol}(\boldsymbol{c}_\Sigma) = \sum_{l_1=0}^{L_\Sigma}\sum_{m_1=-l_1}^{l_1}\sum_{l_2=0}^{L_\Sigma}\sum_{m_2=-l_2}^{l_2}\sum_{l_3=0}^{L_\Sigma}\sum_{m_3=-l_3}^{l_3} \frac{c_{\Sigma,l_1,m_1}c_{\Sigma,l_2,m_2}c_{\Sigma,l_3,m_3}}{3} \int_0^{2\pi}\int_0^{\pi} Y_{l_1}^{m_1} Y_{l_2}^{m_2} Y_{l_3}^{m_3} \sin\theta \mathrm{d}\theta\mathrm{d}\varphi,$$

where the integral over the triple product in the above expression can be analytically evaluated using the Wigner-3j symbols; cf. Wigner [153]. Since this work is concerned with incompressible flows, a hypersurface description implying a linear volume operator (in terms of $\boldsymbol{c}_\Sigma$) is advantageous. Motivated by eq. (2.15), we expand the third power of the radius $R$ in terms of spherical harmonics $Y_l^m(\varphi,\theta)$, i.e.

$$R^3(\varphi,\theta;\boldsymbol{c}_\Sigma) = \sum_{l=0}^{L_\Sigma}\sum_{m=-l}^{l} c_{\Sigma,lm} Y_l^m(\varphi,\theta), \tag{2.18}$$

producing the convenient expression

$$\mathrm{vol}(\boldsymbol{c}_\Sigma) = \frac{\sqrt{4\pi}}{3} c_{\Sigma,00}. \tag{2.19}$$

Introducing $\boldsymbol{y}_\Sigma(\varphi,\theta) := [Y_l^m(\varphi,\theta)]$ yields

$$R = \langle \boldsymbol{c}_\Sigma, \boldsymbol{y}_\Sigma\rangle^{\frac{1}{3}}, \quad R_\varphi = \frac{\langle \boldsymbol{c}_\Sigma, \partial_\varphi \boldsymbol{y}_\Sigma\rangle}{3\langle \boldsymbol{c}_\Sigma, \boldsymbol{y}_\Sigma\rangle^{\frac{2}{3}}} \quad \text{and} \quad R_\theta = \frac{\langle \boldsymbol{c}_\Sigma, \partial_\theta \boldsymbol{y}_\Sigma\rangle}{3\langle \boldsymbol{c}_\Sigma, \boldsymbol{y}_\Sigma\rangle^{\frac{2}{3}}}. \tag{2.20}$$

Henceforth, representatives of this class are referred to as *perturbed spheres*.

### 2.2.1. Curvature of hypersurfaces embedded in $\mathbb{R}^3$

Let $\boldsymbol{F} : \mathbb{R}^2 \mapsto \mathbb{R}^3$ be a twice continuously differentiable map defining the orientable hypersurface

$$\Sigma = \{\boldsymbol{F}(u,v) : (u,v) \in \mathcal{B}\} \tag{2.21}$$

with some compact $\mathcal{B} \subset \mathbb{R}^2$. The outer unit normal to $\Sigma$ can be computed as

$$\boldsymbol{n}_\Sigma(u,v) := \frac{\boldsymbol{F}_u \times \boldsymbol{F}_v}{\|\boldsymbol{F}_u \times \boldsymbol{F}_v\|}. \tag{2.22}$$

The metric and shape tensor, respectively, are

$$\boldsymbol{G}(u,v) := \begin{bmatrix} \langle \boldsymbol{F}_u, \boldsymbol{F}_u\rangle & \langle \boldsymbol{F}_u, \boldsymbol{F}_v\rangle \\ \langle \boldsymbol{F}_v, \boldsymbol{F}_u\rangle & \langle \boldsymbol{F}_v, \boldsymbol{F}_v\rangle \end{bmatrix} \qquad \text{and} \qquad \boldsymbol{L}(u,v) := \begin{bmatrix} \langle \boldsymbol{F}_{uu}, \boldsymbol{n}_\Sigma\rangle & \langle \boldsymbol{F}_{uv}, \boldsymbol{n}_\Sigma\rangle \\ \langle \boldsymbol{F}_{vu}, \boldsymbol{n}_\Sigma\rangle & \langle \boldsymbol{F}_{vv}, \boldsymbol{n}_\Sigma\rangle \end{bmatrix}. \tag{2.23}$$

From the above quantities we may compute the Weingarten tensor

$$\boldsymbol{W} := \boldsymbol{G}^{-1}\boldsymbol{L} = \begin{bmatrix} \langle \boldsymbol{F}_v, \boldsymbol{F}_v\rangle & -\langle \boldsymbol{F}_u, \boldsymbol{F}_v\rangle \\ \langle -\boldsymbol{F}_v, \boldsymbol{F}_u\rangle & \langle \boldsymbol{F}_u, \boldsymbol{F}_u\rangle \end{bmatrix} \begin{bmatrix} \langle \boldsymbol{F}_{uu}, \boldsymbol{F}_u \times \boldsymbol{F}_v\rangle & \langle \boldsymbol{F}_{uv}, \boldsymbol{F}_u \times \boldsymbol{F}_v\rangle \\ \langle \boldsymbol{F}_{vu}, \boldsymbol{F}_u \times \boldsymbol{F}_v\rangle & \langle \boldsymbol{F}_{vv}, \boldsymbol{F}_u \times \boldsymbol{F}_v\rangle \end{bmatrix} \|\boldsymbol{F}_u \times \boldsymbol{F}_v\|^{-3}, \tag{2.24}$$

which is invariant under rotation. For a detailed treatment of differential geometry, the reader is referred to the book of Kühnel [79]. While the metric and shape tensor are respectively symmetric, it is worth noting that the Weingarten tensor does not share this property in general. Let $\{\kappa, \boldsymbol{w}\}_i$ denote the eigenpairs of $\boldsymbol{W}$, where the eigenvalues correspond to the principal curvatures $\kappa_i$. By superposition of the tangents $\langle \boldsymbol{w}_i, \boldsymbol{e}_1\rangle \boldsymbol{F}_u + \langle \boldsymbol{w}_i, \boldsymbol{e}_2\rangle \boldsymbol{F}_v$, the associated principal tangents are obtained. Furthermore, the sum of the principal curvatures, which corresponds to the trace of the Weingarten map, is commonly referred to as *mean curvature*, i.e.

$$\kappa_\Sigma := \kappa_1 + \kappa_2, \tag{2.25}$$

which is connected to the unit normal from eq. (2.22) by

$$\kappa_\Sigma = -\operatorname{div}_\Sigma \boldsymbol{n}_\Sigma. \tag{2.26}$$

The principal unit tangents emerge from

$$\boldsymbol{\tau}_i(u,v) = \frac{\boldsymbol{F}_u\langle \boldsymbol{w}_i, \boldsymbol{e}_u\rangle + \boldsymbol{F}_v\langle \boldsymbol{w}_i, \boldsymbol{e}_v\rangle}{\|\boldsymbol{F}_u\langle \boldsymbol{w}_i, \boldsymbol{e}_u\rangle + \boldsymbol{F}_v\langle \boldsymbol{w}_i, \boldsymbol{e}_v\rangle\|}, \tag{2.27}$$

constituting the orthonormal system $\{\boldsymbol{n}_\Sigma, \boldsymbol{\tau}_1, \boldsymbol{\tau}_2\}$; cf. fig. (2.3) for an illustration. For any point $\boldsymbol{x}_0 \in \Sigma$, with $\boldsymbol{n}_0 := \boldsymbol{n}_\Sigma(\boldsymbol{x}_0)$ and $\boldsymbol{b}(\alpha; \boldsymbol{x}_0) := \cos\alpha\boldsymbol{\tau}_1(\boldsymbol{x}_0) + \sin\alpha\boldsymbol{\tau}_2(\boldsymbol{x}_0)$, the intersection of $\Sigma$ with a plane spanned

by $\{\boldsymbol{n}_0, \boldsymbol{b}\}$, i.e.

$$\boldsymbol{s}_\mathrm{n}(\alpha) := \{\boldsymbol{x} \in \Sigma : \langle \boldsymbol{x} - \boldsymbol{x}_0, \boldsymbol{n}_0 \times \boldsymbol{b}(\alpha; \boldsymbol{x}_0)\rangle = 0\}, \tag{2.28}$$

is called a *normal section* or *normal curve*. Its curvature at $\boldsymbol{x}_0$ can be connected to the WEINGARTEN tensor by

$$\kappa^\mathrm{n}(\boldsymbol{b}(\alpha); \boldsymbol{x}_0) = \boldsymbol{w}(\boldsymbol{b}(\alpha))^\mathsf{T} \boldsymbol{W}(\boldsymbol{x}_0) \boldsymbol{w}(\boldsymbol{b}(\alpha)) \qquad \text{with} \qquad \boldsymbol{w}(\boldsymbol{b}) := \begin{bmatrix} \langle \boldsymbol{b}, \boldsymbol{\tau}_1 \rangle \\ \langle \boldsymbol{b}, \boldsymbol{\tau}_2 \rangle \end{bmatrix}. \tag{2.29}$$

It is worth noting that the normal curvature is symmetric with respect to the direction $\boldsymbol{b}$ of the section, i.e. $\kappa^\mathrm{n}(\boldsymbol{b}; \boldsymbol{x}_0) = \kappa^\mathrm{n}(-\boldsymbol{b}; \boldsymbol{x}_0)$. This relation is commonly referred to as EULER's theorem of differential geometry, which can be conveniently expressed as

$$\begin{aligned} \kappa^\mathrm{n}(\boldsymbol{b}(\alpha); \boldsymbol{x}_0) &= \frac{\kappa_1 + \kappa_2}{2} + \frac{\kappa_1 - \kappa_2}{2} \cos 2\alpha \\ &= \tilde{\kappa}_0(\boldsymbol{x}_0) + \tilde{\kappa}_1(\boldsymbol{x}_0) \cos 2\alpha' + \tilde{\kappa}_2(\boldsymbol{x}_0) \sin 2\alpha'. \end{aligned} \tag{2.30}$$

The coefficients $\{\tilde{\kappa}_i\}$ of the second expression resemble an instance of the invariants of the WEINGARTEN tensor for a tangential coordinate system, rotated by some given $\alpha_0$ with $\alpha' = \alpha - \alpha_0$. Figure (2.3) provides an illustration. In what follows, we briefly exemplify the above expressions for two special classes of maps.

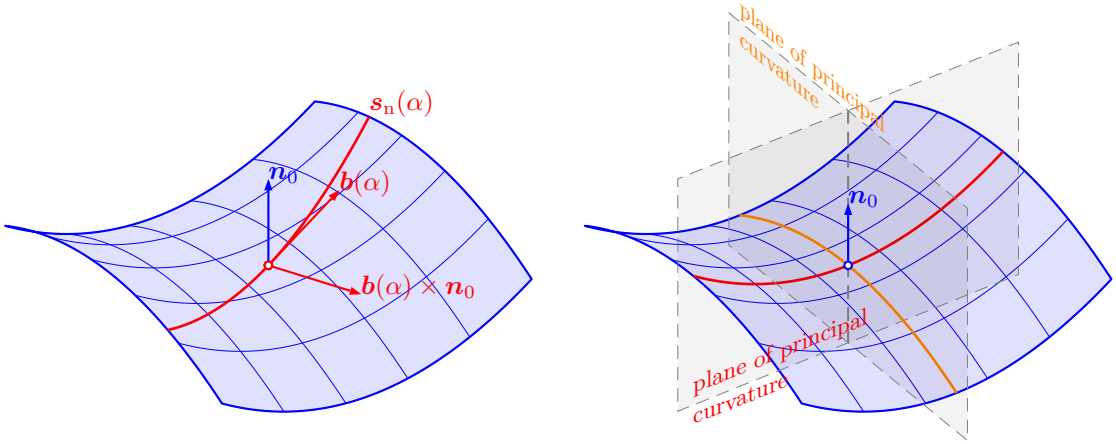


Figure 2.3.: Normal section of $\Sigma$ at $\boldsymbol{x}_0$ (left; cf. eq. (2.28)) and planes of principal curvature (right).

### Graph representation

Let $h : \mathbb{R}^2 \mapsto \mathbb{R}$ with $h(0,0) = 0$ be sufficiently smooth, $\{\boldsymbol{\tau}_u, \boldsymbol{\tau}_v, \boldsymbol{n}_0\}$ linearly independent unit vectors s.t. $\langle \boldsymbol{\tau}_u, \boldsymbol{n}_0 \rangle = \langle \boldsymbol{\tau}_v, \boldsymbol{n}_0 \rangle = 0$ and $\boldsymbol{x}_0 \in \mathbb{R}^3$. Note that linear independence implies $(-1, 1) \ni \langle \boldsymbol{\tau}_u, \boldsymbol{\tau}_v \rangle =: \psi$. Then $\Sigma$, cf. eq. (2.21), can be represented as the graph of $h$, i.e.

$$\boldsymbol{F}(u, v; \boldsymbol{x}_0) = \boldsymbol{x}_0 + u\boldsymbol{\tau}_u + v\boldsymbol{\tau}_v + h(u, v)\boldsymbol{n}_0. \tag{2.31}$$

The Weingarten map given in eq. (2.24) takes the form

$$\boldsymbol{W}(u,v;\psi,\boldsymbol{x}_0) = \frac{\begin{bmatrix}(1+h_v^2)h_{uu}-(h_uh_v+\psi)h_{uv} & (1+h_v^2)h_{uv}-(h_uh_v+\psi)h_{vv}\\ (1+h_u^2)h_{uv}-(h_uh_v+\psi)h_{uu} & (1+h_u^2)h_{vv}-(h_uh_v+\psi)h_{uv}\end{bmatrix}}{(1+h_u^2+h_v^2-\psi^2-2\psi h_uh_v)^{\frac{3}{2}}}. \tag{2.32}$$

If the tangent vectors $\boldsymbol{\tau}_u$ and $\boldsymbol{\tau}_v$ are orthogonal ($\psi = 0$), the mean curvature from eq. (2.25) becomes

$$\kappa_\Sigma = \frac{(1+h_v^2)h_{uu}+(1+h_u^2)h_{vv}-2h_{uv}h_uh_v}{(1+h_u^2+h_v^2)^{\frac{3}{2}}}. \tag{2.33}$$

For coordinate systems which are tangential to $\Sigma$ in $\boldsymbol{x}_0$, i.e. if $\operatorname{span}(\boldsymbol{\tau}_u,\boldsymbol{\tau}_v) = \operatorname{span}(\boldsymbol{F}_u(0,0;\boldsymbol{x}_0),\boldsymbol{F}_v(0,0;\boldsymbol{x}_0))$, it holds that $h_u(0,0) = h_v(0,0) = 0$ and, hence, eq. (2.32) simplifies to

$$\boldsymbol{W}(0,0;\psi,\boldsymbol{x}_0) = \frac{1}{(1-\psi^2)^{\frac{3}{2}}}\begin{bmatrix}h_{uu}-\psi h_{uv} & h_{uv}-\psi h_{vv}\\ h_{uv}-\psi h_{uu} & h_{vv}-\psi h_{uv}\end{bmatrix}. \tag{2.34}$$

The inverse function theorem states that any differentiable manifold can locally be represented by a graph, implying that, irrespective of the original parametrization, the Weingarten map admits three invariants for arbitrary but constant $\psi \in (-1,1)$. Appendix A.3 shows that, locally, any sufficiently smooth hypersurface can be represented as the graph of a function.

**Spherical coordinates**

For star-shaped hypersurfaces parametrized over $\mathbb{S}^2$, cf. section 2.2, the tangent space is spanned by

$$\boldsymbol{R}_\varphi = R_\varphi \boldsymbol{e}_r + R\sin\theta\,\boldsymbol{e}_\varphi \qquad \text{and} \qquad \boldsymbol{R}_\theta = R_\theta \boldsymbol{e}_r + R\boldsymbol{e}_\theta, \tag{2.35}$$

implying the outer unit normal

$$\boldsymbol{n}_\Sigma = \frac{\boldsymbol{R}_\theta \times \boldsymbol{R}_\varphi}{\|\boldsymbol{R}_\theta \times \boldsymbol{R}_\varphi\|} = \frac{R\boldsymbol{e}_r - R_\theta \boldsymbol{e}_\theta - \frac{R_\varphi}{\sin\theta}\boldsymbol{e}_\varphi}{\sqrt{R^2+R_\theta^2+\frac{R_\varphi^2}{\sin^2\theta}}}. \tag{2.36}$$

Plugging the tangents from eq. (2.35) and the second derivatives

$$\begin{aligned}\boldsymbol{R}_{\theta\theta} &= (R_{\theta\theta}-R)\boldsymbol{e}_r + 2R_\theta \boldsymbol{e}_\theta,\\ \boldsymbol{R}_{\varphi\varphi} &= R_{\varphi\varphi}\boldsymbol{e}_r + 2R_\varphi \sin\theta\,\boldsymbol{e}_\varphi + R\sin\theta\,\partial_\varphi \boldsymbol{e}_\varphi,\\ \boldsymbol{R}_{\varphi\theta} &= R_{\varphi\theta}\boldsymbol{e}_r + R_\varphi \boldsymbol{e}_\theta + (R\cos\theta + R_\theta\sin\theta)\boldsymbol{e}_\varphi,\end{aligned} \tag{2.37}$$

into eq. (2.24), we obtain the metric tensor

$$\boldsymbol{G} = \begin{bmatrix}R_\theta^2+R^2 & R_\theta R_\varphi\\ R_\theta R_\varphi & R_\varphi^2+R^2\sin^2\theta\end{bmatrix} \quad \text{with} \quad \det\boldsymbol{G} = R^2\left(\left(R^2+R_\theta^2\right)\sin^2\theta + R_\varphi^2\right), \tag{2.38}$$

as well as the shape tensor

$$\boldsymbol{L} = \frac{R\begin{bmatrix} (R(R_{\theta\theta} - R) - 2R_\theta^2)\sin\theta & (R_{\varphi\theta}R - R_\theta R_\varphi)\sin\theta - R_\varphi(R\cos\theta + R_\theta\sin\theta) \\ \text{sym.} & (RR_{\varphi\varphi} - 2R_\varphi^2)\sin\theta - R^2\sin^3\theta + RR_\theta\sin^2\theta\cos\theta \end{bmatrix}}{\sqrt{\det \boldsymbol{G}}}. \tag{2.39}$$

**Degeneration at the poles** Plugging eq. (2.13) into eq. (2.36) and evaluating for $\theta \in \{0, \pi\}$ produces an expression of type $\frac{0}{0}$. Hence, the evaluation requires the application of the rule of L'HÔSPITAL. One obtains

$$\lim_{\sin\theta\to 0} \frac{R_\varphi}{\sin\theta} = \left.\frac{R_{\varphi\theta}}{\cos\theta}\right|_{\theta\in\{0,\pi\}} = \cos\theta R_{\varphi\theta}|_{\theta\in\{0,\pi\}}\,, \tag{2.40}$$

producing the normal

$$\boldsymbol{n}_\Sigma|_{\theta\in\{0,\pi\}} = \frac{R\boldsymbol{e}_r - R_\theta\boldsymbol{e}_\theta - R_{\varphi\theta}\boldsymbol{e}_\varphi}{\sqrt{R^2 + R_\theta^2 + R_{\varphi\theta}^2}} = \frac{[R_{\varphi\theta}\sin\varphi - R_\theta\cos\varphi, -R_{\varphi\theta}\cos\varphi - R_\theta\sin\varphi, R]^\mathsf{T}}{\cos\theta\sqrt{R^2 + R_\theta^2 + R_{\varphi\theta}^2}}. \tag{2.41}$$

Exploiting the periodicity implied by the conditions in eq. (2.13) shows that, despite the apparent dependence on the azimuthal angle $\varphi$, it holds that $\partial_\varphi \boldsymbol{n}_\Sigma|_{\theta\in\{0,\pi\}} = \boldsymbol{0}$. Despite the existence of the normal, combining eq. (2.13) and eq. (2.38) reveals that the basis $\{\boldsymbol{R}_\varphi, \boldsymbol{R}_\theta\}$ degenerates due to $\boldsymbol{R}_\varphi|_{\theta\in\{0,\pi\}} = \boldsymbol{0}$. Since this also implies the non-invertibility of the metric tensor $\boldsymbol{G}$, cf. eq. (2.23), a graph parametrization of $\Sigma$ is applied for the computation of the three invariants of the WEINGARTEN tensor $\boldsymbol{W}_0$ at the poles. In what follows, only the north pole is considered, i.e. let $\boldsymbol{x}_0 := \boldsymbol{R}(0,0)$; the calculations are readily transferred to $\theta = \pi$. The derivations below extend the results of Wolter and Tuohy [155], who propose the following procedure for the computation of the aforementioned invariants at $\boldsymbol{x}_0$ with $\boldsymbol{n}_0 := \boldsymbol{n}_\Sigma(\boldsymbol{x}_0)$ from eq. (2.41):

1. Select three unit tangents $\boldsymbol{\tau}_i$ such that $\langle\boldsymbol{\tau}_i, \boldsymbol{n}_0\rangle = 0$ ,$\langle\boldsymbol{\tau}_1, \boldsymbol{\tau}_3\rangle = 0$ and $\langle\boldsymbol{\tau}_2, \boldsymbol{\tau}_3\rangle \in (-1, 1) \setminus \{0\}$.

2. Compute the normal curvatures $\kappa_i^\mathrm{n} := \kappa^\mathrm{n}(\boldsymbol{\tau}_i)$ associated to $\boldsymbol{\tau}_i$.

3. Exploit the connection of the WEINGARTEN map and the normal curvature given in eq. (2.29) in combination with the special form of the WEINGARTEN map for the graph case, cf. eq. (2.34) for $\psi = \langle\boldsymbol{\tau}_1, \boldsymbol{\tau}_3\rangle = 0$, to obtain

$$\begin{aligned} &W_{0,11} = \kappa_1^\mathrm{n} (= h_{uu}), \quad W_{0,22} = \kappa_3^\mathrm{n} (= h_{vv}) \quad \text{and} \\ &W_{0,12} = W_{0,21} = \frac{\kappa_2^\mathrm{n} - \langle\boldsymbol{\tau}_1, \boldsymbol{\tau}_2\rangle^2\kappa_1^\mathrm{n} - \langle\boldsymbol{\tau}_1, \boldsymbol{\tau}_3\rangle^2\kappa_3^\mathrm{n}}{2\langle\boldsymbol{\tau}_1, \boldsymbol{\tau}_2\rangle\langle\boldsymbol{\tau}_3, \boldsymbol{\tau}_2\rangle} (= h_{uv}). \end{aligned} \tag{2.42}$$

In essence, the above algorithm exploits EULER's theorem of differential geometry, cf. eq. (2.30), namely by (i) choosing some $\alpha_0$ corresponding to a spatially fixed tangential coordinate system, (ii) evaluating the normal curvatures at three different positions $\{\alpha_i\}$ and (iii) inferring the invariants of the WEINGARTEN tensor. Note that the work of Wolter and Tuohy [155] also covers the intricate computation of derivatives of the curvature. However, the application to spherical coordinates requires some modifications, which are outlined in what follows. First, note that the map given in eq. (2.10) induces a family of *isoparametric*

curves

$$\boldsymbol{s}_{\mathrm{n}}(\theta;\varphi_0) = \{R(\varphi_0,\theta)\boldsymbol{e}_r(\varphi_0,\theta) : \theta \in [0,\pi]\}, \tag{2.43}$$

with isoparameter $\varphi_0 \in [0, 2\pi)$. The tangent and normal, respectively, are

$$\boldsymbol{\tau}^{\mathrm{iso}}(\varphi_0) := \left[\frac{R\boldsymbol{e}_\theta + R_\theta \boldsymbol{e}_r}{\sqrt{R^2+R_\theta^2}}\right](\varphi_0,0) \quad \text{and} \quad \boldsymbol{n}^{\mathrm{iso}}(\varphi_0) := \left[\frac{R\boldsymbol{e}_r - R_\theta \boldsymbol{e}_\theta}{\sqrt{R^2+R_\theta^2}}\right](\varphi_0,0). \tag{2.44}$$

Despite the fact that the isoparametric curve is confined by a plane, i.e. $\boldsymbol{s}_{\mathrm{n}}(\theta;\varphi_0) \subset \mathrm{span}(\boldsymbol{\tau}^{\mathrm{iso}}, \boldsymbol{n}^{\mathrm{iso}})$, it is not a normal section of $\Sigma$, since the normals of $\Sigma$ and $\boldsymbol{s}_{\mathrm{n}}$ at $\boldsymbol{x}_0$ do not coincide in general[1], i.e. $\langle \boldsymbol{n}_0, \boldsymbol{n}^{\mathrm{iso}}(\varphi_0)\rangle = \frac{\sqrt{R^2+R_\theta^2}}{\sqrt{R^2+R_\theta^2+R_{\varphi\theta}^2}} \neq 1$. To obtain the normal curvature of $\Sigma$ from the isoparametric curve, let

$$\kappa^{\mathrm{iso}}(\varphi_0) := \langle \partial_\theta \boldsymbol{\tau}^{\mathrm{iso}}\big|_{\theta=0}, \boldsymbol{n}_0\rangle = \left[\frac{(R_{\theta\theta}-R)R - 2R_\theta^2}{(R^2+R_\theta^2)\sqrt{R^2+R_\theta^2+R_{\varphi\theta}^2}}\right](\varphi_0,0), \tag{2.45}$$

i.e. the computation is carried out using $\boldsymbol{n}_0 = \boldsymbol{n}_\Sigma(\boldsymbol{x}_0)$ instead of $\boldsymbol{n}^{\mathrm{iso}}(\boldsymbol{x}_0)$. Let $\boldsymbol{\tau}_1 = \boldsymbol{\tau}^{\mathrm{iso}}(0)$. Finding an orthogonal vector $\boldsymbol{\tau}_3 = \boldsymbol{\tau}^{\mathrm{iso}}(\bar\varphi)$ is equivalent to finding a root of

$$\langle \boldsymbol{\tau}^{\mathrm{iso}}(0), \boldsymbol{\tau}^{\mathrm{iso}}(\bar\varphi)\rangle = \frac{R^2(1+\cos\bar\varphi) + R_\theta(0,0)R_\theta(0,\bar\varphi)}{\sqrt{R^2+R_\theta(0,0)}\sqrt{R^2+R_\theta(0,\bar\varphi)}}, \tag{2.46}$$

which, due to the strong non-linearity, is cumbersome. Thus, a modification of the approach of Wolter and Tuohy [155] is proposed:

1. Select three azimuthal angles $\{\varphi_0^m\}_{m=1}^3$ such that the associated tangents $\boldsymbol{\tau}_m^{\mathrm{iso}} := \boldsymbol{\tau}^{\mathrm{iso}}(\varphi_0^m)$ are linearly independent, say, e.g., $\varphi_0^m = \pi\frac{m-1}{4}$. For ease of notation, let $\gamma = \langle \boldsymbol{\tau}_1^{\mathrm{iso}}, \boldsymbol{\tau}_3^{\mathrm{iso}}\rangle$, $\mu = \langle \boldsymbol{\tau}_1^{\mathrm{iso}}, \boldsymbol{\tau}_2^{\mathrm{iso}}\rangle$ and $\nu = \langle \boldsymbol{\tau}_2^{\mathrm{iso}}, \boldsymbol{\tau}_3^{\mathrm{iso}}\rangle$, which are connected to the angles within the tangential system used in eq. (2.30) via $\gamma = \cos\alpha_3'$, $\mu = \cos\alpha_2'$ and $\nu = \cos(\alpha_3' - \alpha_1')$.
2. Choose the basis vectors $\boldsymbol{\tau}_1 := \boldsymbol{\tau}_1^{\mathrm{iso}}$ and $\boldsymbol{\tau}_3 := \frac{\boldsymbol{\tau}_3^{\mathrm{iso}} - \gamma\boldsymbol{\tau}_1^{\mathrm{iso}}}{\sqrt{1-\gamma^2}}$, implying that $\psi = \langle \boldsymbol{\tau}_1, \boldsymbol{\tau}_3\rangle = 0$.
3. Evaluate the associated normal curvatures $\{\kappa_m^{\mathrm{iso}}\}_{m=1}^3$, cf. eq. (2.29), using eq. (2.45).
4. Compute the component vectors $\boldsymbol{w}(\boldsymbol{\tau}_m^{\mathrm{iso}})$, cf. the second expression in eq. (2.29), to obtain

$$\boldsymbol{w}(\boldsymbol{\tau}_1^{\mathrm{iso}}) = [1,0]^{\mathsf{T}}, \quad \boldsymbol{w}(\boldsymbol{\tau}_2^{\mathrm{iso}}) = \left[\mu, \frac{\nu-\gamma\mu}{\sqrt{1-\gamma^2}}\right]^{\mathsf{T}}, \quad \text{and} \quad \boldsymbol{w}(\boldsymbol{\tau}_3^{\mathrm{iso}}) = \left[\gamma, \sqrt{1-\gamma^2}\right]^{\mathsf{T}}.$$

5. Using again eq. (2.29) yields a linear system of equations governing the elements of $\boldsymbol{W}_0$, which by exploiting $W_{0,11} = \kappa_1^{\mathrm{iso}}$ and $W_{0,12} = W_{0,21}$ reduces to

$$\begin{bmatrix} 2\mu\frac{\nu-\gamma\mu}{\sqrt{1-\gamma^2}} & \frac{(\nu-\gamma\mu)^2}{1-\gamma^2} \\ 2\gamma\sqrt{1-\gamma^2} & 1-\gamma^2 \end{bmatrix} \begin{bmatrix} W_{0,12} \\ W_{0,22} \end{bmatrix} = \begin{bmatrix} \kappa_2^{\mathrm{iso}} - \mu^2\kappa_1^{\mathrm{iso}} \\ \kappa_3^{\mathrm{iso}} - \gamma^2\kappa_1^{\mathrm{iso}} \end{bmatrix}. \tag{2.47}$$

[1] The normals coincide iff $R_{\varphi\theta} \equiv 0$, which is the case for some classes of hypersurfaces, e.g., ellipsoids, whose semiaxes are aligned with the coordinate axes. Hence, one has to be careful when selecting cases for numerical verification.

Note that the solution of Wolter and Tuohy [155] is retrieved for $\gamma = 0$; cf. eq. (2.42).

Equation (2.47) is invertible iff $(\mu - \gamma\nu)(\nu - \gamma\mu) \neq 0$, resembling the condition of linear independence imposed on the evaluation directions $\{\boldsymbol{\tau}_m^{\text{iso}}\}$. In general, it holds that $\varphi - \alpha' \neq \text{const}$, cf. eq. (2.30), i.e. the angle $\alpha'$ associated to the tangential plane cannot be obtained from the azimuthal angle $\varphi$ by shift. This becomes clear if one considers that the associated normals $\boldsymbol{n}_0$ and $\boldsymbol{n}^{\text{iso}}$, resembling the respective axes of rotation, do not coincide. When choosing $\varphi_0^1 = 0$ and $\varphi_0^3 = \frac{\pi}{2}$ as above, one obtains $\gamma \sim 10^{-4}$ for the cases considered in this thesis, corresponding to an angular misalignment of approx. $10^{-3}$ degrees; cf. fig. (2.4) for an exemplary illustration.

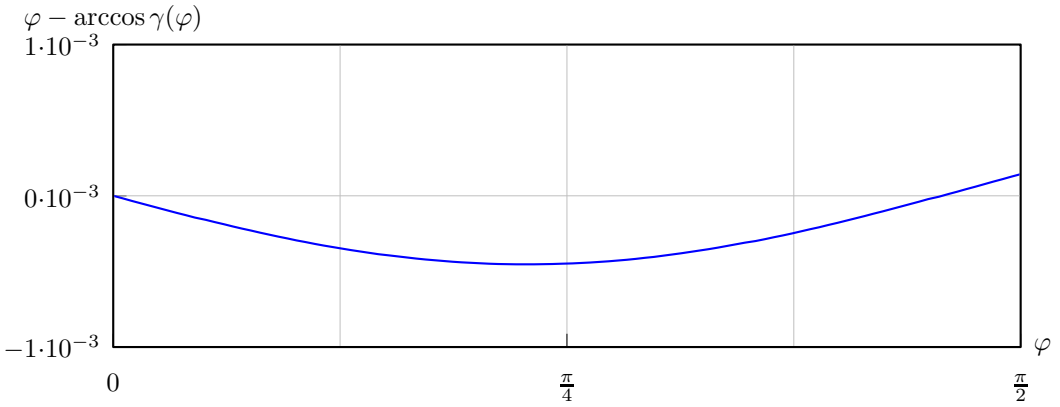


Figure 2.4.: Angular misalignment of azimuthal angle $\varphi$ and angle $\alpha'$ associated to tangential plane (perturbed sphere (cf. eq. (2.18)) with $L_\Sigma = 8$; randomly generated coefficients $\boldsymbol{c}_\Sigma$ with variance $\hat{\sigma}^2 = 10^{-4}$).

# 3. Numerical method

The objective of the present chapter can be cast as follows: section 3.1 introduces the flow solver employed for the numerical integration of the NAVIER-STOKES equations. This thesis is concerned with two-phase flows inherently containing free interfaces, which are represented by discrete volume fractions. To obtain continuous information suitable for both qualitative and quantitative analysis, sections 3.2 and 3.3 are devoted to the extraction of hypersurface representations by means of global fitting and principal component analysis. Within section 3.4, the aforementioned tools are applied within a numerical simulation of fluid particles freely rising in ambient media.

## 3.1. The flow solver FS3D

The software **F**ree **S**urface **3D** was originally developed by Rieber [120] at the *Institut für Thermodynamik der Luft- und Raumfahrt* (ITLR) at University Stuttgart. Since then, the code has been massively extended both at the ITLR and the department *Mathematische Modellierung & Analysis* (MMA) at TU Darmstadt. Among its applications are, e.g., freely rising droplets (Albert et al. [5]), binary droplet collision (Focke and Bothe [48, 49], Liu and Bothe [83, 84]), species transport (Fleckenstein and Bothe [47], Weiner and Bothe [149]), falling films (Albert et al. [3]) or thermocapillary flows (Ma and Bothe [88], Fath and Bothe [45]).

FS3D employs a time-explicit finite volume approach on a CARTESIAN mesh to numerically solve the two-phase NAVIER-STOKES equations in three spatial dimensions. A cuboidal domain $\Omega$ is decomposed into $N_{\Omega,i} \times N_{\Omega,j} \times N_{\Omega,k}$ spatially fixed control volumes $\Omega_{ijk}$ of size $\Delta x_i \times \Delta y_j \times \Delta z_k$, where two adjacent control volumes share a face. The decomposition comprises ghost control volumes, which were proposed by Blazek [16] and LeVeque [82]. These additional control volumes at the domain boundaries allow for the application of a single discretization scheme everywhere in the interior of the domain and facilitate decomposition for parallel implementation; cf. fig. (3.1).

The variable arrangement is staggered, as proposed by Harlow and Welch [61], i.e. the discrete pressures are assigned to the cell centers, whereas the velocity components are assigned to the respective faces. Versteeg and Malalasekera [147] show that otherwise the pressure and velocity fields may decouple and exhibit unphysical checkerboard patterns. The Volume-of-Fluid (VOF) approach of Hirt and Nichols [64] is exploited to capture the deformable interface $\Sigma$, where to every control volume one assigns a so-called volume fraction $0 \leq f_{ijk} \leq 1$, indicating the fraction of, say, the disperse phase. Therefore, $f = 1$ ($f = 0$) corresponds to a control volume located entirely within the disperse (continuous) phase, whereas a control volume $\Omega_{ijk}$ with $0 < f_{ijk} < 1$ contains fractions of both phases and, hence, a patch of the interface $\Sigma$. Figure (3.2) illustrates the setup. The concept described above produces a so-called *one-phase* formulation of the NAVIER-STOKES equations given in section 2.1, i.e. the equations hold everywhere in the domain. The evaluation of phase-dependent quantities is carried out based on the

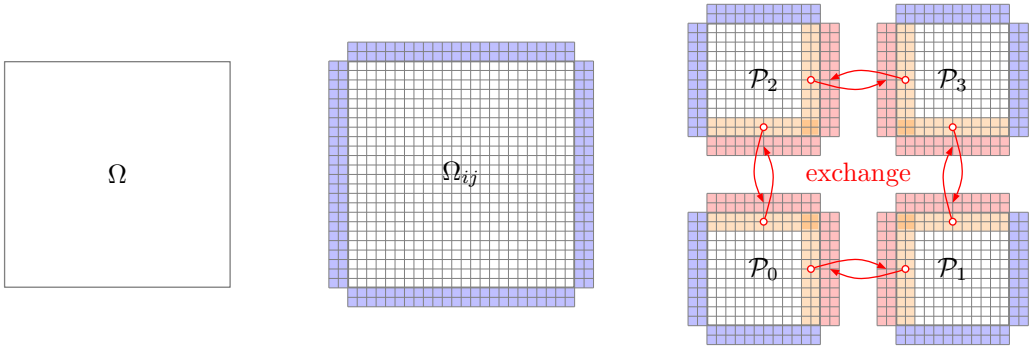


Figure 3.1.: Computational domain $\Omega$ (left) and decomposition $\Omega_{ij}$ (center) with ghost cells (■: boundary, ■: interior target, ■: interior source) and parallelization strategy for 4 processes $\{\mathcal{P}_i\}$ (right).

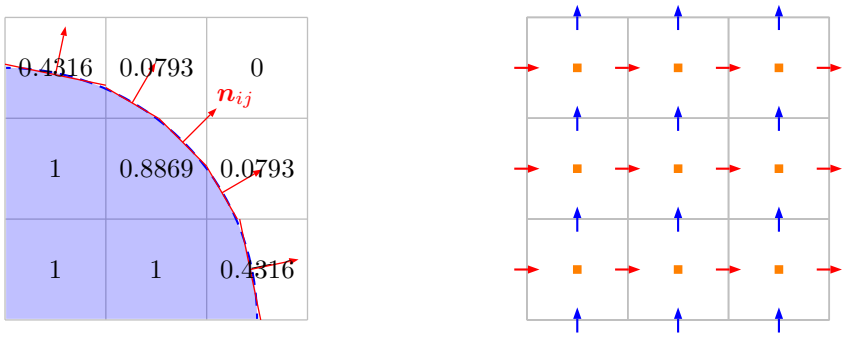


(a) volume fractions

(b) staggered arrangement

Figure 3.2.: Sketch of computational grid in two spatial dimensions: disperse phase (blue) inducing volume fractions $0 \leq f_{ij} \leq 1$ with outer normals $\boldsymbol{n}_{ij}$ (left) and staggered arrangement (right) of velocity components $u_{ij}$ (→), $v_{ij}$ (↑) and pressures $p_{ij}$ (■).

volume fractions $f_{ijk}$. One obtains

$$\partial_t(\rho \boldsymbol{u}) + \nabla \cdot (\rho \boldsymbol{u} \otimes \boldsymbol{u}) = -\nabla p + \nabla \cdot \left(\mu \left(\nabla \boldsymbol{u} + \nabla \boldsymbol{u}^{\mathsf{T}}\right)\right) + \rho \boldsymbol{g} + \boldsymbol{f}_\Sigma, \tag{3.1}$$

$$\nabla \cdot \boldsymbol{u} = 0, \tag{3.2}$$

$$\partial_t f + \langle \boldsymbol{u}, \nabla f \rangle = 0, \tag{3.3}$$

where the influence of surface tension is considered in the form of body forces

$$\boldsymbol{f}_\Sigma = \sigma \kappa_\Sigma \boldsymbol{n}_\Sigma. \tag{3.4}$$

In what follows, we shall briefly discuss the concept of the solution of equations (3.1) to (3.3).

## Momentum balance

The discretization of the convective terms in eq. (3.1) resorts to a GODUNOV scheme in combination with the operator splitting introduced by Strang [133]. The transport of any quantity is split into three subsequent one-dimensional transports along the respective CARTESIAN axes, where an appropriate permutation provides second order accuracy. The operator splitting significantly reduces both the implementation complexity and the computational requirements. In order to correctly capture the coupling of tangential stresses at the free surface, a combination of arithmetic and harmonic averaging of viscosities in the interface cells, as introduced in Tryggvason et al. [145], is used.

## Time step size

The time-explicit EULER integration employs the minimum of

$$\Delta t_{\mathrm{CFL}} = \frac{\Delta x}{\|\boldsymbol{u}\|_\infty}, \quad \Delta t_{\mathrm{vis}} = \frac{\Delta x^2}{6 \max\{\nu_L, \nu_G\}} \quad \text{and} \quad \Delta t_{\mathrm{sft}} = \sqrt{\frac{(\rho_L + \rho_G)\Delta x^3}{4\pi\sigma}}. \tag{3.5}$$

While $\Delta t_{\mathrm{vis}}$ and $\Delta t_{\mathrm{sft}}$ can be computed a priori for constant material parameters, the maximum velocity $\|\boldsymbol{u}\|_\infty$ is a dynamic output of the flow solver. Hence, the adjustment of the step size is performed in each time step.

## Boundary conditions

Within this work, the conditions prescribed on the segments of $\partial\Omega = \bigcup_k \partial\Omega_k$ are:

**symmetric** $\langle \boldsymbol{u}, \boldsymbol{n}_{\partial\Omega} \rangle|_{\partial\Omega} = \langle \nabla p, \boldsymbol{n}_{\partial\Omega} \rangle|_{\partial\Omega} = 0$

**const. pressure** $p|_{\partial\Omega} = \text{const.}$

For the simulation of buoyant particles shown in section 3.4, a windowing technique is applied to prevent the disperse phase from leaving the domain. Once the center of mass of the particle leaves the cell it was located in during initialization, a layer-of-cells-wise shift of the variables (in the direction opposing the movement) is triggered. This considerably reduces the size of the required simulation domains.

**Note 3.1** (Spectral effects)**.** *Note that the windowing scheme causes a violation of the divergence criterion by introducing zero velocities at the inflow boundary, resulting in spurious accelerations of the droplet. However, numerical experiments have shown that this effect is negligible, since the amplitudes are small and the corresponding frequencies are well above those of physical interest.*

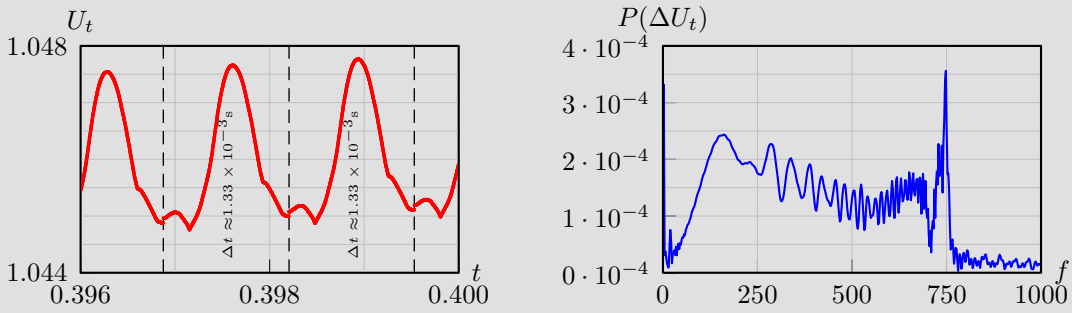


*The left figure shows the rise velocity in* $\frac{\text{cm}}{\text{s}}$ *of a buoyancy-driven droplet (*$\tilde{\mu} = 25$*,* $d = 0.5$mm*,* $\frac{d}{\Delta x} = 36$*), simulated with the windowing technique (*$\Omega = [0, 10\frac{2}{3}d]^2$*,* $N = 384$*). With a terminal velocity of* $U_t \approx 1.053\,07\frac{\text{cm}}{\text{s}}$*, the droplet center passes through a computational cell (*$\Delta x = 1.388 \times 10^{-3}$cm*) in approx.* $1.329 \times 10^{-3}$s*. This triggers the windowing algorithm and introduces a discontinuity in the velocity, indicated by the dashed lines in the left figure. The high-frequency, small-amplitude oscillations are numerical artifacts. The power spectrum of the acceleration (right) supports this finding by exhibiting a distinct peak at* 748.318Hz*, as compared to the expected* 758.21Hz*.*

## Volume conservation

As FS3D resorts to an explicit temporal discretization scheme, the velocity fields $\boldsymbol{u}'$ resulting from superpositions will in general violate the condition on the divergence given in eq. (3.2). To restore this property in a discrete sense, the projection method of Chorin [30] is applied, which in essence exploits the Helmholtz theorem. The pressure $p$ is governed by the Poisson-type equation

$$\nabla \cdot \left(\rho^{-1} \nabla p\right) = \frac{\nabla \cdot \boldsymbol{u}'}{\Delta t}, \tag{3.6}$$

whose solution is obtained by a specifcally designed multi-grid solver; see Rieber [120] for details. The solenodial velocity field $\boldsymbol{u}$ is obtained from the projection induced by the gradient of the pressure $p$ via

$$\boldsymbol{u} = \boldsymbol{u}' - \frac{\Delta t}{\rho} \nabla p. \tag{3.7}$$

## Advection of the volume fractions

In order to sustain a sharp interface, i.e. to avoid numerical smearing of the interface across several layers of cells, a geometrical transport of the volume fractions as proposed by Rider and Kothe [119] is applied. Their **P**iecewise **L**inear **I**nterface **C**alculation method (PLIC, cf. below) comprises a cell-based reconstruction of the interface using the normal $\boldsymbol{n}_{ijk}$ and subsequent intersection with the cell

face which is parallely shifted according to the velocity component. Figure (3.3) provides a sketch of the computation of the flux volume $\Delta f_{ijk}$ for the advection in $y$-direction. In consistence with the treatment

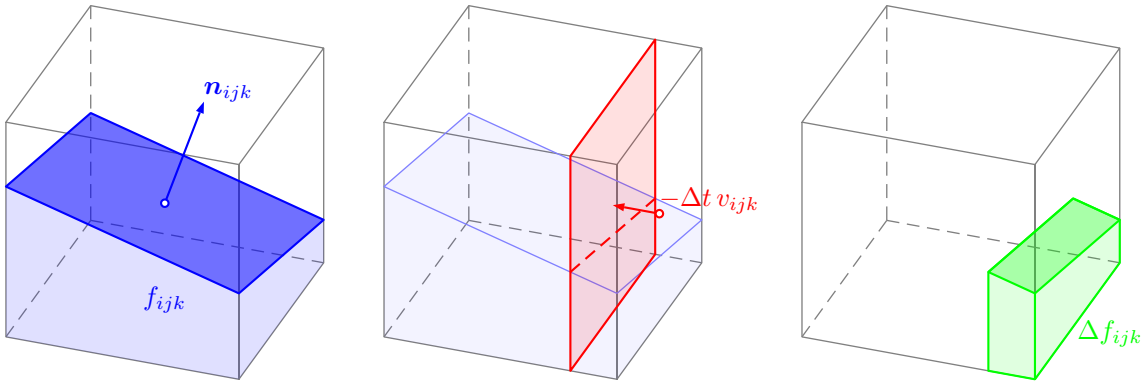


Figure 3.3.: Geometrically split advection of volume fraction field.

of the convective term, the operator splitting of Strang [133] is applied for the geometrical transport.

## Interface reconstruction (PLIC)

The reconstruction method of Rider and Kothe [119] produces a locally planar approximation, where the patches $\Sigma_{ijk} \subset \Omega_{ijk}$ are not necessarily connected; cf. fig. (3.2(a)). For a computational cell $\Omega_{ijk}$, given the cell-centered volume fraction $f_{ijk}$ and the normal $\boldsymbol{n}_{ijk}$, the concept can be described as follows: starting with the cell center as base point, the latter is shifted along the direction of $\boldsymbol{n}_{ijk}$ until the induced matches the prescribed volume fraction. Figure (3.4) illustrates the concept. Throughout this thesis, the intersections of the plane with the cell edges are employed for the interface fitting described in section 3.2.

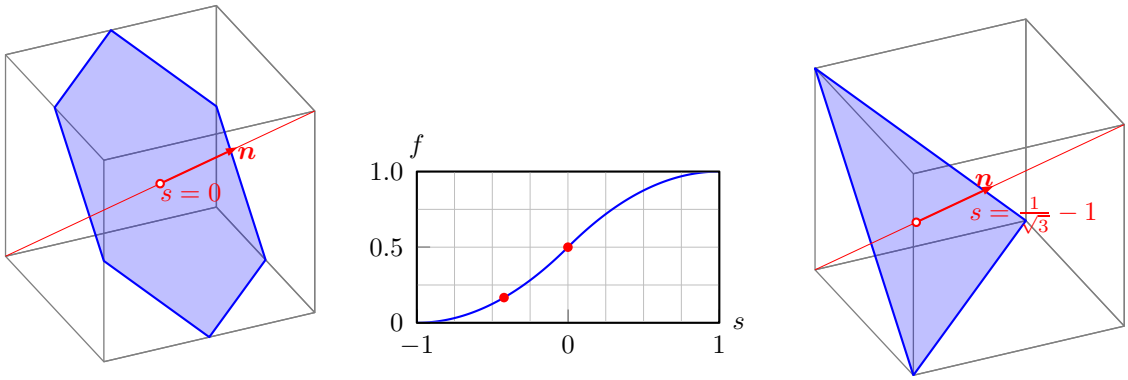


(a) $f(0) = \frac{1}{2}$ (b) $f(s)$ (c) $f(1/\sqrt{3} - 1) = \frac{1}{6}$

Figure 3.4.: Reconstruction of the interface from volume fractions $f_{ijk}$ and normals $\boldsymbol{n}_{ijk}$ (PLIC).

## Surface tension

The evaluation of the capillary forces in eq. (3.4) employs the normal computation of Youngs [158], where kernel smoothing is applied. In order to avoid parasitic currents, cf. Renardy and Renardy [116], the flow solver FS3D resorts to the continuum surface force discretization introduced by Brackbill et al. [23], in the balanced formulation proposed by Francois et al. [51]. The curvature required for the evaluation of eq. (3.4) is computed from height functions as proposed by Popinet [109], where, as opposed to the computation of the normal fields for the geometric transport, no smoothing is applied to the volume fractions. A detailled discussion of the properties of the height function algorithm is postponed to chapter 5.

## Initial conditions

Within the scope of this thesis, the initial velocities are zero. The initial volume fractions resemble the domains occupied by the respective phases induced by a user-specified hypersurface; cf. fig. (3.2(a)). Since the present analysis focusses on fluid particles, spheres with and without perturbations are of interest, where the accuracy of the initial volume fractions is of paramount importance. Unless explicitly stated otherwise, their numerical computation employs the algortihm introduced in chapter 4, where the respective algorithm parameters are given as required.

## Top level algorithm

Figure (3.5) provides a flowchart of FS3D. After intialization, the following steps are executed sequentially for each time step: first, the velocities are updated by convective accelerations, based on which the geometric transport is performed. After imposing viscous forces, surface tension effects and gravity forces, the pressure projection is employed to obtain a solenoidal velocity field.

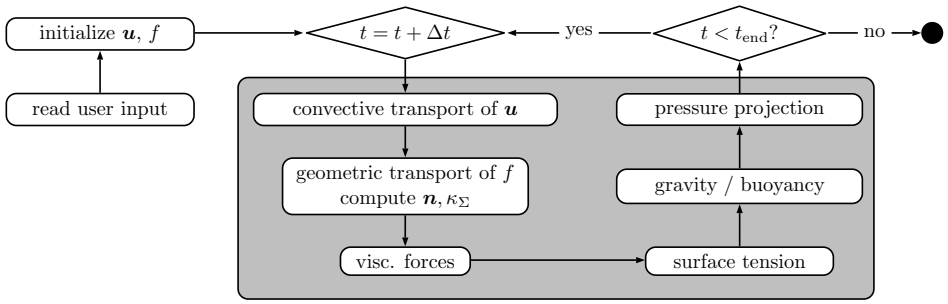


Figure 3.5.: Flowchart of the flow solver FS3D.

For ease of notation, one step of the time integration is written as

$$[\boldsymbol{u}^{n+1}, f^{n+1}] = \boldsymbol{f}(\boldsymbol{u}^n, f^n). \tag{3.8}$$

## 3.2. Extraction of hypersurfaces from volume fractions

Let $\{\boldsymbol{x}_k\}_{k=1}^{N_\mathcal{S}} \subset \mathbb{R}^3$ be a discrete set of points to which we seek to fit a continuous hypersurface $\Sigma$, whose description resorts to a vector of parameters $\boldsymbol{c}_\Sigma$ of finite size; cf. section 2.2. Without loss of generality, let the centroid of $\{\boldsymbol{x}_k\}_{k=1}^{N_\mathcal{S}}$ coincide with the origin. The hypersurface $\Sigma$ is assumed to admit a globally explicit parametrization over some $\mathcal{B} \subset \mathbb{R}^2$, i.e.

$$\Sigma = \{\boldsymbol{F}_\Sigma(\boldsymbol{t}; \boldsymbol{c}_\Sigma) : \boldsymbol{t} \in \mathcal{B}\} \quad \text{or, equivalently,} \quad \Sigma = \{\boldsymbol{x} \in \mathbb{R}^3 : \phi_\Sigma(\boldsymbol{x}; \boldsymbol{c}_\Sigma) = 0\}, \tag{3.9}$$

with the surjective projection $\boldsymbol{t} = \mathcal{P}_\Sigma(\boldsymbol{x}) := \boldsymbol{F}_\Sigma^{-1}(\boldsymbol{x})$. For the purpose of the present application, it is crucial to state that the projection cannot be a function of the parameters $\boldsymbol{c}_\Sigma$. The optimal vector of parameters minimizes

$$\mathcal{E}^\mathcal{S}(\boldsymbol{c}_\Sigma) := \frac{1}{N_\mathcal{S}} \sum_{k=1}^{N_\mathcal{S}} \phi_\Sigma^2(\boldsymbol{x}_k; \boldsymbol{c}_\Sigma), \tag{3.10}$$

constituting a nonlinear equation in general. However, several technically relevant classes of hypersurfaces admit a level-set function of type $\phi_\Sigma(\boldsymbol{x}; \boldsymbol{c}_\Sigma) = \langle \boldsymbol{\Phi}_\Sigma(\boldsymbol{x}), \boldsymbol{c}_\Sigma \rangle + q(\boldsymbol{x})$, which is assumed to be the case henceforth; cf. section 2.2.

**Note 3.2** (Linear level-set functions)**.** *For an ellipsoid with semiaxes $\{a, b, c\}$ centered at $\mathbf{0}$, one obtains*

$$\phi_\Sigma(\boldsymbol{x}; \boldsymbol{c}_\Sigma) = \frac{x^2}{a^2} + \frac{y^2}{b^2} + \frac{z^2}{c^2} - 1 \quad \textit{or} \quad \boldsymbol{c}_\Sigma = [a^{-2}, b^{-2}, c^{-2}], \quad \Phi_\Sigma(\boldsymbol{x}) = x_i^2 \boldsymbol{e}_i \quad \textit{and} \quad q(\boldsymbol{x}) = -1,$$

*where a hypersurface parametrized in spherical coordinates $\varphi(\boldsymbol{x})$ and $\theta(\boldsymbol{x})$, whose radius $R$ is expanded in terms of spherical harmonics, cf. eqs. (2.18) and (2.20), admits*

$$\phi_\Sigma(\boldsymbol{x}; \boldsymbol{c}_\Sigma) = R(\varphi, \theta; \boldsymbol{c}_\Sigma) - \sqrt{\langle \boldsymbol{x}, \boldsymbol{x} \rangle} \quad \textit{or} \quad \Phi_\Sigma(\boldsymbol{x}) = [Y_l^m(\varphi, \theta)]^\mathsf{T} \quad \textit{and} \quad q(\boldsymbol{x}) = -\sqrt{\langle \boldsymbol{x}, \boldsymbol{x} \rangle}.$$

*Note that, in the latter case, the projection $\mathcal{P}_\Sigma(\boldsymbol{x}_k)$ corresponds to spherical coordinates; cf. section 1.2.*

Then, minimizing eq. (3.10) reduces to solving the symmetric linear system

$$\boldsymbol{A}\boldsymbol{c}_\Sigma = \boldsymbol{b} \quad \text{with} \quad \boldsymbol{A} = \sum_{k=1}^{N_\mathcal{S}} [\boldsymbol{\Phi}_\Sigma \otimes \boldsymbol{\Phi}_\Sigma](\boldsymbol{x}_k) \quad \text{and} \quad \boldsymbol{b} = \sum_{k=1}^{N_\mathcal{S}} [q\boldsymbol{\Phi}_\Sigma](\boldsymbol{x}_k). \tag{3.11}$$

Let us note in passing that, if the set of points $\{\boldsymbol{x}_k\}_{k=1}^{N_\mathcal{S}} = \bigcup_p \{\{\boldsymbol{x}_k\}_{k=1}^{N_p}\}_p$ is distributed over multiple processors (see fig. (3.1)), the quantities in eq. (3.11) are obtained from summation over $p$, implying that this procedure is well suited for parallel computations. Figure (3.6) provides a brief convergence analysis of the above method, where the fitted hypersurface is a perturbed sphere of degree $L_\Sigma^{\text{fit}}$. The nodes $\{\boldsymbol{x}_k\}_{k=1}^{N_\mathcal{S}}$ are obtained from intersecting the PLIC planes with the cell edges for linear volume fractions, where spheres ($R = {}^{91}/_{100}$) and perturbed spheres with degree $L_\Sigma \in \{3, 6, 9\}$ and variance $\hat{\sigma}^2 \in \{10^{-4}, 5 \times 10^{-4}\}$ are considered. Figure (4.23) in section 4.6 below provides an exemplary illustration. In accordance with

eq. (3.10), the error measures of $L_2$- and $L_\infty$-type are

$$\mathcal{E}_2^{\mathcal{S}}(\boldsymbol{c}_\Sigma) := \sqrt{\frac{1}{N_{\mathcal{S}}}\sum_{k=1}^{N_{\mathcal{S}}}\phi_\Sigma^2(\boldsymbol{x}_k;\boldsymbol{c}_\Sigma)} \quad \text{and} \quad \mathcal{E}_\infty^{\mathcal{S}}(\boldsymbol{c}_\Sigma) := \max_k|\phi_\Sigma(\boldsymbol{x}_k;\boldsymbol{c}_\Sigma)|. \tag{3.12}$$

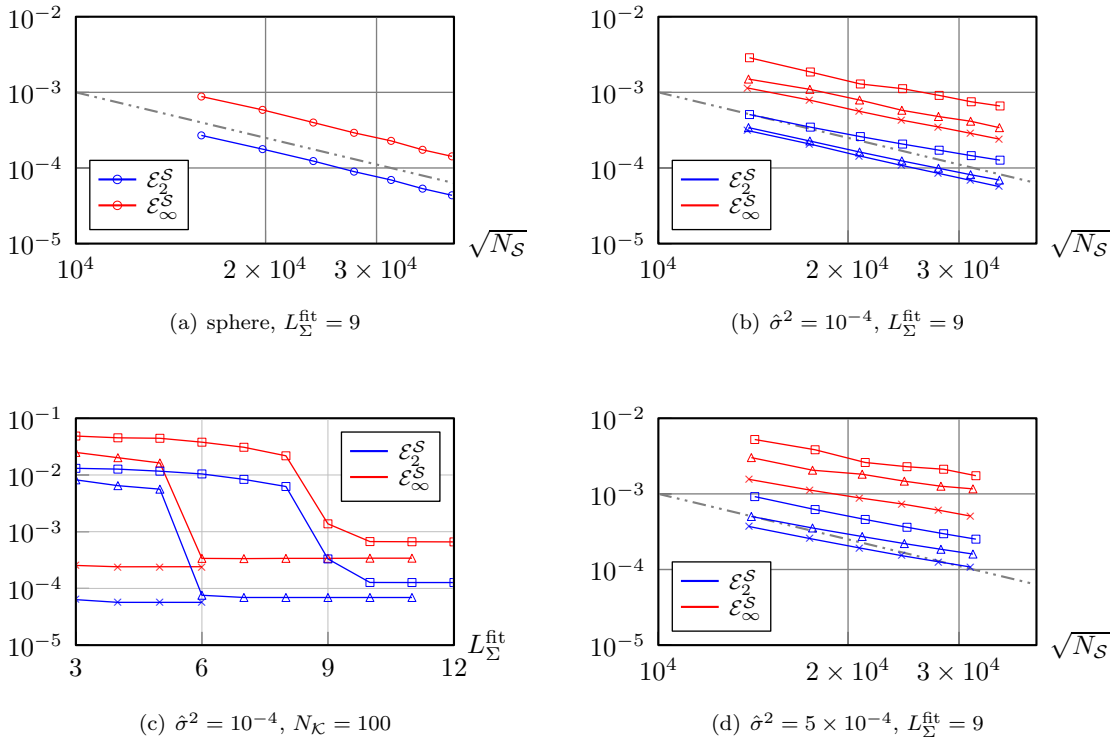


(a) sphere, $L_\Sigma^{\text{fit}} = 9$

(b) $\hat{\sigma}^2 = 10^{-4}$, $L_\Sigma^{\text{fit}} = 9$

(c) $\hat{\sigma}^2 = 10^{-4}$, $N_{\mathcal{K}} = 100$

(d) $\hat{\sigma}^2 = 5\times10^{-4}$, $L_\Sigma^{\text{fit}} = 9$

Figure 3.6.: Shape errors $\mathcal{E}_2^{\mathcal{S}}$ from eq. (3.12) for (a) sphere ($\circ$) and perturbed spheres centered in $[-1,1]^3$ with base radius $R_0 = \frac{4}{5}$ and $L_\Sigma \in \{3(\times), 6(\triangle), 9(\square)\}$ as function of ((b),(d)) resolution $N_{\mathcal{K}} \in \{40, 50, \ldots, 100\}$ for different variances $\hat{\sigma}^2$ and (c) degree of the shape approximation.

The findings can be summarized as follows:

1. Recalling that $\sqrt{N_{\mathcal{S}}} \sim N_{\mathcal{K}}$, it is evident that second-order convergence with spatial resolution is obtained for all norms employed here, both for spheres (fig. (3.6(a))) and perturbed spheres of different variance and degree $L_\Sigma$ (figs. (3.6(b)/(d))). The global error measures from eq. (3.12) reach values between $10^{-5}$ and $10^{-2}$, suggesting that the fitted hypersurface represents the set $\{\boldsymbol{x}_k\}_{k=1}^{N_{\mathcal{S}}}$ sufficiently accurate.

2. For fixed spatial resolution $N_{\mathcal{K}} = 100$ and variance $\hat{\sigma}^2 = 10^{-2}$ the graphs in fig. (3.6(c)) show that the degree of fitting must suffice $L_\Sigma^{\text{fit}} \geq L_\Sigma$, where violating this condition roughly increases the global error by two orders of magnitude in the cases presented here. However, increasing $L_\Sigma^{\text{fit}}$ beyond $L_\Sigma$ has no beneficial effect. This is a direct consequence of the fact that the spherical harmonics form an orthonormal basis on $\mathbb{S}^2$. Hence, if one seeks to fit a closed hypersurface to a set of nodes, the selection of an appropriate $L_\Sigma^{\text{fit}}$ requires either some a priori knowledge or successively

increasing $L_\Sigma^{\text{fit}}$ until the error reaches an acceptable level.

3. Numerical experiments for other values of $\hat{\sigma}^2$, corresponding to stronger perturbation of the spherical surface, were conducted as well. However, they are not reported since they are in qualitative argeement and do not provide notable further insights.

The above conclusions should be ammended by a comment on their transferability. For general non-spherical hypersurfaces, the smallest enclosing sphere, also called Brillouin sphere, determines the convergence properties of the spherical harmonics series; cf. fig. (3.7) for an illustration. However, the derivation of general statements is a delicate task. E.g., for an ellipsoid with semiaxes $a > b > c > 0$, Pick et al. [105] and Balmino [11] have shown that convergence of the spherical harmonic series requires the semi-axes of the ellipsoid to suffice $a > b > c > \frac{a}{\sqrt{2}}$, implying that, for such hypersurfaces, very large $L_\Sigma^{\text{fit}}$ may be required. Recalling that (i) the computational effort increases as $\left(L_\Sigma^{\text{fit}}+1\right)^2$ and (ii) the numerical evaluation of the spherical harmonics raises numerical difficulties for large $L_\Sigma^{\text{fit}}$, cf. Homes and Featherstone [68], accentuates the practical limitations.

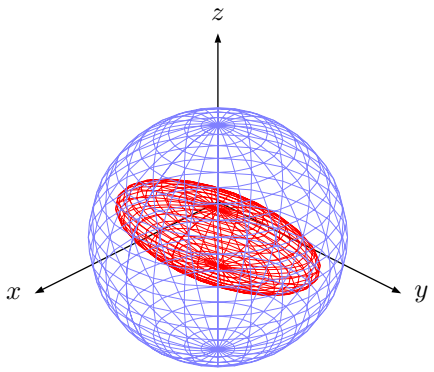


Figure 3.7.: Ellipsoid (red) and associated Brillouin sphere (blue).

While solving the minimization problem in eq. (3.10) allows extracting detailed information, in some cases more general properties of the point set may be of interest. Hence, the upcoming section 3.3 introduces a principal component analysis.

## 3.3. Principal component analysis

As above, let $\{\boldsymbol{x}_k\}_{k=1}^{N_S} \subset \mathbb{R}^3$ be a discrete set of points whose centroid is denoted by $\boldsymbol{x}_0$. The eigenvectors $\boldsymbol{t}_{\text{PCA},i}$ of the covariance matrix

$$\boldsymbol{C} = \frac{1}{N}\sum_{k}^{N} (\boldsymbol{x}_k - \boldsymbol{x}_0) \otimes (\boldsymbol{x}_k - \boldsymbol{x}_0) \tag{3.13}$$

coincide with the principal directions of the set, where the associated eigenvalues $\lambda_i$ are the principal variances. Henceforth, we denote the eigenvector associated to the smallest eigenvalue as *first principal direction* $\boldsymbol{c}_{\text{PCA}}$. Figure (3.8) exemplifies the concept in two spatial dimensions. Note that, if all nodes $\boldsymbol{x}_k$ are located on an ellipsoid with semiaxes $a_i$, the principal variances suffice $\lambda_i = {}^{a_i^2}/_3$.

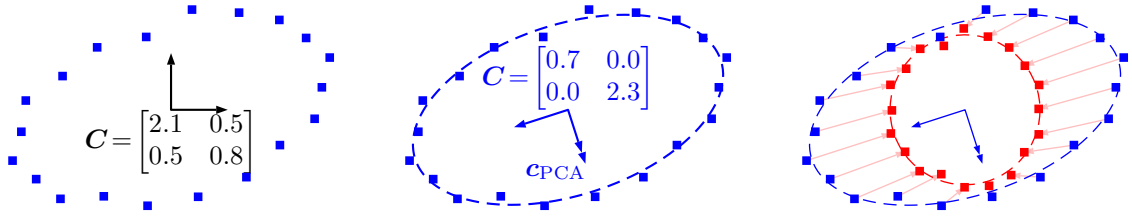


(a) referential (b) principal (c) compression (cf. eq. (3.14))

Figure 3.8.: Concept of principal component analysis for nodes (■) with referential (a), principal (b) coordinate system and respective covariance matrix $\boldsymbol{C}$ from eq. (3.13). The dashed line indicates the ellipses defined by the principal variances.

To overcome the influence of the Brillouin sphere, cf. section 3.2, one may apply a so-called *ellipsoid compression*. With $\boldsymbol{C} = \boldsymbol{T}_{\mathrm{PCA}}\boldsymbol{\Lambda}\boldsymbol{T}_{\mathrm{PCA}}^{\mathsf{T}}$, one obtains the compressed nodes (■ in fig. (3.8(c))) as

$$\tilde{\boldsymbol{x}}_k = \operatorname{diag}\left\{\frac{1}{\sqrt{3\lambda_i}}\right\}\boldsymbol{T}_{\mathrm{PCA}}^{\mathsf{T}}(\boldsymbol{x}_k - \boldsymbol{x}_0). \tag{3.14}$$

For sets that do not contain outliers, as shown in fig. (3.8(c)), the ratios of the semiaxes $(a_{\mathrm{comp}}, b_{\mathrm{comp}}, c_{\mathrm{comp}})$ of the smallest ellipsoid containing the compressed nodes are approximately 1, implying that faster convergence of the spherical harmonics series can be expected. Section 3.4 presents an application of the shape analysis concepts given above.

## 3.4. Shape analysis of freely rising fluid particles

**Note 3.3** (Publication)**.** *The results shown below are an epitome of*

*[5] C. Albert,* ***J. Kromer****, A. M. Robertson, and D. Bothe. Dynamic behaviour of buoyant high viscosity droplets rising in a quiescent liquid.* Journal of Fluid Mechanics*, 778:485–533, 2015.*

*to which the author contributed an application of the shape analysis concepts introduced in sections 3.2 and 3.3.*

Highly viscous droplets can be considered as a relevant intermediate case between free rigid particles and bubbles, where the diameters of the droplets under consideration here range from 0.5mm to 16mm. While freely rising due to buoyancy, the particles exhibit a variety of dynamic paths, where some of the droplets are subject to strong deformation and shape oscillations; cf. fig. (3.9(a)).

The goal of the shape analysis was twofold. In a descriptive sense, the interface can be captured in qualitative (class of hypersurface) and quantitative (associated shape error) terms, which allows identifying regimes and their respective transitions (e.g., spherical–ellipsoidal), based on the hypersurface parameters. E.g., the 5.7mm droplet depicted in fig. (3.10) exhibits a dynamic rocking motion in the fixed frame of reference, while its shape is virtually constant in the comoving principal system. Fig-

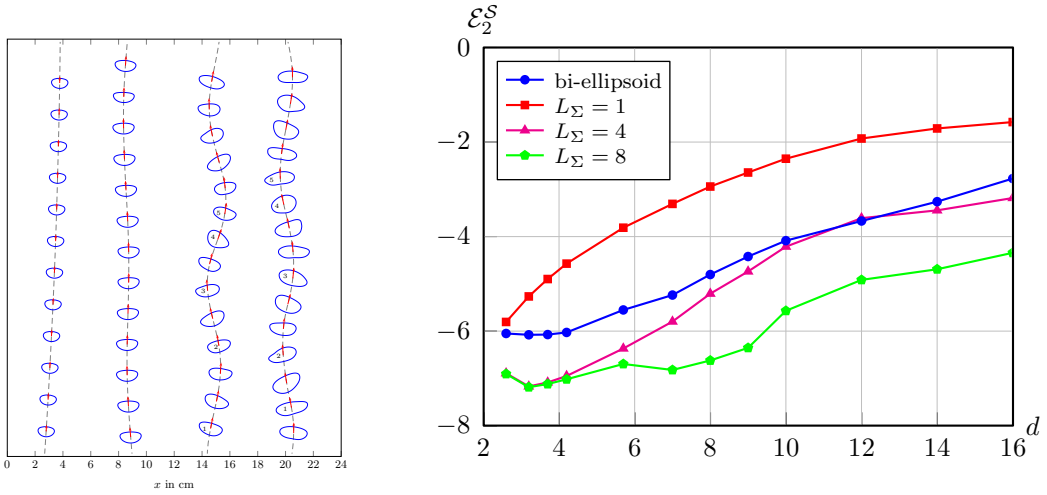


(a) 10, 12, 14 and 16mm

(b) shape errors $\mathcal{E}_2^{\mathcal{S}}$

Figure 3.9.: Rise paths and shapes (a) of corn oil droplets rising in water with (b) associated shape errors.

ure (3.9(b)) gathers the shape errors $\mathcal{E}_2^{\mathcal{S}}$, induced by bi-ellipsoid fitting (cf. section 3.4.2 in Albert et al. [5]) and spherical harmonics of different order $L_\Sigma$, as a function of the droplet diameter. Note that for $d \leq 4.2$mm, the errors induced by the bi-ellipsoid and the spherical harmonics of order $L_\Sigma \in \{4, 8\}$ remain virtually constant, implying that the description is sensible with both classes of hypersurfaces. It is worth noting that, for $d \leq 4.2$mm, using the spherical harmonics decomposition ($L_\Sigma = 8$ corresponds to $(L_\Sigma + 1)^2 = 81$ coefficients) reduces $\mathcal{E}_2^{\mathcal{S}}$ only by one order of magnitude compared to the bi-ellipsoid (4 coefficients, $\mathcal{E}_2^{\mathcal{S}} = \mathcal{O}(10^{-6})$). For increasing droplet diameter, however, the dynamic shapes become more complex, cf. fig. (3.9(a)), implying that an accurate shape description requires a richer class of hypersurfaces with more parameters.

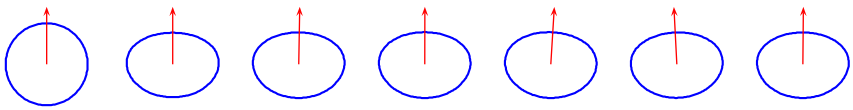

Figure 3.10.: Shape evolution of corn oil droplet ($d = 5.7$mm) released from rest (left) over time ($\Delta t = 5$s).

Furthermore, an understanding of the correlation between instantaneous geometrical and kinetic quantities can be established, e.g., say, between the first principal direction $\boldsymbol{c}_{\mathrm{PCA}}$ and the velocity of the center of mass ($\rightarrow$ in fig. (3.9(a))). As can be seen from fig. (3.11(a)), the first principal axis $\boldsymbol{c}_{\mathrm{PCA}}$ of the 5.7mm droplet shows good agreement with the rise velocity vector after the initial acceleration phase, i.e. for $t \geq 3$s. There is no significant phase shift, suggesting that path and shape changes occur essentially simultaneously. Further, the evolution of the azimuthal and polar angles indicate a nearly vertical rise direction, accompanied by back and forth azimuthal rotations. Note that the agreement for the polar angle (RMS: $6.50 \times 10^{-5}$) is better than for the azimuthal angle (RMS: $-4.54 \times 10^{-4}$). The droplet deforms to a bi-ellipsoidal shape during the acceleration phase and retains its shape while undergoing

rocking movement, cf. fig. (3.10). Figure (3.11(b)) depicts the angular decomposition of the first principal axis $\boldsymbol{c}_{\mathrm{PCA}}$ and the center of mass velocity over time for the 16mm droplet, which again show overall good agreement. However, contrary to the smaller droplets, there is a distinguishable backward phase shift of the principal axis' polar and azimuthal angle, accompanied by an amplitude deviation of the azimuthal angle. This indicates that path changes follow the shape change with a slight delay, due to stronger inertia influences.

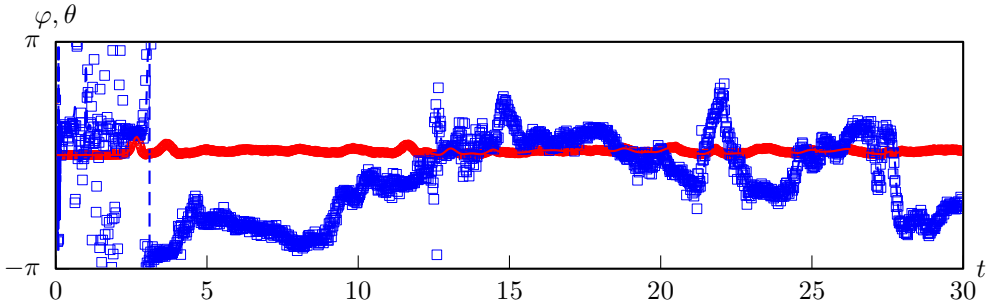


(a) $d = 5.7\mathrm{mm}$, $d/\Delta x = 20$

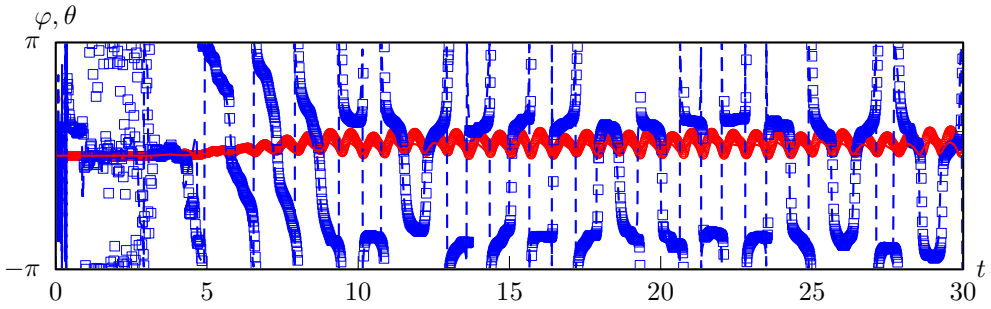


(b) $d = 16\mathrm{mm}$, $d/\Delta x = 60$

Figure 3.11.: Azimuthal ($\varphi$) and polar ($\theta$) angle of principal axis $\boldsymbol{c}_{\mathrm{PCA}}$ ($\varphi$: $\circ$, $\theta$: $\square$) and center velocity ($\varphi$: solid, $\theta$: dashed) for corn oil droplet over time in s.

# 4. Highly accurate computation of volume fractions

To solve an initial value two-phase flow problem, the volume fractions $f_{ijk}$ need to be computed for a given domain and hypersurface; cf. fig. (3.2(a)) in chapter 3. If accurate initial values are required, this task becomes particularly challenging for curved hypersurfaces, but also for seemingly simple ones, i.e. whose description involves only a small set of parameters, e.g., ellipsoids. Thus, the objective of this chapter is to develop a numerical method for the accurate computation of those volume fractions. Furthermore, accurate volume fractions are required for testing algorithms designed to estimate curvature from volume fractions, which is the subject of section 5.4.

**Note 4.1** (Publication)**.** *The present chapter is an extended version of*

*[78]* ***Johannes Kromer*** *and Dieter Bothe. Highly accurate computation of volume fractions using differential geometry.* Journal of Computational Physics*, 396:761–784, 2019.*

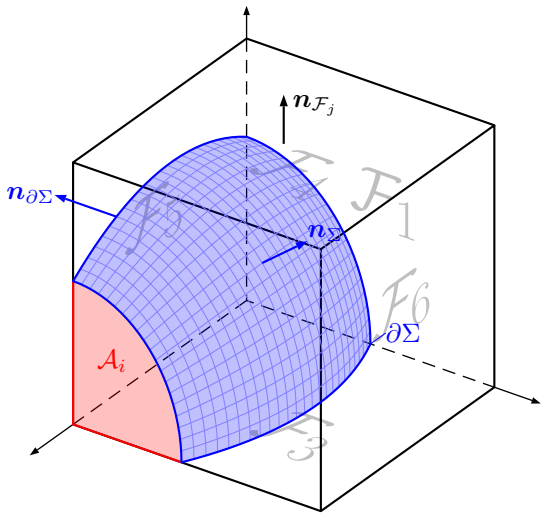


Figure 4.1.: Intersected cell $\mathcal{K}$ with relevant quantities.

The remainder of this chapter is organized as follows: section 4.1 provides a survey of the relevant literature contributions, followed by a detailled formulation of the problem in section 4.2. Before section 4.4 introduces the notation and derives mathematical details for two and three spatial dimensions, section 4.3 outlines the algorithm strategy. Some basic facts from differential geometry are placed to appendix A.3.

Since the representation of hypersurfaces is of key importance, subsection 4.4.2 comprises the introduction of local coordinates, as well as an approximation using the WEINGARTEN map. Subsequently, we introduce the LAPLACE-BELTRAMI operator, both in local coordinates and in a comprehensible level-set notation. For certain classes of hypersurfaces, eq. (4.3) admits analytical solutions, which will be presented and employed to discuss the admissibility of boundary conditions for eq. (4.3). Finally, section 4.4 comprises the numerical solution approaches, namely the comparison of coefficients of polynomials as well as the PETROV-GALERKIN approach, with a focus on the parameter set $\mathcal{S}_\Gamma$ of the graph representation of $\Gamma$. Section 4.5 introduces the numerical algorithm, where details of the implementation are provided both for the approximation of the hypersurface and the assembly and solution of the linear system of equations resulting from the variational formulation. Moreover, we provide some details of the coefficient comparison. Section 4.6 is concerned with several numerical experiments for $d = 3$ spatial dimensions and discusses the results. We compare our results to analytical solutions obtained for spheres and briefly exemplify the significance of accuracy of volume fraction computation for spurious currents. Finally, section 4.7 concludes the presented work and formulates a further outlook.

## 4.1. Literature review

The computation of volumes emerging from the intersection of curved hypersurfaces and polygonally bounded domains (e.g., polyhedra and cuboids) has been addressed in several publications up to this date. Some of the presented approaches exploit the application of appropriate divergence theorems in order to reduce the integral dimension, while others employ direct quadrature. The third class of approaches resorts to a recursive local grid refinement, coupled with a linear approximation of the interface, e.g., Cummins et al. [35] or Lopez and Hernandez [85]. The recent work of Jones et al. [74] covers the initialization of volume fractions on unstructured grids in two and three spatial dimensions. Their approach consists of decomposing the mesh in simplices and subsequently computing the intersection volume by direct quadrature. The authors report high accuracy in terms of volume computation for spheres and show that their method is capable of initializing intersections of spheres and hyperboloids, i.e. domains with non-smooth boundaries. Strobl et al. [134] propose a computationally efficient and robust method for the computation of volume overlaps of spheres and tetrahedra, wedges and hexahedra. The approach of Bná et al. [17, 18] involves direct computation of integrals with discontinuous integrands by means of quadrature, where the boundaries of the integration domain are computed by a root finding algorithm. While their algorithm involves quite some computational effort, it is able to handle non-smooth hypersurfaces. Min and Gibou [94] develop an algorithm for geometric integration over irregular domains. To obtain the hypersurface position of an intersected polyhedron, the level-set function is evaluated at the corners, allowing for a linear approximation of its respective roots on the edges. Subsequent decomposition of the polyhedron into simplices allows for straightforward evaluation of the desired integrals. Smereka [131] and the series of papers by Wen [150, 151, 152] are concerned with the numerical evaluation of $\delta$-function integrals in three spatial dimensions. Considering a cuboid intersected by a hypersurface, the concept of Wen is to rewrite the integral over a three-dimensional $\delta$-function as an integral over one of the cell faces, where the integrand is a one-dimensional $\delta$-function. All of the above approaches, however, imply considerable computational effort and complex case-dependent implementations. Hahn [60] introduced a library of four independent routines for multidimensional numerical integration, three of which employ Mone-Carlo integration and the fourth resorts to a globally adaptive subdivision scheme. While methods

based on Monte-Carlo integration allow for a wider range of potential application, the errors qualitatively decrease as $\frac{1}{\sqrt{N}}$, where $N$ is the number of evaluations of the level-set function, implying comparatively high computational effort to obtain the accuracy desired in our case.

Despite covering a different set of applications, namely the computation of integrals over implicitly given hypersurfaces, the work of Müller et al. [96] is close in spirit to the present chapter. The concept underlying their approach is the construction of quadrature nodes and weights from a given level-set function, where the computation of a divergence-free basis of polynomials allows reducing the spatial problem dimension by one. By recursive application of this concept, integrals over implicitly defined domains and hypersurfaces in $\mathbb{R}^3$ are transformed to line-integrals; cf fig. (4.1) for a schematic illustration. While the method of Müller et al. [96] is computationally highly efficient and exhibits high accuracy, the numerical tests shown by the authors only cover level-set functions of low polynomial order, i.e. hypersurfaces with few geometric details and exclusively globally convex ones. In section 4.6, we provide results for both locally and globally non-convex hypersurfaces.

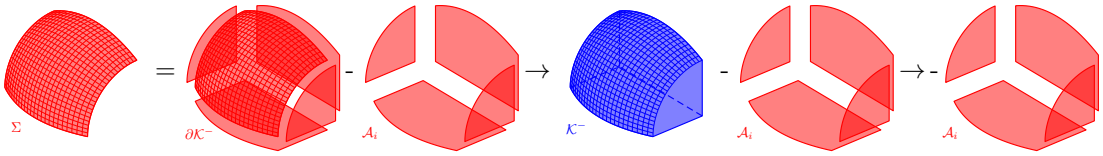


Figure 4.2.: Transformation of integration domain as applied by Müller et al. [96].

## 4.2. Problem formulation

We first provide some relevant notation needed to precisely formulate the problem under consideration and to sketch the approach proposed in this work. The hypersurface $\Sigma \subset \mathcal{K}$ induces a pairwise disjoint decomposition $\mathcal{K} = \Sigma \cup \mathcal{K}^+ \cup \mathcal{K}^-$, where we call $\mathcal{K}^-$ and $\mathcal{K}^+$ the *interior* and *exterior* subdomain, respectively. For the numerical approximation, the embedding domain $\mathcal{K}$ is decomposed into a set of pairwise disjoint cells $\mathcal{K}_i$, some of which are intersected by $\Sigma$, i.e. they contain patches $\Sigma_i := \Sigma \cap \mathcal{K}_i$ of the hypersurface. Note that $\Sigma = \bigcup \Sigma_i$. Any intersected cell again admits a disjoint decomposition into the hypersurface patch $\Sigma_i$, as well as an interior ($\mathcal{K}_i^-$) and exterior ($\mathcal{K}_i^+$) segment. The allocation property is inherited from the global decomposition of the embedding space, implying that, in a global sense, any $\boldsymbol{x} \in \mathcal{K}_i \setminus \Sigma_i \subset \mathcal{K} \setminus \Sigma$ is either interior or exterior. It is important to note that, locally, $\partial\Sigma_i \neq \emptyset$, even if the hypersurface is globally closed, i.e. $\partial\Sigma = \emptyset$. Figure (4.3) exemplifies the notation.

Henceforth, we are concerned with a single intersected cell $\mathcal{K}_i$, which is why we drop the cell index $i$ for ease of notation. The hypersurface patch $\Sigma \subset \mathcal{K} \subset \mathbb{R}^d$, with $d \in \{2, 3\}$ denoting the spatial dimension, is assumed to be twice continuously differentiable with a simply connected, piecewise smooth boundary $\partial\Sigma \neq \emptyset$. Furthermore, the following assumptions are imposed:

i. $\mathcal{K}$ is convex with a boundary composed of planar polygons, $\partial\mathcal{K} = \bigcup \mathcal{F}_k$. For technical simplicity, however, let $\mathcal{K}$ be (i.a) a non-degenerate cuboid whose (i.b) faces $\mathcal{F}_k$ are respectively parallel to one of the coordinate planes. While none of these assumptions inflicts the generality of the algorithm, they significantly reduce the complexity of the involed expressions. Assumption (i.a) allows for a single parametrization of the boundary curve segment $\partial\Sigma_k = \Sigma \cap \mathcal{F}_k$; for general (non-convex) polyhedra, the representation potentially requires a cumbersome piecewise definition; cf. fig. (4.4).

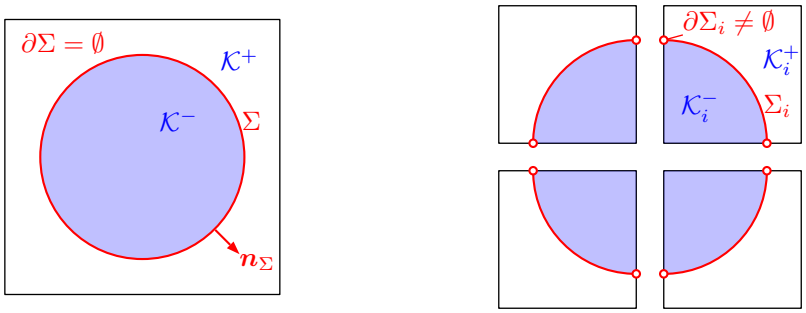


Figure 4.3.: Illustration of the decomposition induced by a closed hypersurface $\Sigma$.


Figure 4.4.: Single and piecewise definition of boundary curve segment $\partial\Sigma_k$.

Assumption (i.b) implies $\boldsymbol{n}_{\mathcal{F}_k} \in \{\pm\boldsymbol{e}_1, \pm\boldsymbol{e}_2, \pm\boldsymbol{e}_3\}$, which will be useful below for the derivation of some analytical results in subsection 4.4.6.

ii. Both the interior and exterior segment contain at least one of the vertices of $\mathcal{K}$, i.e. the hypersurface boundary $\partial\Sigma$ is not entirely contained in a single face $\mathcal{F}_k$.

iii. The division induced by the hypersurface yields simply connected sets $\mathcal{K}^\pm$ and $\Sigma$, implying that $\mathcal{K}$ contains a single patch of the hypersurface. This assumption resembles a resolution constraint to the underlying spatial discretization.

iv. For the principal curvatures $\kappa_i$, it holds that $\kappa_i d_\mathcal{K} \lessapprox 10^{-2}$, where $d_\mathcal{K}$ is a characteristic length of the cell $\mathcal{K}$, e.g. the smallest edge length if $\mathcal{K}$ is a cuboid. Note that this assumption actually is a resolution requirement.

Figure (4.5) illustrates selected admissible and non-admissible setups. We are interested in the evaluation of

$$\mathrm{vol}(\mathcal{K}^-) = \int_{\mathcal{K}^-} 1 \,\mathrm{d}\boldsymbol{x} \tag{4.1}$$

and employ the Gaussian divergence theorem to get

$$\mathrm{vol}(\mathcal{K}^-) = \frac{1}{d} \int_{\partial\mathcal{K}^-} \langle \boldsymbol{x} - \boldsymbol{x}_{\mathrm{ref}}, \boldsymbol{n}_{\partial\mathcal{K}^-} \rangle \,\mathrm{d}o = \frac{1}{d} \left[ \int_{\partial\mathcal{K}^- \setminus \Sigma} \langle \boldsymbol{x} - \boldsymbol{x}_{\mathrm{ref}}, \boldsymbol{n}_{\partial\mathcal{K}^-} \rangle \,\mathrm{d}o + \int_{\Sigma} \langle \boldsymbol{x} - \boldsymbol{x}_{\mathrm{ref}}, \boldsymbol{n}_\Sigma \rangle \,\mathrm{d}o \right], \tag{4.2}$$

where $\boldsymbol{n}_\Sigma$ denotes the unit normal to $\Sigma$, pointing towards the exterior and $\boldsymbol{x}_{\mathrm{ref}} \in \mathbb{R}^d$ is an arbitrary

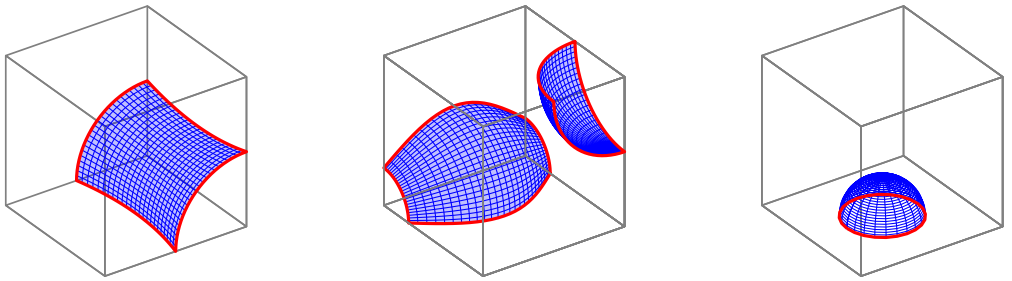

(a) admissible setup

(b) **non**-admissible setup: the hypersurface patch $\Sigma$ is not connected (violation of iii)

(c) **non**-admissible setup: all corners are located in the exterior/interior segment (violation of ii)

Figure 4.5.: Admissible and non-admissible intersection topologies of hypersurface $\Sigma$ and cell $\mathcal{K}$.

but constant reference. Unless stated differently, we may assume $\boldsymbol{x}_{\text{ref}} \equiv \mathbf{0}$ without loss of generality. Note that, by assumption, $\mathcal{A} = \partial\mathcal{K}^- \setminus \Sigma$ is a piecewise planar domain, which considerably simplifies the numerical approximation of the associated integral; cf. fig. (4.1). For some classes of hypersurfaces, namely cylinders and spheres, the expressions on the right hand side of eq. (4.2) can be computed analytically; the latter case is discussed in subsection 4.4.6. For general hypersurfaces, however, the evaluation of the surface integral features some difficulties, one being the implicit definition of the integration domain itself. The key idea of the presented approach is the exploitation of the surface divergence theorem associated to $\Sigma$. For this purpose, assume for the moment that a sufficiently smooth $u$ is a given solution of the Laplace-Beltrami equation

$$\Delta_\Sigma u = \langle \boldsymbol{x}, \boldsymbol{n}_\Sigma \rangle \qquad \text{on } \Sigma, \tag{4.3}$$

where $\Delta_\Sigma$ denotes the Laplace-Beltrami operator; cf. subsection 4.4.3. The existence and regularity of the solution $u$ can be proven by application of the according theorems of elliptic partial differential equations. At this point, it is worth noting that the regularity of $u$ crucially depends on the regularity of the underlying hypersurface $\Sigma$. However, since we only consider hypersurfaces of class $\mathcal{C}^\infty$ within this work, $u$ exhibits maximal regularity. Then, application to the rightmost expression in eq. (4.2) yields

$$\int_\Sigma \langle \boldsymbol{x}, \boldsymbol{n}_\Sigma \rangle \, \mathrm{d}o = \int_{\partial\Sigma} \langle \nabla_\Sigma u, \boldsymbol{n}_{\partial\Sigma} \rangle \, \mathrm{d}l, \tag{4.4}$$

where $\nabla_\Sigma$ and $\boldsymbol{n}_{\partial\Sigma}$ denote the surface gradient associated to $\Sigma$ and the outward-pointing boundary normal, respectively; cf. again fig. (4.1) and appendix A.3 for a definition. Note that $\boldsymbol{n}_{\partial\Sigma}$ is in the tangent space of $\Sigma$ at $\boldsymbol{x}$, i.e. $\boldsymbol{n}_{\partial\Sigma} \in T_\Sigma(\boldsymbol{x})$. Equation (4.4) also illustrates why $\Sigma$ is required to exhibit a non-empty boundary $\partial\Sigma \neq \emptyset$. To see this, recall that, for a sphere of radius $R$, i.e. $\Sigma = \partial\mathcal{B}_R(\mathbf{0})$, with $\partial\Sigma = \emptyset$ and $|\Sigma| = 4\pi R^2$ one obtains the contradiction

$$4\pi R^2 = \int_\Sigma 1 \, \mathrm{d}o \overset{\lightning}{=} \int_{\partial\Sigma} \langle \nabla_\Sigma u, \boldsymbol{n}_{\partial\Sigma} \rangle \, \mathrm{d}s = 0. \tag{4.5}$$

**Note 4.2** (Application on closed hypersurfaces)**.** *By definition, closed hypersurfaces $\Sigma$ have an empty boundary, i.e. $\partial\Sigma = \emptyset$. For sufficiently regular functions $g, u : \Sigma \mapsto \mathbb{R}$, s.t. $\Delta_\Sigma u = g$, applying the surface divergence theorem yields*

$$\int_\Sigma g \mathrm{d}o \overset{!}{=} \int_{\partial\Sigma} \langle \nabla_\Sigma u, \boldsymbol{n}_{\partial\Sigma} \rangle \mathrm{d}l = 0, \tag{4.6}$$

*implying that we can only find a solution to $\Delta_\Sigma u = g$ for functions $g$ with zero average on $\Sigma$. For the general case, i.e. $\int_\Sigma g \mathrm{d}o \neq 0$, it is required to decompose the hypersurface into $K \geq 2$ pairwise disjoint patches with non-empty boundary, i.e. $\Sigma = \bigcup_{k=1}^{N} \Sigma_k$ with $\partial\Sigma_k \neq \emptyset$. Then, one can find $k$ local solutions $u_k$ such that*

$$\int_\Sigma g \mathrm{d}o = \sum_{k=1}^{K} \int_{\Sigma_k} g \mathrm{d}o = \sum_{k=1}^{K} \int_{\partial\Sigma_k} \langle \nabla_\Sigma u_k, \boldsymbol{n}_{\partial\Sigma_k} \rangle \mathrm{d}l. \tag{4.7}$$

*However, in general, the $u_k$ will only admit regularity on the patches $\Sigma_k$, but not globally on $\Sigma$.*

The introduction of appropriate boundary conditions for eq. (4.3) and properties of the sought solution are deferred to subsection 4.4.1. For the numerical solution of eq. (4.3) for general classes of hypersurfaces within this work, we approximate the hypersurface locally and apply two different approaches: (i) a variational formulation of eq. (4.3), using a Petrov-Galerkin approach. While the test functions are chosen to be Legendre polynomials, the choice of the Ansatz functions has to be in accordance with the structure of the right-hand side, i.e. $\langle \boldsymbol{x}, \boldsymbol{n}_\Sigma \rangle$. (ii) A comparison of polynomial coefficients. The meaning and motivation for this choice will become clear below.

## 4.3. Overall strategy

The strategy of the presented algorithm consists of two parts. At first, the hypersurface $\Sigma$, being defined implicitly as the zero iso-contour of a level-set function $\phi \in \mathcal{C}^2(\mathcal{K})$, is locally represented as the graph of a (height) function $h_\Sigma$ over some parameter set $\mathcal{S}_\Sigma \subset \mathbb{R}^{d-1}$, i.e.

$$\Sigma = \{ \boldsymbol{g}_\Sigma(\boldsymbol{t}) : \boldsymbol{t} \in \mathcal{S}_\Sigma \} \qquad \text{with} \qquad \boldsymbol{g}_\Sigma = [\boldsymbol{t}, h_\Sigma(\boldsymbol{t})]^\mathsf{T}, \tag{4.8}$$

and parameters $\boldsymbol{t} := \{t_i, \ldots, t_{d-1}\}$. The coordinate system based in $\boldsymbol{x}_0 \in \Sigma$ is spanned by the unit normal and the $d-1$ eigenvectors $\boldsymbol{\tau}_i$ of the associated Weingarten map, i.e. the directions of the principal curvatures. The associated eigenvalues are the principal curvatures $\kappa_i$, corresponding to the reciprocal radii of the osculating circles. Hence, a local approximation yields a purely quadratic height function $h_\Gamma$. For the remainder of this work, the approximated hypersurface will be denoted by $\Gamma$, where quantities and operators introduced for $\Sigma$ are defined analogously. Subsection 4.4.2 covers the mathematical details of the approximation. However, in what follows, we assume the base point $\boldsymbol{x}_0$, the coordinate system $\{\boldsymbol{\tau}_i, \boldsymbol{n}_\Sigma\}$ and the principal curvatures $\kappa_i$ to be given. Exploiting the graph representation of the interface

allows to transform the integration domain to the associated parameter set $\mathcal{S}_\Sigma$, i.e.

$$\int_\Sigma \langle \boldsymbol{x}, \boldsymbol{n}_\Sigma \rangle \, \mathrm{d}o = \int_{\mathcal{S}_\Sigma} \langle \boldsymbol{g}_\Sigma(\boldsymbol{t}), \boldsymbol{n}_\Sigma\left(\boldsymbol{g}_\Sigma(\boldsymbol{t})\right) \rangle \mathcal{DF}(\boldsymbol{g}_\Sigma) \, \mathrm{d}\boldsymbol{t}, \tag{4.9}$$

with $\mathcal{DF}(\boldsymbol{g}_\Sigma) := \sqrt{\det\left(\boldsymbol{J}_{\boldsymbol{g}_\Sigma}^{\mathsf{T}} \boldsymbol{J}_{\boldsymbol{g}_\Sigma}\right)}$ the functional determinant of $\boldsymbol{g}_\Sigma$, where $\boldsymbol{J}_{\boldsymbol{g}_\Sigma}$ denotes the Jacobian. To facilitate the numerical treatment, the parameter set is approximated by a polygon which, in general, is neither a super- nor a subset of the true parameter set; cf. fig. (4.9). We will discuss the implications of this property in subsection 4.4.4. The second part of the strategy is a numerical solution of the surface Laplace-Beltrami equation. The first concept comprises the application of a Petrov-Galerkin approach on the variational formulation, i.e. $\Delta_\Gamma u = \langle \boldsymbol{x}, \boldsymbol{n}_\Gamma \rangle$ is replaced by

$$\sum_{j=1}^{N} \hat{u}_j \int_\Gamma \varphi_i^{\mathrm{t}} \Delta_\Gamma \varphi_j^{\mathrm{a}} \, \mathrm{d}o = \int_\Gamma \langle \boldsymbol{x}, \boldsymbol{n}_\Gamma \rangle \varphi_i^{\mathrm{t}} \, \mathrm{d}o \qquad \forall \quad 1 \leq i \leq N \qquad \text{with} \qquad u = \sum_{j=1}^{N} \hat{u}_j \varphi_j^{\mathrm{a}}, \tag{4.10}$$

where $\varphi_i^{\mathrm{t}}$ and $\varphi_j^{\mathrm{a}}$ are the test and Ansatz functions, respectively. The derivation of eq. (4.10), along with a sketch of the solution strategy, are the subject of subsection 4.4.4. The second concept involves the comparison of coefficients of a polynomial expression, allowing to restrict the deviation of the exact and numerical solution to polynomials of higher order, which become negligible for sufficiently small parameter sets. Subsection 4.4.5 provides the details.

## 4.4. Mathematical concept of the approach

### 4.4.1. Boundary conditions

Note that the application of the divergence theorem, cf. eq. (4.4), does not require any boundary conditions for the sought function $u$. In order to facilitate numerical treatment by exploitation of divergence theorems, it is favorable to prescribe boundary conditions of either Dirichlet or Neumann type. While in theory, the problem at hand does admit solutions fulfilling Dirichlet conditions, say, e.g., $u|_{\partial\Sigma} = 0$, the desired application of the surface divergence theorem, cf. eq. (4.4), obviously prohibits homogeneous boundary conditions of Neumann type, because

$$\int_{\partial\Sigma} \langle \nabla_\Sigma u, \boldsymbol{n}_{\partial\Sigma} \rangle \, \mathrm{d}s = 0 \quad \text{for} \quad \nabla_\Sigma u|_{\partial\Sigma} = \boldsymbol{0}. \tag{4.11}$$

In the context of the numerical algorithm presented here, however, we are only interested in the approximation of *any* regular solution $u$, whose surface gradient is evaluated on $\partial\Sigma$. With an appropriate Ansatz space ensuring regularity, both the variational formulation and the comparison of coefficients provide a unique solution. Hence, the presented approach does not require to specify particular boundary conditions. The admissibility of Dirichlet boundary conditions is deferred to the last paragraph in subsection 4.4.3. For further mathematical details on the existence of solutions, the reader is referred to the book of Prüss and Simonett [112] and the references given therein.

### 4.4.2. Approximation of hypersurfaces in local coordinates

As shown in appendix A.3, under the general assumptions formulated above, the hypersurface patch $\Sigma$ can be parametrized as the graph of a height function, i.e.

$$\Sigma = \{\boldsymbol{x}_0 + t_i\boldsymbol{\tau}_i + h_\Sigma(\boldsymbol{t})\boldsymbol{n}_0 : \boldsymbol{t} \in \mathcal{S}_\Sigma\} \quad \text{with} \quad h_\Sigma \in \mathcal{C}^2(\mathcal{S}_\Sigma) \quad \text{and} \quad \boldsymbol{n}_0 := \boldsymbol{n}_\Sigma(\boldsymbol{x}_0), \tag{4.12}$$

where $\{\boldsymbol{\tau}_i, \boldsymbol{n}_0\}$ forms an orthonormal system for fixed $\boldsymbol{x}_0$. Also, an appropriate shift of coordinates ensures $\boldsymbol{x}_0 = \boldsymbol{0}$. Recall that, for ease of notation, the EINSTEIN summation convention is employed, e.g., $t_i\boldsymbol{\tau}_i$ denotes $\sum_{i=1}^{d-1} t_i\boldsymbol{\tau}_i$. The computation of the height function $h_\Sigma = h_\Sigma(\boldsymbol{t}; \boldsymbol{x}_0)$ requires to solve the nonlinear implicit equation $\phi_\Sigma(\boldsymbol{x}_0 + t_i\boldsymbol{\tau}_i + h_\Sigma\boldsymbol{n}_0) = 0$. Since this may be cumbersome, we choose to approximate the hypersurface around $\boldsymbol{x}_0$ by the graph of an approximated height function, based on the principal curvatures provided by the WEINGARTEN map. We obtain

$$\Gamma = \{\boldsymbol{g}_\Gamma(\boldsymbol{t}) : \boldsymbol{t} \in \mathcal{S}_\Gamma\} \quad \text{with} \quad \boldsymbol{g}_\Gamma(\boldsymbol{t}) := \boldsymbol{x}_0 + t_i\boldsymbol{\tau}_i + h_\Gamma\boldsymbol{n}_0, \tag{4.13}$$

where the height function reads

$$h_\Gamma = \frac{1}{2}\sum_{i=1}^{d-1} \kappa_i t_i^2, \qquad \text{with} \qquad \|h_\Sigma - h_\Gamma\| = \mathcal{O}(\|\boldsymbol{t}\|^3), \tag{4.14}$$

where the third-order approximation, in combination with the tangential coordinate system, produces the purely quadratic form. Note that, in general, as mentioned above, the respective parameter sets do *not* coincide, i.e. $\mathcal{S}_\Sigma \neq \mathcal{S}_\Gamma$. However, the parameter set deviation $\Delta\mathcal{S}_\Sigma := (\mathcal{S}_\Sigma \setminus \mathcal{S}_\Gamma) \cup (\mathcal{S}_\Gamma \setminus \mathcal{S}_\Sigma)$ will be small if the characteristic length $d_\mathcal{K}$ of cell $\mathcal{K}$ suffices $d_\mathcal{K}\kappa_i \leq 10^{-2}$; see fig. (4.6(b)) for an illustration.

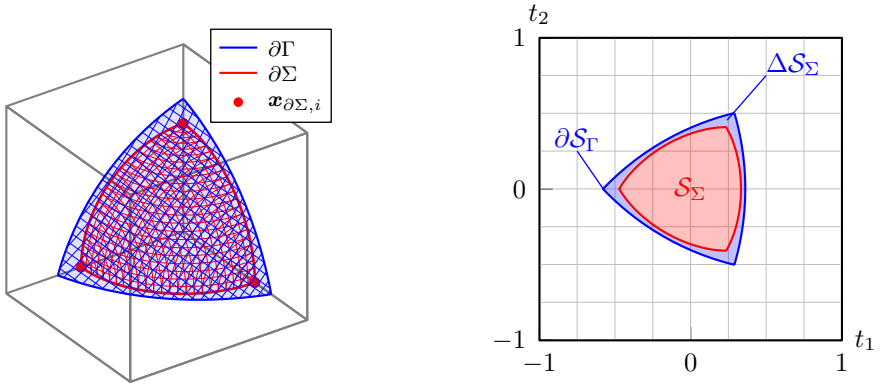


(a) hypersurface patches

(b) associated parameter sets

Figure 4.6.: Deviation of parameter sets induced by approximation (light blue) of the hypersurface $\Sigma = \partial\mathcal{B}_R(\boldsymbol{0}) \cap \mathcal{K}$ (red mesh) around $\boldsymbol{x}_0 = \frac{1}{3}[1,1,1]$ with $\kappa_i = \frac{1}{R}$ and $\boldsymbol{n}_0 = \frac{-1}{\sqrt{3}}[1,1,1]$. In general, it holds that $\mathcal{S}_\Gamma \not\supset \mathcal{S}_\Sigma$, i.e. the parameter set of the approximation does not contain the true parameter set (nor vice versa).

Furthermore, the graph representation of $\Sigma$, cf. eq. (4.13), allows to assign to any $f : \Sigma \mapsto \mathbb{R}$ a function $f^\Sigma : \mathcal{S}_\Sigma \mapsto \mathbb{R}$ with $f^\Sigma := f \circ \boldsymbol{g}_\Sigma$.

### 4.4.3. Representations of the Laplace-Beltrami operator

On a curved manifold $\Sigma$, the correspondent to the LAPLACE operator $\Delta u = \partial_{ii} u$ in EUCLIDEAN space, being defined as the divergence of the gradient of a scalar function, is the LAPLACE-BELTRAMI operator (associated to $\Sigma$), defined as $\Delta_\Sigma u := \operatorname{div}_\Sigma \nabla_\Sigma u$. In what follows, we derive the concrete form of the LAPLACE-BELTRAMI operator for implicitly (in terms of a level-set) and explicitly (as the graph of a function) defined hypersurfaces. For the level-set case, the authors could not find the specific representations in the literature. Furthermore, we present specific analytical solutions of the LAPLACE-BELTRAMI equation emerging from the computation of volumes, cf. eq. (4.3). In the sequel, $\Gamma$ represents a member of the class of hypersurfaces given by eq. (4.13).

**Level-set representation** For a hypersurface $\Sigma \subset \mathbb{R}^d$ defined by the iso-contour of a smooth level-set $\phi_\Sigma \in \mathcal{C}^2(\mathbb{R}^d)$, one obtains

$$\Delta_\Sigma u = \boldsymbol{P}_\Sigma : \nabla^2 u - \frac{\langle \nabla u, \nabla \phi_\Sigma \rangle}{\langle \nabla \phi_\Sigma, \nabla \phi_\Sigma \rangle} \left( \boldsymbol{P}_\Sigma : \nabla^2 \phi_\Sigma \right) = \boldsymbol{P}_\Sigma : \nabla^2 u - \langle \nabla u, \boldsymbol{n}_\Sigma \rangle \frac{\boldsymbol{P}_\Sigma : \nabla^2 \phi_\Sigma}{\langle \nabla \phi_\Sigma, \nabla \phi_\Sigma \rangle^{\frac{1}{2}}}, \tag{4.15}$$

where $\boldsymbol{P}_\Sigma := \boldsymbol{I} - \boldsymbol{n}_\Sigma \otimes \boldsymbol{n}_\Sigma$ denotes the tangential projection. Here, we would like to emphasize the relation to the mean curvature given in eq. (2.26), i.e.

$$\kappa_\Sigma := -\operatorname{div}_\Sigma \boldsymbol{n}_\Sigma = \sum_{i=1}^{d-1} \kappa_i = -\frac{\boldsymbol{P}_\Sigma : \nabla^2 \phi_\Sigma}{\langle \nabla \phi_\Sigma, \nabla \phi_\Sigma \rangle^{\frac{1}{2}}}. \tag{4.16}$$

**Graph representation ($d = 2$)** If the hypersurface is given as the graph of a sufficiently smooth function $h_\Sigma(\boldsymbol{t}) : \mathcal{S}_\Sigma \mapsto \mathbb{R}$ with parameter set $\mathcal{S}_\Sigma \subset \mathbb{R}$, introducing $\partial_i := \frac{\partial}{\partial t_i}$ and $\partial_{ij} := \frac{\partial^2}{\partial t_i \partial t_j}$, one obtains

$$\Delta_\Sigma u = \partial_{11} u \frac{1}{1 + (\partial_1 h_\Sigma)^2} - \partial_1 u \frac{\partial_{11} h_\Sigma \partial_1 h_\Sigma}{\left(1 + (\partial_1 h_\Sigma)^2\right)^2}. \tag{4.17}$$

The above form is easily derived from eq. (4.15) with $\phi(\boldsymbol{t}) = t_2 - h_\Sigma(t_1)$ and $u(\boldsymbol{t}) = u(t_1)$. For height functions of purely quadratic form, i.e. $h_\Gamma = \frac{\kappa t_1^2}{2}$, cf. eq. (4.13), eq. (4.17) becomes

$$\Delta_\Gamma u = \partial_{11} u \frac{1}{1 + \kappa^2 t_1^2} - \partial_1 u \frac{\kappa^2 t_1}{(1 + \kappa^2 t_1^2)^2}. \tag{4.18}$$

The right-hand sides become

$$\langle \boldsymbol{x}, \boldsymbol{n}_\Sigma \rangle = \frac{h_\Sigma - \partial_1 h_\Sigma t_1}{\sqrt{1 + (\partial_1 h_\Sigma)^2}} \qquad \text{and} \qquad \langle \boldsymbol{x}, \boldsymbol{n}_\Gamma \rangle = \frac{-\kappa_1 t_1^2}{2\sqrt{1 + \kappa_1^2 t_1^2}}. \tag{4.19}$$

**Graph representation ($d = 3$)** By arguments analogous to those given above, for the case of three spatial dimensions we have $\phi(\boldsymbol{t}) = t_3 - h_\Sigma(t_1, t_2)$, yielding

$$\begin{aligned}\Delta_\Sigma u = {} & \partial_{11} u \frac{1 + \partial_2 h_\Sigma^2}{1 + \partial_1 h_\Sigma^2 + \partial_2 h_\Sigma^2} + \partial_{22} u \frac{1 + \partial_1 h_\Sigma^2}{1 + \partial_1 h_\Sigma^2 + \partial_2 h_\Sigma^2} - \partial_{12} u \frac{2 \partial_1 h_\Sigma \partial_2 h_\Sigma}{1 + \partial_1 h_\Sigma^2 + \partial_2 h_\Sigma^2} \\ & - \frac{\partial_1 u \partial_1 h_\Sigma + \partial_2 u \partial_2 h_\Sigma}{\left(1 + \partial_1 h_\Sigma^2 + \partial_2 h_\Sigma^2\right)^2} \left( \partial_{11} h_\Sigma \left(1 + \partial_2 h_\Sigma^2\right) + \partial_{22} h_\Sigma \left(1 + \partial_1 h_\Sigma^2\right) - 2 \partial_{12} h_\Sigma \partial_1 h_\Sigma \partial_2 h_\Sigma \right), \end{aligned} \tag{4.20}$$

which in the purely quadratic case, i.e. with $h_\Gamma = \frac{\kappa_1 t_1^2 + \kappa_2 t_2^2}{2}$, simplifies to

$$\begin{aligned}\Delta_\Gamma u = {} & \partial_{11} u \frac{1 + \kappa_2^2 t_2^2}{1 + \kappa_1^2 t_1^2 + \kappa_2^2 t_2^2} + \partial_{22} u \frac{1 + \kappa_1^2 t_1^2}{1 + \kappa_1^2 t_1^2 + \kappa_2^2 t_2^2} - \partial_{12} u \frac{2 \kappa_1 \kappa_2 t_1 t_2}{1 + \kappa_1^2 t_1^2 + \kappa_2^2 t_2^2} \\ & - \frac{\partial_1 u \kappa_1 t_1 + \partial_2 u \kappa_2 t_2}{\left(1 + \kappa_1^2 t_1^2 + \kappa_2^2 t_2^2\right)^2} \left( \kappa_1 \left(1 + \kappa_2 t_2^2\right) + \kappa_2 \left(1 + \kappa_1 t_1^2\right) \right). \end{aligned} \tag{4.21}$$

Note that the application of the operator given in eq. (4.21) to a function preserves the following symmetry:

$$\begin{aligned} u(t_1, t_2) = u(t_1, -t_2) &\implies [\Delta_\Sigma u(\boldsymbol{t})]_{|\boldsymbol{t}=[x_1, x_2]} = [\Delta_\Sigma u(\boldsymbol{t})]_{|\boldsymbol{t}=[x_1, -x_2]} \\ u(t_1, t_2) = u(-t_1, t_2) &\implies [\Delta_\Sigma u(\boldsymbol{t})]_{|\boldsymbol{t}=[x_1, x_2]} = [\Delta_\Sigma u(\boldsymbol{t})]_{|\boldsymbol{t}=[-x_1, x_2]} \end{aligned}. \tag{4.22}$$

Analogously to the case above, the right-hand sides become

$$\langle \boldsymbol{x}, \boldsymbol{n}_\Sigma \rangle = \frac{h_\Sigma - \partial_1 h_\Sigma t_1 - \partial_2 h_\Sigma t_2}{\sqrt{1 + \left(\partial_1 h_\Sigma\right)^2 + \left(\partial_2 h_\Sigma\right)^2}} \qquad \text{and} \qquad \langle \boldsymbol{x}, \boldsymbol{n}_\Gamma \rangle = \frac{-\kappa_1 t_1^2 - \kappa_2 t_2^2}{2\sqrt{1 + \kappa_1^2 t_1^2 + \kappa_2^2 t_2^2}}. \tag{4.23}$$

**Analytical solutions for $\Delta_\Gamma u = \langle \boldsymbol{x}, \boldsymbol{n}_\Gamma \rangle$** For non-planar hypersurfaces $\Gamma$ in two spatial dimensions with arbitrary but constant $\kappa \in \mathbb{R}$, combining eq. (4.18) and eq. (4.19), we obtain the family of solutions

$$u(t_1; \kappa) = u_0 + \left( \frac{1}{18\kappa^3} - \frac{1 + \kappa^2 t_1^2}{30\kappa^3} \right) \left(1 + \kappa^2 t_1^2\right)^{\frac{3}{2}}, \tag{4.24}$$

where choosing $u_0 = -\frac{1}{45\kappa^3}$ ensures $u(0; \kappa) = 0$. For planar hypersurfaces, the solution becomes trivial, since $\lim_{\kappa \to 0} u(t_1; \kappa) = 0$. The existence of an analytical solution implies that the computation of the volume (i.e. the area, since we consider $d = 2$ here) only requires to compute the two intersections, denoted $t_1^\pm$, of the approximated hypersurface $\Gamma$ with the cell boundary $\partial\mathcal{K}$, e.g. by a simple NEWTON algorithm. The $t_1^\pm$ are then plugged into eq. (4.24) to obtain the surface gradient $\nabla_\Sigma u|_{t_1 = t_1^\pm}$, which is then used to evaluate the inner product with the boundary normal $\boldsymbol{n}_{\partial\Sigma}$. Figure (4.7) illustrates the relevant quantities. Also, an advantage of our approach becomes evident in fig. (4.7(a)): for $d = 2$, the approximated hypersurface is not required to be the graph of a function whose independent variable varies along one of the cell edges.

In three spatial dimensions, cf. eq. (4.21) and eq. (4.23), a family of analytical solutions can be given for coinciding and constant principal curvatures $\kappa_1 = \kappa_2 = \kappa$, yielding

$$u(\boldsymbol{t}; \kappa) = u_0 + \left( \frac{1}{24\kappa^3} - \frac{1 + \kappa^2 t_1^2 + \kappa^2 t_2^2}{40\kappa^3} \right) \left(1 + \kappa^2 t_1^2 + \kappa^2 t_2^2\right)^{\frac{3}{2}}. \tag{4.25}$$

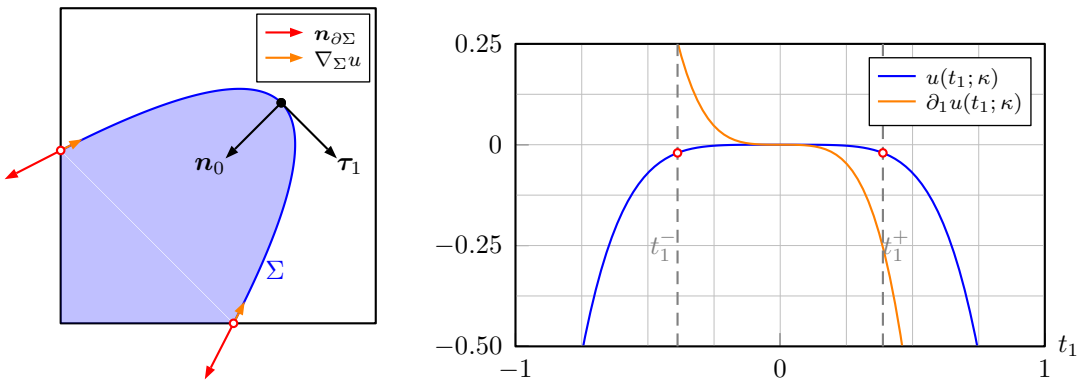


(a) hypersurface patch

(b) analytical solution, cf. eq. (4.24)

Figure 4.7.: Hypersurface patch with $\kappa = 8$, $\boldsymbol{n}_0 = \frac{1}{\sqrt{2}}[-1,-1]^\mathsf{T}$, $\boldsymbol{x}_0 = \frac{7}{10}[1,1]^\mathsf{T}$.

By choosing $u_0 = -\frac{1}{60\kappa^3}$, one obtains $u(\mathbf{0};\kappa) = 0$. For the non-trivial case $\kappa \neq 0$, the iso-contours of the analytical solution, i.e. $\mathcal{I}(u;\alpha) := \{\boldsymbol{t} \in \mathbb{R}^2 : u(\boldsymbol{t};\kappa) = \alpha\}$, are circles. This implies that, for $\alpha \neq 0$ on a polygonal parameter set $\mathcal{S}_\Gamma$, which is preferable for numerical implementation, the function $u_{|\partial\mathcal{S}_\Gamma}$ cannot be constant, especially $u|_{\partial\mathcal{S}_\Gamma} \neq 0$; cf. fig. (4.8). This imposes crucial restrictions on the numerical algorithm for the solution of the variational problem, if, e.g., one seeks to exploit partial integration; cf. eq. (A.19).

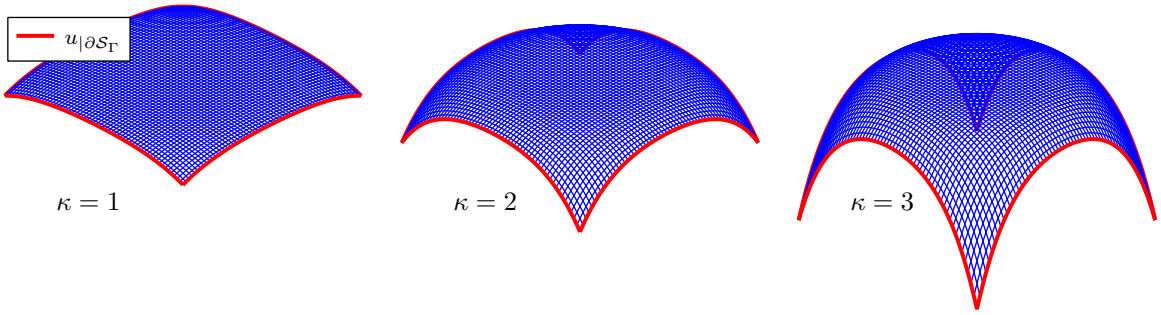


Figure 4.8.: Visualization of eq. (4.25) for $\mathcal{S}_\Gamma = [-1,1]^2$ and various $\kappa$.

For the general case $\kappa_1 \neq \kappa_2$, an analytical solution could not be found by the author. Hence, we transform the problem into its variational formulation, in order to make it accessible for numerical treatment.

### 4.4.4. Variational formulation and Petrov-Galerkin ansatz

The present subsection is devoted to the variational formulation of $\Delta_\Gamma u = \langle \boldsymbol{x}, \boldsymbol{n}_\Gamma \rangle$ for hypersurfaces $\Gamma \subset \mathbb{R}^3$ defined by eq. (4.13), following a standard approach: we multiply by a test function $\varphi_i^\mathrm{t} \in \mathcal{F}_N^\mathrm{t}$, approximate the sought solution $u$ by a series of $N$ ansatz functions $\varphi_j^\mathrm{a} \in \mathcal{F}_N^\mathrm{a}$ and numerically integrate over $\Gamma$. The analytical solution given in eq. (4.25) is desired to be an element of the ansatz function space. However, its properties prohibit an application of DIRICHLET boundary conditions on polygonally

bounded parameter sets, and NEUMANN boundary conditions are incompatible with our approach. Hence, we do not apply partial integration. Further details of the function spaces are provided below. As stated in subsection 4.4.2, due to the explicit parametrization, any function $f$ mapping from the hypersurface $\Gamma$ may be expressed as $f^\Gamma = f \circ \boldsymbol{g}_\Gamma$, with $f^\Gamma : \mathcal{S}_\Gamma \mapsto \mathbb{R}$. Exploiting the integral transformation from eq. (4.9), one obtains

$$\sum_{j=1}^{N} \hat{u}_j \int_{\mathcal{S}_\Gamma} \varphi_i^{\mathrm{t}}(\boldsymbol{t}) \Delta_\Gamma \varphi_j^{\mathrm{a}}(\boldsymbol{t}) \mathcal{DF}(\boldsymbol{g}_\Gamma(\boldsymbol{t})) \mathrm{d}\boldsymbol{t} = \int_{\mathcal{S}_\Gamma} f^\Gamma(\boldsymbol{t}) \varphi_i^{\mathrm{t}}(\boldsymbol{t}) \mathcal{DF}(\boldsymbol{g}_\Gamma(\boldsymbol{t})) \mathrm{d}\boldsymbol{t} \qquad \text{or} \qquad \boldsymbol{A}_\Gamma \hat{\boldsymbol{u}} = \boldsymbol{b}_\Gamma, \tag{4.26}$$

with the functional determinant $\mathcal{DF}(\boldsymbol{g}_\Gamma) := \langle \nabla\phi_\Gamma, \nabla\phi_\Gamma \rangle^{\frac{1}{2}} = \sqrt{1 + \kappa_1^2 t_1^2 + \kappa_2^2 t_2^2}$ corresponding to the area of an infinitesimal hypersurface element; cf. subsection 4.4.3.

**Approximation of the parameter set** A direct numerical quadrature of eq. (4.26) is difficult due to the potentially non-polygonal shape of the parameter set $\mathcal{S}_\Gamma$. Therefore we approximate the parameter set by a polygon spanned by the projection of the intersections of the hypersurface with the cell edges; cf. fig. (4.9(b)).

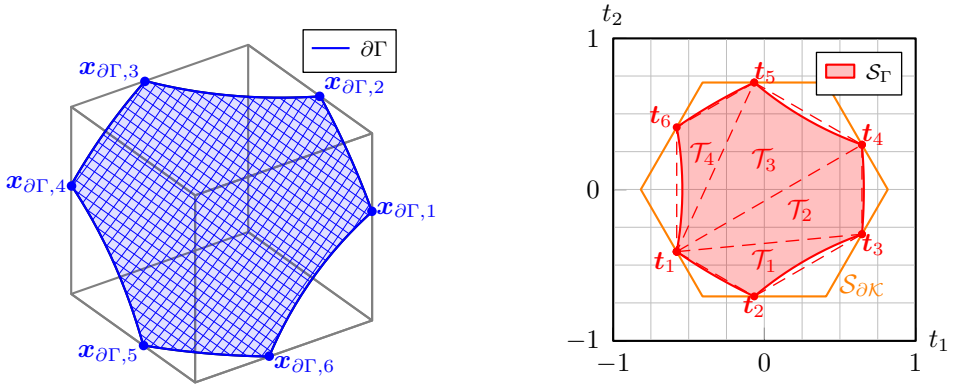


(a) hypersurface patch

(b) true and triangulated parameter set

Figure 4.9.: Hypersurface ($\boldsymbol{x}_0 = \frac{6}{10}[1,1,1]$, $\kappa_i = -\frac{1}{2}$ and $\boldsymbol{n}_0 = \frac{-1}{\sqrt{3}}[1,1,1]$) with true (shaded) and triangulated (dashed lines) parameter set, where $\mathcal{S}_{\partial\mathcal{K}}$ is the projection of the cell boundary. Note that the polygon spanned by the projections of the edge intersections (•) does not contain the true parameter set, nor vice versa, i.e. $\bigcup_k \mathcal{T}_k \not\supset \mathcal{S}_\Gamma$ and $\bigcup_k \mathcal{T}_k \not\subset \mathcal{S}_\Gamma$, in general.

The integration over the approximated parameter set $\mathcal{S}_\Gamma \approx \bigcup_k \mathcal{T}_k$ can then be performed by transformation of the respective triangles to the referential square $\mathcal{S}_0 := [0,1]^2$ (via the referential triangle $\mathcal{T}_0$) and standard GAUSS-LEGENDRE quadrature, i.e.

$$\int_{\mathcal{T}_k} f(\boldsymbol{t})\, \mathrm{d}\boldsymbol{t} = \int_{\mathcal{T}_0} f(\boldsymbol{T}_k(\boldsymbol{u}))\, \|\det \boldsymbol{J}_{\boldsymbol{T}_k}\|\, \mathrm{d}\boldsymbol{u} = \int_{\mathcal{S}_0} f(\boldsymbol{T}_k(\boldsymbol{T}_{\mathcal{S}}(\boldsymbol{u})))\, u_1 \|\det \boldsymbol{J}_{\boldsymbol{T}_k}\|\, \mathrm{d}\boldsymbol{u} \approx \sum_i f(\hat{\boldsymbol{t}}_{k,i}) \omega_{k,i}^\Gamma, \tag{4.27}$$

where $\hat{\boldsymbol{t}}_{i,k} \in \mathcal{T}_k$ are the quadrature nodes with associated weights $\omega_{k,i}^\Gamma$; cf. fig. (4.10) for an illustration.

Although it would be more convenient to approximate the parameter set by, say, the projection of the cell boundary $\mathcal{S}_{\partial\mathcal{K}}$, numerical experiments have shown that the quality of the parameter set approximation

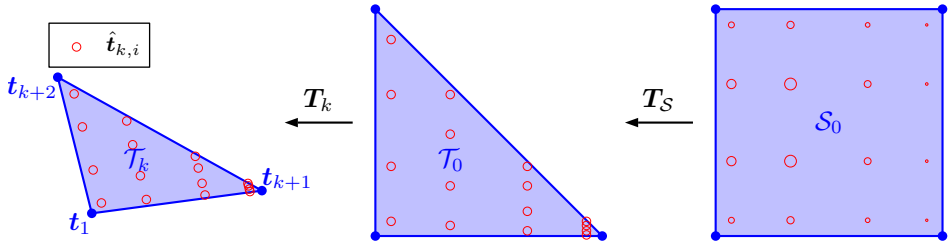


Figure 4.10.: Transformation of triangular integration domain $\mathcal{T}_k \subset \mathbb{R}^2$ to $\mathcal{S}_0$. In the reference square, the circle sizes indicate the relative magnitude of the weights $\omega^{\Gamma}_{k,i}$.

is crucial for the overall accuracy of the algorithm. The accuracy especially suffers from a coarse parameter set approximation for $\kappa_1 \neq \kappa_2$, rapidly decreasing for increasing $||\kappa_1| - |\kappa_2||$.

**The choice of Ansatz and test functions** In order for eq. (4.26) to be a well-posed problem for $\hat{\boldsymbol{u}}$, the regularity required for the test functions is $\varphi_i^{\mathrm{t}} \in \mathcal{F}_N^{\mathrm{t}} \subset L^2(\mathcal{S}_\Gamma)$ and for the ansatz functions $\varphi_j^{\mathrm{a}} \in \mathcal{F}_N^{\mathrm{a}} \subset H_2^2(\mathcal{S}_\Gamma)$, respectively. Since the test functions need not contain any information on the underlying hypersurface, let $\mathcal{F}_N^{\mathrm{t}} = \mathcal{L}_N(t_1) \otimes \mathcal{L}_N(t_2)$, where $\mathcal{L}_N(x) := \{P_k(x) : 0 \leq k \leq N\}$ is the set of Legendre polynomials up to order $N$. Preliminary numerical experiments indicated that the ansatz functions $\varphi_i^{\mathrm{a}}$ have to be chosen in accordance with both the underlying hypersurface $\Gamma$ and the right-hand side. Here, the ansatz functions contain the norm of an infinitesimal surface element, i.e.

$$\varphi_i^{\mathrm{a}} := \varphi_i^{\mathrm{t}} \langle \nabla\phi_\Gamma, \nabla\phi_\Gamma \rangle^{\frac{3}{2}} = \varphi_i^{\mathrm{t}} \left(1 + \kappa_1^2 t_1^2 + \kappa_2^2 t_2^2\right)^{\frac{3}{2}}. \tag{4.28}$$

This choice also ensures that the analytical solution for the volume computation case ($f = \langle \boldsymbol{x}, \boldsymbol{n}_\Gamma \rangle$) given in eq. (4.25) is an element of $\mathrm{span}(\mathcal{F}_N^{\mathrm{a}})$, which is not possible by choosing polynomial ansatz functions. Also, we would like to emphasize that the above mentioned symmetry properties of the Laplace-Beltrami operator, cf. eq. (4.22), for purely quadratic hypersurfaces allow to remove those Legendre polynomials with odd order.

### 4.4.5. Equating polynomial coefficients

Within this subsection, let $g := 1 + \kappa_1^2 t_1^2 + \kappa_2^2 t_2^2$ for ease of notation and assume that $u : \mathbb{R}^2 \mapsto \mathbb{R}$ is polynomial. Note that for the gradient and Hessian matrix, respectively, one obtains

$$\begin{aligned}
\partial_i \left(u\sqrt{g^3}\right) &= \frac{1}{\sqrt{g}} \left[g^2 \partial_i u + \frac{3}{2} u g \partial_i g\right], \\
\partial_{ij} \left(u\sqrt{g^3}\right) &= \frac{1}{\sqrt{g}} \left[g^2 \partial_{ij} u + \frac{3g}{2} \left(\partial_i g \partial_j u + \partial_j g \partial_i u + u \partial_{ij} g\right) + \frac{3u}{2} \partial_i g \partial_j g\right],
\end{aligned} \tag{4.29}$$

where the expressions in parentheses are also polynomial. Inserting the above into the definition of the surface Laplace-Beltrami operator, cf. eq. (4.21), and comparing the result with the right-hand side, cf. eq. (4.23), it becomes evident that the product on the left-hand side of

$$\sqrt{g} \left(\Delta_\Gamma \left(u\sqrt{g^3}\right) - \langle \boldsymbol{x}, \boldsymbol{n}_\Gamma \rangle\right) = 0 \tag{4.30}$$

is a polynomial expression. In fact, one obtains

$$\begin{aligned}\sqrt{g}\Delta_\Gamma\left(t_1^m t_2^n\sqrt{g^3}\right) = \;& (\kappa_1^2(m^2+4m+3)+(n^2+4n+3)\kappa_2^2-\kappa_1\kappa_2(2mn+m+n))t_1^m t_2^n \\ &+(\kappa_1^2\kappa_2^2(m^2+4m+3)-\kappa_1\kappa_2^3(2mn+6m+n+3))t_1^m t_2^{n+2} \\ &+(\kappa_1^2\kappa_2^2(n^2+4n+3)-\kappa_1^3\kappa_2(2mn+6n+m+3))t_1^{m+2}t_2^n \\ &+2\kappa_2^2(m^2-m)t_1^{m-2}t_2^{n+2}+(n^2-n)t_1^m t_2^{n-2}+(m^2-m)t_1^{m-2}t_2^n \\ &+\kappa_2^4(m^2-m)t_1^{m-2}t_2^{n+4}+2\kappa_1^2(n^2-n)t_1^{m+2}t_2^{n-2} \\ &+\kappa_1^4(n^2-n)t_1^{m+4}t_2^{n-2}. \end{aligned} \tag{4.31}$$

Furthermore, the symmetry of $\langle \boldsymbol{x}, \boldsymbol{n}_\Gamma\rangle$ implies that any solution $u$ of eq. (4.30) can only contain even powers of $t_i$, hence we choose the ansatz

$$u = \sum_{i=0}^{I}\sum_{j=0}^{J}\hat{u}_{ij}t_1^{2i}t_2^{2j}, \tag{4.32}$$

where the $(I+1)(J+1)$ coefficients $\hat{\boldsymbol{u}} := \{\hat{u}_{ij}\}$ are obtained from comparison of polynomial coefficients. As can be seen from eq. (4.31), the modified Laplace-Beltrami operator $\tilde{\Delta}_\Gamma u := \sqrt{g}\Delta_\Gamma(u\sqrt{g^3})$ expands the polynomial span of its argument, implying that the system of equations governing the coefficients $\hat{u}_{ij}$ will be overdetermined for general $\kappa_1 \neq \kappa_2$, since

$$\sum_{i=0}^{I}\sum_{j=0}^{J}\hat{u}_{ij}\tilde{\Delta}_\Gamma(t_1^{2i}t_2^{2j}) - \sqrt{g}\langle \boldsymbol{x}, \boldsymbol{n}_\Gamma\rangle = \sum_{i=0}^{I+2}\sum_{j=0}^{J+2}\beta_{ij}(\hat{\boldsymbol{u}};\kappa_1,\kappa_2)\, t_1^{2i}t_2^{2j}. \tag{4.33}$$

Solving eq. (4.30) exactly is equivalent to finding $\hat{\boldsymbol{u}}$ such that $\boldsymbol{\beta}(\hat{\boldsymbol{u}};\kappa_1,\kappa_2) = \boldsymbol{0}$. Since $\boldsymbol{\beta}$ is linear in $\hat{\boldsymbol{u}}$, we may write

$$\boldsymbol{B}_\Gamma\hat{\boldsymbol{u}} = \boldsymbol{q}_\Gamma \qquad \text{with} \qquad \boldsymbol{B}_\Gamma \in \mathbb{R}^{K\times(I+1)(J+1)} \quad \text{and} \quad \boldsymbol{q}_\Gamma \in \mathbb{R}^K, \tag{4.34}$$

where the number of rows $K$ is a function of maximum polynomial orders $I, J$ with $K \geq (I+1)(J+1)$. Numerical experiments for $1 \leq I, J \leq 6$ indicate that (i) the matrix $\boldsymbol{B}_\Gamma$ does not have full rank, i.e. $\operatorname{rank}(\boldsymbol{B}_\Gamma) < K$, and (ii) the rank of $\boldsymbol{B}_\Gamma$ is $(I+1)(J+1)$, cf. tab. (4.1). Assume that the elements in $\boldsymbol{\beta}$ (corresponding to the rows in $\boldsymbol{B}_\Gamma$) are sorted in ascending order with respect to the corresponding powers of $\boldsymbol{t}$. Looping over all $K$ rows in $\boldsymbol{B}_\Gamma$, the $m$-th row is discarded if it is linear dependent on the $m-1$ previous rows. The polynomials whose coefficients cannot be eliminated are of higher order, i.e. $\mathcal{O}(\|\boldsymbol{t}\|^{2I+2})$. In the limiting case $\kappa_1 = \kappa_2$, this approach produces the analytical solution given in eq. (4.25). We would like to emphasze that due to $\operatorname{rank}(\boldsymbol{B}_\Gamma) = (I+1)(J+1)$, the reduced form of eq. (4.34) can be solved exactly. The full expansion of the first three entries of the coefficient vector is provided in appendix A.4.

Table 4.1.: Number of coefficients $K$ over various $I = J$, with the apparent relation $K-(I+1)^2 = 4I+2$.

| $I$ | 1 | 2 | 3 | 4 | 5 | 6 |
|---|---|---|---|---|---|---|
| $K$ | 10 | 19 | 30 | 43 | 58 | 75 |
| $K-(I+1)^2$ | 6 | 10 | 14 | 18 | 22 | 26 |

### 4.4.6. An analytical solution for spheres

As stated above, an analytical evaluation of the volume integral in eq. (4.2) is possible for spheres. Choosing the reference to coincide with the centroid of the sphere, i.e. $\Sigma := \partial\mathcal{B}_R(\boldsymbol{x}_0)$ with $\boldsymbol{x}_{\text{ref}} := \boldsymbol{x}_0$, one obtains

$$\int_\Sigma \langle \boldsymbol{x} - \boldsymbol{x}_0, \boldsymbol{n}_\Sigma \rangle \, \mathrm{d}o = R \int_\Sigma 1 \, \mathrm{d}o. \tag{4.35}$$

Applying the surface divergence theorem from eq. (4.4) requires to solve eq. (4.3) with constant right-hand side, i.e. we seek a function $u : \Sigma \mapsto \mathbb{R}$ such that $\Delta_\Sigma u = 1$. For obvious reasons, it is convenient to employ spherical coordinates, where after rearrangement the Laplace-Beltrami equation takes the form

$$\sin\theta \partial_\theta(\sin\theta u_\theta) + u_{\varphi\varphi} = R^2 \sin^2\theta. \tag{4.36}$$

The right-hand side of the above equation is a function of the polar angle $\theta$ only, thus let $u = u(\theta)$ with $u(0) = 0$. The latter assumption removes the ambiguity induced by the shift invariance of eq. (4.36). We obtain the solution

$$\tilde{u}(\theta) = R^2 \left(\log 2 - \log(1 + \cos\theta)\right). \tag{4.37}$$

In Cartesian coordinates, eq. (4.37) reads

$$\tilde{u}(z) = R^2 \left(\log 2 - \log\left(1 + \frac{z}{R}\right)\right) \quad \text{with} \quad \nabla_\Sigma \tilde{u} = \tilde{u}_z \boldsymbol{P}_\Sigma \boldsymbol{e}_z = \left[\frac{xz}{R+z}, \frac{yz}{R+z}, z - R\right]^\mathsf{T}. \tag{4.38}$$

The integrand emerging from the application of the surface divergence theorem, cf. eq. (4.4), becomes

$$\langle \nabla_\Sigma \tilde{u}, \boldsymbol{n}_{\partial\Sigma_k} \rangle = \frac{\nabla\tilde{u}^\mathsf{T} \boldsymbol{P}_\Sigma \boldsymbol{n}_{\mathcal{F}_k}}{\sqrt{\boldsymbol{n}_{\mathcal{F}_k}^\mathsf{T} \boldsymbol{P}_\Sigma \boldsymbol{n}_{\mathcal{F}_k}}} = R \begin{cases} \frac{\pm x_0 z}{(R+z)\sqrt{R^2 - x_0^2}} & \boldsymbol{n}_{\mathcal{F}_k} = \pm\boldsymbol{e}_1 \;\; (x = x_0) \\ \frac{\pm y_0 z}{(R+z)\sqrt{R^2 - y_0^2}} & \boldsymbol{n}_{\mathcal{F}_k} = \pm\boldsymbol{e}_2 \;\; (y = y_0) \\ \frac{\mp\sqrt{R^2 - z_0^2}}{z_0 + R} & \boldsymbol{n}_{\mathcal{F}_k} = \pm\boldsymbol{e}_3 \;\; (z = z_0) \end{cases}, \tag{4.39}$$

where $\boldsymbol{n}_{\mathcal{F}_k}$ is the outward pointing normal of the face containing $\partial\Sigma_k$; cf. fig. (4.1). Recall that the boundary curve $\partial\Sigma = \bigcup_k \partial\Sigma_k$ is composed of piecewise planar segments, which by assumption are parallel to one of the coordinate planes, implying that the segements $\partial\Sigma_k$ are sectors of circles; cf. fig. (4.11).

The aforementioned properties suggest a polar parametrization $\partial\Sigma_k = \{\boldsymbol{F}_{\partial\Sigma}(\psi) : \psi \in [\psi_k^0, \psi_k^1]\}$ with

$$\boldsymbol{F}_{\partial\Sigma}(\psi) = \begin{cases} \left[x_0, \sqrt{R^2 - x_0^2}\sin\psi, \sqrt{R^2 - x_0^2}\cos\psi\right]^\mathsf{T} & x = x_0 \\ \left[\sqrt{R^2 - y_0^2}\sin\psi, y_0, \sqrt{R^2 - y_0^2}\cos\psi\right]^\mathsf{T} & y = y_0 \\ \left[\sqrt{R^2 - z_0^2}\cos\psi, \sqrt{R^2 - z_0^2}\sin\psi, z_0\right]^\mathsf{T} & z = z_0 \end{cases}. \tag{4.40}$$

Inserting the parametrization given in eq. (4.40) into the integrand of eq. (4.39) allows for an analytical

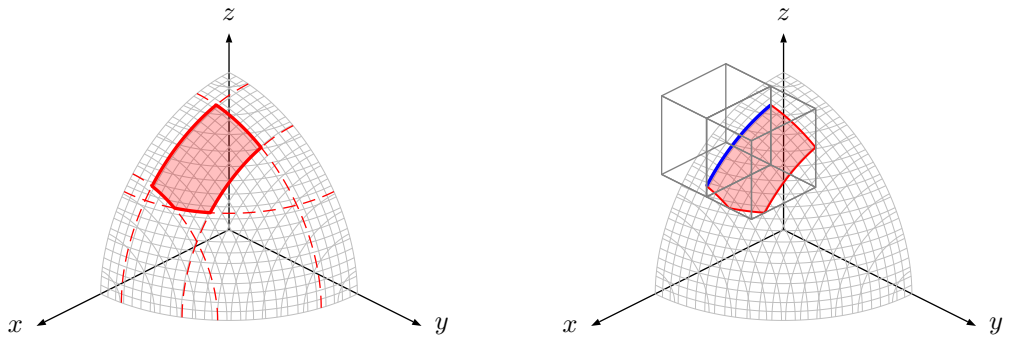


(a) sphere patch $\Sigma$ (b) shared boundary segment $\partial\Sigma_k$

Figure 4.11.: Sphere patch $\Sigma$ confined by sectors of circles with different radii (dashed lines in (a)) and computational cells sharing a segment of $\partial\Sigma$ (blue line in (b)); cf. eq. (4.41) and note (4.3).

evaluation of the boundary integral

$$\int_{\Sigma} 1 \,\mathrm{d}o = \int_{\partial\Sigma} \langle \nabla_{\Sigma}\tilde{u}, \boldsymbol{n}_{\partial\Sigma}\rangle \,\mathrm{d}s = \sum_{k=1}^{6} \int_{\partial\Sigma_k} \langle \nabla_{\Sigma}\tilde{u}, \boldsymbol{n}_{\partial\Sigma_k}\rangle \,\mathrm{d}s \tag{4.41}$$

where

$$\int_{\partial\Sigma_k} \langle \nabla_{\Sigma}\tilde{u}, \boldsymbol{n}_{\partial\Sigma_k}\rangle \,\mathrm{d}s = \mu(\boldsymbol{n}_{\mathcal{F}_k}) \begin{cases} \mathcal{M}(\psi_k^1; R, x_0) - \mathcal{M}(\psi_k^0; R, x_0) & x = x_0 \\ \mathcal{M}(\psi_k^1; R, y_0) - \mathcal{M}(\psi_k^0; R, y_0) & y = y_0 \\ (z_0 - R)(\psi_k^1 - \psi_k^0) & z = z_0 \end{cases} . \tag{4.42}$$

For $0 < |a| < R$ the primitive of the integrant in eq. (4.39) reads

$$\begin{aligned} \mathcal{M}(\psi; R, a) &:= \int \frac{a\sqrt{R^2 - a^2}\cos\psi}{(R + \sqrt{R^2 - a^2}\cos\psi)} \mathrm{d}\psi \\ &= Ra\psi - 2R^2 \left( \arctan\left( \frac{\sqrt{R^2 - a^2}}{a} \tan\frac{\psi}{2} \right) + \Delta_{\mathcal{M}}(\psi; a) \right) . \end{aligned} \tag{4.43}$$

The numerical evaluation of eq. (4.41) forms two obstacles: (i) The discontinuity of tan and arctan translates to eq. (4.43), which is removed by applying the shift

$$\Delta_{\mathcal{M}}(\psi; a) = \begin{cases} \pi \,\mathrm{sign}\,(\psi) & |\psi| > \pi, a > 0 \\ 0 & (|\psi| \le \pi, a > 0) \text{ or } (|\psi| > \pi, a < 0) \\ -\pi \,\mathrm{sign}\,(\psi) & |\psi| < \pi, a < 0 \end{cases} ; \tag{4.44}$$

cf. fig. (4.12) for an illustration. (ii) The decomposition of the boundary $\partial\Sigma$ in eq. (4.41) requires a correction of the orientation induced by the case-dependent polar parametrization given in eq. (4.40). In

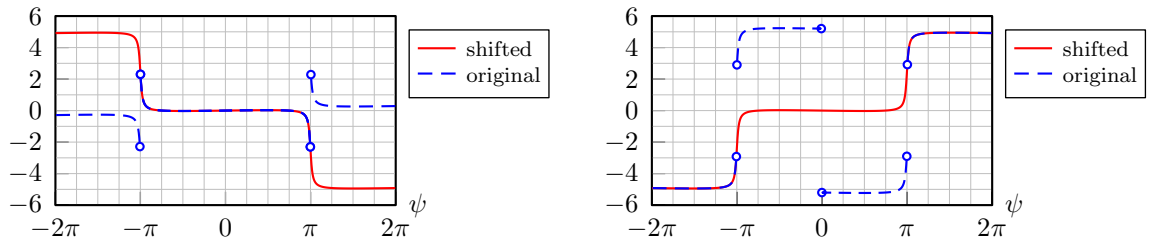


(a) $a = \frac{1}{20}$ (b) $a = -\frac{1}{20}$

Figure 4.12.: Illustration of eq. (4.43) with and without the shift of eq. (4.44) for $R = \frac{91}{100}$ and $a = \pm\frac{1}{20}$.

combination with the sign ambiguity of eq. (4.39) one obtains

$$\mu(\boldsymbol{n}_{\mathcal{F}_k}) := \begin{cases} -1 & x = x_0 \\ 1 & \text{else} \end{cases} . \tag{4.45}$$

Equation (4.45) ensures that the concatenation of the segments $\partial\Sigma_k$ parametrized using eq. (4.40) forms a closed path. Hence, the volume fractions induced by spheres can be computed up to machine precision. Figure (4.13) exemplifies the global volume error as a function of the resolution per spatial direction $N_{\mathcal{K}}$. The fact that the volume error increases with increasing resolution can be attributed to accumulation of floating point errors resulting from the summation of $\sqrt{N_\Sigma} \sim N_{\mathcal{K}}$ numbers.

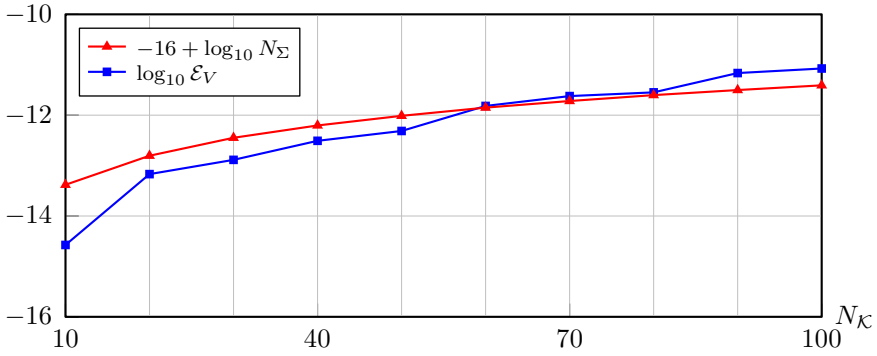


Figure 4.13.: Global volume error for a sphere with radius $R = \frac{91}{100}$ centered in $[-1, 1]^3$.

**Note 4.3** (Computational efficiency)**.** *Figure (4.11(b)) illustrates that the segments $\partial\Sigma_k$ are shared by their respectively parenting cell. Hence, the numerical evaluation of the rightmost expression in eq. (4.41) has to be carried out once per face, which allows for consistent and efficient implementation.*

## 4.5. The numerical algorithm

Figure (4.14) contains a schematic flowchart of the developed numerical algorithm. Note that, due to the cell-based application, the presented algorithm parallelizes trivially. The intersections $\boldsymbol{x}_{\partial\Sigma,k}$ of the true hypersurface $\Sigma$ with the cell edges are computed by NEWTON iteration with a tolerance of $10^{-12}$. The level-set function is approximated by a third-order polynomial based on the values of the level-set function $\phi_\Sigma$ and its gradient $\nabla\phi_\Sigma$, evaluated at the cell corners. If the hypersurface is parameterizable over some parameter set $\mathcal{S}_\Sigma$, i.e. $\Sigma = \{\boldsymbol{g}_\Sigma(\boldsymbol{t}) : \boldsymbol{t} \in \mathcal{S}_\Sigma\}$, the centroid of the polygon spanned by the edge intersections is projected onto $\mathcal{S}_\Sigma$ to obtain $\hat{\boldsymbol{t}}_{\partial\Sigma} := \boldsymbol{g}_\Sigma^{-1}(\hat{\boldsymbol{x}}_{\partial\Sigma})$, with $\hat{\boldsymbol{x}}_{\partial\Sigma} = {}^1\!/_N \sum_{k=1}^N \boldsymbol{x}_{\partial\Sigma,k}$ and $\boldsymbol{g}_\Sigma^{-1} : \mathbb{R}^d \mapsto \mathcal{S}_\Sigma$ surjective. The base point is then obtained as $\boldsymbol{x}_0 = \boldsymbol{g}_\Sigma(\hat{\boldsymbol{t}}_{\partial\Sigma})$. For hypersurfaces that are not parameterizable in the above sense, a metric projection dependent on the class of the respective hypersurface is applied. The principal curvatures $\kappa_i$ and associated directions $\boldsymbol{\tau}_i$ define the approximated hypersurface $\Gamma$, whose intersections $\boldsymbol{x}_{\partial\Gamma,k}$ with the cell edges, after projection onto the tangential plane via $\mathcal{P}_\Gamma(\boldsymbol{x}) := [\boldsymbol{\tau}_1, \boldsymbol{\tau}_2]^\mathsf{T}(\boldsymbol{x} - \boldsymbol{x}_0)$, provide the vertices $\boldsymbol{t}_k$ of the parameter set polygon $\mathcal{S}_\Gamma \approx \bigcup_k \mathcal{T}_k$; cf. again fig. (4.9). Due to the polynomial character of the underlying equation, cf. subsection 4.4.5, it is possible to approximate the solution either by a variational formulation or by comparison of polynomial coefficients. In the latter case, the coefficients associated to the ansatz functions $\varphi_k^\mathrm{a}$ can be evaluated directly. The first case, i.e. the application of PETROV-GALERKIN approach, however requires to assemble a linear system, which is solved employing the `LAPACK` routines `dgetrf` and `dgetrs`. Numerical experiments have shown that for very small hypersurface patches ($|\Gamma| \leq 10^{-7}$), the system may become ill-posed. For those non-invertible matrices $\boldsymbol{A}_\Gamma$, the principal curvatures $\kappa_i$ are set to zero, corresponding to a planar approximation, and the edge intersections $\boldsymbol{x}_{\partial\Gamma,k}$ are recomputed. After assembling the solution $u$, the rightmost expression of eq. (4.2) can be evaluated. The integral over the hypersurface is evaluated using eq. (4.4) on $\partial\Gamma = \bigcup_k \partial\Gamma_k$, where the details are given in subsection 4.5.2. A cell face $\mathcal{F}_k$ with a non-zero contribution to eq. (4.2) is either intersected by $\Gamma$ or interior (i.e., $\phi_\Gamma(\boldsymbol{x}) < 0 \quad \forall \boldsymbol{x} \in \mathcal{F}_k$), where in the first case the area is computed by standard quadrature. If the computed volume is negative or exceeds the volume of the containing cell, the curvatures $\kappa_i$ are set to zero, and the edge intersections $\boldsymbol{x}_{\partial\Gamma,k}$ are recomputed, as in the case of a non-invertible $\boldsymbol{A}_\Gamma$. This case will be referred to as *out-of-bounds* below.

### 4.5.1. Topological considerations

The decomposition of an intersected cell $\mathcal{K}$ requires a hierarchically consistent evaluation of the topological properties of its vertices $\{\boldsymbol{\nu}_i\}$, edges $\{\mathcal{E}_k\}$ and faces $\{\mathcal{F}_i\}$. Induced by the orientable hypersurface $\Gamma$, the status $\mathfrak{S}$ of any of the aforementioned entities is either interior ($\mathfrak{S} = -1$), intersected ($\mathfrak{S} = 0$) or exterior ($\mathfrak{S} = 1$). The hierarchically lowest entity is a vertex $\boldsymbol{\nu}_i$, whose status, in theory, is uniquely determined by the sign of the associated level-set value. However, for the purpose of numerical robustness, it is advantageous to employ

$$\mathfrak{S}(\boldsymbol{\nu}_i) := \begin{cases} 0 & |\phi_\Gamma(\boldsymbol{\nu}_i)| < \epsilon_\mathfrak{S} \\ \operatorname{sign}\left(\phi_\Gamma(\boldsymbol{\nu}_i)\right) & |\phi_\Gamma(\boldsymbol{\nu}_i)| \geq \epsilon_\mathfrak{S} \end{cases}, \tag{4.46}$$

where, throughout this thesis, $\epsilon_\mathfrak{S} = 10^{-14}$ was used; cf. section 1.3. Subsequently, tab. (4.2) provides the status of an edge $\mathcal{E}_k$ with vertices $\{\boldsymbol{\nu}_i, \boldsymbol{\nu}_j\}$. In order to avoid redundancies when counting the number of intersected edges, an edge is considered intersected iff $\mathfrak{S}(\boldsymbol{\nu}_j) = -\mathfrak{S}(\boldsymbol{\nu}_i)$. This implies that edges with

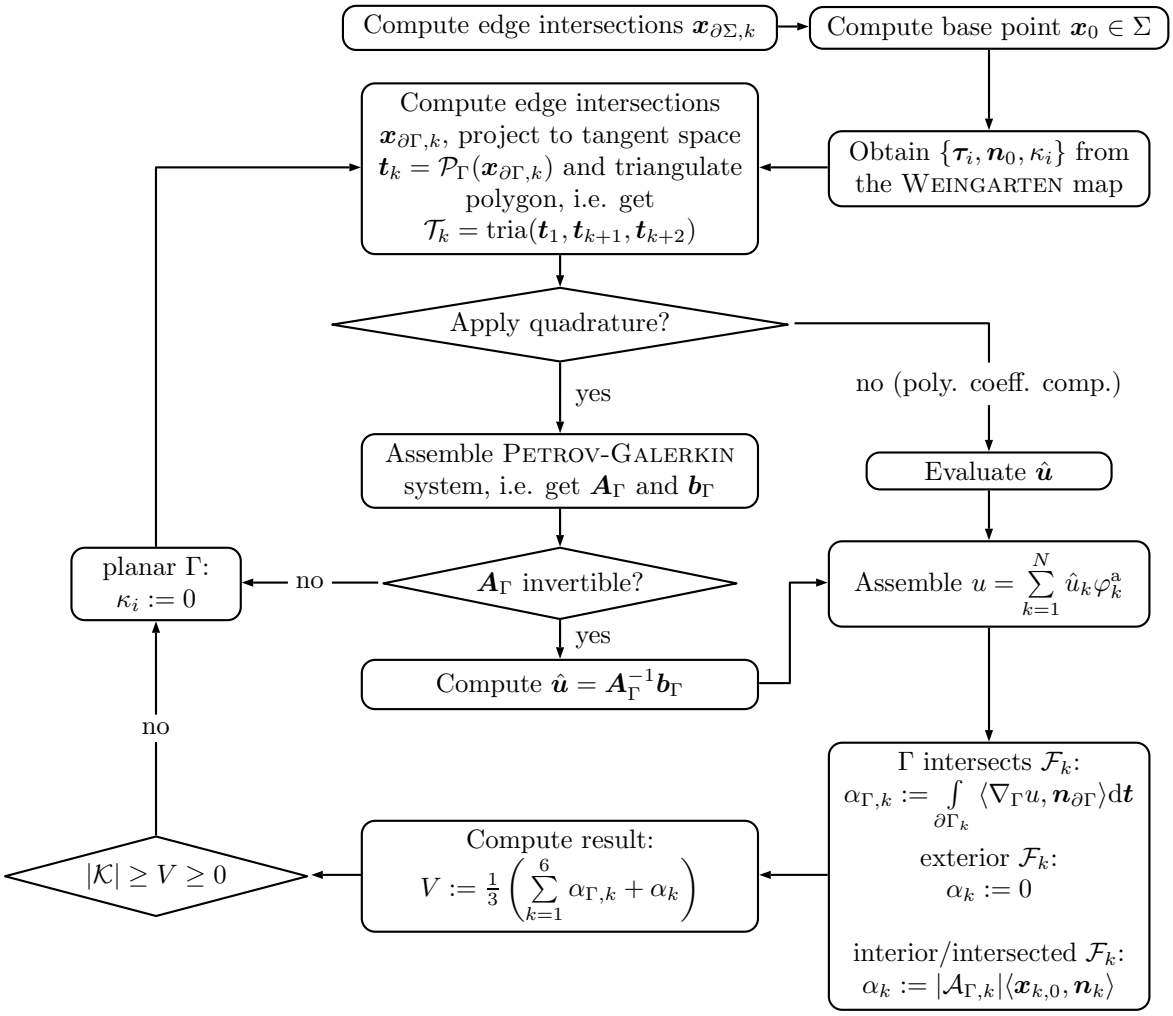


Figure 4.14.: Flowchart of the initialization algorithm.

one intersected vertex are either exterior or interior, corresponding to columns 3 to 8 in tab. (4.2). For curved hypersurfaces $\Gamma \subset \mathbb{R}^3$, if both vertices of an edge are intersected (second column in tab. (4.2)), a unique status assignment based on the level-set values is not possible. The ambivalence can be removed by considering the gradient at one of the vertices, i.e.

$$\mathfrak{S}(\mathcal{E}_k) = \text{sign}\left(\langle \nabla \phi_\Gamma(\boldsymbol{\nu}_i), \boldsymbol{\nu}_j - \boldsymbol{\nu}_i \rangle - \epsilon_{\mathfrak{S}}\right) \quad \text{if} \quad \mathfrak{S}(\boldsymbol{\nu}_i) = \mathfrak{S}(\boldsymbol{\nu}_j) = 0. \tag{4.47}$$

Figure (4.15) depicts an illustration.

The status of a polygonal face $\mathcal{F}_k$ with vertices $\{\boldsymbol{\nu}_i\}$ and edges $\{\mathcal{E}_j\}$ is determined by

$$\mathfrak{S}(\mathcal{F}_k) = \begin{cases} \pm 1 & \mathfrak{S}(\mathcal{E}_j) = \pm 1 \quad \forall j, \\ 0 & \exists!(i,j) \begin{pmatrix} ((\mathfrak{S}(\boldsymbol{\nu}_i) = \mathfrak{S}(\boldsymbol{\nu}_j) = 0) \wedge (i \neq j) \wedge (\mathfrak{S}(\mathcal{E}_m) \neq 0 \quad \forall m)) \oplus \\ ((\mathfrak{S}(\mathcal{E}_i) = \mathfrak{S}(\mathcal{E}_j) = 0) \wedge (i \neq j) \wedge (\mathfrak{S}(\boldsymbol{\nu}_m) \neq 0 \quad \forall m)) \oplus \\ (\mathfrak{S}(\boldsymbol{\nu}_i) = \mathfrak{S}(\mathcal{E}_j) = 0) \end{pmatrix}, \end{cases} \tag{4.48}$$

Table 4.2.: Edge status as function of the statūs of the associated vertices.

| $\mathfrak{S}(\boldsymbol{\nu}_i)$ | $\pm1$ | 0 | $-1$ | 0 | $-1$ | 1 | 0 | 1 |
|---|---|---|---|---|---|---|---|---|
| $\mathfrak{S}(\boldsymbol{\nu}_j)$ | $\mp1$ | 0 | 0 | $-1$ | $-1$ | 0 | 1 | 1 |
| $\mathfrak{S}(\mathcal{E}_k)$ | 0 | $\pm1$ | $-1$ | $-1$ | $-1$ | 1 | 1 | 1 |

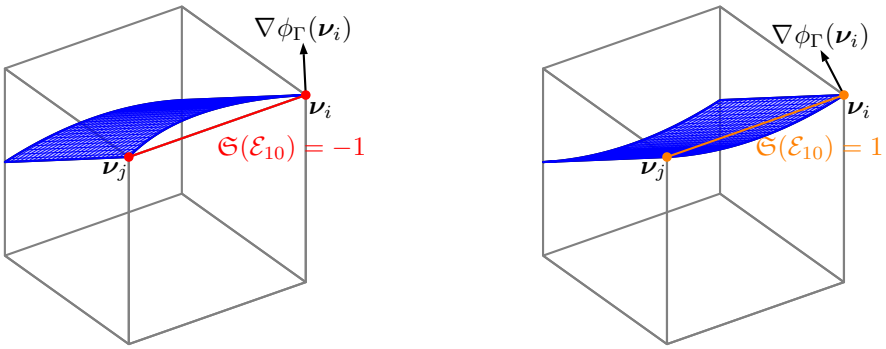


Figure 4.15.: Computational cell with intersection ambivalence on $\mathcal{E}_{10}$: while in both cases the vertices are located on $\Gamma$, the evaluation of the level-set gradient at $\boldsymbol{\nu}_i$ allows for a unique status assignment.

where $\oplus$ denotes *exclusive or* for logical statements. Equation (4.48) states that a face $\mathcal{F}_k$ is considered interior (exterior), iff all associated edges are interior (exterior). An intersected face requires that either (i) exactly two vertices (edges) are intersected, while the remaining edges (vertices) are interior/exterior, or (ii) exactly one edge and one vertex are intersected, while the remaining edges and vertices are interior/exterior. Note that, while the assignments given in tab. (4.2) are respectively bijective, there are combinations of vertex and edge statūs that are not covered by eq. (4.48). Such an exception occurs, for example, if respectively two vertices of a rectangular face are interior and exterior and diagonally opposing vertices exhibit different statūs. Finally, the intersection status of a cell is obtained from the statūs of its associated faces via

$$\mathfrak{S}(\mathcal{K}_k) = \begin{cases} \pm1 & \mathfrak{S}(\mathcal{F}_j) = \pm1 \quad \forall j, \\ 0 & \text{else.} \end{cases} \tag{4.49}$$

For the remainder of this work, the number of interface cells $N_\Sigma$ in a background grid denotes the number of cells whose status is 0.

### 4.5.2. Numerical quadrature of curve integrals

The present subsection is concerned with the evaluation of integrals of the form $\int_{\partial\Gamma} \langle \nabla_\Gamma u, \boldsymbol{n}_{\partial\Gamma} \rangle \mathrm{d}l$, where $u : \Gamma \mapsto \mathbb{R}$ is the numerical solution of eq. (4.26). As stated above, cf. fig. (4.5), a boundary curve segment $\partial\Gamma_k = \partial\Gamma \cap \mathcal{F}_k$ contained in the face $\mathcal{F}_k$ can be parameterized as the graph of a height function, whose ordinate $\mu$ varies along the line connecting two intersections $\{\boldsymbol{x}_{\partial\Gamma_k,j}\}_{j=1}^2 \subset \mathcal{F}_k$, i.e.

$$\partial\Gamma_k = \{\boldsymbol{g}_{\partial\Gamma,k}(\mu) : \mu \in [0,1]\} \quad \text{with} \quad \boldsymbol{g}_{\partial\Gamma,k} := \boldsymbol{x}_{\partial\Gamma,1} + \mu\boldsymbol{b}_k + h_{\partial\Gamma,k}(\mu)\boldsymbol{n}_k. \tag{4.50}$$

The employed local coordinate system is composed by

$$\boldsymbol{b}_k := \boldsymbol{x}_{\partial\Gamma_k,2} - \boldsymbol{x}_{\partial\Gamma_k,1} \quad \text{and} \quad \boldsymbol{n}_k := \frac{\boldsymbol{n}_{\mathcal{F},k} \times \boldsymbol{b}_k}{\|\boldsymbol{b}_k\|} \operatorname{sign}\left(\langle \boldsymbol{n}_{\mathcal{F},k} \times \boldsymbol{b}_k, \boldsymbol{n}_0 \rangle\right). \tag{4.51}$$

Note that the multiplication with the sign of the inner product in eq. (4.51) ensures that $\int_0^1 h_{\partial\Gamma,k(\mu)} \mathrm{d}\mu$ produces the correct contribution to the interior area $|\mathcal{A}_k|$; cf. fig. (4.16).

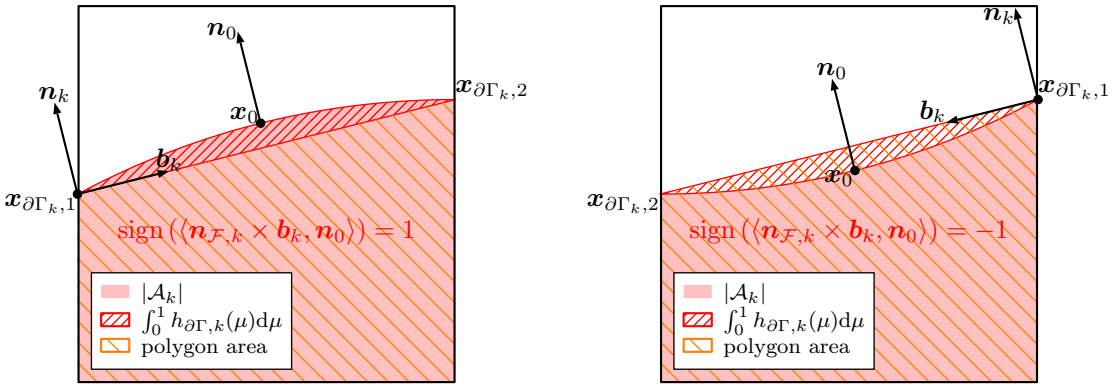


Figure 4.16.: Positive (left) and negative (right) contribution of area under the graph of $\boldsymbol{g}_{\partial\Gamma,k}$ to $|\mathcal{A}_k|$. The polygon is spanned by the intersections $\{\boldsymbol{x}_{\partial\Gamma_k,j}\}_{j=1}^2$ and the interior face vertices.

By equating the expressions in eq. (4.50) and eq. (4.13) and computing the appropriate inner products for $i \in \{1,2\}$, one obtains

$$t_i = \langle \boldsymbol{x}_{0,k} - \boldsymbol{x}_0, \boldsymbol{\tau}_i \rangle + \mu \langle \boldsymbol{b}_k, \boldsymbol{\tau}_i \rangle + \langle \boldsymbol{n}_k, \boldsymbol{\tau}_i \rangle h_{\partial\Gamma,k} =: \alpha_i + \mu\beta_i + \gamma_i h_{\partial\Gamma,k}, \tag{4.52}$$

$$\frac{1}{2}\left(\kappa_1 t_1^2 + \kappa_2 t_2^2\right) = \langle \boldsymbol{x}_{0,k} - \boldsymbol{x}_0, \boldsymbol{n}_0 \rangle + \mu \langle \boldsymbol{b}_k, \boldsymbol{n}_0 \rangle + \langle \boldsymbol{n}_k, \boldsymbol{n}_0 \rangle h_{\partial\Gamma,k} =: \alpha_3 + \mu\beta_3 + \gamma_3 h_{\partial\Gamma,k}. \tag{4.53}$$

Inserting eq. (4.52) in eq. (4.53) and rearranging yields the implicit quadratic relation

$$c_{2,k} h_{\partial\Gamma,k}^2 + c_{1,k}(\mu) h_{\partial\Gamma,k} + c_{0,k}(\mu) = 0 \tag{4.54}$$

for the sought height $h_{\partial\Gamma,k}$, whose coefficients are

$$\begin{aligned} c_{0,k} &= \frac{\mu^2}{2}(\kappa_1\beta_1^2 + \kappa_2\beta_2^2) + \mu(\kappa_1\alpha_1\beta_1 + \kappa_2\alpha_2\beta_2 - \beta_3) + \frac{1}{2}(\kappa_1\alpha_1^2 + \kappa_2\alpha_2^2) - \alpha_3, \\ c_{1,k} &= \mu(\kappa_1\beta_1\gamma_1 + \kappa_2\beta_2\gamma_2) + \kappa_1\alpha_1\gamma_1 + \kappa_2\alpha_2\gamma_2 - \gamma_3, \\ c_{2,k} &= \frac{1}{2}(\kappa_1\gamma_1^2 + \kappa_2\gamma_2^2). \end{aligned} \tag{4.55}$$

Despite the possibility of explicitly calculating the roots of eq. (4.54), we prefer to apply a Newton algorithm. Also, the derivative of the height function $h_{\partial\Gamma,k}$ with respect to $\mu$, which is required in eq. (4.58) below for the integral transformation, can be computed by differentiating eq. (4.54) and rearranging, i.e.

$$\frac{\partial h_{\partial\Gamma,k}}{\partial\mu} = -\frac{\partial_\mu c_{0,k} + h_{\partial\Gamma,k}\partial_\mu c_{1,k}}{2h_{\partial\Gamma,k}c_{2,k} + c_{1,k}}. \tag{4.56}$$

The boundary normal emerges from the projection of the face normal $\boldsymbol{n}_{\mathcal{F},k}$ onto the tangent space, i.e.

$$\boldsymbol{n}_{\partial\Gamma,k}(\boldsymbol{t}) = \frac{\boldsymbol{P}_\Gamma \boldsymbol{n}_{\mathcal{F},k}}{\|\boldsymbol{P}_\Gamma \boldsymbol{n}_{\mathcal{F},k}\|}. \tag{4.57}$$

Finally, the curve integral is transformed as

$$\int_{\partial\Gamma_k} \langle \nabla_\Gamma u, \boldsymbol{n}_{\partial\Gamma,k} \rangle(\boldsymbol{t}) \, \mathrm{d}l = \int_0^1 \langle \nabla_\Gamma u, \boldsymbol{n}_{\partial\Gamma,k} \rangle \left(\boldsymbol{g}_{\partial\Gamma,k}(\mu)\right) \sqrt{1 + \partial_\mu h^2_{\partial\Gamma,k}} \, \mathrm{d}\mu, \tag{4.58}$$

where the numerical evaluation is, once again, carried out by standard Gauss-Legendre quadrature. Figure (4.17) illustrates the relevant quantities.

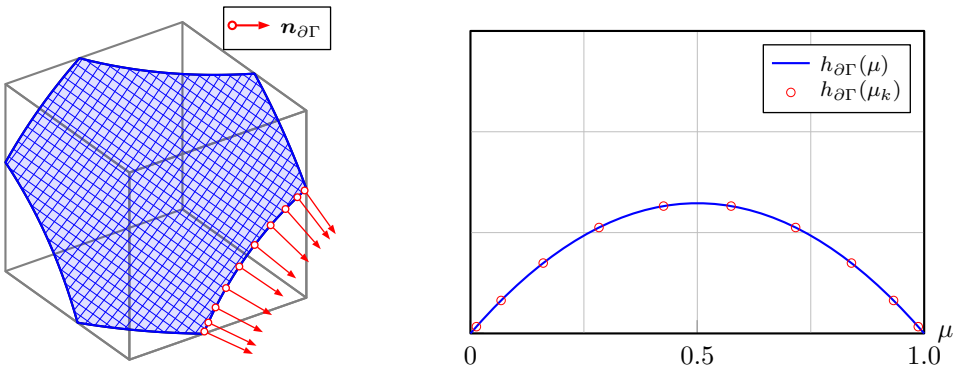


Figure 4.17.: Relevant quantities for numerical quadrature of curve integrals, where the boundary normals are evaluated for $M = 10$ quadrature nodes on the parameter set $\mathcal{S}_{\partial\Gamma} = [0, 1]$.

## 4.6. Numerical results

The present section gathers some numerical results for three classes of hypersurfaces, which are commonly encountered in the initial configuration of two-phase flow simulation: (i) Ellipsoids with distinct and identical semi-axes $(a, b, c)$, the latter of course resembling spheres. (ii) Hypersurfaces with rotational symmetry along the $z$-axis, whose radius is a quadratic function of the $z$-coordinate and (iii) perturbed spheres with base radius $R_0$ and variance $\hat{\sigma}^2$; cf. eq. (2.18). We are interested in the global relative volume error

$$\mathcal{E}^V := \left| 1 - \frac{\sum_k^{N_\Sigma} V_k}{\mathrm{vol}(\Sigma)} \right|, \tag{4.59}$$

To highlight the importance of accurate initial data, subsection 4.6.6 briefly exemplifies the reduction of spurious currents for a stationary droplet in zero gravity. Subsection 4.6.7 provides information on the performance of the present implementation.

Since the numerical evaluation of the original equation, cf. eq. (4.3), involves two significant distinguishable error sources, namely the approximation of the hypersurface and the numerical approximation of the variational problem, the convergence with increasing resolution is bounded by the approximation

accuracy. Hence, due to the symmetry of local quadratic approximation of the hypersurface, one can expect third-order convergence in space. The number of cells $\mathcal{K}_i$ intersected by the hypersurface $\Sigma$ is denoted $N_\Sigma$, which is not an input parameter. In figs. (4.19) and (4.21), the computation of the referential error employs a discretization of the hypersurface parameter set $\mathcal{S}_\Sigma$ into $N_\mathcal{S}^2$ subdomains. In order to achieve comparability in terms of resolution, the errors produced by our algorithm are plotted over $\sqrt{N_\Sigma}$, approximately resembling the interface resolution per spatial dimension, i.e. $N_\mathcal{S}^2 \sim N_\Sigma$.

### 4.6.1. Numerical setup

The domain $\mathcal{K} = [-1, 1]^3$ under consideration is evenly discretized by $N_\mathcal{K}$ cells per spatial dimension, where the center of volume coincides with the center of the domain. For both the Petrov-Galerkin (PG) and the polynomial comparison (PC) approach, the number of ansatz functions is $N \in \{4, 9\}$, corresponding to products of even Legendre polynomials up to and including second ($M = 2$) and fourth-order ($M = 4$), respectively; cf. eq. (4.28). The Gauss-Legendre quadrature of eq. (4.26) is carried out using $(2M + 2)^2$ nodes per triangle, cf. eq. (4.27). For the quadrature on the boundary curve segments $\partial\Gamma_k$, cf. eq. (4.58), $2M + 6$ nodes are used. For all cases investigated below, there are no cells for which the coefficient matrix $\boldsymbol{A}_\Gamma$ is non-invertible; cf. eq. (4.34) and the flowchart in fig. (4.14). Moreover, for ellipsoids and hyperboloids of revolution, no occurrences of *out-of-bounds* are detected, while for perturbed spheres the maximum number encoutered was 3.

### 4.6.2. Referential volumes

In order to separately analyze the error contribution of the local surface approximation, we compute the theoretical minimum error of the volume computation. The referential volumes are obtained as follows: the rectangular parameter set $\mathcal{S} = [\alpha_1, \beta_1] \times [\alpha_2, \beta_2]$ is discretized in $N_\mathcal{S} \times N_\mathcal{S}$ equally sized rectangular pairwise disjoint subdomains $\mathcal{S}_{ij}$, i.e. $\mathcal{S} = \bigcup_{i,j=1}^{N_\Sigma} \mathcal{S}_{ij}$ with

$$\mathcal{S}_{ij} = \left[\alpha_1 + \frac{\beta_1 - \alpha_1}{N_\Sigma}(i-1), \alpha_1 + \frac{\beta_1 - \alpha_1}{N_\Sigma} i\right] \times \left[\alpha_2 + \frac{\beta_2 - \alpha_2}{N_\Sigma}(j-1), \alpha_2 + \frac{\beta_2 - \alpha_2}{N_\Sigma} j\right]. \tag{4.60}$$

The approximate hypersurface patch $\Gamma_{ij}$ is obtained by Taylor expansion of the height function $h_\Sigma$ around the respective center of $\mathcal{S}_{ij}$, providing $\{\kappa_i, \boldsymbol{\tau}_i, \boldsymbol{n}_0\}$. Next, we explicitly compute a set of $N_{\text{quad}}^2 = 64$ quadrature weights and nodes $\{(\omega_k, \boldsymbol{x}_k)\}_{ij}$ with $\boldsymbol{x}_k \in \Sigma_{ij}$ which is projected to the approximate parameter set space, yielding $\{(\omega_k, \boldsymbol{b}_k)\}_{ij}$. Finally, the approximate volume $V_{ij}^\Gamma$ is computed by evaluating the approximate height functions, while the true volume $V_{ij}^\Sigma$ is computed from the true height function, analytically where possible. For the hypersurfaces under consideration here, tab. (4.3) gathers the relevant quantities. The global volume error then can be cast as

$$\mathcal{E}_{\text{ref}}^V := \left| 1 - \left( \sum_{i=1}^{N_\mathcal{S}} \sum_{j=1}^{N_\mathcal{S}} V_{ij}^\Gamma \right) \left( \sum_{i=1}^{N_\mathcal{S}} \sum_{j=1}^{N_\mathcal{S}} V_{ij}^\Sigma \right)^{-1} \right|, \tag{4.61}$$

i.e. eq. (4.61) resembles an "upper bound" for the accuracy of the numerical implementation.

Table 4.3.: Analytical volume segments for hypersurfaces under consideration for the numerical experiments, where the evaluation is carried out analytically for ellipsoids and hyperboloids of revolution.

| class | parameters | $\mathcal{S}_\Sigma$ | $V_{ij}^\Sigma$ |
|---|---|---|---|
| **hyperb. of rev.** | $(r_0, \Delta r)$ | $[0, 2\pi) \times [-1, 1]$ | $\int_{z_i}^{z_{i+1}} \int_{\varphi_i}^{\varphi_{i+1}} \frac{\left(r_o + \Delta r z^2\right)^2}{2} \mathrm{d}\varphi \mathrm{d}z$ |
| **ellipsoid** | $(a, b, c)$ | $[0, 2\pi) \times [0, \pi]$ | $\frac{abc}{3}(\cos\theta_j - \cos\theta_{j-1})(\varphi_{i+1} - \varphi_i)$ |
| **pert. sphere** | $(R_0, \sigma_0)$ | $[0, 2\pi) \times [0, \pi]$ | $\frac{1}{3} \int_{\varphi_i}^{\varphi_{i+1}} \int_{\theta_j}^{\theta_{j+1}} R^3 \sin\theta \mathrm{d}\theta \mathrm{d}\varphi$ |

**Note 4.4** (Convergence analysis)**.** *Within the convergence analysis of subsections 4.6.3, 4.6.4 and 4.6.5, the referential volume error $\mathcal{E}_{\mathrm{ref}}^V$ of eq. (4.61) is denoted by • in figs. (4.19), (4.20), (4.21) and (4.23). Furthermore, • denotes the standard linear approximation ($\kappa_i \equiv 0$; cf. fig. (4.14)). The dashed-dotted gray lines indicate convergence, where the order corresponds to the number of dots.*

### 4.6.3. Ellipsoids

Figure (4.19) gathers the global numerical volume error for ellipsoids with different semi-axes, where the black and orange full circles denote the referential error of eq. (4.61) and the error obtained by linear approximation of the hypersurface, respectively. In general, the relative error decreases with increasing spatial resolution, commencing from between $10^{-3}$ and $10^{-4}$ for the lowest resolution of $N_{\mathcal{K}} = 10$ and reaching $10^{-8}$ for spheres and $10^{-7}$ for non-degenerate ellipsoids, i.e. those with different semi-axes, respectively. For the latter, the experimental order of convergence varies between 3.00 and 4.15, where in the cases presented here larger variations of curvatures do not necessarily produce lower orders of convergence; cf. fig. (4.18).

For all cases considered here, the absolute error of the Petrov-Galerkin approach lies approx. two orders of magnitude below the error induced by linear approximation, indicating the benefits of exploiting local curvature information. Also, the Petrov-Galerkin approach outperforms the polynomial comparison for $N = 4$ ansatz functions. As fig. (4.19) indicates, the polynomial comparison requires $N = 9$ ansatz functions (PC9) to produce results equivalent to (PG4). Polynomial comparison with $N = 4$ ansatz functions (PC4) in general exhibits second order convergence in space, with the absolute error being roughly one order of magnitude below the linear approximation. This is due to the non-local character of the weak formulation underlying the Petrov-Galerkin approach, allowing for partial compensation of the higher order terms, which are neglected within the polynomial comparison. Moreover, increasing the number of ansatz functions to $N = 9$ (PG9) does not improve the accuracy of the Petrov-Galerkin approach, implying that terms of fourth-order in $t_i$ do not contribute significantly to the solution $u(\boldsymbol{t}; \kappa_i)$, irrespective of the sign and value of the principal curvatures; in fact, the observations of this paragraph extend to all classes of hypersurfaces investigated in this section, see figs. (4.21) and (4.23).

For spheres, cf. fig. (4.19(d)), the Petrov-Galerkin approach yields fourth-order convergence.

**Note 4.5** (Approximation quality)**.** *For spheres, due to symmetry, the local approximation of the height function, cf. eq. (4.14), includes no odd orders, implying that* $\|h_\Sigma - h_\Gamma\| = \mathcal{O}(\|\boldsymbol{t}\|^4)$.

Also, there is virtually no difference between the PETROV-GALERKIN approach and the polynomial comparison, both for $N = 4$ and $N = 9$ ansatz functions. This is to be expected because the ansatz space $\mathcal{F}_4^{\mathrm{a}}$ already contains the analytical solution for $\kappa_1 = \kappa_2 = \kappa$, hence an expansion cannot increase accuracy, since $\mathcal{F}_9^{\mathrm{a}} \supset \mathcal{F}_4^{\mathrm{a}}$.

Let $\beta := c/a$ be the ratio of the smallest and largest semi-axis. Figure (4.18) depicts the experimental order of convergence as a function of $\beta \in [1/2, 95/100]$, comparing the uniform variation of one (*oblate*) and two (*prolate*) semi-axes. For both oblate and prolate ellipsoids, the experimental order of convergence is approx. four, virtually independent of $\beta$. For the oblate ellipsoid with $\beta = 3/5$, cf. fig. (4.19(a)), the experimental order of convergence for PG4 drops to 3 due to sporadic increments in the absolute error magnitude. However, since we obtain fourth-order convergence in space for both smaller and larger values of $\beta$, we can deduce that this is caused by disadvantageous cancellation of local errors. An advantageous pronouncement of the aforementioned effect occurs for $N_{\mathcal{K}} = 20$ in PC9, where we obtain an absolute error of approx. $10^{-8}$, as compared to approx. $10^{-6}$ for $N_{\mathcal{K}} = 30$.

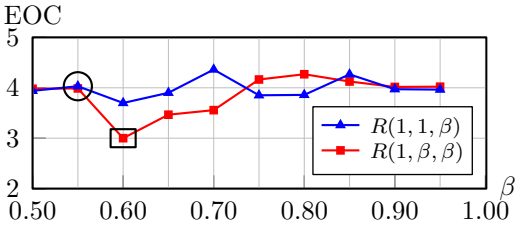


Figure 4.18.: Experimental order of convergence of PG4 for $10 \leq N_{\mathcal{K}} \leq 100$ cells per spatial direction for oblate (▲) and prolate (■) ellipsoids over varying ratio of semi-axes ($R = 0.99$). Figure (4.19) below provides the underlying relative errors as a function of the spatial resolution $N_{\mathcal{K}}$, where the points marked by the circle/square correspond to ((b), (c)) / (a).

### Comparison to analytical solution

As stated in subsection 4.4.6, the volume fractions can be computed analytically for spheres. Figure (4.20) illustrates various aspects of the volume fraction deviations for linear and quadratic hypersurface approximation, respectively. Due to the spatial symmetry of the sphere, it is sufficient to consider the first octant. The findings can be summarized as follows:

1. The linear approximation induces negative deviations between $-3.7 \times 10^{-3}$ and $-5.9 \times 10^{-9}$. Due to the convexity of $\Sigma$, the inherent overestimation is a direct consequence of the locally tangential approximations $\Gamma_k$. On the other hand, the quadratic approximation produces both positive and negative deviations between $-1.8 \times 10^{-7}$ and $4.3 \times 10^{-8}$, i.e. the magnitude is around four orders of magnitude below the linear case.

2. Figure (4.20(c)) plots the error over the size of the parameter set $\mathcal{S}_{\Gamma,k}$, which can be interpreted as an indicator for the size of the hypersurface patch contained in the respective cell. The error in

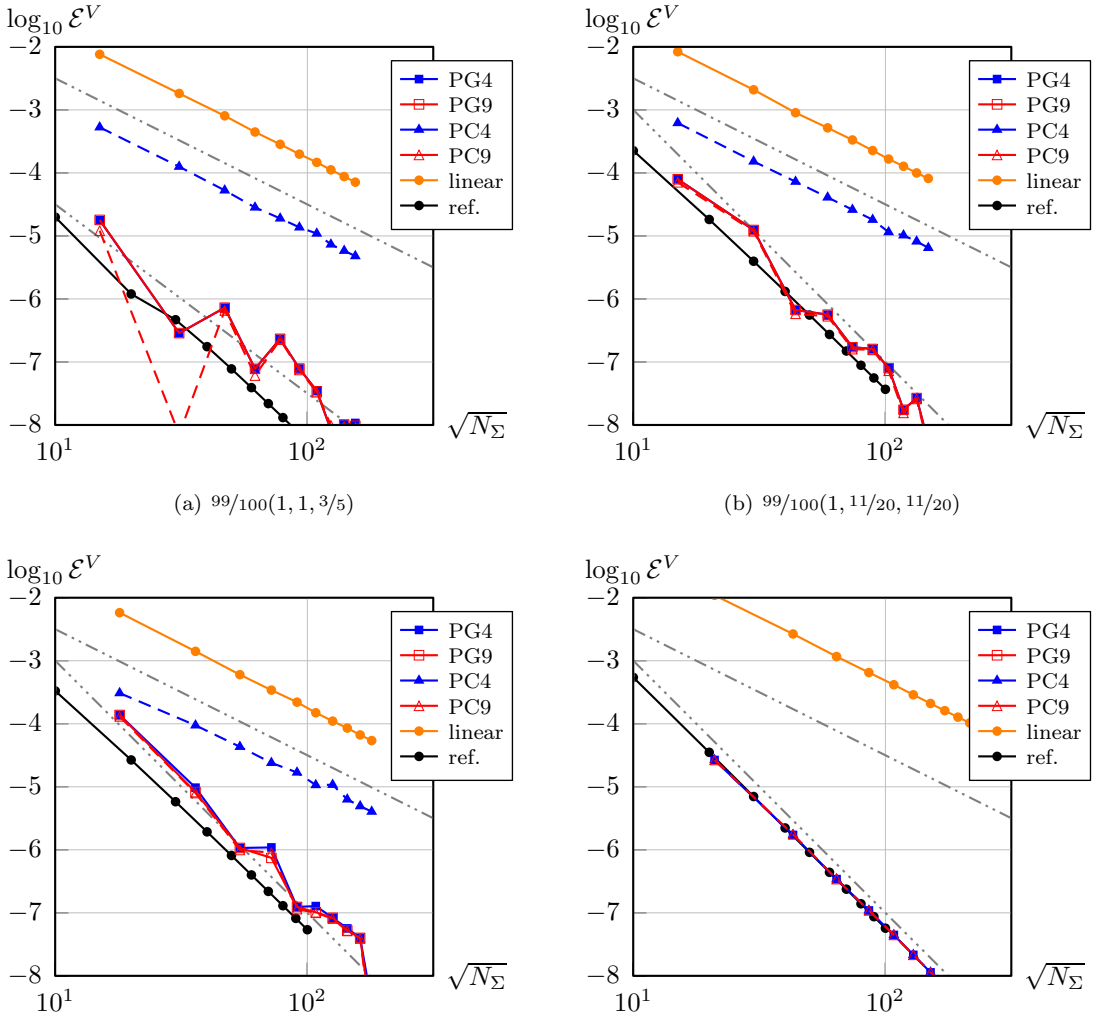


(a) $^{99}/_{100}(1, 1, ^3/_5)$

(b) $^{99}/_{100}(1, ^{11}/_{20}, ^{11}/_{20})$

(c) $^{99}/_{100}(1, 1, ^{11}/_{20})$

(d) $^{99}/_{100}(1, 1, 1)$

Figure 4.19.: Volume error from eq. (4.59) (ellipsoids; subcaptions denote semi-axes) over number of intersected cells $N_\Sigma$; cf. note (4.4). (PG) denotes the results obtained with the Petrov-Galerkin approach, (PC) refers to polynomial comparison.

both the quadratic and the linear case increases quadratically with increasing size of the parameter set. In accordance with figs. (4.20(a)) and (4.20(b)), the absolute difference is approximately four orders of magnitude. However, the variance is larger for the quadratic volume fractions, which can be attributed to the complexity of their numerical computation. The coincidence of the curves for $|\mathcal{S}_{\Gamma,k}| \leq 10^{-4}\Delta x^2$ with values in $[10^{-12}, 10^{-8}]$ implies that for cells containing small hypersurface patches, commonly corresponding to volume fractions close to 0 or 1, the approximation quality becomes insignificant.

3. The effect of the spatial resolution $N_{\mathcal{K}}$ is depicted in fig. (4.20(d)). As expected, the deviations for linear (quadratic) volume fractions decrease as $\Delta x$ ($\Delta x^2$), both for the $L_2$- and $L_\infty$-norm, where

$$\mathcal{E}_2^f := \sqrt{\frac{1}{N_\Sigma}\sum_{k=1}^{N_\Sigma}(\mathcal{E}_k^f)^2} \quad \text{and} \quad \mathcal{E}_\infty^f := \max_k |\mathcal{E}_k^f| \quad \text{with} \quad \mathcal{E}_k^f := f_k^{\text{exact}} - f_k. \tag{4.62}$$

4. The spatial distribution of the errors in both cases closely resembles the structure of the underlying Cartesian grid: the regions around the intersections with the Cartesian axes exhibit the smallest errors, whereas the maximum deviations occur in the direction of the $\{xy, xz, yz\}$- and $xyz$-diagonals. A distinct and prominent feature of both approximations is the chessboard structure in the region of the $xyz$-diagonal: very small and very large deviations occur in neighboring cells, which is a direct result of the positive relation to size of the parameter set, cf. fig. (4.20(c)). This is especially disadvantageous if one seeks to compute curvature numerically by differentiation of volume fractions; cf. subsection 4.6.6.

5. The results are not changed if the analytical solution of the variational ansatz in eq. (4.26) is prescribed, i.e. the errors depicted are solely related to the approximation of the hypersurface.

### 4.6.4. Hyperboloids of revolution

Hyperboloids of revolution can be described by level-set functions of type

$$\phi_\Sigma(\boldsymbol{x}; r_0, \Delta r) = x^2 + y^2 - \left(r_0 + \Delta r\, z^2\right)^2. \tag{4.63}$$

Figure (4.21) shows the referential, cf. eq. (4.61), and numerical global volume error for hyperboloids of revolution with different radius variations $\Delta r$. The observations concerning the evolution of the global error basically correspond to those of the ellipsoids. At this point, it is worth noting that we obtain fourth-order convergence for (globally) non-convex hypersurfaces, cf. figures 4.21(b) and (d). This is to be expected for reasons analogous to those given in note (4.5).

### 4.6.5. Perturbed spheres

Perturbed spheres can be described in spherical coordinates by level-set functions of type

$$\phi_\Sigma(\boldsymbol{r}; R_0, \hat{\sigma}^2) = r^2 - R^2(\varphi, \theta; R_0, \hat{\sigma}^2), \tag{4.64}$$

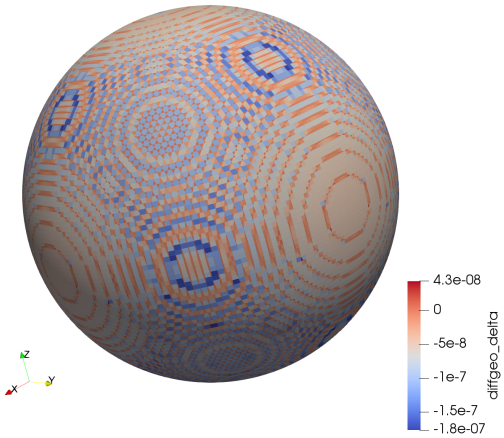


(a) $f_k^{\text{exact}} - f_k^{\text{quad}}$ (▲ in (c))

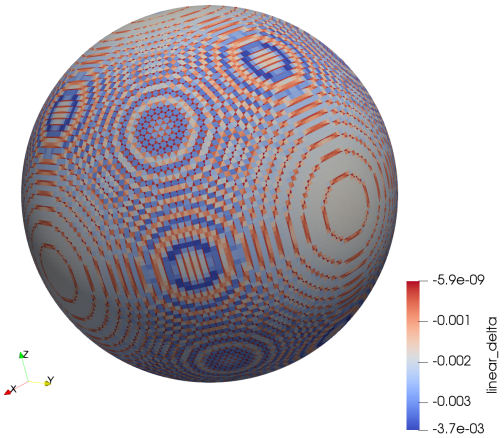


(b) $f_k^{\text{exact}} - f_k^{\text{lin}}$ (■ in (c))

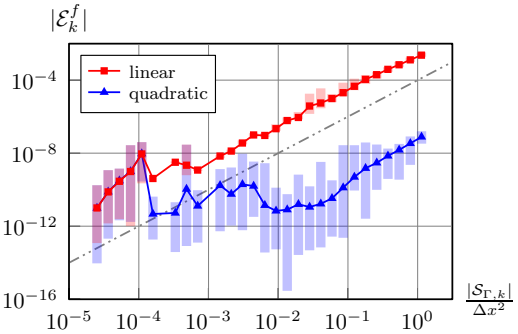


(c) average ((b): ■ and (a): ▲) and min./max. deviation (bar) of volume fractions as function of normalized parameter set size for $N_{\mathcal{K}} = 100$.

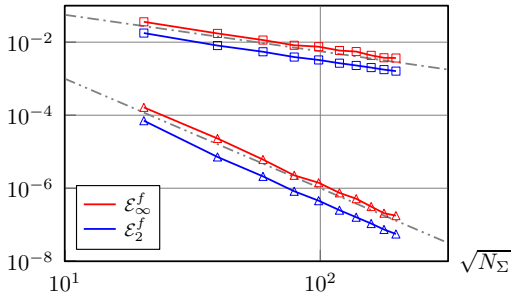


(d) global errors from eq. (4.62) for linear (□) and quadratic approximation (△) as function of spatial resolution $\sqrt{N_\Sigma} \sim N_{\mathcal{K}}$.

Figure 4.20.: Deviation of linear and quadratic volume fractions from exact values (cf. subsection 4.4.6) for sphere with $R = \frac{91}{100}$ centered in $[-1, 1]^3$ ((a),(b)) over surface ($N_{\mathcal{K}} = 100$), as function of (c) the normalized parameter set size ($\Delta x = 2N_{\mathcal{K}}^{-1}$; cf. section 4.5) and (d) spatial resolution.

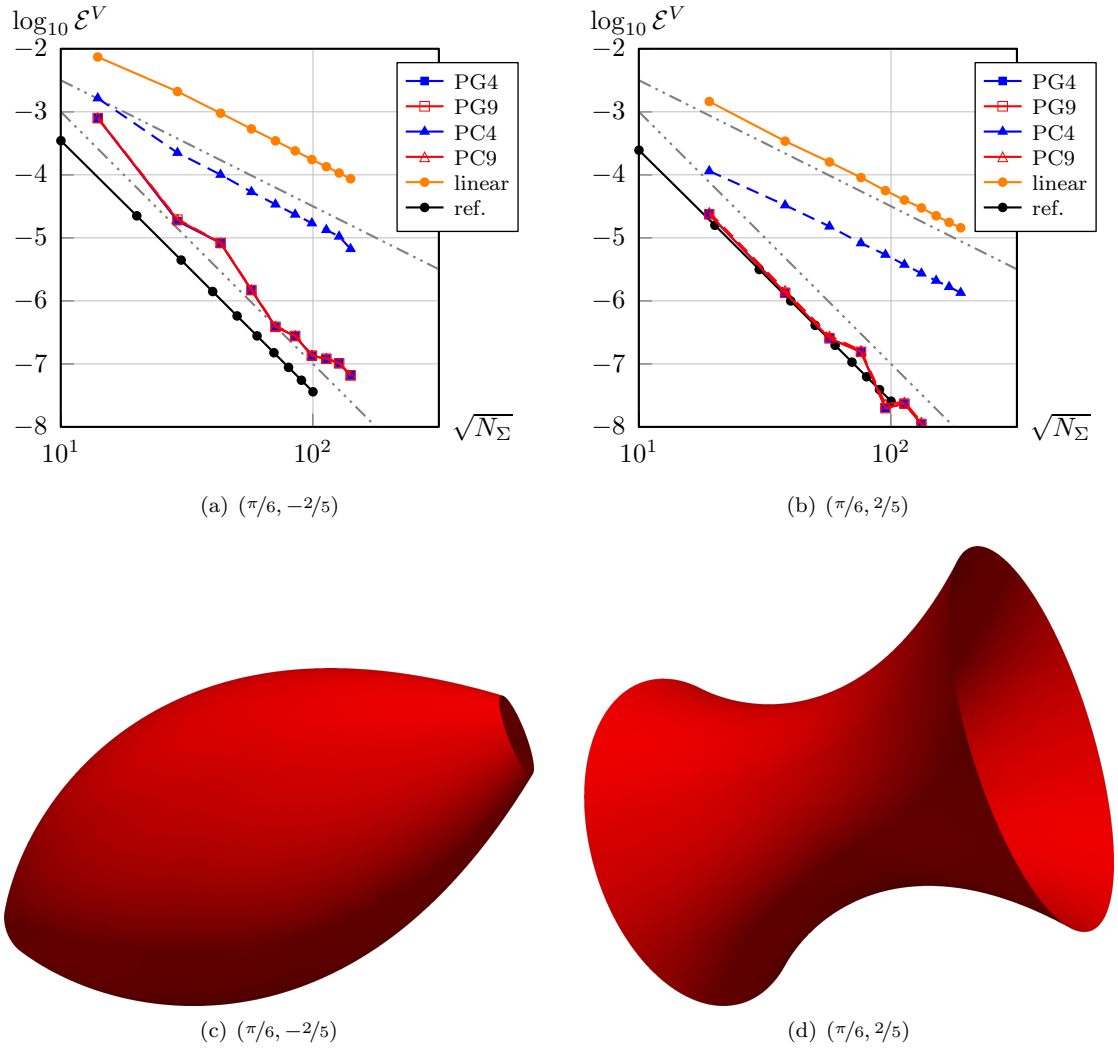


(a) $(\pi/6, -2/5)$

(b) $(\pi/6, 2/5)$

(c) $(\pi/6, -2/5)$

(d) $(\pi/6, 2/5)$

Figure 4.21.: Volume error from eq. (4.59) (hyperboloid of revolution; subcaptions correspond to the parameters in tab. (4.3)) over number of intersected cells $N_\Sigma$ with illustrations; cf. note (4.4).

where the thrid power of the radius is expanded in terms of tesseral spherical harmonics, up to and including order $L_\Sigma \in \{3, 6, 9\}$; cf. eq. (2.18). Recall that the reason for expanding the third power of the radius instead of the radius itself is that the computation of the enclosed volume becomes trivial. The $(L_\Sigma + 1)^2$ coefficients $c_l^m$ are randomly generated using the method of Box and Muller [22] given in section 1.3, i.e.

$$c_l^m = \begin{cases} \sqrt{4\pi} R_0^3 & l = 0 \\ \hat{\sigma}\sqrt{-2\log\gamma_1}\cos(2\pi\gamma_2) & l > 0 \end{cases} \qquad \text{with} \qquad \gamma_{1,2} \sim \mathcal{U}(0,1), \tag{4.65}$$

where $R_0$ is henceforth referred to as the *referential radius*. In general, the observations concerning convergence and absolute error magnitude, which have been established in subsection 4.6.3, hold for the perturbed spheres as well. However, there are two characteristic differences. First, it is worth noting that the referential errors, cf. eq. (4.61), obtained from direct quadrature with $N_{\text{quad}} = 64$ nodes (see figures 4.23(a), (c) and (e)) are larger than those obtained by application of our approach (excluding PC4), indicating its performance for locally non-convex hypersurfaces. If the deviation from the sphere is small, which is the case for $L_\Sigma = 3$, the polynomial comparison performs better in terms of absolute errors. Second, while there were no cells whose volume fractions were out-of-bounds in the test cases described in subsections 4.6.3 and 4.6.4, this phenomenon occurs for perturbed spheres. However, in the cases investigated here, the maximum number of those cells is three (obtained for $L_\Sigma = 9$ with PC9), corresponding to 0.01% of the intersected cells; the affected cells share the property of having volume fractions close to 0 or 1. Note that the inverse relation is not true, i.e. cells with volume fractions close to 0 or 1 are generally not affected; cf. fig. (4.22) for details. These over- or undershoots, respectively, can be explained as follows: if all intersection points $\boldsymbol{x}_\Sigma$ are located in the very vicinity of corners, as illustrated in fig. (4.22), even small values of $d_\mathcal{K}\kappa_i$ can cause $\partial\Gamma \not\subseteq \mathcal{K}$. In other words, even small relative curvatures of the boundary curve potentially cause the latter to leave the cell under consideration. However, due to the aforementioned prerequisites concerning the intersection, this effect is expected to occur relatively rarely.

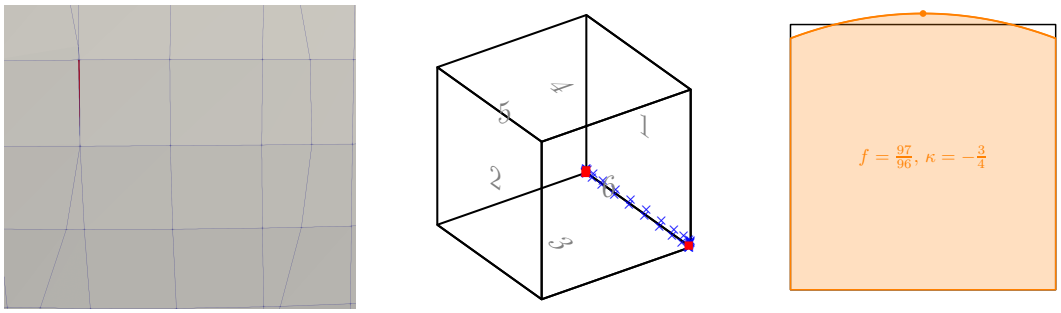


Figure 4.22.: Left: surface mesh (red: out-of-bounds cells) for $L_\Sigma = 9$ and $N_\mathcal{K} = 90$ (PG4 result: $-6.09 \times 10^{-11}$ and $-9.45 \times 10^{-8}$); center: cell (volume $1.097 \times 10^{-5}$) with hypersurface intersections $\boldsymbol{x}_\Sigma$ (■) and quadrature nodes $\boldsymbol{x}_{\partial\Gamma}$ (×); right: boundary curve $\partial\Gamma_k$ partially outside of face $\mathcal{F}_k$.

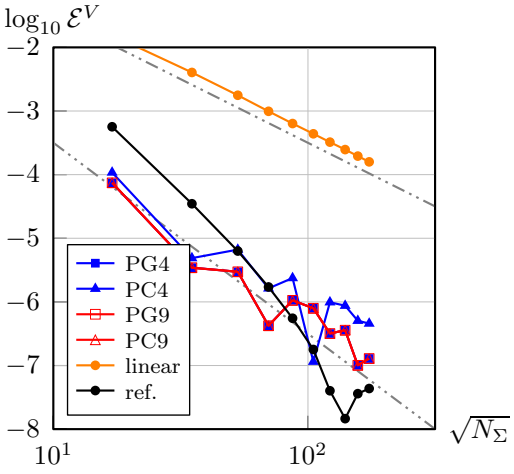


(a) rel. volume error

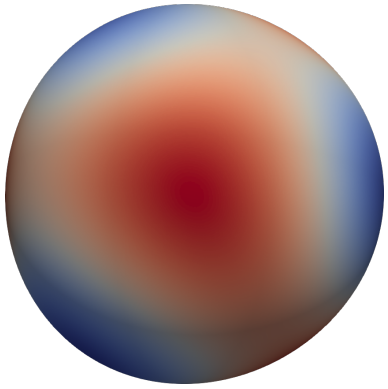

(b) $\kappa_1 + \kappa_2 \in [-2.7, -2.2]$

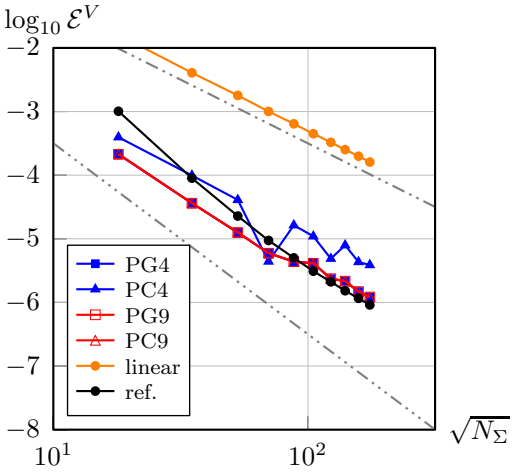


(c) rel. volume error

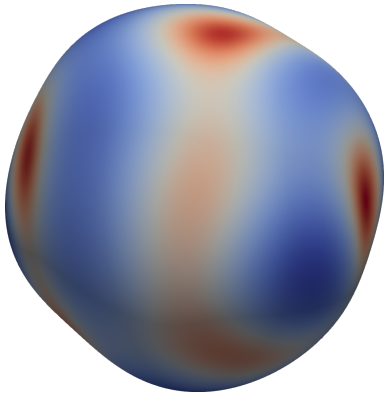

(d) $\kappa_1 + \kappa_2 \in [-4.3, 0.25]$

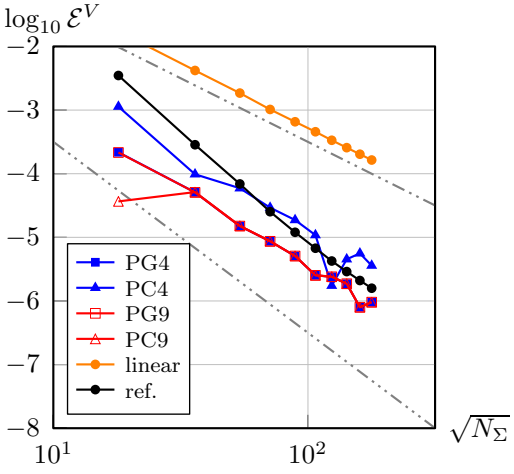


(e) rel. volume error

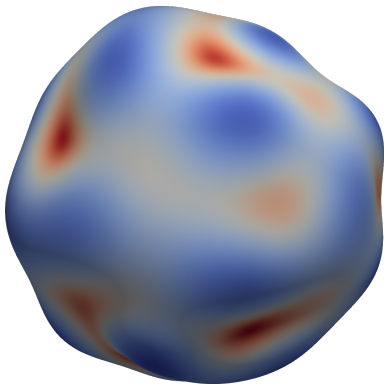

(f) $\kappa_1 + \kappa_2 \in [-7, 12]$

Figure 4.23.: Volume error from eq. (4.59) (perturbed sphere with $R_0 = \frac{4}{5}$ and $\hat{\sigma}^2 = 5 \times 10^{-4}$; top to bottom row: $L_\Sigma \in \{3, 6, 9\}$) over number of intersected cells $N_\Sigma$ with illustrations; cf. note (4.4).

### 4.6.6. Spurious currents

In simulations of two-phase flows with significant influence of surface tension (also called *capillary* flows), parasitic or spurious numerical currents occur in the vicinity of the interface, due to imbalances of the surface tension force and the pressure jump across the interface. In case of a stagnant fluid particle in the absence of gravity, these spurious currents induce unphysical fluid motion, spoiling the theoretical stability of the spherical shape; cf. Harvie et al. [62]. In order to exemplify the influence of the initial data, we consider a spherical water droplet of radius $R = \frac{3}{4}$cm in air ($\rho_{\text{water}} = 9.982 \times 10^{-1} \frac{\text{g}}{\text{cm}^3}$, $\mu_{\text{water}} = 1.2 \times 10^{-2}$g/cms, $\rho_{\text{air}} = 1.2 \times 10^{-3} \frac{\text{g}}{\text{cm}^3}$, $\mu_{\text{air}} = 1.8 \times 10^{-4}$g/cms and $\sigma = 72.5 \frac{\text{g}}{\text{s}^2}$), centered in $[-1, 1]^3$ with equidistant spatial resolution of $N_{\mathcal{K}} = 100$ via the flow solver FS3D described in section 3.1. The curvature is computed using the height-function approach of Popinet [109]; cf. section 5.2 for details. Figure (4.24) exemplifies the $3 \times 10^{-3} \frac{\text{cm}}{\text{s}}$ iso-surface of the velocity norm $\|\boldsymbol{u}\|$ after 10 timesteps with $\Delta t = 9.36 \times 10^{-5}$s, along with the relative curvature error $\mathcal{E}_\kappa := 1 - \kappa_{\Sigma,\text{num}} R/2$. Besides the reduction of the maximum amplitude by approx. 70% ($\max\|\boldsymbol{u}_{\text{linear}}\| = 2.3806 \times 10^{-2} \frac{\text{cm}}{\text{s}}$ and $\max\|\boldsymbol{u}_{\text{quadratic}}\| = 6.4576 \times 10^{-3} \frac{\text{cm}}{\text{s}}$), the quadratic approximation of the hypersurface considerably reduces the spatial extension of the spurious currents. This can be attributed to the reduction of the relative curvature error by one order of magnitude, which in turn is a direct result of the increased accuracy in the volume fractions. See subsection 5.4.2 for a detailed discussion.

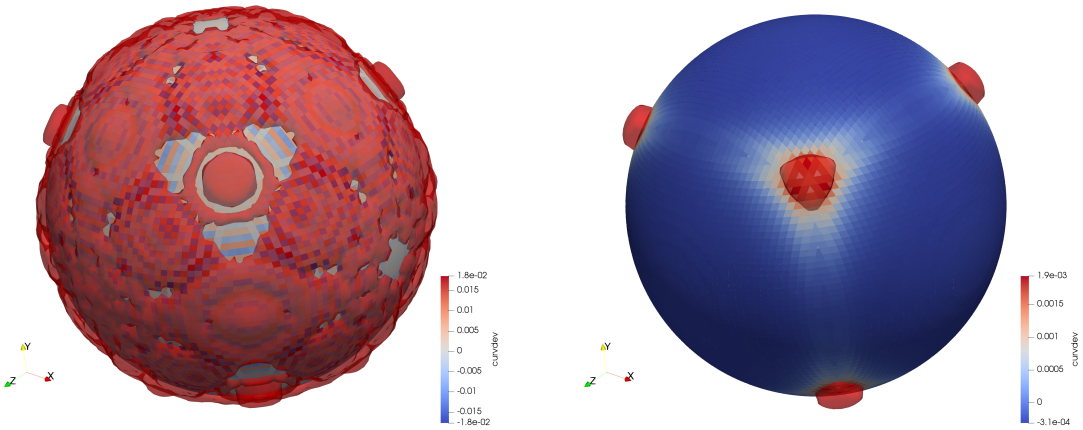


(a) linear (b) quadratic

Figure 4.24.: Iso-surface ($3 \times 10^{-3} \frac{\text{cm}}{\text{s}}$) of velocity norm $\|\boldsymbol{u}\|$ after 10 time steps for stationary droplet in the absence of gravity. The colour of the surface corresponds to the curvature errors obtained from linear and quadratic hypersurface approximation, respectively. See section 5.4 for a detailed description of the curvature computation.

### 4.6.7. Performance measurement

Table (4.4) compiles the results of a simple runtime measurement, comparing the present algorithm with linear and quadratic approximation to the algorithm sketched in subsection 4.4.6. The main findings are: (i) Due to the enhanced mathematical complexity, the overall runtime of the present algorithm is about 10 to 30 times higher than the exact initialization. However, the present algorithm is applicable to a huge set of classes of hypersurfaces, whereas exact solutions exist only for a very small set of classes of

hypersurfaces, i.e. spheres and cylinders. (ii) In the case of linear approximation, the analytical solution to eq. (4.26) is $\hat{\boldsymbol{u}} \equiv \mathbf{0}$, making the assembly and solution of the linear system obsolete. Comparing the second and third row in tab. (4.4) allows to identify this to account for the major increment of the total computation time, since the remaining contributions are all about equal. Of course, the analytical solution for eq. (4.26) can be prescribed for spheres as well, allowing for a comparable total runtime in the quadratic approximation case. However, in order to provide realistic time measuremtns for general cases, i.e. where the analytical solution is not known, we have included the assembly and solution of the linear system. We would like to emphasise that the original intention of this algorithm was the initialization of volume fraction fields. Hence, compared to the runtime of the flow solver, the execution time is negligible in almost every application.

Table 4.4.: Absolute timing results (in seconds; Intel Xeon(R) CPU E3-1231 v3 @ 3.40GHz × 8; Ubuntu 18.04.2 LTS) comparing the present approach with linear ($\kappa_i \equiv 0$) and quadratic ($\kappa_i \neq 0$) approximation of hypersurface. The values in column *solution* refer to the assembly and solution of eq. (4.26), whereas the values in column *evaluation* correspond to the time spent on evaluating eq. (4.58). The underlying test case was a sphere of radius $R = \frac{3}{4}$ centered in $[-1, 1]^3$ with $N_{\mathcal{K}} = 100$.

| | shared | | per cell ($N_\Sigma$=26528) | | | | **total** |
|---|---|---|---|---|---|---|---|
| | setup | intersection | diff. geo. | solution | evaluation | *total* | **runtime** |
| **exact** | $1 \times 10^{-5}$ | $3.76 \times 10^{-3}$ | – | – | $6.16 \times 10^{-6}$ | $6.16 \times 10^{-6}$ | $1.68 \times 10^{-1}$ (3%) |
| $\kappa_i \equiv 0$ | $5.19 \times 10^{-3}$ | $2.35 \times 10^{-1}$ | $9.87 \times 10^{-7}$ | $5.22 \times 10^{-6}$ | $4.22 \times 10^{-5}$ | $5.32 \times 10^{-5}$ | 1.68 (31%) |
| $\kappa_i \neq 0$ | $5.16 \times 10^{-3}$ | $2.36 \times 10^{-1}$ | $1.02 \times 10^{-6}$ | $1.47 \times 10^{-4}$ | $4.27 \times 10^{-5}$ | $1.96 \times 10^{-4}$ | 5.46 (100%) |

## 4.7. Conclusion

We have introduced a robust algorithm capable of computing volumes of domains which emerge from the intersection of cuboids and implicitly given hypersurfaces, where the novelty of the approach consists in the explicit exploitation of curvature information, i.e. principal curvatures and axes, in combination with the application of the surface divergence theorem. The solution of the emerging PDE is approximated by means of a Petrov-Galerkin ansatz. The following main conclusions are drawn:

1. The local approximation of second order, exploiting geometrical (i.e. principal curvature) information from the Weingarten map, allows to obtain up to fourth-order convergence with spatial resolution. For all cases considered here, the absolute error is approximately three orders of magnitude below the error obtained by linear approximation of the hypersurface.

2. For spheres, the volume fractions can be computed exactly. The relative deviation of the volume fractions induced by quadratic (linear) approximation is of order $10^{-6}$ ($10^{-4}$).

3. Fourth-order convergence is obtained for both convex and (globally and locally) non-convex hypersurfaces.

4. The proposed Petrov-Galerkin approach outperforms the polynomial comparison for an equal number of ansatz functions in terms of the absolute error, on average by one order of magnitude.

Moreover, the results are robust with respect to the size of hypersurface patches, corresponding to the size of the parameter domains of the quadrature; cf. fig. (4.25) for an illustration.

5. If (i) the principal curvatures are identical or (ii) one of the principal curvatures is zero, there is an analytical solution to the Laplace-Beltrami equation, which allows to compute the volume integrals exactly (with respect to the approximated hypersurface). This also considerably reduces the computational effort.

6. The improved accuracy allows to significantly reduce parasitic currents in numerical simulations.

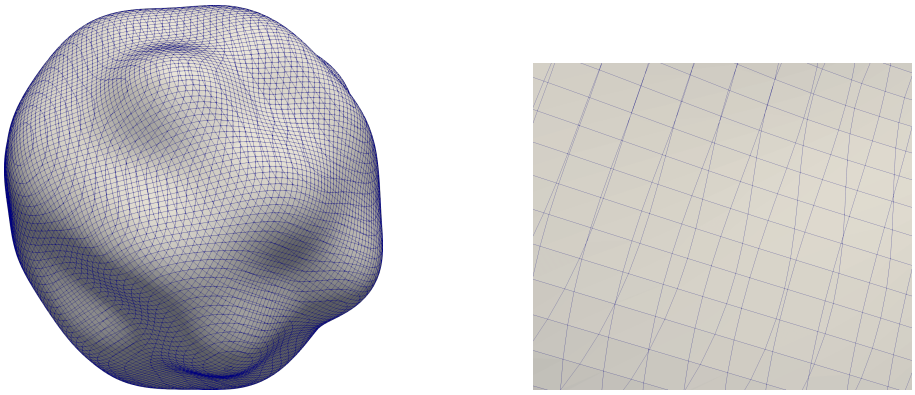

(a) surface mesh (b) close-up

Figure 4.25.: Exemplified surface mesh for perturbed sphere with $L_\Sigma = 9$ where the cuboidal domain was discretized in $N_\mathcal{K} = 100$ cells per spatial direction. The close-up displays hypersurface patches with a wide range of sizes.

In future work, the numerical methods presented above can be extended to other right-hand sides of eq. (4.3), especially for polynomials and constants, including the computation of surface area as an important special case.

# 5. Curvature computation

The present chapter covers the computation of discrete mean curvature from volume fractions on Cartesian grids, where the goal is to establish an in-depth understanding of the properties of the errors.

It is notoriuously difficult to obtain accurate curvature estimates, due to the discontinuous character of the volume fractions, since the majority of the algorithms found in literature require the computation of second derivatives in one form or another. The disadvantageous influence of the discontinuity can be alleviated by smoothing the volume fractions, e.g., by applying a convolution; cf. Williams et al. [154]. However, as pointed out by Renardy et al. [118, 117], smoothing the discontinuos volume fraction field gives rise to numerical artifacts of its own and tends to suppress surface tension effects in spatial regions where the curvature is large. Furthermore, the volume fractions are subject to passive transport, potentially introducing and amplifying noise, whose structure may be affected by, e.g., the numerical transport algorithm, the background mesh or the quality of the initial volume fractions. To the best of our knowledge, there are no literature contributions concerning the influence of volume fractions on the curvature estimates in detail.

The flow solver FS3D resorts to the curvature computation introduced by Popinet [109], who combines a height function method with case-dependent fall-back strategies employing a parabolic fit of interface nodes. The height function method essentially consists of finding a local graph representation of the interface and exploiting differential geometry for the evaluation of the curvature; cf. section 2.2. In fact, many of the approaches presented in literature resort, in one form or another, to this concept. Since we seek to assess its performance with respect to volume fraction quality, the present chapter desists from an analysis of the fall-back strategies.

This chapter is organized as follows: section 5.1 conducts a thorough review of the literature. Due to the inherent difference in mathematical and computational complexity, two and three spatial dimensions are considered separately. A detailed discussion of the height function method is offered in section 5.2, followed by some theoretical considerations in section 5.3. These will serve as a benchmark for the numerical assessment of the performance of the height function algorithm for selected classes of hypersurfaces in section 5.4, which covers measures of $L_2$- and $L_\infty$-type, accompanied by local and statistical information. A conclusion along with the formulation of a strategy to overcome the encountered drawbacks of the method are subject of sections 5.6 and 5.5, respectively.

## 5.1. Literature review

The vast majority of the algorithms proposed in literature can be attributed to one of the three classes:

i. Recalling that for the mean curvature it holds that $\kappa_\Sigma = -\operatorname{div}_\Sigma \boldsymbol{n}_\Sigma$, one may apply **direct differentiation**, where the normal is approximated by either a finite difference or finite volume scheme. Raessi et al. [114] however show that methods of this type do not exhibit convergence with spatial resolution.

ii. **Convolution** methods apply a smoothing kernel to the volume fractions to reduce numerical noise; see Denner [38] for a detailed discussion of methods of type (i) and (ii).

iii. Exploiting that, for sufficient resolution, locally the hypersurface can be represented as the graph of a function, **height function** methods have proven second-order covergence with spatial resolution along with comparatively small implementation effort on CARTESIAN grids. Since the numerical flow solver FS3D resorts to such an approach, this class will be the subject of the upcoming analysis.

(iv.) Besides the established approaches, resorting to the above set of fundamental concepts, there are also very recent developments employing novel techniques. Among those, machine learning (Patel et al. [104], Qi et al. [113]) or point-cloud sampling (Kassar et al. [75]) shall be mentioned here. E.g., Patel et al. [104] report that their machine learing approach „*easily outperforms the convolution method and even matches the accuracy of the height function method for some test cases.*“

**Two spatial dimensions**

The supposedly first application of the height function algorithm is ascribed to Torrey et al. [143] by Popinet [109]. However, the authors were unable to obtain a copy, such that the provenience of the method cannot be established doubtlessly at this point. The article of Chorin [31] proposes an iterative algorithm for finding the osculating circle from volume fractions. Poo and Ashgriz [108] consider CARTESIAN grids and propose a graph representation of the hypersurface using a second-order polynomial. The coefficients are found by enforcing volume conservation in the respective neighborhood of the intersected cell. They also report curvature errors for circles to become most prominent in the diagonals. Brackbill et al. [23] compute the curvature as the divergence of the normal; cf. eq. (2.26). Cummins et al. [35] assess the performance of three curvature computation algorithms (height function, convolution and reconstructed distances) by comparing accuracy and robustness for spheres and sinusoidal waves in two spatial dimensions, where their height function approach is based on the work of Sussman [135]. They conclude that, for circular interfaces, the height function method exhibits second-order convergence of the $L_2$- and $L_\infty$-errors with spatial resolution ($5 \leq {}^{R}/_{\Delta x} \leq 40$), along with providing the smallest error levels. Gerlach et al. [53] employ an instance of the PROST method developed by Renardy and Renardy [116], where the coefficients of the parabola are computed by minimizing an error function using the pattern search algorithm of Hooke and Jeeves [69]. The findings include significant reduction of spurious currents due to the superior accuracy of the curvatures provided by PROST. An interface reconstruction using volume conserving splines was introduced by Ginzburg and Wittum [55], where the authors find that, for some numerical test cases, „*the amplitude of spurious currents is reduced by a factor of 20–500.*“. Sussman [135] estimates curvature for height functions in polar coordinates and Sussman and Ohta [136] compute height functions from asymmetric stencils, where both report second-order convergence with spatial resolution. Bornia et al. [21] comment on the properties and limitations of the height function algorithm, providing formulae for the quadratic reconstruction and fourth-order accurate expressions of the normal and curvature. A parabolic reconstruction of the interface on unstructured meshes is investigated by Evrard et al. [43], where the coefficients are obtained by solving a local non-linear minimization problem. The authors report accuracy and convergence analogous to the height function algorithm. For circles, ellipses and sinusodial waves on CARTESIAN, triangular and polygonal meshes, the authors report second-order convergence of both $L_2$- and $L_\infty$-errors. The work of Ito et al. [71] employs a height function based approach for the computation of curvature on unstructured meshes. The direction of the assembly is

based on preliminary normal information. The authors report second-order (first-order) convergence for the normals (curvature) of circles and sinusoidal waves on unstructured tetrahedral meshes. Also, they provide some results for the ZALESAK slotted disk test case. The work of Francois and Swartz [50] extends the analysis of the height function algorithm to non-uniform rectangular grids by providing theoretical and numerical results. Their findings include that second-order (third-order) convergence of curvature (normal) estimates can be obtained. Guo et al. [59] investigate the influence of curvature errors on spurious currents in microchannel annular flows. By means of an axisymmetric height function method, they find that the magnitude of spurious currents is reduced by up to three orders of magnitude for the test cases reported.

### Three spatial dimensions

The numerical method developed by Renardy and Renardy [116] involves the fitting of a parabola that best represents the volume fraction data. Its coefficients are computed by minimizing the deviation of the volume fractions from those induced by the parabola using a NEWTON iteration, where the derivatives of the volume operator are evaluated by finite differences. While the authors report significant reduction of spurious currents, which are closely related to the computation of curvature, unfortunately they do not provide numerical convergence results for the curvature itself. The works of Renardy and Renardy [116] and Evrard et al. [43] both apply an integral approach to the computation of curvature abdicating the numerical computation of derivatives of volume fractions. Their results indicate the superiority of this concept, despite the fact that both the implementation effort and required computational ressources are substantially higher. Section 5.5 introduces an approach of this type. Lopez et al. [86] propose an improvement of the height function algorithm which resorts to case-dependent adjustment of the finite difference operators, where the parameter $\gamma \in \{0, 0.2\}$ is set based on the normal orientation via $\cos\theta_{\mathrm{red}}$; cf. eq. (5.17) in section 5.3 and fig. (5.4). Their modification can be interpreted as a laterally symmetric smoothing of the finite difference derivatives; cf. fig. (5.1). The authors provide a heuristic method for the determination of the parameter $\gamma$ based on examining spheres. Bogner et al. [20] investigate

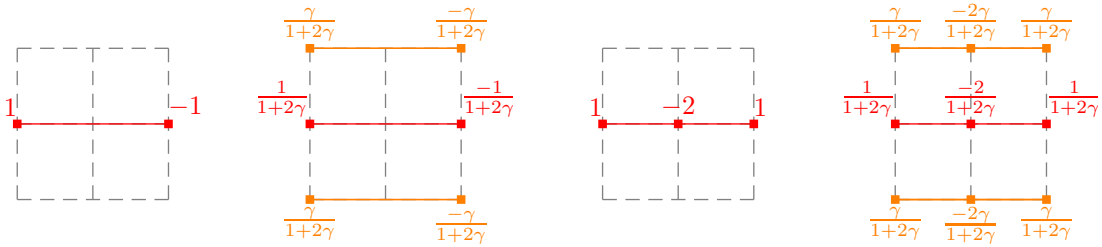


Figure 5.1.: Standard (1,3) and smoothed (2,4) weights for finite difference schemes ($\Delta x = 1$) for first and second derivative introduced by Lopez et al. [86].

the effect of curvature calculation on simulations in the context of a lattice BOLTZMANN method by comparing three different methods of curvature computation, namely (i) finite difference approximation from smoothed volume fractions (cf. Williams et al. [154]), (ii) triangular reconstruction and (iii) least-squares based reconstruction of the interface. They find that the $L_2$-error of the curvature of an uniformly translated sphere is lowest when applying a finite difference scheme, indicating its potential on CARTESIAN grids. Evrard et al. [44, fig. 8] perform surface reconstruction from volume fraction data in three spatial

dimensions. They report second-order convergence of $L_2$- and $L_\infty$-errors obtained by parabolic fitting of reconstructed vertices for spheres. Ivey and Moin [72] examine accurate interface normal and curvature estimates on three-dimensional unstructured non-convex polyhedral meshes for cylinders, spheres and ellipsoids. They also apply the smoothing of Lopez et al. [86]; cf. fig. (5.1). They find first- to second-order convergence of the $L_1$-error with interface resolution. Lopez and Hernandez [85] introduce a correction of the partial derivatives of the height functions based on local information. They find that „*a substantial improvement in the accuracy of the interface curvature computation can be efficiently achieved*“. A hybrid approach, combining the convolution of volume fractions with generalized height functions, is developed by Patel et al. [103]. They report second-order convergence of curvature errors with spatial resolution. The underlying volume fractions are computed by a combination of linear approximation and local refinement, and are shown to exhibit second-order convergence. A least-squares approach for the computation of curvature from volume fractions (CELESTE) is introduced by Denner and van Wachem [39]. However, the authors do not explicitly report their findings in terms of convergence of curvature errors. Owkes and Desjardins [101] propose a method for the mesh decoupling of the height function method. The decoupling is realized by assembling the heights in a direction respectively normal to the interface, which requires previous reconstruction and intersection operations. For spheres, the authors report second-order convergence for the $L_2$-error, whereas the $L_\infty$-error fails to converge. While the two-dimensional results resort to exact volume fractions, the authors do not comment on the quality of the volume fractions for three spatial dimensions. Furthermore, it is worth noting that the numerical experiments of Owkes and Desjardins [101] also comprise very coarse resolutions for which height functions cannot be found for all cells.

## 5.2. The height function algorithm

In what follows we describe the implementation of the height function method in three spatial dimensions on CARTESIAN grids, as proposed by Popinet [109]. For the purpose of a basic analysis, we assume an equidistant spatial discretization.

**Note 5.1** (Terminology)**.** *In the literatue, there are two different variants of the height function method; cf. Cummins et al. [35]. The* ***standard*** *variant (i) assembles the heights $\bar{h}_{u,v}$ (cf. eq. (5.4)) strictly in the direction of the largest normal component and (ii) computes curvatures in intersected cells only if the reconstructed node $\boldsymbol{x}_\Gamma$ (■) lies within the respective cell $\mathcal{K}$ (left).*

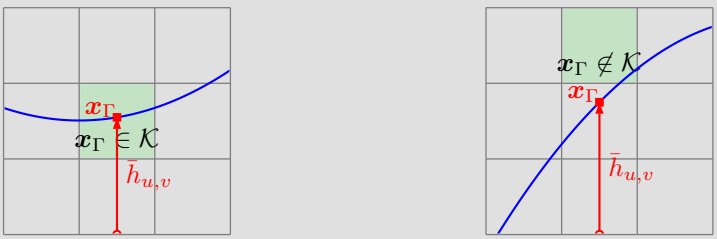


*The* ***generalized*** *variant is subject to neither of the these restrictions, where the present implementation is of the latter type.*

We seek to approximate the mean curvature $\kappa_\Sigma$ in interface cells $\mathcal{K}_{ijk}$, which are identified by their volume fraction $f_{ijk}$ via $0 < f_{ijk} < 1$. However, within a numerical implementation the aforementioned condition is converted[1] to the status

$$\mathfrak{S}(\mathcal{K}_{ijk}) = \begin{cases} -1 & f_{ijk} \leq \epsilon_\Sigma \\ 0 & \epsilon < f_{ijk} < 1 - \epsilon_\Sigma \\ 1 & f_{ijk} \geq 1 - \epsilon_\Sigma \end{cases}, \tag{5.1}$$

with some prescribed tolerence, say, e.g., $\epsilon_\Sigma = 10^{-6}$. The concept of the algorithm can be stated as follows: assuming that, locally, the hypersurface is the graph of a height function[2], cf. eq. (2.31) and appendix A.3, over one of the coordinate planes $\{\{yz\}, \{xz\}, \{xy\}\}$, the mean curvature can be computed from eq. (2.33). With $\mathcal{K}_{ijk}$ denoting the interface cell under consideration let

$$\mathcal{N}(N_u, N_v, N_w) = \{\mathcal{K}_{uvw} : (u, v, w) \in [i - N_u, i + N_u] \times [j - N_v, j + N_v] \times [k - N_w, k + N_w]\} \tag{5.2}$$

be the symmetric rectangular array of neighboring cells. In what follows, we assume that the lateral extent is one, while the cranial extent is $N_\mathrm{h}$ and introduce the *stencils*

$$\mathcal{S}_{xy}(N_\mathrm{h}) = \mathcal{N}(1, 1, N_\mathrm{h}), \quad \mathcal{S}_{xz}(N_\mathrm{h}) = \mathcal{N}(1, N_\mathrm{h}, 1) \quad \text{and} \quad \mathcal{S}_{yz}(N_\mathrm{h}) = \mathcal{N}(N_\mathrm{h}, 1, 1), \tag{5.3}$$

which can be decomposed into (i) a $3 \times 3$ array of columns $\mathcal{C}_{u,v}$ of length $2N_\mathrm{h} + 1$ or (ii) $2N_\mathrm{h} + 1$ layers $\mathcal{L}_w$ of size $3 \times 3$; cf. fig. (5.2) for an illustration. In a manner analogous to eq. (5.1), a layer $\mathcal{L}$ is considered interior/exterior ($\mathfrak{S}(\mathcal{L}) = \mp 1$) if all contained cells are interior/exterior and intersected ($\mathfrak{S}(\mathcal{L}) = 0$) otherwise. A stencil is considered admissible if it contains a sequence of layers whose statūs undergo a transition of type interior–interface–exterior, where more than one intersected layer may be contained. Figure (5.2(a)) and (b) illustrate the concept for columns where one and two cells, respectively, are intersected. To a column $\mathcal{C}_{u,v}$ in an admissible stencil one may assign the discrete height $\bar{h}_{u,v}$ by summing the volume fractions of cells in intersected layers, ensuring that the heights share a common reference. In the $\{xy\}$ case we obtain

$$\bar{h}_{u,v} = \sum_{w=-N_\mathrm{h}}^{N_\mathrm{h}} f_{i,j,k+w} \Delta z \, (1 - |\mathfrak{S}(\mathcal{L}_w)|), \tag{5.4}$$

the adaption to the cases $\{yz\}$ and $\{xz\}$ is straightforward. Figure (5.2(c)) exemplifies the resulting discrete heights. Employing the standard finite difference operators, cf. eq. (5.10) below, the discrete curvature in the stencil center is computed by evaluating the mean curvature of a graph with derivatives obtained by finite differences, cf. eq. (2.33), via

$$\kappa_\mathrm{num} = \frac{h_{xx}^\mathrm{FD}(1 + (h_y^\mathrm{FD})^2) + h_{yy}^\mathrm{FD}(1 + (h_x^\mathrm{FD})^2) - 2h_{xy}^\mathrm{FD} h_x^\mathrm{FD} h_y^\mathrm{FD}}{(1 + (h_x^\mathrm{FD})^2 + (h_y^\mathrm{FD})^2)^{\frac{3}{2}}}. \tag{5.5}$$

If there exists more than one admissble stencil, e.g., say, if the hypersurface can be represented as a graph

[1] Note that the *default* tolerance for the comparison of real numbers $\epsilon_\mathrm{zero} = 10^{-14}$, cf. section 1.3, cannot be employed here due to the application within FS3D.

[2] There may be more than one admissible representation, i.e. there may exist parametrizations over $\{xz\}$ and $\{xy\}$.

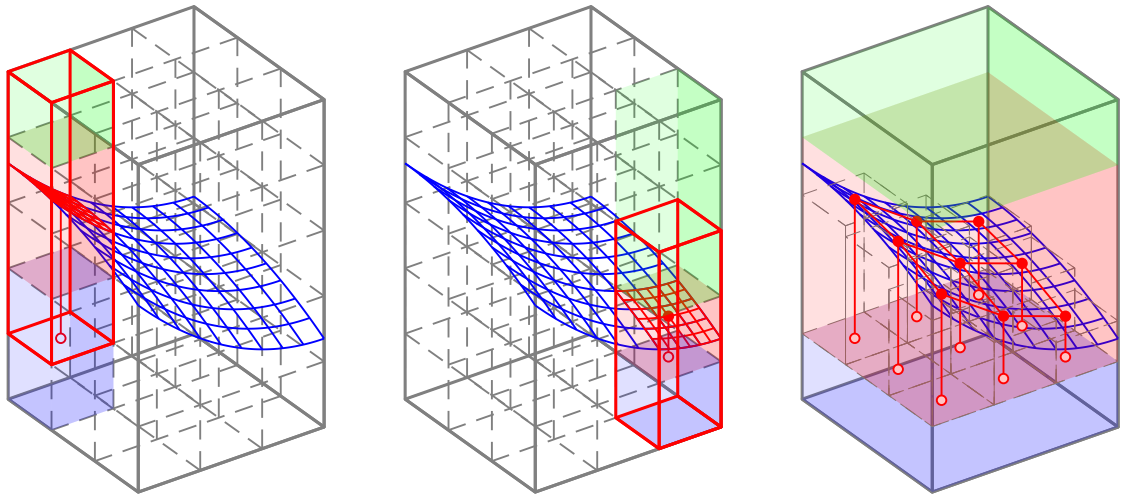

(a) column $\mathcal{C}_{-1,1}$ (b) column $\mathcal{C}_{1,-1}$ (c) stencil with $\bar{h}_{u,v}$

Figure 5.2.: Stencil for assembly of discrete height functions over $\{xy\}$-plane with base size $3 \times 3$. In (a) and (b) the solid red frame indicates the section of the respective column within which the transition from interior (blue, $\mathfrak{S}(\mathcal{K}) = -1$) to exterior (green, $\mathfrak{S}(\mathcal{K}) = 1$) occurs, where the intersected cells ($\mathfrak{S}(\mathcal{K}) = 0$) are marked by red shade. (c) gathers the discrete heights $\bar{h}_{i,j}$ for all columns and illustrates the intersection status $\mathfrak{S}(\mathcal{L}_w)$ of the layers.

over the $\{xy\}$- and $\{xz\}$-plane, Popinet [109] suggests to choose the cranial orientation of the stencil to coincide with the largest absolute component of the discrete normal of the volume fraction field. For the numerical results presented below, the method of Youngs [158] was employed, i.e.

$$\boldsymbol{n}^f_{ijk} := \frac{[f_{i+1,j,k} - f_{i-1,j,k}, f_{i,j+1,k} - f_{i,j-1,k}, f_{i,j,k+1} - f_{i,j,k-1}]^\mathsf{T}}{\sqrt{(f_{i+1,j,k} - f_{i-1,j,k})^2 + (f_{i,j+1,k} - f_{i,j-1,k})^2 + (f_{i,j,k+1} - f_{i,j,k-1})^2}}. \tag{5.6}$$

This recipe will henceforth be referred to as *largest normal component*. While Popinet [109] offers an empirically motivated rationale for this choice, we shall see in section 5.3 that for spheres there is a rigourous substantiation. From eq. (5.4) it is evident that the quality of the volume fractions may affect the heights $\bar{h}_{ij}$ differently, since different stencils will in general contain a different number of intersected cells and layers. Thus, it is interesting to also consider the minimum number of intersected layers (cells) in the stencil as a selection criterion for the height function basis. In the vast majority of the interface cells the recipies described above produce coinciding stencils. However, if the normal orientation is close to either (i) one of the space diagonals or (ii) to one of the plane diagonals, i.e.

$$\langle \boldsymbol{n}^f, \pm\boldsymbol{e}_1 \pm \boldsymbol{e}_2 \pm \boldsymbol{e}_3 \rangle \approx \sqrt{3} \quad \text{or} \quad \langle \boldsymbol{n}^f, \pm\boldsymbol{e}_i \pm \boldsymbol{e}_j \rangle \approx \sqrt{2} \quad \forall (i,j) \in \{(1,2),(1,3),(2,3)\}, \tag{5.7}$$

the recipies may produce different results.

## 5.3. Theoretical results

Let $\Sigma$ be a hypersurface which, in a neighborhood $\mathcal{B} = [x_0 - \epsilon, x_0 + \epsilon] \times [y_0 - \epsilon, y_0 + \epsilon]$ of some $(x_0, y_0)$, is the graph of a sufficiently smooth height function $h : \mathcal{B} \mapsto \mathbb{R}$ with, say, $h(x_0, y_0) = 0$. We seek to compute an approximation of the mean curvature at $(x_0, y_0)$, cf. eq. (2.33), from average values of $h$; cf. fig. (5.3) for a sketch of the concept. The neighborhood $\mathcal{B}$ is decomposed into a $3 \times 3$ array of rectangular patches

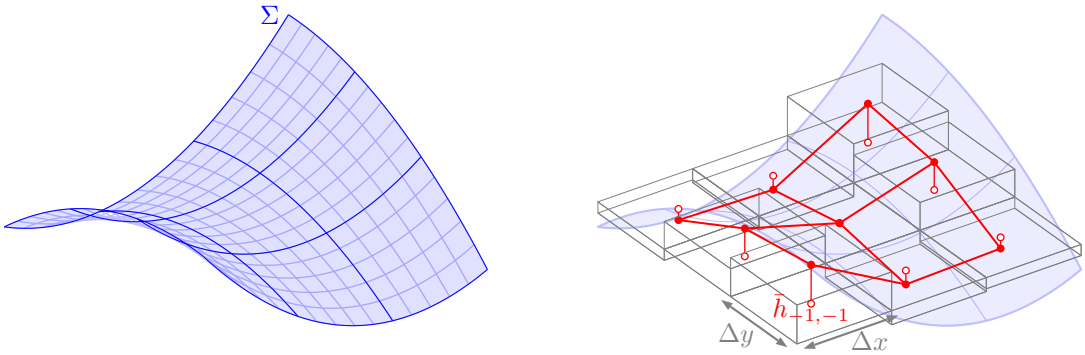


Figure 5.3.: Hypersurface $\Sigma$ as graph of a height function with array of averaged heights $\bar{h}_{ij}$.

of size $\Delta x \Delta y$, i.e. the average heights become

$$\bar{h}(x_0, y_0; \Delta x, \Delta y) := \frac{1}{\Delta x \Delta y} \int_{x_0 - \frac{\Delta x}{2}}^{x_0 + \frac{\Delta x}{2}} \int_{y_0 - \frac{\Delta y}{2}}^{y_0 + \frac{\Delta y}{2}} h(x, y) \, \mathrm{d}y \, \mathrm{d}x. \tag{5.8}$$

In order to numerically estimate the mean curvature, an approximation of the first and second derivatives of $h$ is required. Introducing

$$\bar{h}_{ij} := \bar{h}(x_0 + i\Delta x, y_0 + j\Delta y), \tag{5.9}$$

and inserting the standard finite differences

$$\begin{aligned}
h_x^{\mathrm{FD}} &:= \frac{\bar{h}_{1,0} - \bar{h}_{-1,0}}{2\Delta x}, \quad h_y^{\mathrm{FD}} := \frac{\bar{h}_{0,1} - \bar{h}_{0,-1}}{2\Delta y}, \\
h_{xx}^{\mathrm{FD}} &:= \frac{\bar{h}_{1,0} - 2\bar{h}_{0,0} + \bar{h}_{-1,0}}{\Delta x^2}, \quad h_{yy}^{\mathrm{FD}} := \frac{\bar{h}_{0,1} - 2\bar{h}_{0,0} + \bar{h}_{0,-1}}{\Delta y^2}, \\
h_{xy}^{\mathrm{FD}} &:= \frac{\bar{h}_{1,1} - \bar{h}_{-1,1} - \bar{h}_{1,-1} + \bar{h}_{-1,-1}}{4\Delta x \Delta y},
\end{aligned} \tag{5.10}$$

into eq. (2.33) yields

$$\kappa_\Sigma^{\mathrm{FD}} = \frac{h_{xx}^{\mathrm{FD}} \left(1 + (h_y^{\mathrm{FD}})^2\right) + h_{yy}^{\mathrm{FD}} \left(1 + (h_x^{\mathrm{FD}})^2\right) - 2 h_{xy}^{\mathrm{FD}} h_x^{\mathrm{FD}} h_y^{\mathrm{FD}}}{\left(1 + (h_x^{\mathrm{FD}})^2 + (h_y^{\mathrm{FD}})^2\right)^{\frac{3}{2}}}. \tag{5.11}$$

In order to obtain some basic insights, the upcoming analysis examines the equidistant case $\Delta x = \Delta y$. The devitation of the finite difference approximation from the exact mean curvature can be expressed as

$$\Delta\kappa := \kappa_\Sigma - \kappa_\Sigma^{\mathrm{FD}} = D(h)\Delta x^2 + \mathcal{O}(\Delta x^3), \tag{5.12}$$

where the implied second-order convergence for $\Delta x \to 0$ is well known in literature; cf., e.g., Sussman [135], Cummins et al. [35] or Helmsen and Colella [63]. Bornia et al. [21] provide some analytical results for Cartesian meshes in two spatial dimensions. However the structure of the coefficient $D$, which is a function of the derivatives of $h$ at $(x_0, y_0)$, seems to not have received much attention. In the limiting case $\Delta x \to 0$, one may consider a fourth-order Taylor expansion of $h$, i.e.

$$\begin{aligned} h(x,y) = c_{10}\tilde{x} + c_{01}\tilde{y} &+ \frac{c_{20}\tilde{x}^2 + 2c_{11}\tilde{x}\tilde{y} + c_{02}\tilde{y}^2}{2} \\ &+ \frac{c_{30}\tilde{x}^3 + 3c_{21}\tilde{x}^2\tilde{y} + 3c_{12}\tilde{x}\tilde{y}^2 + c_{03}\tilde{y}^3}{6} \\ &+ \frac{c_{40}\tilde{x}^4 + 4c_{31}\tilde{x}^3\tilde{y} + 6c_{22}\tilde{x}^2\tilde{y}^2 + 4c_{13}\tilde{x}\tilde{y}^3 + c_{04}\tilde{y}^4}{24} + \mathcal{O}(\Delta x^5), \end{aligned} \tag{5.13}$$

where, for ease of notation, let

$$c_{ij}(x_0, y_0) := \partial_x^i \partial_y^j h(x,y)\big|_{x=x_0, y=y_0} \qquad \text{and} \qquad \tilde{x} = x - x_0, \quad \tilde{y} = y - y_0.$$

The sufficiency of considering fourth-order terms can be justifed as follows: the mean curvature $\kappa_\Sigma$ depends on the first and second derivatives only, implying that the order of the Taylor expansion only affects the averaging in eq. (5.8). Thus, the order of the Taylor expansion resembles the data quality, where a second-order expansion is required for the curvature to be non-zero. Since the volume fractions provided by the algorithm introduced in chapter 4 exhibit approximately fourth-order convergence with spatial resolution or can be computed exactly for spheres, the chosen expansion order is deemed to be sufficient for the present purpose; Popinet [110, p. 59] offers a similar argument. Evaluating the integral given in eq. (5.8), using the Taylor expansion from eq. (5.13) and plugging the resulting average heights into eq. (5.12) yields the sought coefficient

$$\begin{aligned} D = &\frac{\left(\frac{3\,c_{01}\left(\frac{5\,c_{03}}{12}+\frac{c_{21}}{12}\right)}{2} + \frac{3\,c_{10}\left(\frac{c_{12}}{12}+\frac{5\,c_{30}}{12}\right)}{2}\right)\left(c_{02}\,\left({c_{10}}^2+1\right) + c_{02}\,\left({c_{01}}^2+1\right) - 2\,c_{01}\,c_{10}\,c_{11}\right)}{\left({c_{01}}^2+{c_{10}}^2+1\right)^{5/2}} \\ &- \frac{\left({c_{10}}^2+1\right)\,\left(\frac{c_{04}}{8}+\frac{c_{22}}{24}\right) + \left({c_{01}}^2+1\right)\,\left(\frac{c_{22}}{24}+\frac{c_{40}}{8}\right) - \frac{c_{10}\left(2\,c_{01}\left(\frac{5\,c_{13}}{6}+\frac{5\,c_{31}}{6}\right)+4\,c_{11}\left(\frac{5\,c_{03}}{12}+\frac{c_{21}}{12}\right)\right)}{4}}{} \\ &- \frac{c_{01}\,c_{02}\,\left(\frac{5\,c_{03}}{12}+\frac{c_{21}}{12}\right) + c_{02}\,c_{10}\,\left(\frac{c_{12}}{12}+\frac{5\,c_{30}}{12}\right) - c_{01}\,c_{11}\,\left(\frac{c_{12}}{12}+\frac{5\,c_{30}}{12}\right)}{\left({c_{01}}^2+{c_{10}}^2+1\right)^{3/2}}. \end{aligned} \tag{5.14}$$

Note that, providing the respective partial derivatives $c_{ij}$, eq. (5.14) is valid for general hypersurfaces. While general statements on the properties of $D$ are barely possible, spheres allow for a detailed analysis. For a sphere with radius $R$ centered at $\mathbf{0}$, i.e. for $h = \sqrt{R^2 - x^2 - y^2}$, the above equation becomes

$$D(x_0, y_0) = -\frac{x_0^6 + y_0^6 - 10R^6 + 27R^4(x_0^2 + y_0^2) - 18R^2(x_0^4 + x_0^2 y_0^2 + y_0^4) + 30(x_0^4 y_0^2 + x_0^2 y_0^4)}{12R^3(R^2 - x_0^2 - y_0^2)^3}. \tag{5.15}$$

Combining eqs. (5.12) and (5.15) yields the second-order approximation of the relative curvature error depending on the spatial position and resolution, i.e.

$$\tilde{\mathcal{E}}_2^{\kappa}(x_0, y_0; R, \Delta x) := -D(x_0, y_0)\frac{R\Delta x^2}{2}. \tag{5.16}$$

Due to the symmetry of the sphere, it is sufficient to consider the first octant. In order to capture the symmetries within the octants let

$$\theta_{\text{red}}(\boldsymbol{x}) := \arccos\frac{\max\{|x|, |y|, |z|\}}{R}, \tag{5.17}$$

which can be thought of as a polar angle, whose corresponding northpole is the respectively nearest intersection with one of the coordinate axes. Figure (5.4) (→,→) provides an illustration. Using eq. (5.17), we define the vicinity

$$\mathcal{V}(\alpha) := \{\boldsymbol{x} \in \Sigma : \theta_{\text{red}}(\boldsymbol{x}) \geq \alpha\}. \tag{5.18}$$

Note that, depending on the position on $\Sigma$, the graph parametrization resorts to a different coordinate

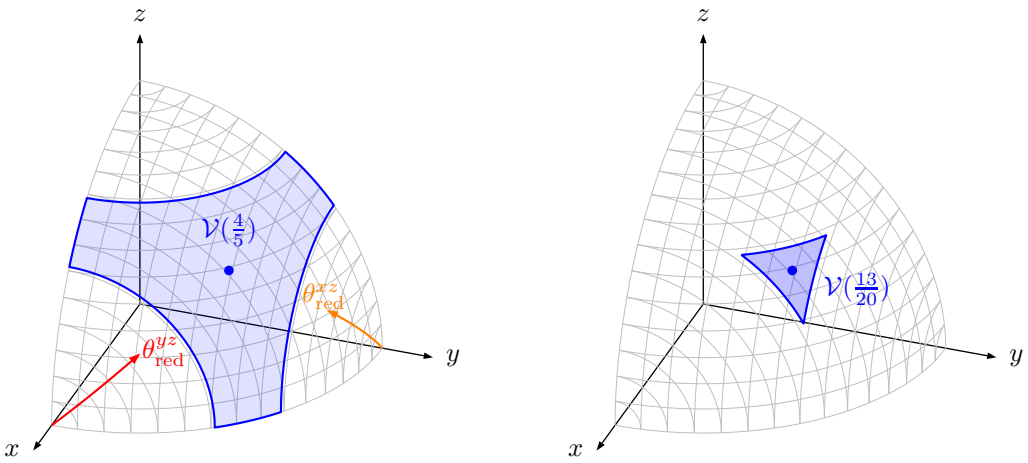


Figure 5.4.: Sphere with polar angle $\theta_{\text{red}}$ and different vicinities of the space diagonal (●); cf. eq. (5.18). E.g., Lopez et al. [86] apply a smoothed finite difference operator in $\mathcal{V}(4/5)$; cf. fig. (5.1).

plane; fig. (5.5(a)) illustrates the respective graph basis. In fact, the graph basis is selected based on the largest normal component, where it becomes evident from the subsymmetries within the first octant shown in fig. (5.5(b)) that this choice minimizes the curvature errors. Hence, we consider only the segment of the first octant for which the $\{xy\}$-plane is the basis, where the statements are readily transferred to the remaining segments; cf. again fig. (5.5(a)). The main implications of fig. (5.5) can be stated as follows:

1. The relative deviation is largest in the space diagonal direction, i.e. for $\varphi = \frac{\pi}{4}$ and $\theta = \arccos\frac{1}{\sqrt{3}}$.
2. For fixed azimuthal position $\varphi$, the relative deviation $\tilde{\mathcal{E}}_2^{\kappa}$ is a strictly monotone function of $\theta$ with a single root (■ in fig. (5.6)), whose position depends on the value of $\varphi$.
3. Figure (5.6) shows that the relative deviation $\tilde{\mathcal{E}}_2^{\kappa}$ remains virtually constant for $0 \leq \theta \leq 35°$ and varying azimuthal angles $\varphi$, while the slope becomes steep beyond the root, causing an increment

in the magnitude by two orders of magnitude for $\varphi \in \{\frac{\pi}{8}, \frac{\pi}{4}\}$.

4. Due to the sign change, the absolute deviation becomes smallest on a triangular region around the space diagonal, which confines the region where the deviations are largest.

Before the next section 5.4 conducts some numerical experiments, we shall summarize the implications of the theoretical considerations presented above. The fourth-order TAYLOR expansion of the height function around the stencil center along with the exact integration provide average heights $\bar{h}_{u,v}$ which are sufficiently accurate for the purpose of this analysis, i.e. if the dominant error contributions are of order $\Delta x^2$. One may deduce that, for sufficiently accurate volume fractions, an appropriate implementation of the height function algorithm reproduces the patterns occuring in fig. (5.5) for spheres. E.g., Patel et al. [103, 104] report such patterns, but without further discussion. Hence, both the spatial patterns and magnitudes of the curvature errors indicate a performance benchmark.

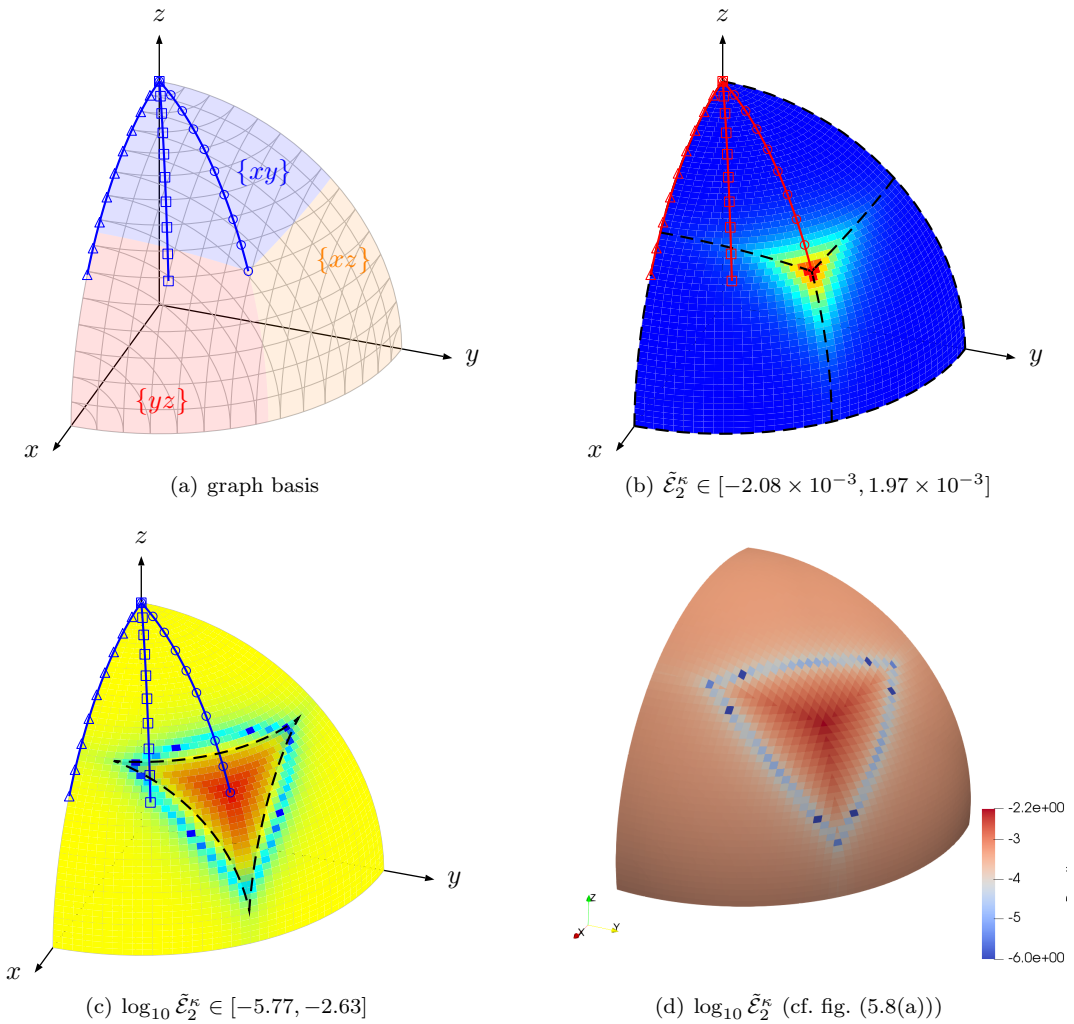


(a) graph basis

(b) $\tilde{\mathcal{E}}_2^\kappa \in [-2.08 \times 10^{-3}, 1.97 \times 10^{-3}]$

(c) $\log_{10} \tilde{\mathcal{E}}_2^\kappa \in [-5.77, -2.63]$

(d) $\log_{10} \tilde{\mathcal{E}}_2^\kappa$ (cf. fig. (5.8(a)))

Figure 5.5.: Second-order approximation of relative curvature error from eq. (5.16) on the first octant of a sphere with radius $R = \frac{91}{100}$ and $\Delta x = \frac{1}{50}$. The curves in fig. (5.6) evaluate the rel. curvature error for iso-sections at $\varphi \in \{0, \frac{\pi}{8}, \frac{\pi}{4}\}$, which are indicated accordingly in (a)-(c). The dashed line in (c) confines the vicinity of the space diagonal ($\alpha = 7/10$; cf. eq. (5.18) and fig. (5.4)).

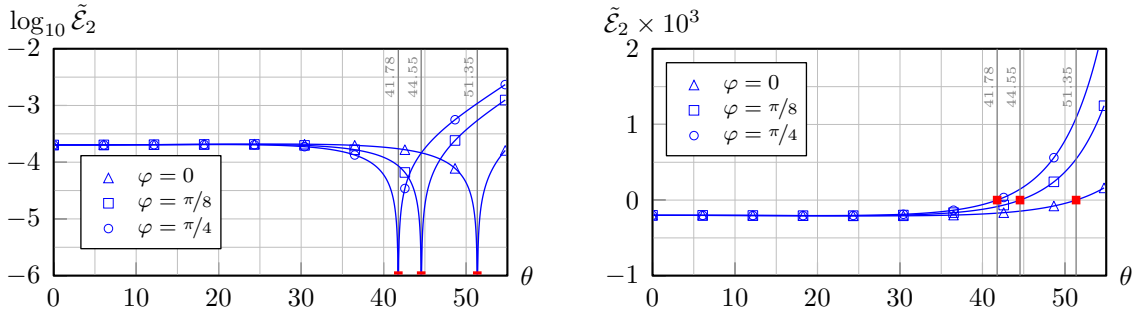


Figure 5.6.: Evaluation of eq. (5.16) over $\theta$ in degrees at different azimuthal positions depicted in fig. (5.5).

## 5.4. Numerical results

In what follows, we apply the height function method introduced in section 5.2 to the volume fraction fields obtained from some technically relevant hypersurfaces. Since spherical particles are of high practical relevance and allow for exact computation of the associated volume fractions, we shall commence by a detailed treatment of this prototypical class. Besides the global error measures of $L_2$- and $L_\infty$-type, we provide both local information in the form of surface patterns as well as some statistical interrelations. Subsequently, these results are extended to general ellipsoids and perturbed spheres, where, of course, the comparison to exact volume fractions is not possible.[3]

**Note 5.2** (Choice of resolution)**.** *The implementation of Popinet [109] features several fall-back strategies for the curvature computation in case no graph base for the height function can be found, which is typically the case in underresolved computations. However, as stated above, the focus of the present analysis lies on the assessment of the height function method itself. Hence, the range of spatial resolutions in the numerical examples presented within this section is* $N_{\mathcal{K}} \in \{40, 50, \ldots, 100\}$*, ensuring that an admissible stencil, cf. fig. (5.2), is found for every intersected cell. Note that the number of intersected cells* $N_\Sigma$*, which is an output of the volume fraction initialization, is related to the total number of cells by* $\sqrt{N_\Sigma} \sim N_{\mathcal{K}}$ *due to the fact that the hypersurface* $\Sigma$ *is of codimension one with respect to its embedding space* $\mathbb{R}^3$*.*

In particular, the following questions shall be addressed:

1. Is the algorithm capable of reproducing accurate curvature estimates for exact volume fractions?
2. How sensitive are the results to the quality of the volume fractions?
3. Due to the spatial discretization of the curvature operator, one has to expect patters resembling the Cartesian grid. What are those patterns and can they be used to substantiate the correction terms?
4. Does the algorithm exhibit the expected convergence behavior for both $L_2$- and $L_\infty$-errors with increasing spatial resolution for non-spherical hypersurfaces?

[3] In theory, the computation of exact volume fractions, e.g. by means of direct quadrature, is always possible. However, for general hypersurfaces, the numerical effort becomes prohibitively large; see, e.g., Wen [150, 152].

The standard error definitions

$$\mathcal{E}_k^\kappa := \frac{\kappa_{\Sigma,k} - \kappa_{\text{num},k}}{|\kappa_{\text{ref}}|}, \qquad \mathcal{E}_2^\kappa := \sqrt{\frac{1}{N_\Sigma}\sum_{k=1}^{N_\Sigma}(\mathcal{E}_k^\kappa)^2} \qquad \text{and} \qquad \mathcal{E}_\infty^\kappa := \max_k |\mathcal{E}_k^\kappa|\,, \tag{5.19}$$

are employed, where $N_\Sigma$ denotes the number of intersected cells and $\kappa_{\text{ref}}$ denotes the referential curvature, allowing to obtain dimensionless quantities. While it seems straightforward to choose a *local* $\kappa_{\text{ref}}$ corresponding to the analytical mean curvature $\kappa_{\Sigma,k}$ used for the computation of the volume fractions, there are two basic considerations governing a suitable choice of $\kappa_{\text{ref}}$: Firstly, $\kappa_{\text{ref}}$ should not depend on the spatial resolution $N_\mathcal{K}$. While this influence can be considered negligible for sufficiently large $N_\mathcal{K}$, the sufficiency of the resolution is unknown a priori and may vary between instances. Secondly, the curvature, e.g. for perturbed spheres, may exhibt sign changes, implying that comparison to the local mean curvture $\kappa_{\Sigma,k}$ potentially produces expressions of type $\frac{0}{0}$, which would deteriorate the meaning of the error measures in eq. (5.19). Hence, we choose a referential curvature[4] induced by the class of the hypersurface, i.e.

$$\kappa_{\text{ref}}^{\text{ellipsoid}} := \min\left\{-\frac{a(b^2+c^2)}{b^2c^2}, -\frac{b(a^2+c^2)}{a^2c^2}, -\frac{c(a^2+b^2)}{a^2b^2}\right\} \qquad \text{and} \qquad \kappa_{\text{ref}}^{\text{pert.sp.}} := -\frac{2}{R_0}. \tag{5.20}$$

The influence of the volume fraction quality on the curvature deviation is assessed by comparing *linear* and *quadratic* local approximation of the hypersurface; cf. the numerical results for the initialization given in section 4.6. In terms of statistical interrelations, it is interesting to investigate the correlation of errors to the number of intersected cells $n_{\mathcal{S}_k,\Sigma}$ and intersected layers $n_{\mathcal{S}_k,\text{l}}$ in the respective height function stencils $\mathcal{S}_k$; cf. fig. (5.2) for an illustration. The computation of the heights $\bar{h}_{u,v}$ given in eq. (5.4) supplies the rationale behind this conjecture: the deviation of the exact average heights and their numerical approximations is solely caused by interface cells. Without a priori knowledge, one must assume that potential errors are randomly distributed among the intersected cells, implying that the sum over a different number of intersected cells introduces a different error contribution.

**Note 5.3** (Paraview figures)**.** *The upcoming subsections frequently feature figures created with* `ParaView`*; cf. section 1.3. While the depicted surface data can be interpreted by the respective color legend along with the captions, all figures share the following properties:*

1. *The surface mesh consists of patches which are not necessarily connected, where every intersected cell $\mathcal{K}_k$ of the* Cartesian *backgroud mesh provides exactly one patch $\Gamma_k$. The patches are non-planar polygons with 3 to 6 nodes, coinciding with the edge intersections $\boldsymbol{x}_{\partial\Gamma_k,i}$ computed by the intialization algorithm; cf. fig. (4.9) in section 4.5 for an illustration.*

2. *The intersection status of a cell $\mathcal{K}_k$ only depends on the respective instance of the hypersurface $\Sigma$; cf. eq. (4.49) in subsection 4.5.1. This implies that the intersection status is not affected by the approximation order of the hypersurface, i.e. the respective surface patches and data elemets admit a bijective assignment, allowing for a cell-wise comparison of linear and quadratic volume fractions.*

[4] For ellipsoids it holds that $\kappa_\Sigma < 0$, i.e. eq. (5.20) corresponds to the largest absolute mean curvature.

3. *The quantities depicted on the surface patches are stored as binary data which are subject to* ***no interpolation*** *or other forms of postprocessing, unless explicitly stated otherwise.*

4. *Despite the intersection criterion based on the volume fraction value, i.e.* $\epsilon < f_k < 1 - \epsilon$ *(see eq. (5.1)), for the sake of consistency we prefer to resort to the intersection status obtained from the initialization algorithm, cf. eq. (4.49) in subsection 4.5.1. This ensures that every interface cell (in a topological sense) is assigned a curvature estimate and removes the potentially biasing influence of a specific choice of the tolerance* $\epsilon$*.*

5. *The figures correspond to a resolution of* $N_{\mathcal{K}} = 100$ *per spatial direction for* $\mathcal{K} = [-1, 1]^3$*. The results for lower resolutions are qualitatively corresponding, hence the exemplary resolution can be considered representative; cf. fig. (5.9). The numerical computation of the mean curvature* $\kappa_\Sigma$ *resorts to the recipe largest normal component; cf. section 5.2.*

**Note 5.4** (Statistical figures)**.** *The statistical representation of the local curvature errors* $\mathcal{E}_k^\kappa$ *defined in eq. (5.19) is given in figures (5.11), (5.14), (5.19), (5.20) and (5.21) for* $N_{\mathcal{K}} = 100$*, where the representative character of these instances was discussed in note 5.3. The horizontal axis denotes the number of intersected layers (*$n_{\mathcal{S},1}$*) or cells (*$n_{\mathcal{S},\Sigma}$*) in the respective stencil; cf. the illustration in fig. (5.2).*

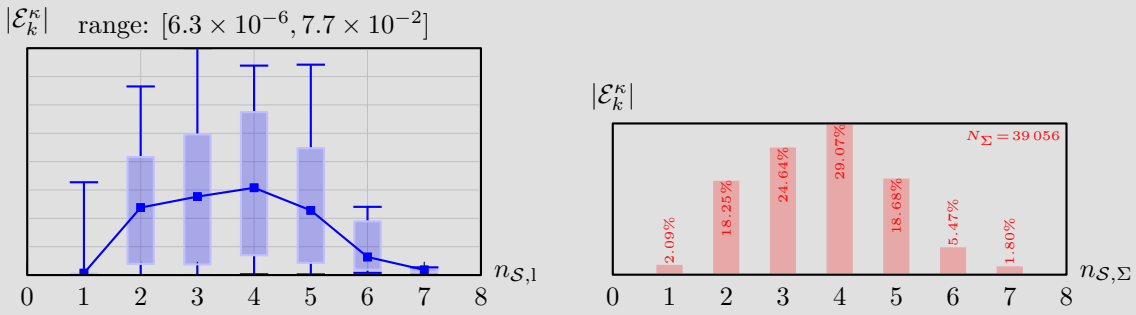


*The figures are of box-plot type and share the following properties:*

1. *At the top edge of the frame the range of the curvature error is given, which potentially differs between instances. (left)*

2. *The whiskers indicate the minimum and maximum of the curvature error whereas the shaded box marks the 10% and 90% quantile, respectively. (left)*

3. *The* ■ *denotes the average magnitude. (left)*

4. *The vertically oriented number represents the ratio of occurrence whereas the* $N_\Sigma$ *corresponds to the total number of interface cells. (right)*

*E.g., in the present case, there are* 39 056 *interface cells within which the error ranges from* $6.3 \times 10^{-6}$ *to* $7.7 \times 10^{-2}$*. For* 24.64% *of the cells, the corresponding stencil exhibits 3 intersected layers. Among*

*those, the relative error embraces values up to* $7.7 \times 10^{-2}$*, where 90% of the values are below* 62.5*% of the associated maximum. However, most (*29.07*%) of the stencils feature 4 intersected layers.*

### 5.4.1. Spheres

Before the discussion of the numerical results, we find it useful to report some details of the algorithmic execution. This establishes a visual understanding of the involved quantities, which helps to interpret the results. Unless stated otherwise, spheres of radius $R = \frac{91}{100}$ are considered here. Further details are gathered in note (5.3). Figure (5.7) depicts the graph basis and the number of admissible stencils on a cell basis. As indicated by fig. (5.5(a)), the employed graph bases exhibit the expected symmetries, both between and within the octants. The *serrated* transition of the graph basis on the connection of the space diagonals can be attributed to the sparse accuracy of the normals, cf. eq. (5.6). Despite the fact that size of the indentations matches the size of the cells, as can be seen from the mesh section in fig. (5.7(a)), a more sophisticated computation of $\boldsymbol{n}_k$ would produce a smoother transition. However, note that, besides this, the quality of the volume fractions has no effect on the aforementioned quantites. As can be seen from figs. (5.7(c)) and (5.7(d)), the number of intersected layers ($1 \leq n_{\mathcal{S},\mathrm{l}} \leq 7$) and cells ($9 \leq n_{\mathcal{S},\Sigma} \leq 27$) in the respective stencils are correlated among each other and to the normal orientation, resembling the Cartesian background grid.

#### Influence of the volume fraction quality (linear/quadratic/exact)

Figure (5.9(a)) gathers the evolution of the error measures given in eq. (5.19). For linear volume fractions, both error measures exhibit virtually constant values of $\mathcal{E}_2^\kappa \approx 2.8 \times 10^{-2}$ and $\mathcal{E}_\infty^\kappa \approx 7.8 \times 10^{-2}$, respectively, where fig. (5.8(c)) shows that for $N_\mathcal{K} = 100$ the local errors range from $-6.8 \times 10^{-2}$ to $7.7 \times 10^{-2}$. Therefore, second-order convergence with spatial resolution cannot be observed. Inspecting fig. (5.8(c)) highlights further disadvantageous features: in the region around the space diagonal, there are three circular regions within which the error admits its largest values (in terms of magnitude), accompanied by a sign change between cells. Here, this so-called *checkerboard* phenomenon is a consequence of the deviation of the linear volume fractions from their exact pendants (cf. fig. (4.20(b))) and directly translates to significant spurious currents, as has been shown in subsection 4.6.6. In general, the errors in fig. (5.8(c)) resemble the structure of the underlying Cartesian grid. However, the fact that the patterns admit no correlation to the number of intersected cells/layers in fig. (5.7(c)) suggests that the spoilage of convergence is caused by the poor volume fraction quality rather than by the discretization scheme. Pohl [107, pp. 29-30] and Patel et al. [103] report simliar patterns, where the results of Popinet [109, fig. 6] suggest analogies to two spatial dimensions. On the other hand, the quadratic and exact volume fractions exhibit second-order convergence as reported in literature, cf. section 5.1. For the finest resolution ($N_\mathcal{K} = 100$), the values range from $-2.8 \times 10^{-3}$ to $2.1 \times 10^{-4}$, i.e. the errors are reduced by a factor of 27.5 in comparison to linear volume fractions. Note that the error values ($\circ/\triangle$ in fig. (5.9(a))) are virtually identical, which is to be expected due to the small deviations of the respective volume fractions ($\approx 10^{-6}$, cf. fig. (4.20(c))). Figure (5.8(d)) shows that the local deviations obtained from exact and quadratic volume fractions are of order $10^{-6}$.

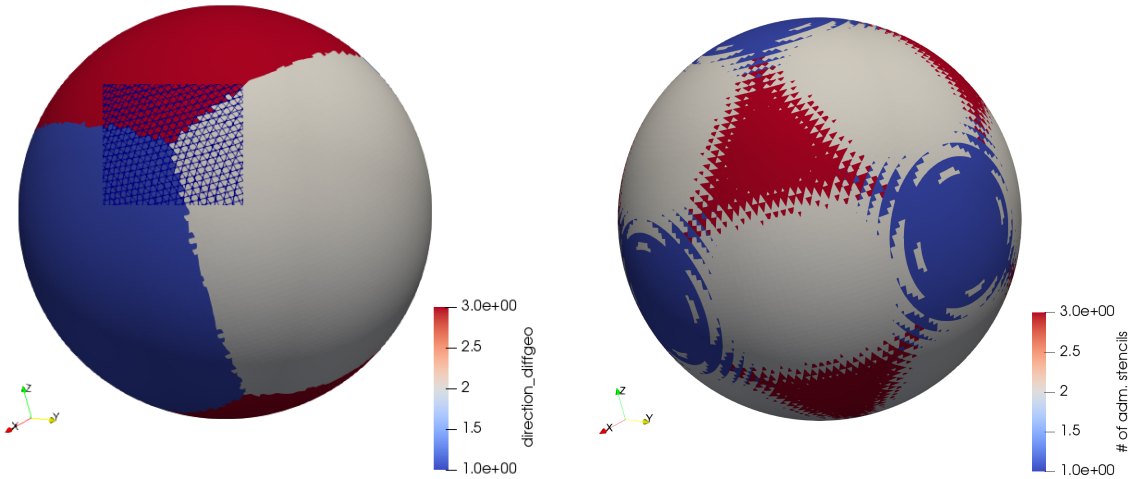


(a) graph basis

(b) number of admissible stencils

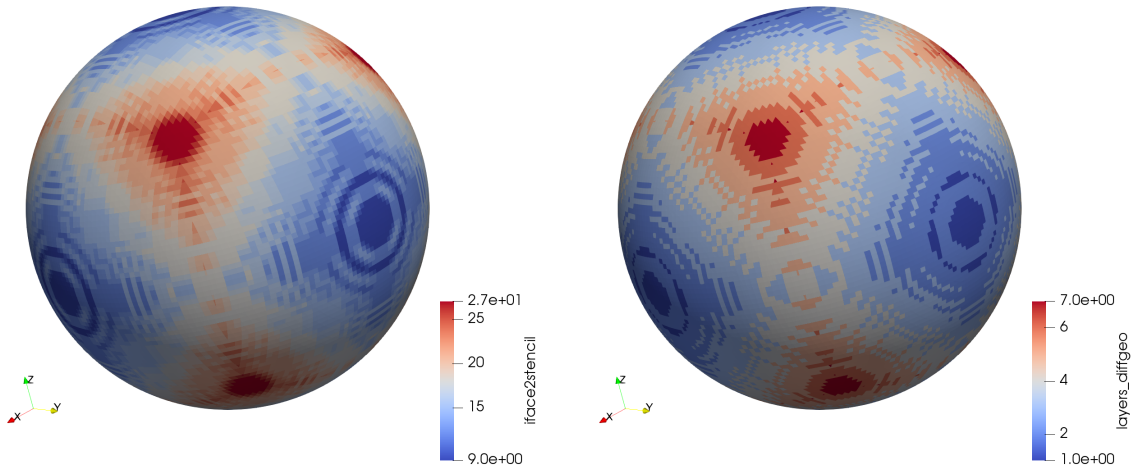


(c) $n_{\mathcal{S},\Sigma}$

(d) $n_{\mathcal{S},1}$

Figure 5.7.: Algorithmic execution quantities for height function method: (a) graph basis (from largest normal component, see fig. (5.5(a))), (b) number of admissible stencils, (c) number of interface cells in stencil and (d) number of intersected layers in stencil; cf. note (5.3).

**Note 5.5** (Exact volume fractions)**.** *In fact, the differences between the results obtained from exact and quadratic volume fractions are barely observable for the resolutions considered here, i.e.* $40 \leq N_{\mathcal{K}} \leq 100$*. This justifies a confinement to quadratic volume fractions for the upcoming analysis.*

The errors depicted in figs. (5.8(a)) and (b) are in excellent agreement with the theoretical prediction of section 5.3, both in magnitude and pattern, as can be seen from figs. (5.5(c)) and (d). When applying a correction of the numerically obtained curvature based on the theoretical prediction in eq. (5.15), one is able to obtain fourth-order convergence ($\diamond$ in fig. (5.9(a))). This is again a direct consequence of the symmetry in eq. (5.10). The apparent correlation to the number of intersected cells and layers in fig. (5.7(c)) suggests that, for spheres, the dominant error contribution for quadratic volume fractions is caused by the discretization scheme.

It is worth noting at this point that the above results establish a **performance benchmark** for the height function algortihm under most beneficial conditions, i.e. exact volume fractions on a CARTESIAN grid whose origin coincides with the center of the sphere.

#### Influence of the volume fraction quality (additive noise)

In order to examine the influence of random mean-free additive noise, let

$$\tilde{f}_k := f_k + (1 - |\mathfrak{S}(\mathcal{K}_k)|)\,\nu_k \qquad \text{with} \quad \nu_k \sim \mathcal{N}(0, \hat{\sigma}^2), \tag{5.21}$$

where the $\nu_k$ are computed using alg. (2). Note that only intersected cells are subject to noise superposition and the biased volume fractions are clipped s.t. $\tilde{f}_k \in [0, 1]$. Figure (5.9(b)) gathers the evolution of $\mathcal{E}_2^\kappa$ and $\mathcal{E}_\infty^\kappa$ for quadratic volume fractions as a function of the variance $\hat{\sigma}^2$ for fixed spatial resolution $N_{\mathcal{K}} = 100$, cleary depicting an increase of the deviation proportional to $\hat{\sigma}$. The observations of fig. (5.9) indicate[5] a relation of type

$$\mathcal{E}^\kappa \sim D_1 \Delta x^2 + D_2 \frac{\hat{\sigma}}{\Delta x^2}, \tag{5.22}$$

where the coefficients $D_i$ depend on the class and instance of the underlying hypersurface. For spheres, the local pendant of $D_1$ corresponds to eq. (5.15). The unpublished work of Fricke et al. [52] offers a rigorous theoretical substantation for eq. (5.22). Figure (5.10) provides the patterns associated to some of the noise instances given in fig. (5.9(b)).

While the spatial structure of the relative deviation is well pertained for $\hat{\sigma}^2 = 10^{-12}$, already increasing $\hat{\sigma}^2$ to $10^{-10}$ strongly obliterates the characteristic peaks at the space diagonals. For larger variances, there is no evident pattern at all, suggesting the conjecture that CARTESIAN grids admit spectrally neutral noise amplification patterns. Let us note in passing that the numerical experiments conducted for multiplicative noise, i.e. for $\tilde{f}_k := (1 + \nu_k) f_k$, are in qualitative accordance with the additive case.

[5] Equation (5.22) is provided by courtesy of **Mathis Fricke** (Dept. of Mathematics, TU Darmstadt).

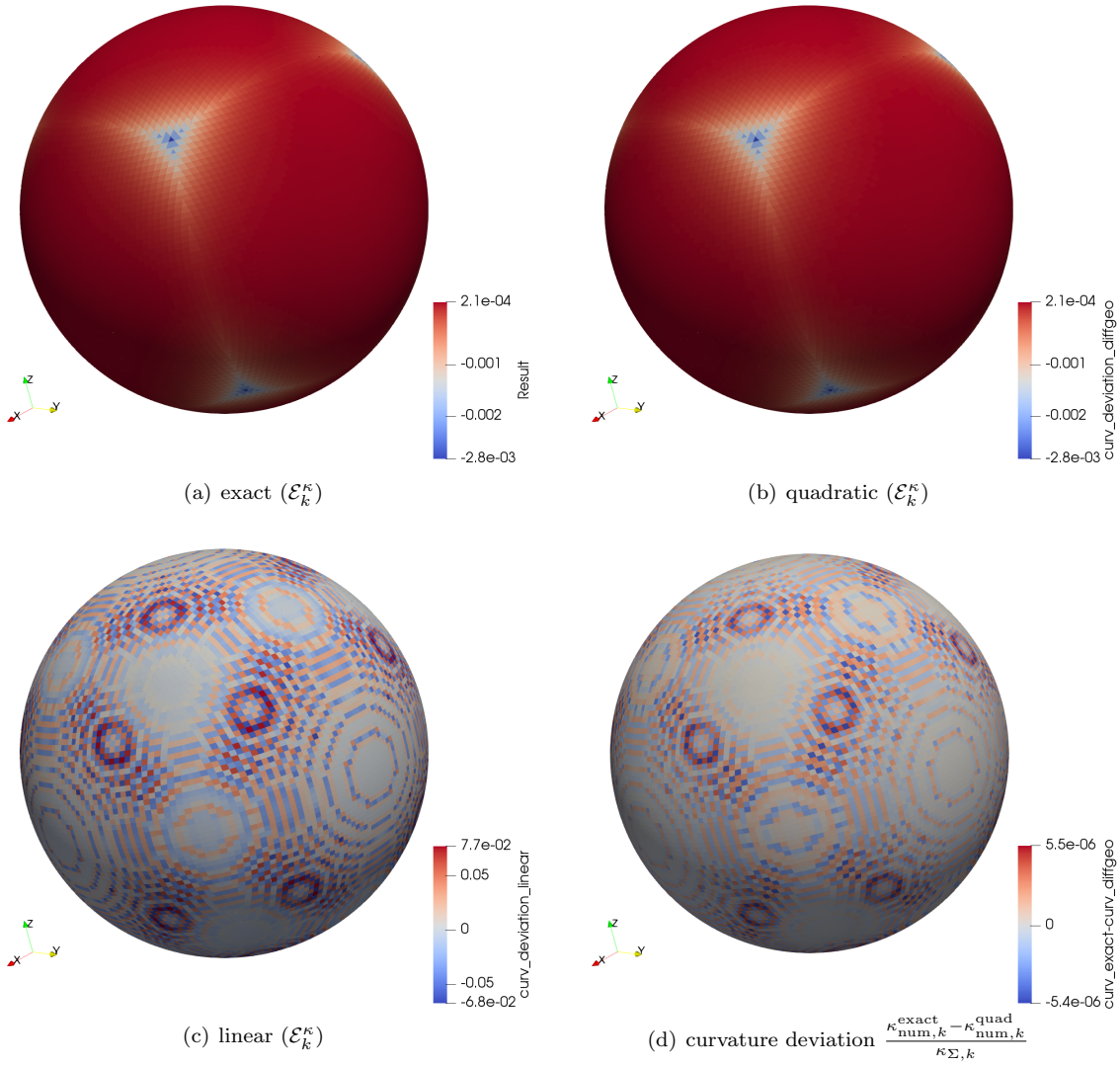


(a) exact ($\mathcal{E}_k^\kappa$)

(b) quadratic ($\mathcal{E}_k^\kappa$)

(c) linear ($\mathcal{E}_k^\kappa$)

(d) curvature deviation $\frac{\kappa_{\mathrm{num},k}^{\mathrm{exact}} - \kappa_{\mathrm{num},k}^{\mathrm{quad}}}{\kappa_{\Sigma,k}}$

Figure 5.8.: Surface patterns of curvature error from eq. (5.19) for exact (a), quadratic (b) and linear volume fractions (c). (d): relative curvature deviation for exact and quadratic volume fractions; cf. note (5.3).

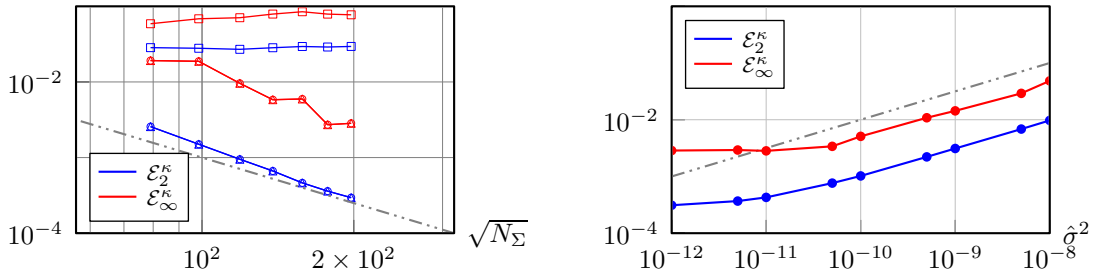


(a) $N_\mathcal{K} \in \{40, 50, \ldots, 100\}$, $\hat{\sigma}^2 = 0$

(b) $\hat{\sigma}^2 \in [10^{-12}, 10^{-8}]$, $N_\mathcal{K} = 100$

Figure 5.9.: Global errors $\mathcal{E}_2^\kappa$ and $\mathcal{E}_\infty^\kappa$ from eq. (5.19) as function of (a): number of intersected cells $N_\Sigma \approx 8N_\mathcal{K}^2$ for linear (□), quadratic (△) and exact (○) volume fractions and (b): additive noise variance from eq. (5.21) on quadratic volume fractions.

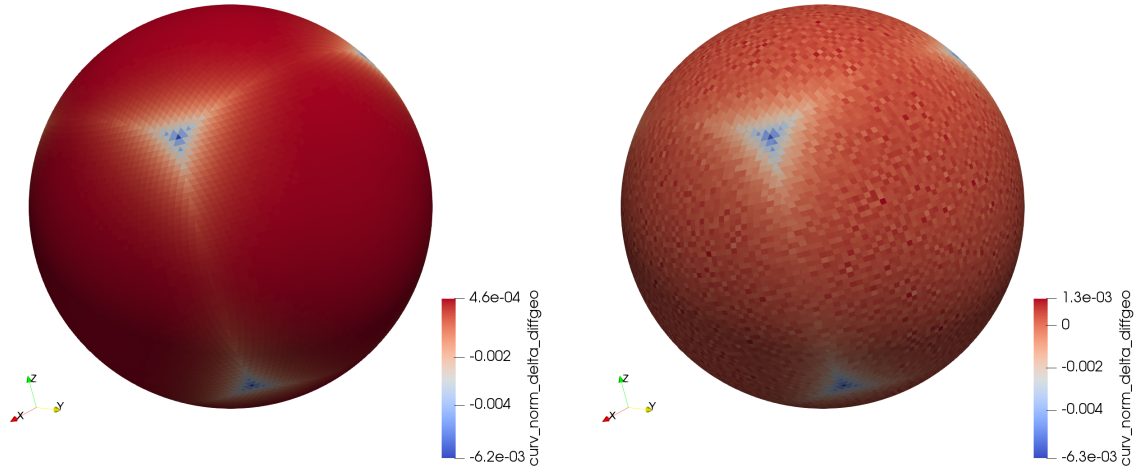


(a) $\hat{\sigma}^2 = 0$

(b) $\hat{\sigma}^2 = 10^{-12}$

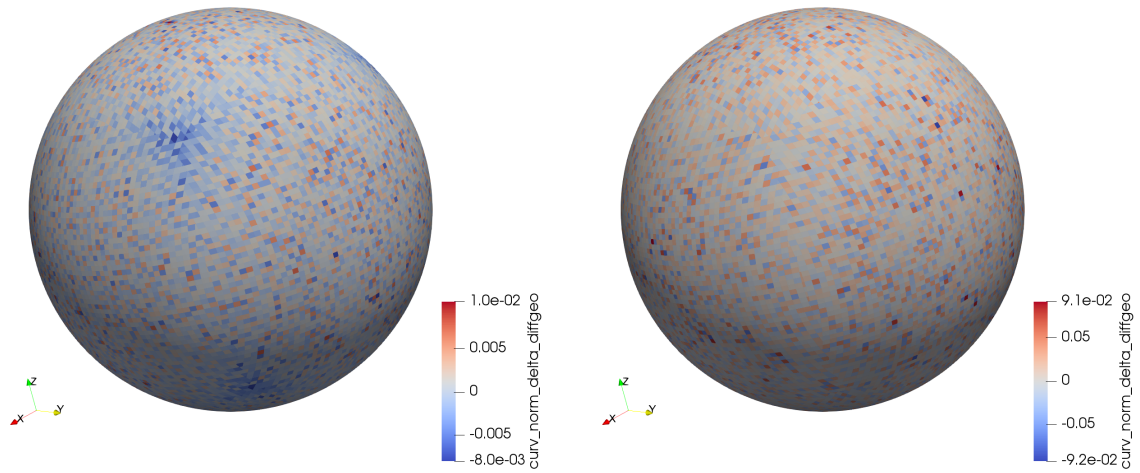


(c) $\hat{\sigma}^2 = 10^{-10}$

(d) $\hat{\sigma}^2 = 10^{-8}$

Figure 5.10.: Curvature error $\mathcal{E}_k^\kappa$ as function of noise variance for fixed spatial resolution; exemplified from fig. (5.9(b)). cf. note (5.3)).

**Statistical interrelations**

Considering the statistical interrelations of fig. (5.11) substantiates the conjectures from the findings above. The essential implications can be cast as follows:

1. The frequency of occurene in terms of intersected layers (center of left column in fig. (5.11)) approximately resembles a normal distribution, where most (29.07%) of the stencils contain 4 intersected layers.

2. For linear volume fractions, the average errors approximately resemble a normal distribution, where the largest values ($7.7 \times 10^{-2}$) occur for stencils with 3 (17) intersected layers (cells). The errors of the regions around the space diagonals (corresponding to $n_{\mathcal{S},\mathrm{l}} \in \{6,7\}/n_{\mathcal{S},\Sigma} > 22$) do not contribute significantly to the global error, since the average error is small and the share of the associated cells accumulates to approximately 7%. This supports the above conjecture that the volume fraction quality rather than the discretization scheme spoils the convergence.

3. For exact and quadratic volume fractions, the curvature error exhibits a positive correlation to the number of intersected cells/layers in the height function stencil. The average error (■ in fig. (5.11)) remains virtually constant for $n_{\mathcal{S},\mathrm{l}} \leq 4$ ($n_{\mathcal{S},\Sigma} \leq 17$), exhibits a minimum at $n_{\mathcal{S},\mathrm{l}} = 5$ ($n_{\mathcal{S},\Sigma} = 20$) and sharply increases for larger values. The spread of the 10%- and 90%-quantiles increases as $n_{\mathcal{S},\mathrm{l}}$ ($n_{\mathcal{S},\Sigma}$), where the largest values occur for the maximum number of intersected layers/cells. For $n_{\mathcal{S},\mathrm{l}} = 7$ ($n_{\mathcal{S},\Sigma} = 27$), the 90%-quantile covers roughly half of the error range, as can be seen from the top right graph in fig. (5.11). Recalling that only 1.74% of the cells are comprised, this implies that a minority of outliers account for a large portion of the error. This is in accordance with the theoretical predictions from above; cf figs. (5.6) and (5.7(c)).

### 5.4.2. Ellipsoids

The results for prolate and obalte ellipsoids differ systematically from those obtained for spheres. The findings are summarized as follows: There is a qualitative correspondence of the results obtained for prolate and oblate ellipsoids. Hence, the statements itemized below for the oblate ellipsoids hold for the prolate case in an analogous manner. In terms of algorithmic quantities, i.e. the number of intersected layers $n_{\mathcal{S},\mathrm{l}}$ and cells $n_{\mathcal{S},\Sigma}$, the patterns for the oblate ellipsoids are in qualitative agreement to those of the sphere, and, hence, will not be reported here; cf. fig. (5.7). Figure (5.12) shows that the second-order convergence of the $L_2$- and $L_\infty$-errors with spatial resolution is lost. While first-order convergence is obtained for quadratic volume fractions, the linear volume fractions seem to exhibit no convergence at all, which was also the case for spheres; cf. fig. (5.9(a)). In comparison to spheres, the global errors are increased by roughly one order of magnitude. The surface patterns of the errors are depicted in fig. (5.13). For quadratic volume fractions, the peaks at the space diagonals, which were prominent for spheres, are no longer present. The patterns found for both linear and quadratic volume fractions in fig. (5.13) resemble those of the sphere. However, the alternation between large positive and negative deviations between neighboring cells is only found in the linear case. The checkerboarding is also prominent in the regions close to the equator; cf. fig. (5.13(b)). Note that or $N_\mathcal{K} = 100$, the ratio of the absolute maxima between linear ($7.6 \times 10^{-2}$) and quadratic ($2.9 \times 10^{-2}$) volume fractions is approximately 2.62 (as compared to 27.5, cf. fig. (5.8)), i.e. the influence of the volume fraction quality is reduced by an order of magnitude.

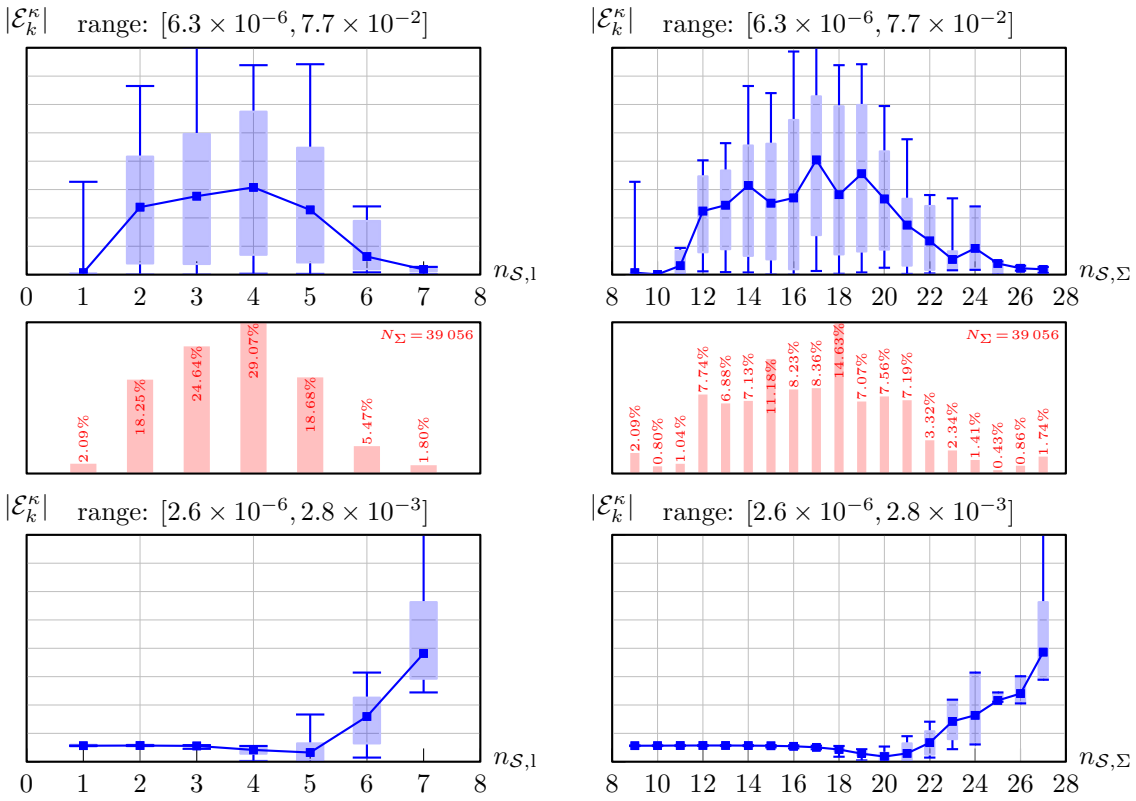


Figure 5.11.: Statistics for curvature errors from eq. (5.19) on sphere for linear (top row) and quadratic (bottom row) volume fractions as function of number of intersected layers (left column) and interface cells (right column); cf. note 5.4.

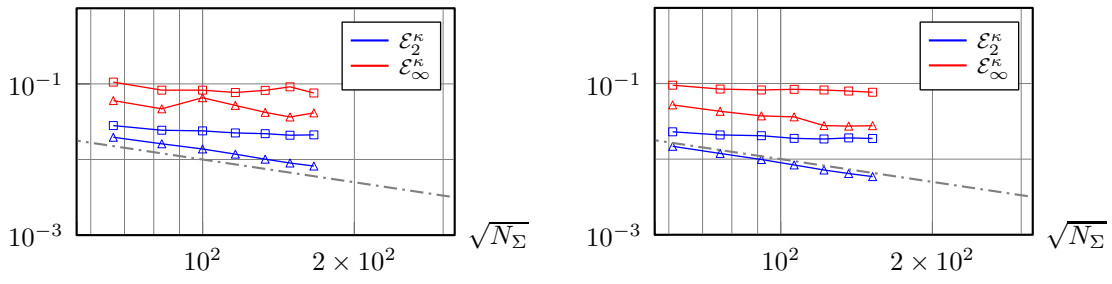


(a) semiaxes $(\frac{91}{100}, \frac{91}{100}, \frac{51}{100})$ (b) semiaxes $(\frac{91}{100}, \frac{71}{100}, \frac{51}{100})$

Figure 5.12.: Global errors $\mathcal{E}_2^\kappa$ and $\mathcal{E}_\infty^\kappa$ from eq. (5.19) as function of number of intersected cells $N_\Sigma$ ($N_\mathcal{K} \in \{40, 50, \ldots, 100\}$) for ellipsoids centered in $[-1, 1]^3$ with linear ($\square$) and quadratic ($\triangle$) volume fractions.

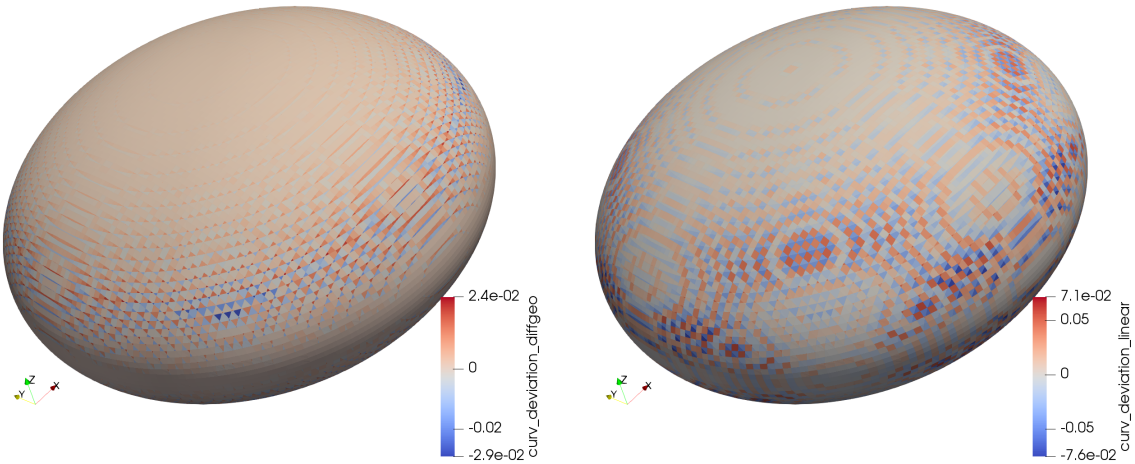


(a) quadratic (b) linear

Figure 5.13.: Surface patterns of curvature error $\mathcal{E}_k^\kappa$ from eq. (5.19) for quadratic (a) and linear volume fractions (b) for oblate ellipsoid with semiaxes $(\frac{91}{100}, \frac{91}{100}, \frac{51}{100})$; cf. note (5.3).

#### Statistical interrelations

Considering the statistical interrelations of fig. (5.14) supports the findings above. For quadratic volume fractions, there is a positive correlation between the number of intersected layers (cells) and the curvature error, indicating the influence of the volume fraction quality. This effect is not present for linear volume fractions, where the errors approximately admit a normal distribution. Furthermore, the deviation of the 90% quantiles from the respective maxima is largest for $2 \leq n_{\mathcal{S},\mathrm{l}} \leq 4$ ($12 \leq n_{\mathcal{S},\Sigma} \leq 18$), corresponding to the largest ratio of occurence, as can be seen from the center row in fig. (5.14). It is worth noting that, due to the larger curvatures, the maximum number of intersected layers and cells, respectively, is raised to 8 (compared to 7 for the spehre) and 30 (compared to 27 for the sphere); cf. fig. (5.11). However, for the quadratic case, the effect on the global error is negligible, since the number of these stencils accumulates to only 0.03% (0.15%). As an overall observation, it is evident that the deviation from spheres significantly reduces the accuracy of curvature estimates both for linear and quadratic volume fractions, despite the fact that the latter exhibit fourth-order convergence in terms of volume conservation; cf. section 4.6.

### 5.4.3. Perturbed spheres

The results for perturbed spheres sustain the findings from above, in the sense that the deviation from a sphere has a negative effect on the errors.

**Note 5.6** (Random parameters)**.** *For perturbed spheres given in eq. (2.18), the coefficients $\mathbf{c}_\Sigma$ are computed randomly following a normal distribution $\mathcal{N}(0, \hat{\sigma}^2)$; cf. section 1.3. However, the results presented within this subsection are robust with respect to the instances of $\mathbf{c}_\Sigma$ for fixed distribution variance $\hat{\sigma}^2$.*

Figure (5.15) plots the errors from eq. (5.19) as a function of the spatial resolution, exhibiting that

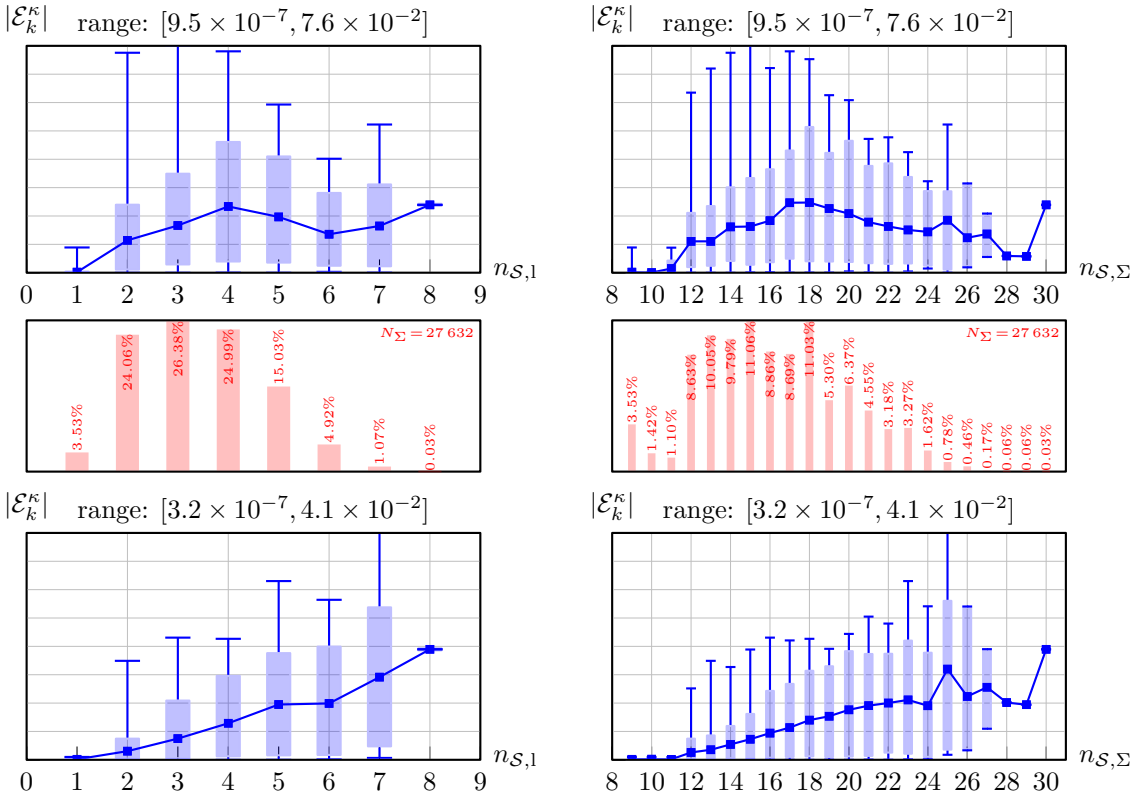


Figure 5.14.: Statistics for curvature errors from eq. (5.19) on oblate ellipsoid for linear (top row) and quadratic (bottom row) volume fractions as function of number of intersected layers (left column) and interface cells (right column); cf. note 5.4.

convergence is lost for both linear and quadratic volume fractions. For $L_\Sigma \in \{3, 6\}$, both $\mathcal{E}_2^\kappa$ and $\mathcal{E}_\infty^\kappa$ **diverge** with spatial resolution, irrespective of the volume fraction quality. The instance for $L_\Sigma = 9$ in fig. (5.15(c)), which behaves as $\mathcal{O}(1)$, is depicted to illustrate that, despite the robustness stated in note (5.6), divergence is not necessarily encountered. However, we would like to emphasize that convergence could not be obtained for perturbed spheres, i.e. $\mathcal{O}(1)$ is obtained at best. For fixed coefficient variance $\hat{\sigma}^2$, the error levels increase with the degree of the spherical haromonics from $\mathcal{O}(10^{-2})$ for $L_\Sigma = 3$ to $\mathcal{O}(10^{-1})$ for $L_\Sigma = 9$, where the values of $\mathcal{E}_2^\kappa$ are roughly one order of magnitude below $\mathcal{E}_\infty^\kappa$. Furthermore, the difference between the errors obtained from linear and quadratic volume fractions, respectively, decreases as $L_\Sigma$ increases: while for $L_\Sigma = 3$ the errors obtained from linear volume fractions are roughly one order of magnitude above the quadratic case, the curves virtually coincide for $L_\Sigma = 9$, with $L_\Sigma = 6$ resembling an intermediate state. This further substantiates the conjecture that the volume fraction quality becomes less significant with stronger deviation from the sphere.

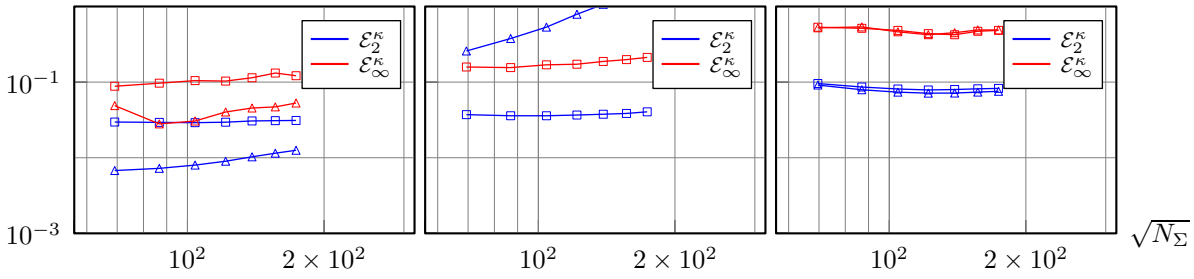


(a) $L_\Sigma = 3$ (b) $L_\Sigma = 6$ (c) $L_\Sigma = 9$

Figure 5.15.: Global errors $\mathcal{E}_2^\kappa$ and $\mathcal{E}_\infty^\kappa$ from eq. (5.19) as function of number of intersected cells $N_\Sigma$ (resulting from $N_\mathcal{K} \in \{40, 50, \ldots, 100\}$ for linear ($\square$) and quadratic ($\triangle$) volume fractions for perturbed sphere with $R_0 = \frac{4}{5}$ centered in $[-1, 1]^3$.

### Surface patterns

The surface patterns for the finest resolution ($N_\mathcal{K} = 100$) offer further insight, where their representative character was discussed in note (5.3). First, note that the respective bottom rows of figs. (5.16), (5.17) and (5.18) exhibit significant checkerboarding of the local curvature errors $\mathcal{E}_k^\kappa$, both for linear and quadratic volume fractions. Hence, the diminishment of the influence of volume fraction quality, as indicated by the ellipsoids above, is continued. The pattern difference obtained for linear and quadratic volume fractions becomes less significant for increasing order $L_\Sigma$. For the smallest order $L_\Sigma = 3$, i.e. if the hypersurface is nearly spherical, the patterns obtained for linear volume fractions (fig. (5.16(d))) are similar to those obtained for spheres; cf. fig. (5.8(c)). The quadratic volume fractions (fig. (5.16(c))), however, exhibit a checkerboard pattern which seems to be related neither to the CARTESIAN grid nor the algorithmic quantities given in fig. (5.16(b)); this visual conjecture is substantiated by the statistical analysis in fig. (5.19) below. The range of error magnitudes is $1.2 \times 10^{-1}$ for linear and $5.3 \times 10^{-2}$ for quadratic volume fractions, corresponding to a ratio of roughly 2. Hence, compared to the sphere (approx. 27.5), a significant reduction of the influence of the volume fraction quality is observed. This trend is continued for $L_\Sigma = 6$ (lin.: $2.1 \times 10^{-1}$, quad.: $1.6 \times 10^{-1}$) and $L_\Sigma = 9$ (lin.: $4.9 \times 10^{-1}$, quad.: $4.8 \times 10^{-1}$), corresponding to ratios of approx. 1.31 ($L_\Sigma = 6$) and 1 ($L_\Sigma = 9$), respectively. In other

words, for $L_\Sigma = 9$ the curvature errors obtained from linear and quadratic volume fractions are virtually coinciding, while the volume erros differ by approximately two orders of magnitude; cf. subsection 4.6.5. For the largest order under consideration here ($L_\Sigma = 9$), the difference of curvature errors induced by linear (fig. (5.18(d))) and quadratic (fig. (5.18(c))) volume fractions is barely visible. As before, a statistical arrangement of the underlying errors, given in figs. (5.20) and (5.21), affirms the aforementioned statements. Comparing the patterns of the errors in figs. (5.16(c)), figs. (5.17(c)) and figs. (5.18(c)) to those of $n_{\mathcal{S},\Sigma}$ (number of intersected cells in the corresponding stencil) in figs. (5.16(b)), figs. (5.17(b)) and figs. (5.18(b)), respectively, suggests a correlation of the aforementioned quantities. For the orders $L_\Sigma \in \{3, 6, 9\}$ considered here, the region around the north pole respectively features concentric ring-shaped shells, within which $n_{\mathcal{S},\Sigma}$ varies slightly, wheres the variation between shells is comparatively large. Visual inspection suggests that the checkerboard structure of the curvature errors is related to the gradient of $n_{\mathcal{S},\Sigma}$. However, a comparison of the minimum and maximum of $n_{\mathcal{S}_k,\Sigma}$ in the $3 \times 3$-neighborhood of the respective cell, which can be considered as an approximation to the aforementioned gradient, did not support this conjecture; cf. fig. (B.1) in the appendix.

#### Statistical interrelations

In terms of statistical interrelations, the implications of figs. (5.19) to (5.21) can be summarized as follows: the influence of the volume fraction quality is diminished for increasing order $L_\Sigma$. For linear volume fractions, the average error (■ in fig. (5.19)) becomes largest for $n_{\mathcal{S},\mathrm{l}} = 4$ ($L_\Sigma = 3$) and $n_{\mathcal{S},\mathrm{l}} = 3$ ($L_\Sigma = 6$), but is virtually independent of $n_{\mathcal{S},\mathrm{l}}$ for $L_\Sigma = 9$. Analagous observations hold for quadratic volume fractions. Also, it is worth noting that the spread between the 90% quantile, indicated by the upper end of the shaded boxes, and the maximum, indicated by the whisker, increases with $L_\Sigma$. For $L_\Sigma = 9$, the 90% quantile is virtually independent of $n_{\mathcal{S},\mathrm{l}}$. Lastly, for all orders $L_\Sigma \in \{3, 6, 9\}$, the peak of the error range is reached for $16 \leq n_{\mathcal{S},\Sigma} \leq 20$, further indicating that the spoilage of convergence is caused by the volume fraction quality rather than the discretization scheme.

#### Comparison of hypersurface position

In order to further investigate the source of the checkerboard patterns, fig. (5.22) compares the nodes $\boldsymbol{x}_{u,v} = [x_u, y_v, h_{u,v}]^\mathsf{T}$ induced by the graph representation of the hypersurface. In fig. (5.22(a)), the heights correspond to the exact values, i.e. $\boldsymbol{x}_{u,v} \in \Sigma$, whereas the heights in fig. (5.22(b)) correspond to $\bar{h}_{u,v}$, i.e. they are obtained from the summation of the volume fractions, cf. eq. (5.4). Note that the relative deviation, plotted in fig. (5.22(c)), is of order $\mathcal{O}(10^{-4})$.

**Note 5.7** (Normalization)**.** *Let us not in passing that, due to the vicinity to the north pole, the heights depicted in fig. (5.22) are of the same order as the referential radius $R_0$, i.e. the relative deviation is in accordance with the volume errors reported in subsection 4.6.5.*

However, there is noise of frequency $\sim \Delta x^{-1}$, leading to substantial amplification when applying finite difference operators, and, in fact, causing the divergence shown in fig. (5.15). This finding once more supports the conjecture that convergence of curvature errors is not only governed by the quality of the volume fractions in the sense of volume accuracy.

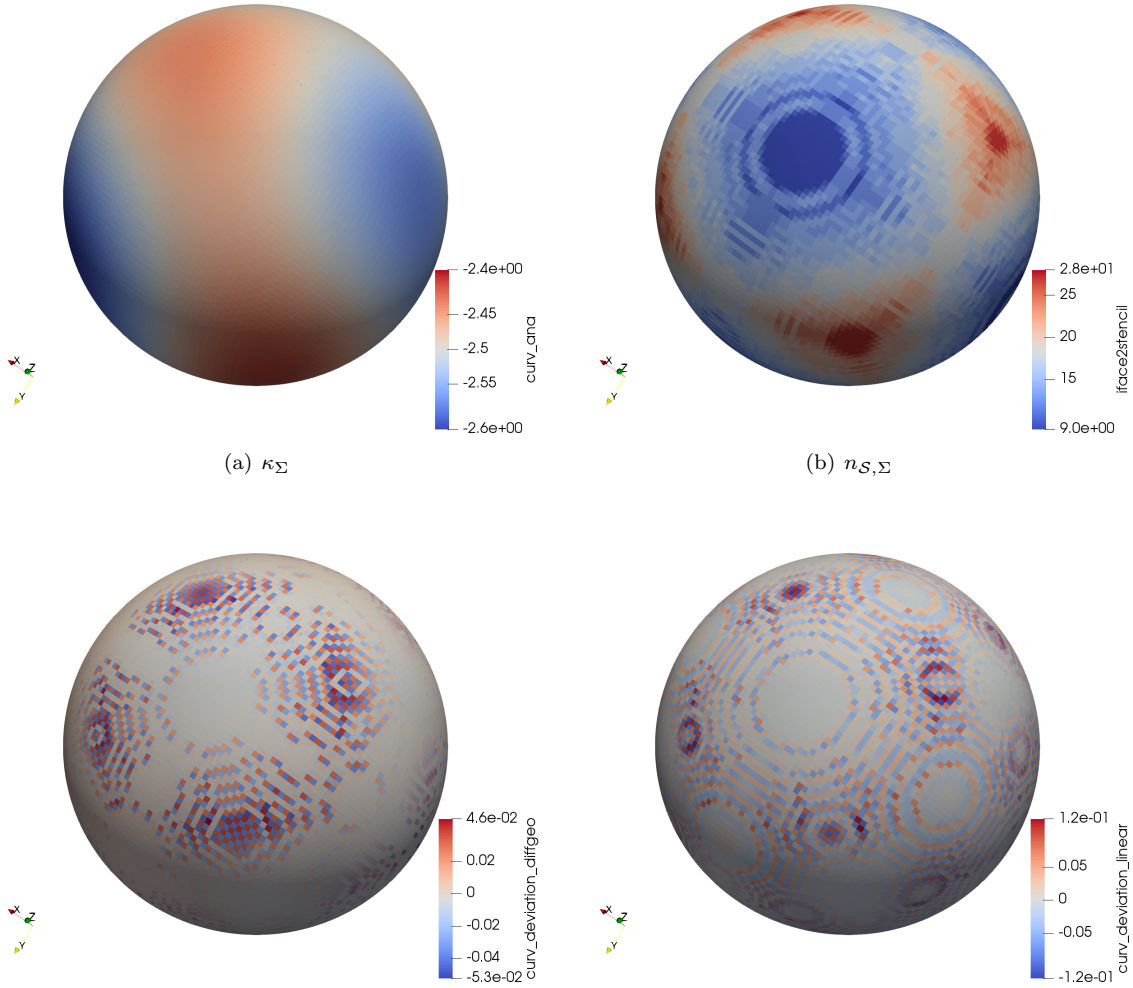


(a) $\kappa_\Sigma$ (b) $n_{\mathcal{S},\Sigma}$

(c) quadratic ($\mathcal{E}_k^\kappa$) (d) linear ($\mathcal{E}_k^\kappa$)

Figure 5.16.: Surface patterns for linear and quadratic volume fractions for perturbed sphere ($R_0 = \frac{4}{5}$, $L_\Sigma = 3$, $\hat{\sigma}^2 = 10^{-4}$, $N_\mathcal{K} = 100$, $\mathcal{K} = [-1, 1]^3$).

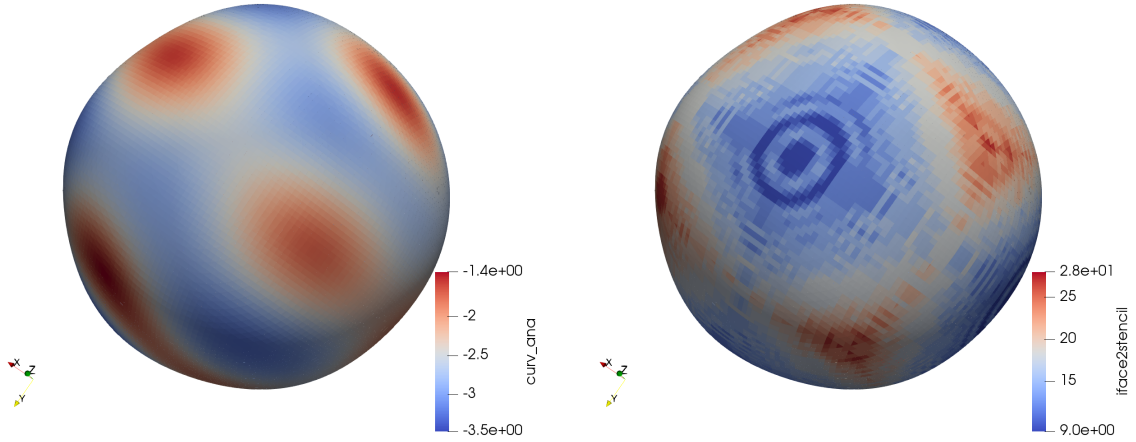


(a) $\kappa_\Sigma$ (b) $n_{\mathcal{S},\Sigma}$

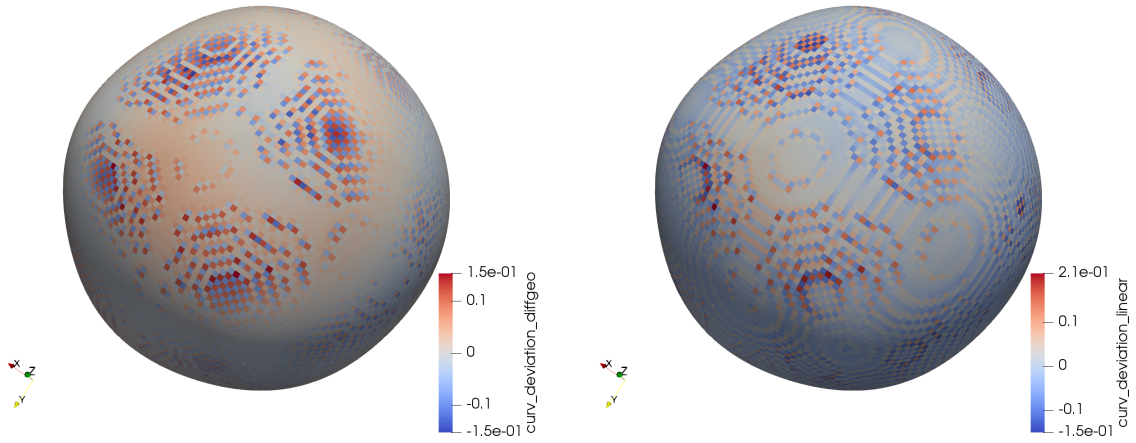


(c) quadratic (d) linear

Figure 5.17.: Surface patterns for linear and quadratic volume fractions for perturbed sphere ($R_0 = \frac{4}{5}$, $L_\Sigma = 6$, $\hat{\sigma}^2 = 10^{-4}$, $N_\mathcal{K} = 100$, $\mathcal{K} = [-1, 1]^3$).

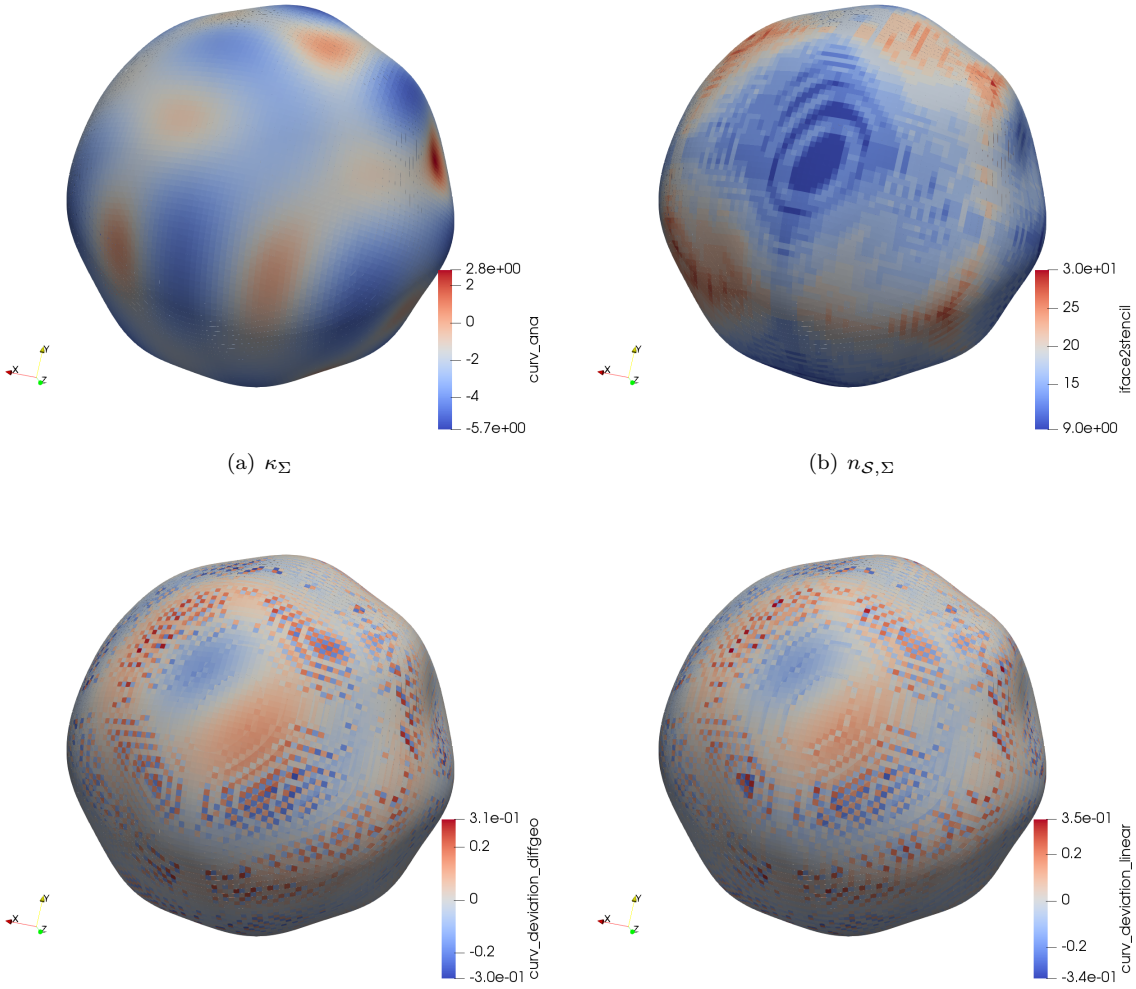


(a) $\kappa_\Sigma$ (b) $n_{\mathcal{S},\Sigma}$

(c) quadratic (d) linear

Figure 5.18.: Surface patterns for linear and quadratic volume fractions for perturbed sphere ($R_0 = \frac{4}{5}$, $L_\Sigma = 9$, $\hat{\sigma}^2 = 10^{-4}$, $N_\mathcal{K} = 100$, $\mathcal{K} = [-1, 1]^3$).

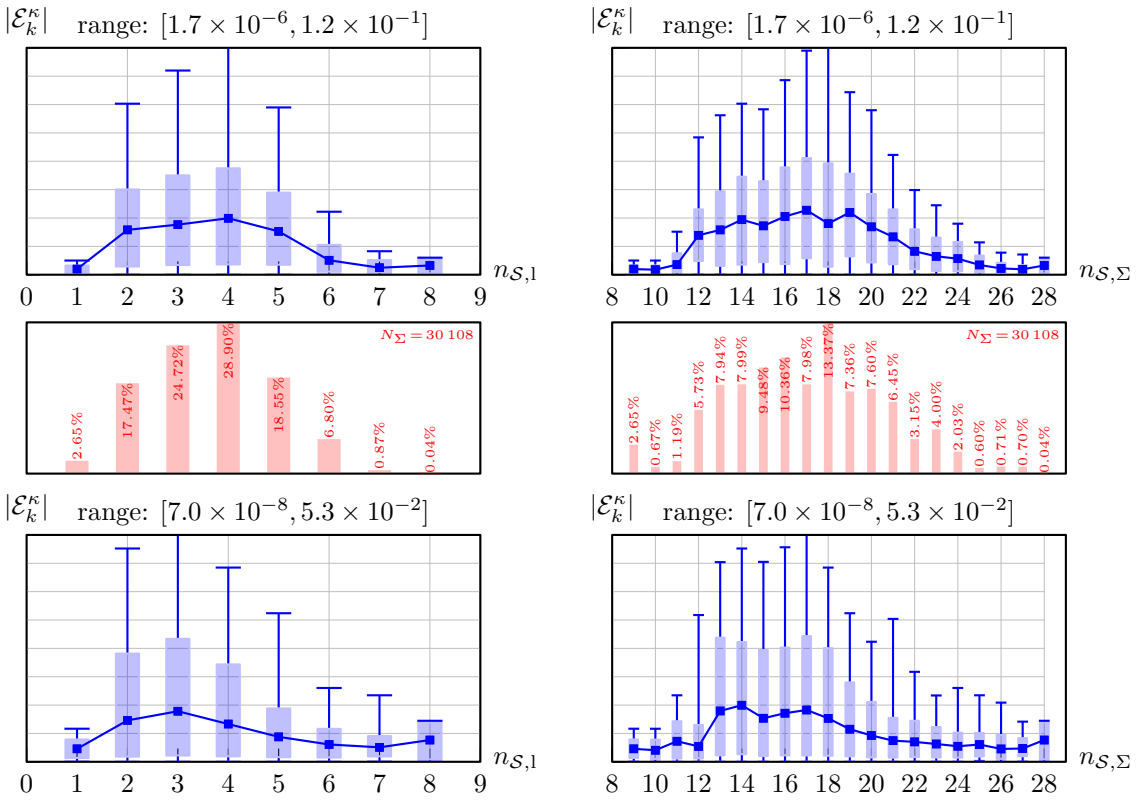


Figure 5.19.: Statistics for curvature errors from eq. (5.19) on perturbed sphere ($L_\Sigma = 3$, $\hat{\sigma}^2 = 10^{-4}$) for different volume fraction qualities as function of number of layers (left column) and interface cells (right column); cf. note 5.4.

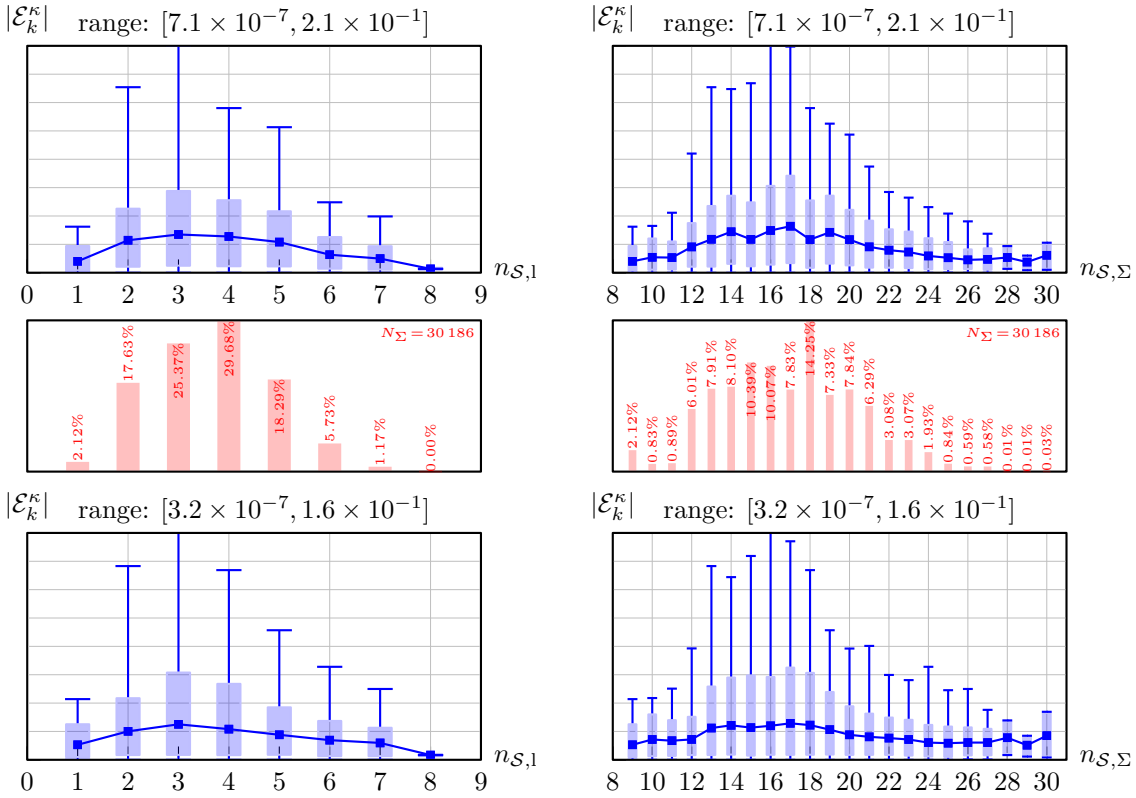


Figure 5.20.: Statistics for curvature errors from eq. (5.19) on perturbed sphere ($L_\Sigma = 6$, $\hat{\sigma}^2 = 10^{-4}$) for different volume fraction qualities as function of number of layers (left column) and interface cells (right column); cf. note 5.4.

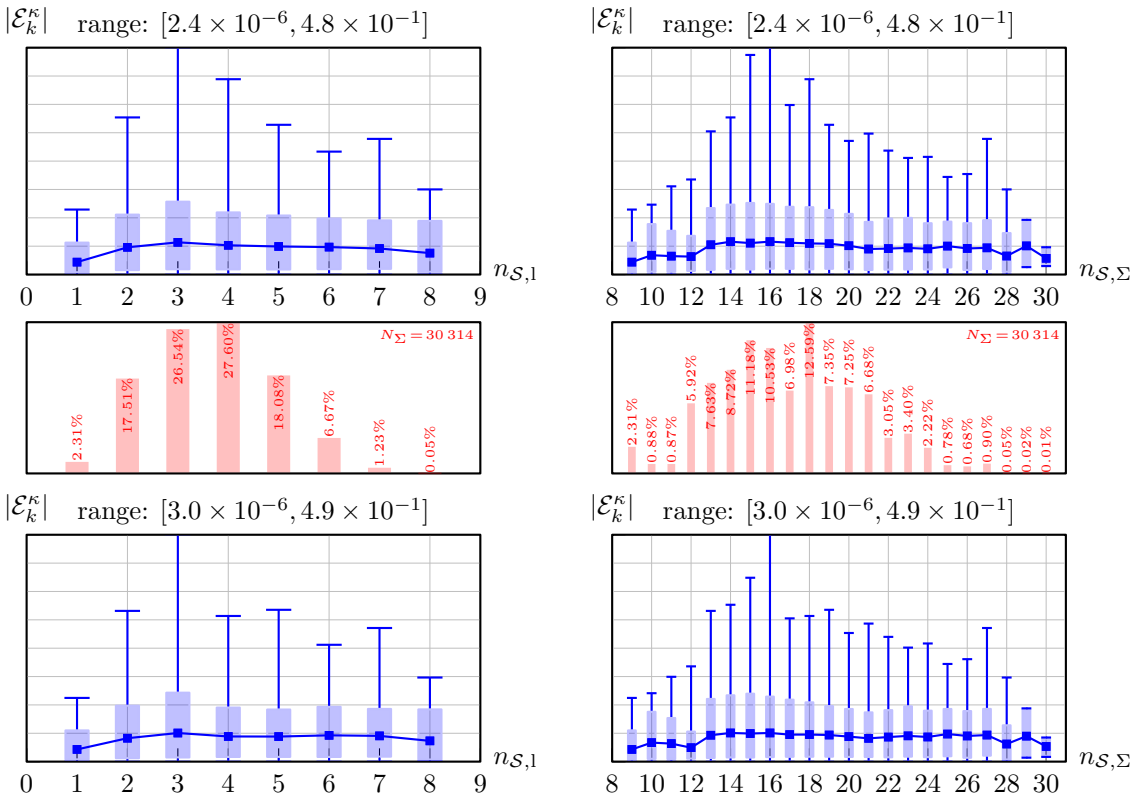


Figure 5.21.: Statistics for curvature errors from eq. (5.19) on perturbed sphere ($L_\Sigma = 9$, $\hat{\sigma}^2 = 10^{-4}$) for different volume fraction qualities as function of number of layers (left column) and interface cells (right column); cf. note 5.4.

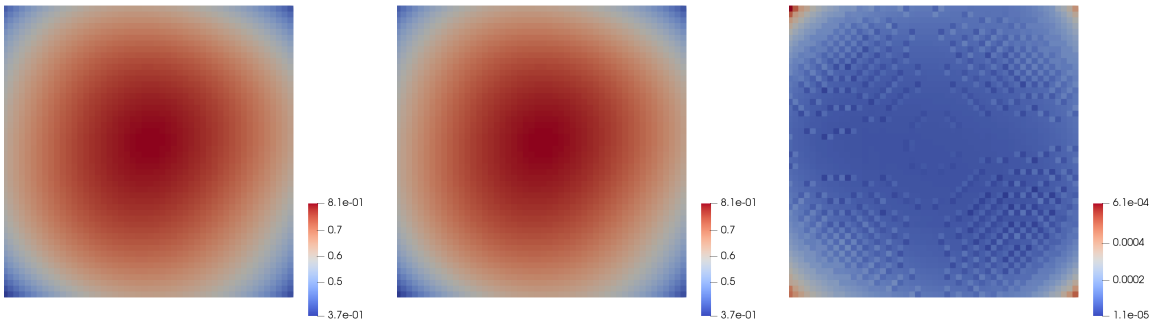


(a) $h_\Sigma(x_u, y_v)$ (b) $\bar{h}_{u,v}$ (c) $1 - \frac{\bar{h}_{u,v}}{h_\Sigma(x_u, y_v)}$

Figure 5.22.: Comparison of heights $\bar{h}_{u,v}$ from volume fractions (cf. eq. (5.4)) and analytical values $h_\Sigma(x_u, y_v)$ at corresponding stencil center $(x_u, y_v)$ for perturbed sphere ($R_0 = \frac{4}{5}$, $L_\Sigma = 6$, $\hat{\sigma}^2 = 10^{-4}$) centered in $[-1, 1]^3$ with $N_\mathcal{K} = 100$. The segment of the hypersurface corresponds to the region around the north pole in fig. (5.17).

### 5.4.4. Dispersion

Figure (5.23) depicts the statistical dispersion

$$D_m = \sqrt{\frac{\frac{1}{m}\sum_{k=1}^{m}\mathcal{E}_k^\kappa}{\frac{1}{N_\Sigma}\sum_{k=1}^{N_\Sigma}\mathcal{E}_k^\kappa}} \qquad \text{with} \qquad \mathcal{E}_k^\kappa \leq \mathcal{E}_{k+1}^\kappa \tag{5.23}$$

of the curvature errors over the normalized number of interface cells, corresponding to an accumulated version of the data in fig. (5.11), fig. (5.14) and figs. (5.19) to (5.21). Note the similarity to the Gini coefficient, being a very common measure for wealth distribution in econometrics. The interpretation is as follows: the dashed line marks an equal distribution of error contributions, i.e. the case where every cell provides an equal share of the total error, which also implies the absence of surface patterns; cf. fig. (5.10). A curve below the dashed line indicates that a smaller fraction of the cells accounts for a larger fraction of the error, and vice versa.

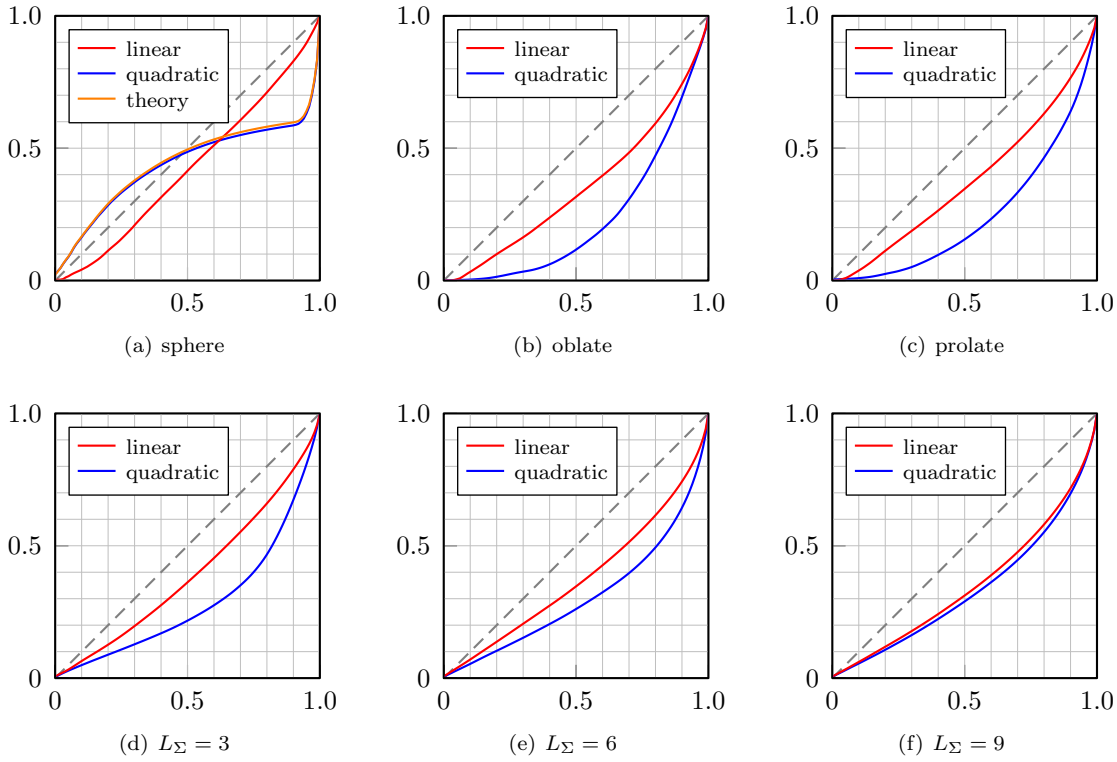


(a) sphere (b) oblate (c) prolate

(d) $L_\Sigma = 3$ (e) $L_\Sigma = 6$ (f) $L_\Sigma = 9$

Figure 5.23.: Dispersion $D_m \in [0, 1]$ from eq. (5.23) of curvature errors over normalized number of intersected cells $\frac{m}{N_\Sigma}$ for ellipsoids and perturbed spheres ($R_0 = \frac{4}{5}$, $\hat{\sigma}^2 = 10^{-4}$) at $N_\mathcal{K} = 100$.

In the case of spheres (fig. (5.23(a))), note that for quadratic volume fractions about 90% of the cells account for only 60% of the accumulated error, whereas for linear volume fractions the same relative error contribution is caused by 62% of the cells. The first 50% of the cells show a below-average contribution to the total error. For ellipsoids and perturbed spheres, note that roughly 20% of the cells accumulate the upper 50% of the total curvature error in the case of quadratic volume fractions, indicating that only

a small fraction of the cells is spoiling the convergence. This is in accordance with the findings of the statistical implications of figs. (5.19) to (5.21). For both, ellipsoids (figs. (5.23(b))-(c)) and perturbed spheres (figs. (5.23(d))-(f)), the dispersion is always below the dashed line.

## 5.5. A tangential paraboloid fit

Let $\{\boldsymbol{x}_k\}_{k=1}^{N_S}$ be a set of nodes which we assume to locally represent the hypersurface $\Gamma$, to which we seek to fit a tangential paraboloid

$$\Gamma = \left\{ \boldsymbol{t} \in \mathbb{R}^2 : \boldsymbol{x}_0 + t_1\boldsymbol{\tau}_1 + t_2\boldsymbol{\tau}_2 + \frac{\boldsymbol{t}^\mathsf{T}\boldsymbol{\kappa}_0\boldsymbol{t}}{2}\boldsymbol{n}_0 \right\}, \tag{5.24}$$

where $\boldsymbol{x}_0$ and $\boldsymbol{\kappa}_0$ respectively denote the base point and curvature tensor. The choice of this class of hypersurfaces is motivated by differential geometry and corresponds, for that reason, to the class of hypersurfaces employed for the computation of volume fractions; cf. chapter 4. Figure (5.24) illustrates the concept in two spatial dimensions. Formal convenience suggests to represent the orthonormal basis $\{\boldsymbol{\tau}_1, \boldsymbol{\tau}_2, \boldsymbol{n}_0\}$ in spherical coordinates. For ease of notation let $\boldsymbol{T} := [\boldsymbol{\tau}_1, \boldsymbol{\tau}_2]$ to obtain

$$\boldsymbol{n}_0 := \begin{bmatrix} \cos\varphi_0 \sin\theta_0 \\ \sin\varphi_0 \sin\theta_0 \\ \cos\theta_0 \end{bmatrix} \quad \text{and} \quad \boldsymbol{T} := \begin{bmatrix} -\sin\varphi_0 & \cos\varphi_0\cos\theta_0 \\ \cos\varphi_0 & \sin\varphi_0\cos\theta_0 \\ 0 & -\sin\theta_0 \end{bmatrix}. \tag{5.25}$$

Note that the tangential coordinates $\boldsymbol{t}$ in eq. (5.24) are obtained by $\boldsymbol{t} = \boldsymbol{T}^\mathsf{T}(\boldsymbol{x} - \boldsymbol{x}_0)$. The base curvature tensor $\boldsymbol{\kappa}_0$ exhibits three invariants corresponding to the principal curvatures $\kappa_i$ and the angular orientation of the principal directions of curvature $\psi$ with respect to $\boldsymbol{\tau}_i$, i.e.

$$\boldsymbol{\kappa}_0 := \begin{bmatrix} \kappa_{20} & \frac{\kappa_{11}}{2} \\ \frac{\kappa_{11}}{2} & \kappa_{02} \end{bmatrix} = \begin{bmatrix} \cos\psi & \sin\psi \\ -\sin\psi & \cos\psi \end{bmatrix} \begin{bmatrix} \kappa_1 & 0 \\ 0 & \kappa_2 \end{bmatrix} \begin{bmatrix} \cos\psi & -\sin\psi \\ \sin\psi & \cos\psi \end{bmatrix}, \tag{5.26}$$

where, in terms of numerical robustness, it is advantageous to choose the first alternative in eq. (5.26), rather than expanding the matrix product. An equivalent representation of the paraboloid $\Gamma$ from eq. (5.24) is obtained from the zero iso-contour of its level-set, i.e.

$$\phi_\Gamma(\boldsymbol{x};\boldsymbol{p}) = (\boldsymbol{x} - \boldsymbol{x}_0)^\mathsf{T}\boldsymbol{T}\boldsymbol{\kappa}_0\boldsymbol{T}^\mathsf{T}(\boldsymbol{x} - \boldsymbol{x}_0) - \langle \boldsymbol{x} - \boldsymbol{x}_0, \boldsymbol{n}_0 \rangle = \langle \boldsymbol{t}, \boldsymbol{t} \rangle_{\boldsymbol{\kappa}_0} - \langle \boldsymbol{x} - \boldsymbol{x}_0, \boldsymbol{n}_0 \rangle. \tag{5.27}$$

Gathering the sought parameters in

$$\boldsymbol{p} = [\boldsymbol{x}_0, \varphi_0, \theta_0, \kappa_{20}, \kappa_{11}, \kappa_{02}]^\mathsf{T}, \tag{5.28}$$

we seek to minimize the weighted sum of the squared level-sets of $\{\boldsymbol{x}_k\}_k^{N_S}$, i.e.

$$\mathcal{E}(\boldsymbol{p}) = \frac{1}{2N}\sum_{k=1}^{N_S} \omega_k \left( \phi_\Gamma^2(\boldsymbol{x};\boldsymbol{p}) + \mathcal{R}^2(\boldsymbol{x};\boldsymbol{p}) \right), \tag{5.29}$$

with positive weights $\omega_k$. The regularizer

$$\mathcal{R}(\boldsymbol{x};\boldsymbol{p}) = \langle \boldsymbol{T}^\mathsf{T}(\boldsymbol{x}-\boldsymbol{x}_0), \boldsymbol{T}^\mathsf{T}(\boldsymbol{x}-\boldsymbol{x}_0)\rangle = \langle \boldsymbol{t}, \boldsymbol{t}\rangle \tag{5.30}$$

is required to resolve the ill-posedness of the minimization problem in eq. (5.29).

**Note 5.8** (Ill-posedness of the minimization problem.)**.** *Let $\{\boldsymbol{x}_k\}_k^{N_\mathcal{S}}$ be a coplanar set with normal, say, $\boldsymbol{n}_0$. The (degenerate) paraboloid minimizing eq. (5.29) obviously is a plane, corresponding to $\boldsymbol{\kappa}_0 = \boldsymbol{0}$. However, any base point $\boldsymbol{x}_0$ sufficing $\langle \boldsymbol{x}_k - \boldsymbol{x}_0, \boldsymbol{n}_0\rangle = 0$ implies that $\mathcal{E}(\boldsymbol{p}) \equiv 0$ in the absence of $\mathcal{R}$.*

Since $\mathcal{R}(\boldsymbol{x}_0;\boldsymbol{p}) = 0$ and $\mathcal{R}(\boldsymbol{x};\boldsymbol{p}) > 0$ for $\boldsymbol{x} \neq \boldsymbol{x}_0$, the effect of the regularizer consists in minimizing the variance of the projected nodes $\boldsymbol{t}_k = \boldsymbol{T}^\mathsf{T}(\boldsymbol{x}_k - \boldsymbol{x}_0)$. Figure (5.24(a)) and (5.24(b)) illustrate the concept. However, it is worth noting that the tangential projector $\boldsymbol{T}$, and hence the regularizer $\mathcal{R}$, depend on the base normal $\boldsymbol{n}_0$ of the paraboloid. Therefore, the aforementioned effect is only present if $\boldsymbol{p}$ is close to the minimum, as can be seen from fig. (5.24(c)). Within the scope of this work, we have found that carefully computed initial values $\boldsymbol{p}_0$, which are given below, ensure the desired behaviour. Due to the non-linearity

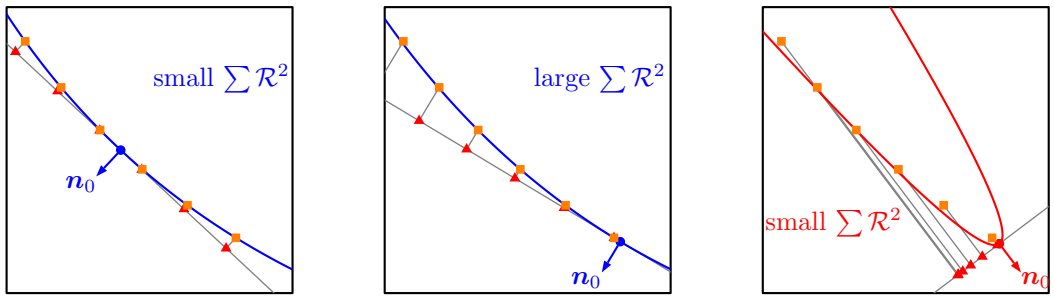


(a) (b) (c)

Figure 5.24.: Variance captured by the regularizer $\mathcal{R}$ in eq. (5.29) with nodes $\boldsymbol{x}_k$ (■) and tangential projections (▲) onto the respective basis.

of eq. (5.29) with respect to the sought parameters $\boldsymbol{p}$, a NEWTON algorithm, with an implementation analogous to alg. (1), is employed. Given some $\boldsymbol{p}_0$, one iteratively computes

$$\boldsymbol{p}_{n+1} = \boldsymbol{p}_n - \left[\nabla^2\mathcal{E}(\boldsymbol{p}_n)\right]^{-1} \nabla\mathcal{E}(\boldsymbol{p}_n). \tag{5.31}$$

Here, $\nabla$ and $\nabla^2$ denote, respectively, the gradient and HESSIAN with respect to $\boldsymbol{p}$. One obtains

$$\begin{aligned} \nabla\mathcal{E}(\boldsymbol{p}) &= \frac{1}{N_\mathcal{S}} \sum_{k=1}^{N_\mathcal{S}} \omega_k \left[\phi_\Gamma \nabla\phi_\Gamma + \omega_k \mathcal{R}\nabla\mathcal{R}\right](\boldsymbol{x}_k;\boldsymbol{p}) \quad \text{and} \\ \nabla^2\mathcal{E}(\boldsymbol{p}) &= \frac{1}{N_\mathcal{S}} \sum_{k=1}^{N_\mathcal{S}} \omega_k \left[\phi_\Gamma \nabla^2\phi_\Gamma + \nabla\phi_\Gamma \otimes \nabla\phi_\Gamma + \mathcal{R}\nabla^2\mathcal{R} + \nabla\mathcal{R} \otimes \nabla\mathcal{R}\right](\boldsymbol{x}_k;\boldsymbol{p}). \end{aligned} \tag{5.32}$$

The initial vector $\boldsymbol{p}_0$ is composed by the centroid of the nodes $\boldsymbol{x}_0 = \frac{1}{N_\mathcal{S}} \sum_{k=1}^{N_\mathcal{S}} \boldsymbol{x}_k$, zero curvature $\boldsymbol{\kappa}_0 = \boldsymbol{0}$

and a base normal corresponding to the first principal direction of $\{\boldsymbol{x}_k\}_{k=1}^{N_S}$, i.e. the eigenvector of the covariance matrix with the smallest associated eigenvalues; cf. section 3.3. Equation (5.24) implies that $\Gamma(\boldsymbol{n}_0, \boldsymbol{\kappa}_0) = \Gamma(-\boldsymbol{n}_0, -\boldsymbol{\kappa}_0)$, resembling the fact that the sign of the principal curvatures depends on the normal orientation. To remove this ambiguity, the gradient of the underlying volume fraction field provides a referential orientation. In what follows, some preliminary numerical experiments are conducted which help to assess the potential of the presented algorithm. Figure (5.25) compares the relative curvature deviation from eq. (5.19) to the results of the height function algorithm provided in secton 5.4. The set of nodes used for the tangential fit is composed of the union of the nodes produced by the height function algorithm, which are transferred to a common frame of reference. Despite preliminary imple-

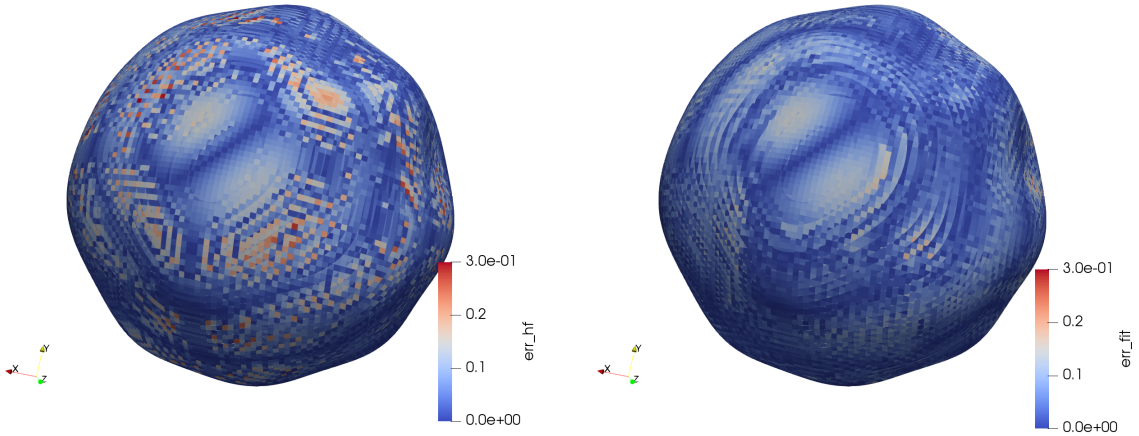


(a) height function

(b) tangential paraboloid fit

Figure 5.25.: Comparison of curvature errors from height function (corresponding to fig. (5.18)) and tangential paraboloid fit for perturbed sphere ($R_0 = \frac{4}{5}$, $L_\Sigma = 9$, $\hat{\sigma}^2 = 10^{-4}$) centered in $[-1, 1]^3$ with $N_\mathcal{K} = 100$.

mentation, the paraboloid fit outperforms the height function algorithm in terms of error magnitudes. As can be seen from fig. (5.25(b)), the tangential fit significantly reduces the checkerboard patters produced by the height function algorithm. Especially, the alternation between large positive and negative deviations is diminished. However, visual inspection of the curvature fields obtained from fitting exhibits that erroneous roughness still remains, hence substantiating the need for further sophistication of curvature computation.

## 5.6. Conclusion

The present chapter has investigated the performance of the height function method in a level of detail previously not available in the literature, where we have considered the influence of volume fraction quality for spheres, ellipsoids and perturbed spheres. Besides the commonly reported global error measures, an in-depth analysis of local quantities accompanied by statistical interrelations was provided. The main conclusions are summarized as follows:

1. An analytical expression for the referential curvature deviation for **spheres** was derived in sec-

tion 5.3, substantiating the second-order convergence of both $L_2$- and $L_\infty$-type error for sufficiently accurate volume fractions. The predicted deviations are reproduced both qualitatively and quantitatively by any appropriate implementation of the height function method, producing distinct symmetric patterns.

2. Numerical experiments provided in section 5.4 indicate that, for **ellipsoids**, the order of convergence is reduced to one, where the characteristic patters observed for spheres are lost. For perturbed spheres, no convergence with spatial resolution could be obtained. This effect was identified to be caused by *relative* height oscillations of small amplitude ($\sim 10^{-4}$) and wavelength $\sim \Delta x$.

3. For non-spherical hypersurfaces, the statistical patterns of linear and quadratic volume fractions exhibit similarities, indicating that **accurate volume fractions** (in the sense of volume conservation) alone are **not sufficient** to obtain second-order convergence.

4. The results obtained by the tangential paraboloid fitting method introduced in section 5.5 indicate the suitability of integral methods of curvature computation, i.e. methods avoiding numerical differentiation. An additional advantage of the presented approach is that the curvature and normal are consistent in the sense that they belong to the same hypersurface. The results of Renardy and Renardy [116] point in the same direction.

# 6. Global linear stability analysis

The prediction of the shapes and paths of fluid particles rising freely under the influence of gravity has been subject of investigation for quite some time, cf., e.g., the book of Clift et al. [32].

The non-linear character of the NAVIER-STOKES equations causes chaotic behavoir (see, e.g., Kida et al. [76]), implying that even a slight variation of relevant flow parameters, like particle volume or density/viscosity ratio, may result in a fundamental change of the flow characteristics. The transition of paths and shapes discussed in section 3.4 forms a prominent example. Establishing an understanding of the mechanisms behind these regime transitions is crucial for many technical applications, covering e.g., meteorology, combustion, and heat/mass transfer processes in bubble columns. However, due to the sensitivity of the underlying flows with respect to interferences, experimental assessment, if possible at all, is notoriously difficult. On the other hand, a numerical investigation inherently allows to obtain local quantities, e.g., velocities or deformations, without interfering with the evolution of the flow.

The aim of this chapter is the design of an algorithm that is capable of extracting the leading eigenvalues of flows involving deformable particles embedded in an ambient fluid in three spatial dimensions. Albert et al. [4], for their part building on Chiba [29], have introduced an analogous algorithm for falling films in two spatial dimensions, hence, the present chapter resembles an extension of their work. However, let us note in passing that the transition from two to three spatial dimensions is highly non-trivial for several reasons. While the fundamental concept of the stability analysis of Albert et al. [4] remains unchanged, the mathematical complexity induced by the consideration of closed hypersurfaces, e.g., in terms of volume conservation, significantly increases. Furthermore, the fact that, on CARTESIAN grids, closed hypersurfaces lack a global graph parametrization introduces numerical artifacts, such as the immanent spatial structure of curvature errors shown in chapter 5. For capillary flows, i.e. when surface tension effects are of key importance, this is especially disadvantageous.

**Note 6.1** (Conceptual differences)**.** *In fact, there are two major differences to the falling film setup in the work of Albert et al. [4]:*

1. *The flow down an inclinded plane yields topological configurations of interfaces that can be globally parametrized as a graph over the aforementioned plane. As discussed in section 5.2, these circumstances are beneficial for the application of the height function algorithm and allow exploiting its full potential. Also, for small perturbations of the steady state, the dominant component of the velocity and, hence, of the geometrically split transport of the volume fractions (cf. fig. (3.3)), is parallel to the plane. Provided sufficiently accurate initial volume fractions, this further reduces the errors of curvature estimation.*

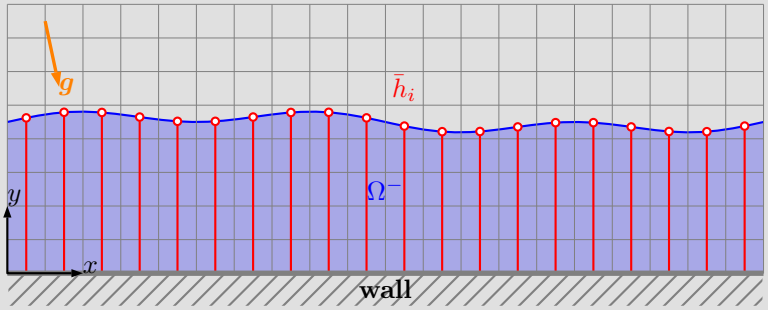


2. *The frame of reference is attached to the inclined plane and, hence, spatially fixed. Considering the topological configuration discussed above, the latter implies that the representation of the interface* $\Sigma$ *in the state vector* $\boldsymbol{\chi} := (\boldsymbol{u}, \boldsymbol{c}_\Sigma)$ *may resort directly to the average heights, i.e.* $\boldsymbol{c}_\Sigma = \{\bar{h}_i\}$*. Thus, the state vector is in consistence with the volume fractions, in the sense that they belong to the same geometrical representation of* $\Sigma$*. Furthermore, the global graph parametrization implies a linear volume (or, in two spatial dimensions, area) operator, since* $|\Omega^-| = \int_0^{\hat{x}} h(x)\mathrm{d}x \approx \sum_{i=1}^{N} \bar{h}_i \Delta x_i$*.*

   *In the context of an otherwise* Cartesian *discretization, however, a parametrization of* $\Sigma$ *in spherical coordinates, which is advantageous for particles, does not admit such an assignment. As a consequence, the representation of* $\Sigma$ *within* $\boldsymbol{\chi}$ *requires a projection, say, onto the space of coefficient vectors describing perturbed spheres of order* $L_\Sigma$*; cf. eq. (2.18) and section 3.2. Unless* $L_\Sigma$ *is chosen very large, which features a significant increment of computational expenses along with numerical difficulties, this projection smoothes those interface perturbations with high spatial frequencies; cf. Homes and Featherstone [68].*

The remainder of this chapter is organized as follows: section 6.1 commences by conducting a review of the relevant literature contributions and locating the present approach in the field of stability analysis. Subsequently, section 6.2 provides the mathematical foundations, where a special focus is put on the connection to the numerical flow solver FS3D; cf. chapter 3. Subsections 6.2.1 and 6.2.2 extend the mathematical formulation by covering the design of an appropriate phase space and a domain transformation, which accounts for the freely deformable interface $\Sigma$. Before section 6.4 outlines the concrete numerical implementation of the algorithm, it is crucial to understand the concept of the so-called *eigenvalue problem*. Hence, section 6.3 establishes the relevant ideas and assesses the method of Arnoldi by investigating an artificial problem. Section 6.5 gathers and interprets the results for stagnant fluid particles in zero gravity. Concluding remarks, along with an indication of the further development of the algorithm, are offered in section 6.6.

## 6.1. Literature review

As stated above, the stability of paths and shapes of fluid and solid particles has long been, and still is, the subject of scientific research. Below, we survey some literature contributions covering various applications, which, however, resembles only a small excerpt of the vast body of available publications.

**Note 6.2** (Further literature)**.** *An extensive review of theoretical, numerical and experimental works on the topic of bubble motion can be found, e.g., in Magnaudet and Eames [89]. Theofilis [142] conducts a thorough review of linear instability analysis, introducing in detail the various underlying concepts and applications. In a preceeding article, Theofilis [141] comprehensively summarizes results from various fields of application, including, e.g., lid-driven and open cavities, flows over steps and crossflows. In his doctoral thesis, de Vries [37] presents a readable survey of the recent contributions in the field of path and shape instability. The author especially provides contributions that highlight the influence of surfactant contamination.*

Zenit and Magnaudet [159] experimentally investigate path instability of spheroidal air bubbles rising in silicone oils, considering aspect ratios of $2 \leq \chi \leq 2.36$. The authors indicate that the „*dominant parameter to trigger the instability is the bubble shape and not the Reynolds number*“. Furthermore, the authors identify the wake instability to be the underlying mechanism, which is caused by the accumulation of surface vorticity above a critical threshold. This work is extended by Zenit and Magnaudet [160], who conduct a series of experiments investigating the relation between size, shape and terminal velocity for rising bubbles, along with the identification of the conditions for the transition from steady to oscillatory paths. The authors find that, once the aspect ratio $\chi$ exceeds a critical value, the axisymmetric wake becomes bifid, inducing a lateral force, which in turn leads to an oblique path. Mougin and Magnaudet [95] numerically investigate the path instability of a massless rising bubble with fixed spheroidal shape. The transition from steady to spiraling and zigzagging paths is found to be caused by the transition from axisymmetric to bifid wakes. The experimental work of Horowitz and Williamson [70] studies the effect of the Reynolds number ($10^2 < Re < 1.5 \times 10^4$) on the dynamics and vortex formation of rigid spheres rising or falling freely through a fluid, where the experiments comprise 133 different configurations of mass ratio $\tilde{m} = \frac{\rho_{\text{sphere}}}{\rho_{\text{ambient}}}$ and $Re$. While falling spheres ($\tilde{m} > 1$) in general are reported to show no vibration, buoyant spheres feature periodical vibrations and zigzagging vertical trajectories below some critical mass ratio, which is virtually independent of $Re$ ($\tilde{m}_{\text{crit}} = 0.4$ for $260 \leq Re \leq 1550$ and $\tilde{m}_{\text{crit}} = 0.6$ for $Re > 1550$). Marginal stability curves of deformable bubbles in the $G$-$Eo$ map ($60 < G < 120$ and $10^{-1} < Eo < 20$) are the subject of Zhou and Dusek [161], where the bubble is considered in the zero viscosity/density limit. The authors identify the surface deformation to be crucial for the loss of stability of the steady axisymmetric flow. Their findings are in good agreement with Tripathi et al. [144], who numerically establish a correlation of shape asymmetry and path instability for a wider parameter range, i.e. $7 \leq G \leq 5 \times 10^2$ and $10^{-1} \leq Eo \leq 2 \times 10^2$. Gomez et al. [57] conduct a global linear instability analysis of flows within the openFOAM solver framework. The basic concept of the algorithm corresponds to Albert et al. [4], while the subject of investigation is a lid-driven cavity flow. Despite the fact that a single-phase configuration is considered, the work of Gomez et al. [57] shows, by reporting excellent agreement with direct numerical simulations and experiments, that matrix-free approaches of global linear stability analysis are feasible in three spatial dimensions. The aforementioned method is extended by Gomez et al. [58] to a shift-invert strategy, indicating the possibility to „*dramatically improve the convergence properties of the Arnoldi iterations*“. Tchoufag et al. [138] perform a global linear stability analysis of the wake and path of buoyancy-driven disks and thin cylinders, where a range of body-to-fluid inertia ratios is considered for $Re \leq 350$. The presented approach involves finding a steady state base

flow, to which a perturbation is added. The employed numerical flow solver allows for direct access of the matrices associated to the linearized problem, from which the spectrum can be computed. Their findings include that „*the first non-vertical regimes generally result from an intrinsic coupling between the body and fluid and not merely from the instability of the sole wake*“, indicating a systematic difference to the cases of bubbles; cf. above. Cano-Lozano et al. [25] perform stability analysis for freely rising bubbles by means of direct numerical simulation of 26 configurations, seeking to identify regions within which transition to path instability occurs. The nondimensional parameters are $59.61 \leq G \leq 350.2$ and $0.1 \leq Eo \leq 10$, which are varied for a set of 5 MORTON numbers with $1.11 \times 10^{-11} \leq Mo \leq 9.9 \times 10^{-6}$. For a viscosity (density) ratio of $10^{-3}$ ($10^{-2}$), the authors report a rich regime of paths, shapes and vortical structures as well as their couplings for bubbles of nearly spheroidal shape. Besides others, their findings provide evidence that a wake instability is not necessarily the cause of path instability. Cano-Lozano et al. [25] thereby extend the works of Cano-Lozano et al. [24, 26], where the latter is considered with realistic (i.e., with fore-aft asymmetry) but fixed shapes obtained for various sets of $G$ and $Bo$ in axisymmetric numerical simulations. The latter in turn is an extension of Tchoufag et al. [137], who investigate stability and sensitivity of oblate spheroidal bubbles of fixed shape. For aspect ratios $2 \leq \chi \leq 2.36$ and $10^2 < Re < 3 \times 10^3$, Magnaudet and Mougin [90] investigate the instability of wakes behind fixed spheroidal bubbles employing direct numerical simulation. They find the maximum and flux rate of the surface vorticity, which cause the instability, to behave as $\chi^{\frac{8}{3}}$ and $\chi^{\frac{7}{2}} Re^{-\frac{1}{2}}$, respectively, where unstable flows are reported to occur for $\chi > 2.21$. Instability of the paths of buoyancy-driven oblate spheroidal bubbles of fixed shape is subject of investigation in Tchoufag et al. [139], where the authors apply a numerical technique introduced by Tchoufag et al. [138]. For aspect ratios $2.1 \leq \chi \leq 2.5$ and $Re \leq 3 \times 10^3$ as the nondimensional parameters, the authors further evidence the role of the wake for the path instability. Yang and Prosperetti [157] investigate the linear stability of the axisymmetric flow past a spheroidal bubble of fixed shape by means of numerical simulations, where bubbles with aspect ration $2 \leq \chi \leq 2.5$ and $Re \leq 660$ are considered. The authors find that path instability occurs for $\chi > 2.1$, substantiating the findings of Magnaudet and Mougin [90]. Very recently, Charin et al. [27] conducted a series of numerical experiments of toluene droplets with diameter $2.2\text{mm} \leq d \leq 3\text{mm}$ rising in water. The authors identify a direct relation of velocity oscillations and variations of the droplet's shape and internal circulation. Furthermore, vorticity is found to accumulate in preferential regions of the drop, causing oscillatory paths.

The contributions itemized above have covered both experimental and numerical investigation, thereby providing an in-depth understanding of the underlying mechanisms. However, to the best of our knowledge, no work conducting linear stability analysis of deformable fluid particles employing a combination of direct numerical simulation and matrix-free KRYLOV methods has been published to date. Edwards et al. [40] examine the applicability of KRYLOV subspace methods for incompressible NAVIER-STOKES equations, where, besides others, the wavy vortex instability in the COUETTE-TAYLOR flow is investigated. The authors especially comment on the numerical performance of their method in terms of implementation effort and computational costs, indicating that matrix-free KRYLOV techniques can be applied to problems in fluid dynamics efficiently, provided that care is taken at their design.

Hence, deriving the conceptual foundation for such an approach precisely constitutes the goal of this chapter.

## 6.2. Mathematical formulation

In this section, we consider a general dynamical system, whose physical state is entirely contained in the state vector $\boldsymbol{\chi}(t) \in \boldsymbol{X}$. Here, $\boldsymbol{X}$ denotes the phase space, containing all admissible physical states of the system. The equation governing the time evolution of the system can be written in the form

$$\frac{\mathrm{d}\boldsymbol{\chi}}{\mathrm{d}t} =: \dot{\boldsymbol{\chi}} = \boldsymbol{f}(\boldsymbol{\chi}), \tag{6.1}$$

with $\boldsymbol{\chi}_0 \in \boldsymbol{X}$ a stationary solution of eq. (6.1), i.e. $\boldsymbol{f}(\boldsymbol{\chi}_0) = \boldsymbol{0}$. Here, the dot denotes the derivative with respect to time. The function $\boldsymbol{f} : \boldsymbol{X} \to \boldsymbol{X}$ is assumed to be continuously differentiable in $\boldsymbol{\chi}_0$. Then, a first order TAYLOR expansion of eq. (6.1) around the stationary state $\boldsymbol{\chi}_0$ yields the governing equation for the evolution of a small normalized perturbation $\epsilon\boldsymbol{\zeta}$, where $\epsilon \in \mathbb{R}^+$ with $\epsilon \ll 1$ and $\|\boldsymbol{\zeta}\| = 1$. With $\boldsymbol{A}_0 := \boldsymbol{J}_{\boldsymbol{f}}(\boldsymbol{\chi}_0)$ denoting the JACOBIAN of $\boldsymbol{f}$ at $\boldsymbol{\chi}_0$ and initial condition $\boldsymbol{\zeta}(0) = \boldsymbol{\zeta}_{\mathrm{ini}}$, one obtains

$$\dot{\boldsymbol{\chi}}_0 + \epsilon\dot{\boldsymbol{\zeta}} = \boldsymbol{f}(\boldsymbol{\chi}_0 + \epsilon\boldsymbol{\zeta}) \quad \Longrightarrow \quad \dot{\boldsymbol{\zeta}}(t) = \boldsymbol{A}_0 \cdot \boldsymbol{\zeta}(t) + \mathcal{O}(\epsilon^2), \tag{6.2}$$

where, in general, the JACOBIAN is non-symmetric, i.e. $\boldsymbol{A}_0 \neq \boldsymbol{A}_0^{\mathsf{T}}$. Note that the superposition of the steady state $\boldsymbol{\chi}_0$ and the perturbation $\boldsymbol{\zeta}$ is itself an element of the phase space, i.e. $\boldsymbol{\chi}_0 + \epsilon\boldsymbol{\zeta} \in \boldsymbol{X}$. This poses certain constraints on the phase space, which is why the details of its design are deferred to subsection 6.2.1. The solution of eq. (6.2) can be expressed as

$$\boldsymbol{\zeta}(t) = \boldsymbol{B}_0(t)\boldsymbol{\zeta}_{\mathrm{ini}} \qquad \text{with} \qquad \boldsymbol{B}_0(t) := e^{t\boldsymbol{A}_0}. \tag{6.3}$$

By $(\lambda^{\boldsymbol{A}_0}, \boldsymbol{\varphi}^{\boldsymbol{A}_0})_i$ we denote the eigenpairs of $\boldsymbol{A}_0$, analogously for $\boldsymbol{B}_0(t)$. For diagonalizable $\boldsymbol{A}_0 = \boldsymbol{V}\boldsymbol{D}\boldsymbol{V}^{-1}$, which is assumed to be the case henceforth, it holds that $e^{\boldsymbol{A}_0} = \boldsymbol{V}e^{\boldsymbol{D}}\boldsymbol{V}^{-1}$, where the spectrum of $\boldsymbol{A}_0$ corresponds to the entries of the diagonal matrix $\boldsymbol{D}$, i.e. $\sigma(\boldsymbol{A}_0) = \{\lambda_i^{\boldsymbol{A}_0}\} = \mathrm{diag}\{\boldsymbol{D}\}$. While the eigenvectors remain unchanged under the exponential transformation, i.e. $\boldsymbol{\varphi}_i^{\boldsymbol{B}_0} = \boldsymbol{\varphi}_i^{\boldsymbol{A}_0}$, the transformed spectrum explicitly depends on time, i.e. $\sigma(\boldsymbol{B}_0)(t) = \exp(t\,\mathrm{diag}\{\boldsymbol{D}\})$. Decomposing the initial perturbation $\boldsymbol{\zeta}_{\mathrm{ini}}$ in terms of the eigenvectors of $\boldsymbol{A}_0$, the leftmost expression in eq. (6.3) becomes

$$\boldsymbol{B}_0(t)\boldsymbol{\zeta}_{\mathrm{ini}} = \boldsymbol{B}_0(t)\sum_{k=0}^{\infty}\beta_k\boldsymbol{\varphi}_k^{\boldsymbol{B}_0} = \sum_{k=0}^{\infty}\beta_k\lambda_k^{\boldsymbol{B}_0}(t)\boldsymbol{\varphi}_k^{\boldsymbol{B}_0} = \sum_{k=0}^{\infty}\beta_k e^{t\lambda_k^{\boldsymbol{A}_0}}\boldsymbol{\varphi}_k^{\boldsymbol{A}_0} \quad \text{with} \quad \beta_k = \langle\boldsymbol{\varphi}_k^{\boldsymbol{A}_0}, \boldsymbol{\zeta}_{\mathrm{ini}}\rangle, \tag{6.4}$$

implying that the real parts of the eigenvalues $\lambda_k^{\boldsymbol{A}_0}$ are decisive for the stability of the time evolution of the perturbation. If the spectrum $\sigma(\boldsymbol{A}_0)$ contains no elements with real part greater than zero, the steady state $\boldsymbol{\chi}_0$ is said to be *stable*, and *unstable*, respectively, if there is at least one eigenvalue in the right half of the complex plane. Henceforth, without loss of generality, assume that the elements in the spectrum of $\boldsymbol{A}_0$ are arranged in descending order of their real part, i.e.

$$\sigma(\boldsymbol{A}_0) = \{\lambda_i^{\boldsymbol{A}_0} : \Re\lambda_i^{\boldsymbol{A}_0} \geq \Re\lambda_{i+1}^{\boldsymbol{A}_0} \quad \forall i\}. \tag{6.5}$$

In a PDE setting, the elements of the phase space $\boldsymbol{X}$ are infinite-dimensional in general. Since the discretized two-phase NAVIER-STOKES equations for incompressible flows are considered as the governing equations in eq. (6.1), the state vector $\boldsymbol{\chi}$ has a finite dimension. In order to obtain physically reliable

results, the flow problems under consideration here typically require a high spatial resolution, implying $\dim(\boldsymbol{\chi}) = \mathcal{O}(10^7)$. This renders the computation of the full spectrum impractical, hence the primary goal of the algorithm is to extract the leading eigenvalue $\lambda_1^{\boldsymbol{A}_0}$ (or, if $\Im\lambda_1^{\boldsymbol{A}_0} \neq 0$, the c.c. pair $\lambda_{1,2}^{\boldsymbol{A}_0}$). For further analysis, additional pairs of eigenvalues might be of interest as well. In what follows, we consider a discretized finite-dimensional approximation of $\boldsymbol{f}$ and, accordingly, of $\boldsymbol{\chi}$; cf. eq. (6.1). The notation introduced above is carried forth. First, recall from section 3.1 that the discretization in time is first-order semi-implicit. With $\boldsymbol{\chi}^n := \boldsymbol{\chi}(n\Delta t)$ the generic formulation reads

$$\frac{\boldsymbol{\chi}^{n+1} - \boldsymbol{\chi}^n}{\Delta t} = \boldsymbol{A}_n \left(\alpha\boldsymbol{\chi}^{n+1} + (1-\alpha)\boldsymbol{\chi}^n\right) \quad \text{with} \quad \boldsymbol{A}_n = \boldsymbol{A}(\boldsymbol{\chi}^n) \quad \text{and} \quad \alpha \in [0,1], \tag{6.6}$$

where $\alpha = 1$ ($\alpha = 0$) corresponds to a fully implicit (explicit) discretization in time. Assuming invertibility of the matrices under consideration, solving eq. (6.6) for the state after one timestep yields

$$\boldsymbol{\chi}^{n+1} = (\boldsymbol{I} - \alpha\Delta t\boldsymbol{A}_n)^{-1}(\boldsymbol{I} + (1-\alpha)\Delta t\boldsymbol{A}_n)\boldsymbol{\chi}^n = \boldsymbol{B}_n\boldsymbol{\chi}^n. \tag{6.7}$$

with

$$\boldsymbol{B}_n := \sum_{k=0}^{\infty} \alpha^k \Delta t^k \boldsymbol{A}_n^k + (1-\alpha)\alpha^k \Delta t^{k+1} \boldsymbol{A}_n^{k+1}. \tag{6.8}$$

Recursive application produces the evolution at time $t + N\Delta t$, which after exploiting eq. (6.7) becomes

$$\boldsymbol{\chi}^N = \left(\prod_{k=0}^{N-1} \boldsymbol{B}_k\right) \boldsymbol{\chi}^0 = \boldsymbol{f}(\boldsymbol{\chi}^0; N, \Delta t). \tag{6.9}$$

Given some initial state $\boldsymbol{\chi}^0$, the numerical flow solver FS3D provides the evolved state as $\boldsymbol{\chi}^N$, where $\boldsymbol{f} : \boldsymbol{X} \mapsto \boldsymbol{X}$ is a nonlinear operator allowing access to neither $\boldsymbol{B}_k$ nor $\boldsymbol{A}_k$; cf. eq. (3.8) in section 3.1.

**Note 6.3** (Matrix-free approaches)**.** *Since access to the matrices is not possible, the extraction of the desired eigenvalues requires a* ***matrix-free*** *approach, where one is only required to provide the action on a prescribed vector. The so-called* ***non-symmetric eigenvalue problem*** *is a complex and fascinating topic of its own and subject to ongoing research. Section 6.3 addresses the aspects relevant to the application here.*

Since the present application covers the evolution of a small perturbation of a steady state, one may assume that $\boldsymbol{A}_k \approx \boldsymbol{A}_0$ and $\boldsymbol{B}_k \approx \boldsymbol{B}_0$, i.e. the JACOBIAN of a steady state remains approximaetly constant for small deviations. Note that the coincidence of notation with the continuous formulation in eq. (6.3) is intended. The implication

$$\boldsymbol{f}(\boldsymbol{\chi}^0; N, \Delta t) \approx \boldsymbol{B}_0^N\boldsymbol{\chi}^0 = (\boldsymbol{I} + N\Delta t\boldsymbol{A}_0)\,\boldsymbol{\chi}^0 + \mathcal{O}(\Delta t^2\|\boldsymbol{A}_0\|^2), \tag{6.10}$$

along with exploiting $\boldsymbol{\chi}^0 = \boldsymbol{\chi}_0 + \epsilon\boldsymbol{\zeta}$, allows to infer the action of $\boldsymbol{A}_0$ on $\boldsymbol{\zeta}$ from the numerical evolutions

of a positive and a negative perturbation via

$$\boldsymbol{A}_0\boldsymbol{\zeta} = \frac{1}{N\Delta t}\left(\frac{\boldsymbol{f}(\boldsymbol{\chi}_0 + \epsilon\boldsymbol{\zeta}; N, \Delta t) - \boldsymbol{f}(\boldsymbol{\chi}_0 - \epsilon\boldsymbol{\zeta}; N, \Delta t)}{2\epsilon} - \boldsymbol{\zeta}\right) + \mathcal{O}(\Delta t\|\boldsymbol{A}_0\|^2). \tag{6.11}$$

In an analogous manner, the action of $\boldsymbol{B}_0$ on $\boldsymbol{\zeta}$ is obtained by

$$\boldsymbol{B}_0\boldsymbol{\zeta} = \frac{\boldsymbol{f}(\boldsymbol{\chi}_0 + \epsilon\boldsymbol{\zeta}; N, \Delta t) - \boldsymbol{f}(\boldsymbol{\chi}_0 - \epsilon\boldsymbol{\zeta}; N, \Delta t)}{2\epsilon} + \mathcal{O}(\Delta t^2\|\boldsymbol{A}_0\|^2). \tag{6.12}$$

Supplemental to eq. (6.2), eq. (6.11) poses two conditions on the design of an appropriate phase space: (i) one needs to compute superpositions of state vectors, posing a highly non-trivial task in the context of flows in three spatial dimensions with deformable interfaces. Furthermore, the evaulation of eq. (6.11) requires the initialization of the flow solver with a perturbed steady state $\boldsymbol{\chi}_0 \pm \epsilon\boldsymbol{\zeta}$. By definition, the steady state $\boldsymbol{\chi}_0$ is an element of the phase space $\boldsymbol{X}$ and, since $\boldsymbol{f} : \boldsymbol{X} \mapsto \boldsymbol{X}$, it is required that the superposition inherits this property, i.e.

$$\boldsymbol{\chi}_0 \pm \epsilon\boldsymbol{\zeta} \in \boldsymbol{X} \quad \forall\epsilon \in \mathbb{R}. \tag{6.13}$$

The upcoming subsections 6.2.1 and 6.2.2 shall address these issues subsequently.

### 6.2.1. A phase space for two-phase flows

As stated above, the phase space $\boldsymbol{X}$ is the set of all feasible, yet not necessarily physically plausible states of the system under consideration. In a two-phase flow within the domain $\Omega$, governed by the Navier-Stokes equations, for a given time $t$, a state vector $\boldsymbol{\chi}(t) := (\boldsymbol{u}(t, \boldsymbol{x}), \boldsymbol{c}_\Sigma(t))$ comprises the velocity field $\boldsymbol{u}(t, \boldsymbol{x})$ and some description $\boldsymbol{c}_\Sigma(t)$ of the interface $\Sigma(t)$, which determines the domains occupied by the respective phases. Furthermore, due to the incompressibility of the flow, the volume of the particle, denoted by $V_0$, must be conserved[1].

#### Velocity field

The velocity field associated to a state vector is solenoidal and exhibits finite kinetic energy, i.e.

$$\nabla \cdot \boldsymbol{u}(t, \boldsymbol{x}) = 0 \quad \text{for} \quad \boldsymbol{x} \in \Omega \qquad \text{and} \qquad \int_{\Omega\setminus\Sigma(t)} \left[\frac{\rho}{2}\langle\boldsymbol{u}, \boldsymbol{u}\rangle\right](t, \boldsymbol{x})\,\mathrm{d}\boldsymbol{x} < \infty. \tag{6.14}$$

Recall from section 2.1 that the velocity and density are phase-specific (the latter being respectively constant), i.e.

$$\boldsymbol{u}(t, \boldsymbol{x}) = \begin{cases} \boldsymbol{u}^-(t, \boldsymbol{x}) & \boldsymbol{x} \in \Omega^-(t) \\ \boldsymbol{u}^+(t, \boldsymbol{x}) & \boldsymbol{x} \in \Omega^+(t) \end{cases} \quad \text{and} \quad \rho(\boldsymbol{x}) = \begin{cases} \rho^-, \boldsymbol{x} & \in \Omega^-(t) \\ \rho^+, \boldsymbol{x} & \in \Omega^+(t) \end{cases}. \tag{6.15}$$

Since the superposition of two solenoidal velocity fields is itself solenoidal, there is no evident restriction in the sense of eq. (6.13). However, recall that the respective phases $\Omega_i^\pm$ of two states $\boldsymbol{\chi}_i$ do not necessarily coincide. Thus, a naive superposition would potentially superpose velocities in $\Omega^-$ with those in $\Omega^+$ or vice versa. See fig. (6.1) for a schematic illustration.

[1] This only holds if the fluid particle does not (partially) leave the domain, which is assumed to be the case here.


(a) $\Omega_1^- \cup \Omega_2^-$ (b) $(\Omega_1^- \setminus \Omega_2^-) \cup (\Omega_2^- \setminus \Omega_1^-)$

Figure 6.1.: Misalignment of bulk phases $\Omega \backslash \Sigma_i$ introduced by interfaces $\Sigma_i$ of two evolved states $\boldsymbol{\chi}_i$.

Despite the fact that, in a numerical sense, such a superposition is possible, it would not be a meaningful operation. A way to assign meaning was introduced by Beale [12] and consists of a transformation to a common referential domain. This will be subject of subsection 6.2.2.

### Hypersurface representation

The hypersurface is required to preserve the initial volume while having finite surface energy, i.e.

$$V_0 = \mathrm{vol}(\boldsymbol{c}_\Sigma) \qquad \text{and} \qquad \mathrm{area}(\sigma; \boldsymbol{c}_\Sigma) < \infty, \tag{6.16}$$

where eq. (2.16) introduces the area operator. We choose the class of hypersurfaces given in section 2.2, i.e. a parametrization in spherical coordinates where the third power of the radius is expanded in spherical harminics of degree $L_\Sigma$, cf. eq. (2.18), implying that the phase space is determined by the initial volume $V_0$ and the expansion order $L_\Sigma$, i.e, $\boldsymbol{X} = \boldsymbol{X}(L_\Sigma, V_0)$. Recalling that the associated volume depends only on the first entry of the coefficient vector, cf. eq. (2.19), it becomes evident that any perturbation $\boldsymbol{\zeta} \in \boldsymbol{X}(L_\Sigma, 0)$, corresponding to $c^{\boldsymbol{\zeta}}_{\Sigma,00} = 0$, fulfills the superposition requirement of eq. (6.13) for arbitrary but constant $\epsilon \in \mathbb{R}$.

### Inner product

Despite the fact that the form of the inner product does not affect the outcome of the stability analysis, we would like to design an inner product with physical meaning. Let the inner product on the phase space be defined[2] as

$$\langle \boldsymbol{\chi}_1, \boldsymbol{\chi}_2 \rangle_{\boldsymbol{X}} := \omega_{\boldsymbol{u}} \langle \boldsymbol{u}_1, \boldsymbol{u}_2 \rangle_{\Omega \setminus \Sigma} + \omega_\Sigma \langle \boldsymbol{c}_{\Sigma,1}, \boldsymbol{c}_{\Sigma,2} \rangle_\Sigma \tag{6.17}$$

with strictly positive weights $(\omega_{\boldsymbol{u}}, \omega_\Sigma)$ where $\omega_{\boldsymbol{u}} + \omega_\Sigma = 1$. In order for eq. (6.17) to define an inner product, both contributions are required to be commutative, associative and homogeneous of degree 1 in

[2] The reason why there is no contribution containing interferences between the velocity $\boldsymbol{u}_i$ and the interface representation $\boldsymbol{c}_{\Sigma,i}$ is that ensuring linearity imposes crucial restrictions on the admissible functional relation, barely allowing the introduction of physical meaning.

both arguments. The inner product for the velocity component is defined as

$$\langle \boldsymbol{u}_1, \boldsymbol{u}_2 \rangle_{\Omega\setminus\Sigma} := \frac{1}{2} \int\limits_{\Omega\setminus\Sigma} \rho(\boldsymbol{x}) \langle \boldsymbol{u}_1, \boldsymbol{u}_2 \rangle \, \mathrm{d}\boldsymbol{x}, \tag{6.18}$$

resembling the kinetic energy for $\boldsymbol{\chi}_1 = \boldsymbol{\chi}_2$. Note that, due to the transformation to the reference state $\boldsymbol{\chi}_0$, cf. subsection 6.2.2 below, the integration domain $\Omega\setminus\Sigma$ is identical for both $\boldsymbol{\chi}_1$ and $\boldsymbol{\chi}_2$. This ensures that only velocities from corresponding fluid phases are multiplied. While the *kinetic energy* contribution in eq. (6.18) clearly fulfills the above requirements, an analogous definition of the rightmost expression in eq. (6.17), e.g. in terms of surface energy, is not possible. To see that the area operator is homogeneous of degree $2/3$ with respect to $\boldsymbol{c}_\Sigma$, simply insert the expressions in eq. (2.20) into eq. (2.16). Hence, we define the interface component of the inner product as follows:

1. Evaluate eq. (2.16) with $f \equiv \sigma$ and consider a mixed inner product in the argument of the square root to obtain

$$\int_{\mathbb{S}^2} \sigma \sqrt{R_1 R_2 \left[ (R_1 R_2 + R_{1,\theta} R_{2,\theta}) \sin^2\theta + R_{1,\varphi} R_{2,\varphi} \right]} \, \mathrm{d}\varphi \mathrm{d}\theta. \tag{6.19}$$

   where $R_i = \langle \boldsymbol{c}_{\Sigma,0} + \boldsymbol{c}_{\Sigma,i}, \boldsymbol{y}_\Sigma \rangle^{\frac{1}{3}}$, cf. eq. (2.20).

2. Assume that the derivatives w. r. t. the polar and azimuthal angle are small in comparison to the radius. Then eq. (6.19) simplifies to

$$\int_{\mathbb{S}^2} \sigma \langle \boldsymbol{c}_{\Sigma,0} + \boldsymbol{c}_{\Sigma,1}, \boldsymbol{y}_\Sigma \rangle^{\frac{1}{3}} \langle \boldsymbol{c}_{\Sigma,0} + \boldsymbol{c}_{\Sigma,2}, \boldsymbol{y}_\Sigma \rangle^{\frac{1}{3}} \sin\theta \, \mathrm{d}\varphi \mathrm{d}\theta. \tag{6.20}$$

3. Apply a Taylor expansion around $\boldsymbol{c}_{\Sigma,i,0} = \boldsymbol{0}$ to eq. (6.20) and subtract the surface energy of the steady state to obtain

$$\int_{\mathbb{S}^2} \sigma \left[ \frac{\langle \boldsymbol{c}_{\Sigma,1} + \boldsymbol{c}_{\Sigma,2}, \boldsymbol{y}_\Sigma \rangle}{3 \langle \boldsymbol{c}_{\Sigma,0}, \boldsymbol{y}_\Sigma \rangle^{\frac{1}{3}}} + \boldsymbol{c}_{\Sigma,1}^{\mathsf{T}} \frac{\boldsymbol{y}_\Sigma \otimes \boldsymbol{y}_\Sigma}{9 \langle \boldsymbol{c}_{\Sigma,0}, \boldsymbol{y}_\Sigma \rangle^{\frac{4}{3}}} \boldsymbol{c}_{\Sigma,2} \right] \sin\theta \, \mathrm{d}\varphi \mathrm{d}\theta. \tag{6.21}$$

4. In order to fulfill the homogeneity requirement, the first term in eq. (6.21) must vanish. This is achieved by approximating the steady state interface $\boldsymbol{c}_{\Sigma,0}$ by a sphere of volume $V_0$, implying that $\sqrt[3]{\langle \boldsymbol{c}_{\Sigma,0}, \boldsymbol{y}_\Sigma \rangle} \approx (3V_0/4\pi)^{\frac{1}{3}}$. Recalling that the inner product is only applied to state vectors with zero volume, i.e. $c_{\Sigma,i,00} \equiv 0$, the definition of $\boldsymbol{y}_\Sigma$ and eq. (A.4) imply that the first summand in eq. (6.21) vanishes after integration.

Finally, we arrive at

$$\langle \boldsymbol{c}_{\Sigma,1}, \boldsymbol{c}_{\Sigma,2} \rangle_\Sigma := \frac{\sigma (4\pi)^{\frac{4}{3}}}{18 (3V_0)^{\frac{4}{3}}} \langle \boldsymbol{c}_{\Sigma,1}, \boldsymbol{c}_{\Sigma,2} \rangle. \tag{6.22}$$

**Note 6.4** (Inner product on nearly spherical hypersurfaces)**.** *A justification of the assumptions made to obtain the quadratic form of the interface component reads as follows: eq. (6.22) describes the increment*

*of surface energy emerging from a small perturbation of a spherical interface of reference, which is strictly positive. However, if the interface of reference already is a perturbed sphere, an additional perturbation may both increase or decrease the surface area and, accordingly, the surface energy. Hence, we cannot expect the approximation to exhibit a purely quadratic form.*

Finally, the inner product and norm, respectively, associated to the phase space can be cast as

$$\langle \boldsymbol{\chi}_1, \boldsymbol{\chi}_2 \rangle_{\boldsymbol{X}} := \frac{1}{2} \int_{\Omega \backslash \Sigma} \rho(\boldsymbol{x}) \langle \boldsymbol{u}_1, \boldsymbol{u}_2 \rangle \, \mathrm{d}\boldsymbol{x} + \frac{\sigma (4\pi)^{\frac{4}{3}}}{18 (3V_0)^{\frac{4}{3}}} \langle \boldsymbol{c}_{\Sigma,1}, \boldsymbol{c}_{\Sigma,2} \rangle, \tag{6.23}$$

$$\| \boldsymbol{\chi} \|_{\boldsymbol{X}} := \sqrt{\langle \boldsymbol{\chi}, \boldsymbol{\chi} \rangle_{\boldsymbol{X}}}. \tag{6.24}$$

While the second summand in eq. (6.23) can be computed directly, the numerical evaluation of the first summand is carried by the following steps: (i) interpolate the velocities from the respective cell faces to the centers, (ii) evaluate the density at the cell centers based on the volume fractions induced by the steady state $\boldsymbol{\chi}_0$ and (iii) compute the sum over all cells, weighted by the relative volume.

### 6.2.2. Domain transformation

Let $\boldsymbol{\chi}_i = (\boldsymbol{u}_i, \boldsymbol{c}_{\Sigma,i})$, $i \in \{1, 2\}$ be two elements of the phase space $\boldsymbol{X}(L_\Sigma, V_0)$ with $\boldsymbol{c}_{\Sigma,1} \neq \boldsymbol{c}_{\Sigma,2}$, i.e. the interfaces $\Sigma_i$ associated to the respective states and, hence, the bulk phases $\Omega \backslash \Sigma_i$, do not coincide; cf. fig. (6.1) for an illustration. This implies that the evaluation of eq. (6.18) cannot readily be performed for phase specific velocity fields $\boldsymbol{u}_i^{\pm}$, cf. eq. (6.15). In order to eliminate the misalignment of the respective bulk phases, we introduce a spatial transformation $\boldsymbol{T}(t, \boldsymbol{x}) : [0, T] \times \Omega \mapsto \Omega$ that

(i) is sufficiently smooth and bijective, i.e. invertible for all $\boldsymbol{x} \in \Omega$,

(ii) preserves the domain boundary, i.e. $\boldsymbol{T}(\partial\Omega) = \partial\Omega$,

(iii) maps the referential interface $\Sigma_0$ onto $\Sigma_i$ and

(iv) maps the referential bulk phases $\Omega \backslash \Sigma_0$ onto their respective counterparts $\Omega \backslash \Sigma_i$.

This concept was originally introduced by Beale [12] and applied, e.g., by Nishida et al. [100]. Figure (6.2) provides a schematic illustration. In what follows, we will formally omit the time dependence and identify

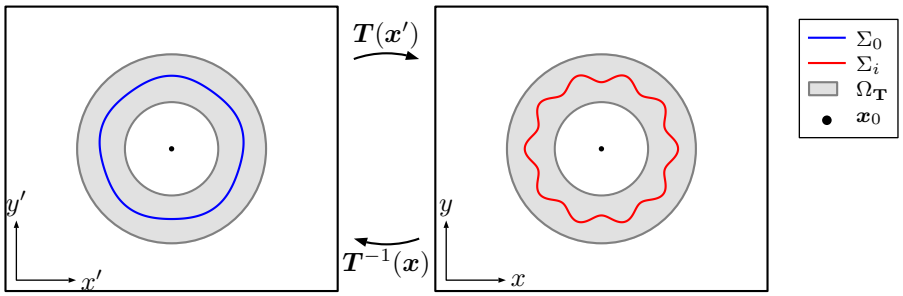


Figure 6.2.: Simulation domain $\Omega$ with transformation domain $\Omega_{\boldsymbol{T}}$.

the coordinates belonging to the referential state by a prime, i.e. the spatial transformation can be generically formulated as

$$\boldsymbol{x} = \boldsymbol{T}(\boldsymbol{x}'). \tag{6.25}$$

With $\boldsymbol{J_T}$ denoting the JACOBIAN of $\boldsymbol{T}$, the transformed velocity field is obtained via

$$\boldsymbol{u}(\boldsymbol{x}) = \left[\frac{1}{\det \boldsymbol{J_T}(\boldsymbol{x}')} \boldsymbol{J_T}(\boldsymbol{x}') \cdot \boldsymbol{u}'(\boldsymbol{x}')\right]\Bigg|_{\boldsymbol{x}'=\boldsymbol{T}^{-1}(\boldsymbol{x})}. \tag{6.26}$$

Recalling from the features of the flow solver provided in section 3.1 that the simulation domain $\Omega$ is cuboidal implies that its boundary $\partial\Omega$ is star-shaped, i.e.

$$\partial\Omega = \{R_{\partial\Omega}(\varphi,\theta)\boldsymbol{e}_r : (\varphi,\theta) \in \mathbb{S}^2\}, \tag{6.27}$$

suggesting the application of spherical coordinates. Furthermore, the transformation can be chosen such that it only affects the norm of a spatial point while pertaining its angular orientation, i.e. $\boldsymbol{x} = r\boldsymbol{e}_r(\varphi,\theta)$ and $\boldsymbol{x}' = r'\boldsymbol{e}_r(\varphi,\theta)$; cf. fig. (6.2). One obtains

$$\boldsymbol{T}(\boldsymbol{x}) = T(r;\varphi,\theta)\boldsymbol{e}_r. \tag{6.28}$$

where the requirements (ii) – (iv) become

$$T(R_{\partial\Omega}) = R_{\partial\Omega}, \quad T(R_0) = R_i \quad \text{and} \quad T(0) = 0 \quad \forall(\varphi,\theta) \in \mathbb{S}^2. \tag{6.29}$$

However, the radius of the domain boundary, cf. eq. (6.27), is not continuously differentable, violating requirement (i). Furthermore, the position of the spherical origin within the simulation domain potentially introduces anisotropy into the transformation. In order to overcome the incompatibility and to avoid any influence of the domain boundary, we introduce a disjoint decomposition of $\Omega$ into a transformation domain $\Omega_{\boldsymbol{T}}$ and an identity domain $\Omega_{\mathbf{1}}$, where fig. (6.2) provides an illustration. Since this thesis investigates slightly deformed spherical particles, a spherical shell enclosing the interfaces $\Sigma_i$ and $\Sigma_0$ seems to be appropriate, i.e.

$$\Omega_{\boldsymbol{T}} := \mathcal{B}_{R_+}(\boldsymbol{x}_\mathrm{c}) \setminus \mathcal{B}_{R_-}(\boldsymbol{x}_\mathrm{c}) \qquad \text{and} \qquad \Omega_{\mathbf{1}} := \Omega \setminus \Omega_{\boldsymbol{T}}, \tag{6.30}$$

where, without loss of generality, we assume that $\boldsymbol{x}_\mathrm{c} = \mathbf{0}$. The constant radii $R_\pm$ of the spherical shell (corresponding to the transformation domain $\Omega_{\boldsymbol{T}}$) are chosen such that

$$R_- < R(\varphi,\theta,\boldsymbol{c}_{\Sigma,i}) < R_+ \qquad \forall(\varphi,\theta) \in \mathbb{S}^2. \tag{6.31}$$

Note that, since $\partial\Omega \subset \Omega_{\mathbf{1}}$, requirement (ii) is fulfilled. From eq. (6.26) it follows that *sufficient* smoothness in the sense of (i) requires $T(r)$ to be twice continuously differentiable. Finally, one obtains the following conditions:

$$T(R_0) = R_i, \quad T(r)\big|_{r\le R_-} = T(r)\big|_{r\ge R_+} = r, \quad \partial_r T(r)\big|_{r=R_\pm} = 1, \quad \partial_r^2 T(r)\big|_{r=R_\pm} = 0, \tag{6.32}$$

suggesting a $6^{\text{th}}$-order polynomial, i.e.

$$T(r) = \begin{cases} r & r \in [0, R_-) \cup (R_+, \infty) \\ r - \frac{(R_0-R_i)(r-R_-)^3(r-R_+)^3}{(R_0-R_-)^3(R_0-R_+)^3} & r \in [R_-, R_+] \end{cases}. \tag{6.33}$$

The derivative with respect to the radius reads

$$\partial_r T(r) = \begin{cases} 1 & r \in [0, R_-) \cup (R_+, \infty) \\ 1 - \frac{6(R_0-R_i)(r-R_-)^2(r-R_+)^2\left(r-\frac{R_+-R_-}{2}\right)}{(R_0-R_-)^3(R_0-R_+)^3} & r \in [R_-, R_+] \end{cases}. \tag{6.34}$$

Combining eq. (6.33) with the conditions imposed on the radius given in eq. (2.13), it becomes evident that

$$\partial_\varphi T(r)|_{\theta\in\{0,\pi\}} = 0. \tag{6.35}$$

For the transformation to be invertible, $\partial_r T(r;\varphi,\theta) > 0$ is required for $(\varphi,\theta) \in \mathbb{S}^2$, imposing the condition

$$\frac{3\sqrt{5}}{125}|R_0 - R_i|(R_+ - R_-)^5 \geq (R_0 - R_+)^3(R_0 - R_-)^3. \tag{6.36}$$

To reduce the number of parameters, let $R_\pm := (1 \pm \alpha_T)\sqrt[3]{3V_0/4\pi}$ with $\alpha_T > 0$. Figure (6.3) exemplifies the range of bijectivity at some fixed angular position for different $\alpha_T$. As can be seen from fig. (6.3), the

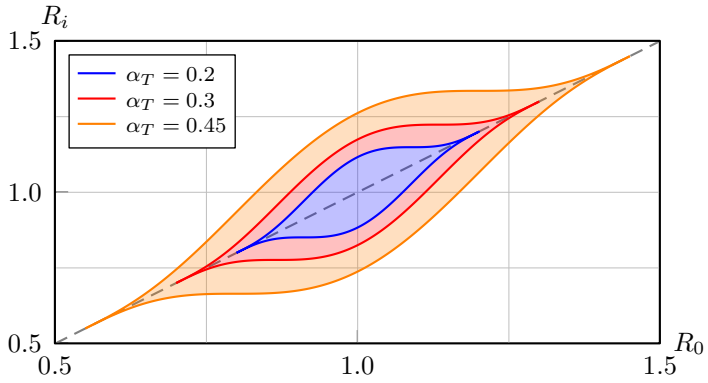


Figure 6.3.: Local range of bijectivity for fixed angular position.

admissible deviation, i.e. $|R_0 - R_i|$, tapers symmetrically towards both boundaries of the transformation domain, i.e. $\partial\mathcal{B}_{R_\pm}(\mathbf{0})$. In other words, the closer the interfaces $\Sigma_0$ and $\Sigma_\text{p}$, respectively, are to the transformation domain boundary $\partial\Omega_{\boldsymbol{T}}$, the smaller the absolute deviation must be to preserve invertibility. Hence, the choice of the extension parameter $\alpha_T$ requires some a-priori knowledge of the deformation.

### The effect on the velocity field

For a transformation of the type provided in eq. (6.26), Bock [19] has shown that the transformed velocity field $\boldsymbol{u}(t,\boldsymbol{x})$ is divergence-free, iff the referential velocity field $\boldsymbol{u}'(\boldsymbol{x}')$ also is divergence-free. Since the transformation in eq. (6.28) is given in spherical coordinates, it is convenient to compute the JACOBIAN

by application of the chain rule, which yields

$$\boldsymbol{J_T}(\boldsymbol{x}') = \frac{\mathrm{d}\boldsymbol{T}(\boldsymbol{x}')}{\mathrm{d}\boldsymbol{x}'} = \frac{\partial \boldsymbol{x}}{\partial \boldsymbol{r}'} \cdot \boldsymbol{J_r} = [\partial_r T(r)\boldsymbol{e}_r, \partial_\varphi T(r)\boldsymbol{e}_r + T(r)\sin\theta \boldsymbol{e}_\varphi, \partial_\theta T(r)\boldsymbol{e}_r + T(r)\boldsymbol{e}_\theta]\, \boldsymbol{J_r}, \quad (6.37)$$

where $\boldsymbol{J_r}$ is the JACOBIAN of the transformation from spherical to CARTESIAN coordinates; cf. eq. (1.2). Due to the degeneration of spherical coordinates at the poles, which has been discussed for curvature computation in subsection 2.2.1, the application of the rule of L'HÔSPITAL is required here as well. After extensive calculus, one obtains

$$\boldsymbol{J_T}(r)|_{\theta\in\{0,\pi\}} = \begin{bmatrix} \frac{T(r)}{r} & 0 & 0 \\ 0 & \frac{T(r)}{r} & 0 \\ \frac{\cos\varphi\partial_\theta T(r) - \sin\varphi\partial_{\varphi\theta} T(r)}{r} & \frac{\sin\varphi\partial_\theta T(r) + \cos\varphi\partial_{\varphi\theta} T(r)}{r} & \partial_r T(r) \end{bmatrix}, \quad (6.38)$$

where, irrespective of limit considerations, the determinant of eq. (6.37) reads

$$\det \boldsymbol{J_T}(r) = \frac{T(r)^2 \partial_r T(r)}{r^2}. \quad (6.39)$$

Due to the polynomial order, the inverse of the transformation, i.e. $[T(r)]^{-1}$, cannot be given analytically in general. Thus, we apply NEWTON's method to numerically invert eq. (6.33), cf. section 1.3, while the associated JACOBIAN is obtained by exploiting the inverse function theorem, i.e. by inverting $\boldsymbol{J_T}$ numerically using the `LAPACK` routine `dgetri`. Note that eq. (6.39) implies that this is always possible under the assumptions made above.

Before we are able to provide a final design of the numerical algorithm for the linear stability analysis, the next section discusses the non-symmetric eigenvalue problem.

## 6.3. The eigenvalue problem

This section is concerned with the computation of some eigenvalues of a large real non-symmetric matrix $\boldsymbol{A} \in \mathbb{R}^{N\times N}$ with $N \sim 10^6$, where direct computation is impractical due to computational costs. As stated above, we are interested in algorithms that do not require an explicit knowledge of the matrix, but rather get by on evaluating the action of the matrix on some given vector; cf. note (6.3). Among these methods, the class of KRYLOV subspace methods is of special interest; for further details, see, e.g., Saad [125, 126]. However, due to the large size of the matrices under consideration here, only a selected part of the spectrum, namely the leading eigenvalues, is of interest. Its extraction poses a non-trivial task, especially for large sparse matrices. We shall commence be outlining the state of literature in subsection 6.3.1. Subsequently, subsection 6.3.2 is devoted to a detailed investigation of the method developed by Arnoldi [7], whose performance is assessed for an artifical problem. Subsection 6.3.3 introduces an augmented version.

### 6.3.1. Literature review

The computation of eigenvalules and -vectors of real non-symmetric matrices has received quite some attention in the literature over the past decades. Within this short survey, only a small and by no means exhaustive selection shall be presented.

**Note 6.5** (Symmetric matrices)**.** *It is worth noting that there is wide range of algorithms for the computation of eigensystems of real symmetric matrices; cf. Davidson [36], Crouzeix et al. [34] or Clint and Jennings [33]. However, due to the tremendous increment in mathematical complexity induced by the loss of symmetry, the case of real non-symmetric matrices has not received such detailed treatment.*

In a pioneering article, Arnoldi [7] introduced a principal of minimized iterations, which is the conceptual foundation of the algorithm employed in this thesis. The Arnoldi method has been conceptually extended ever since its introduction. Saad [123] develops several variations of the Arnoldi method for large non-symmetric real matrices. The software package `ARPACK` provides an implementation of several routines for the solution of large algebraic eigenvalue problems, for which Lehoucq et al. [80] provide both mathematical and implementation details. The remarks given in subsections 6.3.2 and 6.3.3 draw heavily from the aforementioned book. Saad [124], resorting to the work of Manteuffel [91, 92], introduces a coupling of the Arnoldi method with Chebyshev polynomial acceleration, which is further augmented by Ho et al. [66] and Sadkane [128], who introduces a block version. The computation of optimal ellipses, which are required for the construction of the Chebychev polynomials, is subject of Ho [65], where Ashby [8] implements and numerically assesses the aforementioned algorithm in `Fortran`. An implicitly restarted Arnoldi algorithm with spectral shift is treated by Kooper et al. [77], where Nishida and Oyanagi [99] conduct an evaluation of acceleration techniques for restarted Arnoldi methods. In Jia [73], a refined iterative algorithm based on the block Arnoldi process is introduced. Scott [129] proposes an implementation taylored to large sparse matrices. Sorensen [132] proposes an implicit application of polynomial filters in a $k$-step Arnoldi method, which will be discussed in subsection 6.3.3. Bellalij et al. [13, 14] provide some convergence analysis of the Arnoldi method for non-normal matrices. Valdettaro et al. [146] examine convergence behavior and round-off errors of an incomplete Arnoldi-Chebyshev method by comparison of double precision and extended precision computations. Their findings indicate that especially most amplified modes with high spatial frequency are sensitive to round-off errors. Nayar and Ortega [98] investigate the computation of selected eigenvalues of generalized non-symmetric systems. The focus of Natarajan [97] lies on finite element stability problems. Ruhe [122] proposes a two-sided version of the Arnoldi algorithm, which allows for the computation of left eigenvectors as well. Parlett [102] reviews the software for extraction of eigenvalues from sparse systems, while Lehoucq and Scott [81] give an evaluation of various software for the computation of eigenvalues of sparse non-symmetric matrices. Bai [10] reports on the progress of the numerical solution of the non-symmetric eigenvalue problem for real matrices.

### 6.3.2. The Arnoldi method

In his seminal article, Arnoldi [7] introduced a *principle of minimized iterations* to approximate a subset $\{\tilde{\lambda}_i^{\boldsymbol{A}}\}_{i=1}^{M}$ of the spectrum of a real non-symmetric matrix $\boldsymbol{A}$. Without loss of generality, assume that the elements of a spectrum are sorted in decreasing order with respect to their real part, i.e. $\Re\lambda_k \geq \Re\lambda_{k+1}$. In essence, the concept comprises the construction of an orthonormal basis of the Krylov subspace of order $M$, i.e.

$$\mathcal{K}_M(\boldsymbol{A}, \boldsymbol{v}_1) = \{\boldsymbol{v}_1, \boldsymbol{A}\boldsymbol{v}_1, \ldots, \boldsymbol{A}^{M-1}\boldsymbol{v}_1\} \tag{6.40}$$

by means of a GRAM-SCHMIDT orthonormalization. The basic statements itemized below are readily found in textbooks on linear algebra; see, e.g., section 6.2 in the seminal book of Saad [127]. Let $\boldsymbol{A} \in \mathbb{R}^{N\times N}$ be a diagonalizable matrix, i.e.

$$\boldsymbol{A} = \boldsymbol{\Phi}\boldsymbol{\Lambda}\boldsymbol{\Phi}^{-1} \quad \text{with} \quad \boldsymbol{\Phi} = [\boldsymbol{\varphi}_k]_{k=1}^{N} \quad \text{and} \quad \boldsymbol{\Lambda} = \operatorname{diag}\{\lambda_k\}_{k=1}^{N}, \tag{6.41}$$

where $(\lambda, \boldsymbol{\varphi})_k$ denotes the $k$-th eigenpair of $\boldsymbol{A}$. Given a number of iterations $M \leq N$ and some initial $\boldsymbol{v}_1$ with $\|\boldsymbol{v}_1\| = 1$, the goal of the ARNOLDI algorithm is to obtain a factorization

$$\boldsymbol{A}\boldsymbol{V} - \boldsymbol{V}\boldsymbol{H} = \boldsymbol{r}\boldsymbol{e}_M^{\mathsf{T}} \quad \text{with} \quad \boldsymbol{V}^{\mathsf{T}}\boldsymbol{V} = \boldsymbol{I} \quad \text{and} \quad \boldsymbol{V}^{\mathsf{T}}\boldsymbol{r} = \boldsymbol{0}, \tag{6.42}$$

where the eigenpairs of the HESSENBERG matrix $\boldsymbol{H}$ approximate some of the eigenpairs of $\boldsymbol{A}$. Note that the last statement in eq. (6.42) implies that the residual $\boldsymbol{r}$ is orthonormal to the basis $\boldsymbol{V}$. Algorithm (3) provides a flowchart of the procedure.

**Algorithm 3:** The $M$-step ARNOLDI algorithm.

**Data:** matrix $\boldsymbol{A} \in \mathbb{R}^{N\times N}$, number of iterations $M \leq N$, initial vector $\boldsymbol{v}_1$ with $\|\boldsymbol{v}_1\| = 1$
**Result:** orthonormal basis $\boldsymbol{V} = [\boldsymbol{v}_k]_{k=1}^{M}$, upper HESSENBERG matrix $\boldsymbol{H} = H_{ij}\boldsymbol{e}_i \otimes \boldsymbol{e}_j$, residual $\boldsymbol{r}$ s.t. $\boldsymbol{A}\boldsymbol{V} - \boldsymbol{V}\boldsymbol{H} = \boldsymbol{r}\boldsymbol{e}_M^{\mathsf{T}}$.

```
/* first iteration of ARNOLDI factorization                    */
1  r := A v_1; H_{1,1} := ⟨r, v_1⟩; r := r − H_{1,1} v_1;
2  for k = 2, M do
3  |   H_{k,k−1} := √⟨r, r⟩;
4  |   v_k := r / H_{k,k−1};
5  |   r := A v_k;
6  |   for j = 1, k do
7  |   |   H_{j,k} := ⟨r, v_j⟩;
8  |   |   r := r − H_{j,k} v_k;
9  |   end
10 end
```

**Note 6.6** (Properties of the ARNOLDI method)**.** *Saad [127] formulates some general remarks on the* ARNOLDI *method:*

1. *If the initial vector $\boldsymbol{v}_1$ is exactly in an $r$-dimensional invariant subspace of the matrix $\boldsymbol{A}$, the iteration breaks down after $r$ steps because $\|\boldsymbol{v}_r\| = 0$; cf. alg. (3: line 4). This also implies that the extracted eigenvalues $\{\tilde{\lambda}_i^{\boldsymbol{A}}\}_{i=1}^{r}$ are exact. However, for randomly generated initial vectors, the probability of this scenario decreases rapidly with the matrix dimension $N$.*

2. *The vector norm applied in alg. (3) does not affect the validity of the results, but may have severe influence on the rate of convergence.*

3. *Saad [124] further states that a „[...] typical case of poor performance is when the eigenvalues that are to be computed are clustered while the unwanted ones have a very favorable separation [...]“.*

4. *In view of a numerical implementation, it is worth noting that an $M$-step* Arnoldi *factorization requires to store and process $M$ vectors of dimension $N$ along with $M$ evaluations of inner products. Hence, for very large matrices $\boldsymbol{A}$, obtaining convergence by increasing $M$ becomes prohibitive due to the computational requirements.*

5. *For a given matrix $\boldsymbol{A}$, the number of iterations $M$ required to obtain convergence depends on the initial vector $\boldsymbol{v}_1$ as well as on the number of desired eigenvalues $\tilde{\lambda}_k^{\boldsymbol{A}}$. Fazeli et al. [46] discuss an appropriate choice of the subspace iteration parameters by recursive application.*

Assuming that $\boldsymbol{H}$ is diagonalizable, i.e.

$$\boldsymbol{H}\boldsymbol{W} = \boldsymbol{W}\boldsymbol{\Lambda}_M \quad \text{with} \quad \boldsymbol{W} = [\boldsymbol{w}_k]_{k=1}^M \quad \text{and} \quad \boldsymbol{\Lambda}_M = \operatorname{diag}\{\tilde{\lambda}_k\}_{k=1}^M, \tag{6.43}$$

multiplying eq. (6.42) from the right with $\boldsymbol{W}$ and exploiting eq. (6.43) yields

$$\boldsymbol{r}\boldsymbol{e}_M^{\mathsf{T}}\boldsymbol{W} = \boldsymbol{A}\boldsymbol{V}\boldsymbol{W} - \boldsymbol{V}\boldsymbol{H}\boldsymbol{W} = \boldsymbol{A}\boldsymbol{\Phi}_M - \boldsymbol{\Phi}_M\boldsymbol{\Lambda}_M, \tag{6.44}$$

where $\boldsymbol{V}\boldsymbol{W} =: \boldsymbol{\Phi}_M = [\tilde{\boldsymbol{\varphi}}_k]_{k=1}^M$ are the approximations of the eigenvectors of $\boldsymbol{A}$. By computing the norm of the rightmost expression in eq. (6.44) row-wise, one obtains

$$\|(\boldsymbol{A} - \tilde{\lambda}_i\boldsymbol{I})\tilde{\boldsymbol{\varphi}}_i\| = H_{M+1,M}|\langle \boldsymbol{w}_i, \boldsymbol{e}_M\rangle|, \tag{6.45}$$

implying that the approximation quality of the eigenpairs $\{(\tilde{\lambda}, \tilde{\boldsymbol{\varphi}})_k\}_{k=1}^M$ can be assessed solely from the information contained in $\boldsymbol{H}$.

**Note 6.7** (Approximation of eigenpairs.)**.** *However, note that for an eigenpair $(\lambda, \boldsymbol{\varphi})$, it holds that*

$$\|(\boldsymbol{A} - \lambda\boldsymbol{I})\boldsymbol{\varphi}\| = \|\psi(\boldsymbol{A} - \lambda\boldsymbol{I})\boldsymbol{\varphi}\| \quad \textit{for all} \quad \psi \in \mathbb{C} \quad \textit{such that} \quad |\psi| = 1. \tag{6.46}$$

*The implications of eq. (6.46) are crucial for the interpretation of the approximated eigenpairs. Assume that $H_{M+1,M} = 0$, implying that $\boldsymbol{V}$ is an $M$-dimensional subspace of $\boldsymbol{A}$ and the eigenvalues of $\boldsymbol{H}$ are a subset of the spectrum $\sigma(\boldsymbol{A})$. For $\lambda \in \mathbb{R}$, the associated eigenvector can only be determined up to its sign. If $\lambda \in \mathbb{C}$, the associated eigenvector can only be determined up to a rotation in the complex plane. The figure on the right illustrates the complex rotations $\psi_k$ obtained from a full factorization of a randomly generated real matrix. While the $\psi_k$ occur with their respective conjugate as expected, their distribution on the unit circle exhibits no evident pattern, implying that even if the number $M$ of* Arnoldi *iterations coincides with the matrix dimension, the eigenvectors are not retrieved in general. In other words, the* Arnoldi *method produces*

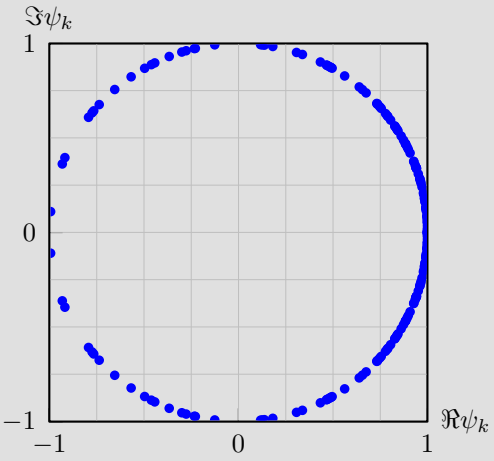

*approximated eigenvalues $\tilde{\lambda}$ along with associated **eigenspaces**, where the basis is arbitrary. Ravibabu and Singh [115] introduce a variant of the* Arnoldi *method capable of also approximating the corresponding eigenvectors, where the authors exploit residuals for the assessment.*

Following Sorensen [132], we introduce a convergence measure by normalizing eq. (6.45) with the spectral norm of $\boldsymbol{H}$, corresponding to the maximum singular value, i.e.

$$\gamma_M^k := \frac{H_{M+1,M}|\langle \boldsymbol{w}_k, \boldsymbol{e}_M \rangle|}{\|\boldsymbol{H}\|_2} = \frac{\|\boldsymbol{r}\||\langle \boldsymbol{w}_k, \boldsymbol{e}_M \rangle|}{\|\boldsymbol{H}\|_2}. \tag{6.47}$$

An eigenvalue $\tilde{\lambda}_k^{\boldsymbol{A}}$ can be considered converged if the associated $\gamma_M^k$ becomes smaller than some prescribed tolerance. The appropriate choice of a tolerance is of course problem-dependent; e.g., Bennani and Braconnier [15] motivate various stopping criteria for eigensolvers based on the Arnoldi method.

**Spectral properties** Saad [123] has shown that the Arnoldi algorithm immanently tends to extract the envelope of the spectrum first, i.e. those eigenvalues with largest magnitude. To see this, recall that the underlying Krylov basis, cf. eq. (6.40), is composed of products of $\boldsymbol{v}_1$ with powers of $\boldsymbol{A}$ up to and including $M$. In fact, after $M$ iterations of the Arnoldi algorithm, the residual is $\boldsymbol{r}_{M+1} = p_M(\boldsymbol{A})$, where $p_M(\boldsymbol{A})$ is polynomial of order $M$. Expanding $\boldsymbol{v}_1$ in the eigenvectors of $\boldsymbol{A}$ yields

$$\boldsymbol{r}_{M+1} = \sum_{k=1}^{N} \langle \boldsymbol{\varphi}_k^{\boldsymbol{A}}, \boldsymbol{v}_1 \rangle p_M(\lambda_k^{\boldsymbol{A}}) \boldsymbol{\varphi}_k^{\boldsymbol{A}}. \tag{6.48}$$

A random initial vector $\boldsymbol{v}_1$ exhibits components of all eigenvectors in general, i.e. $\langle \boldsymbol{\varphi}_k^{\boldsymbol{A}}, \boldsymbol{v}_1 \rangle \neq 0$ for all $1 \leq k \leq N$. Hence, for increasing $M$, the respective components are amplified as $|\lambda_k^{\boldsymbol{A}}|^M$, implying that the eigenvalues with the largest magnitude, i.e. those on the envelope, become dominant. Since we are interested in the leading eigenvalues of $\boldsymbol{A}$, i.e. those with the algebraically largest real part, a direct application to $\boldsymbol{A}$ is disadvantageous. Eriksson and Rizzi [42] suggested combining the Arnoldi method with a spectral transformation, which maps the respectively interesting part of $\sigma(\boldsymbol{A})$ to the envelope. As we seek to extend the work of Albert et al. [4], in the present case an exponential transformation is applied as well. Meerbergen and Roose [93] provide an overview over other matrix transformations for finding the rightmost eigenvalues of large, sparse non-symmetric matrices.

**Exponential transformation of complex numbers** For a complex number $\lambda$, the exponential transformation with $T \in \mathbb{R}^+$ reads

$$\exp(T\lambda) = \exp(T\Re\lambda)\left[\cos(T\Im\lambda) + \imath \sin(T\Im\lambda)\right]. \tag{6.49}$$

To illustrate some of the basic effects of the transformation for an exemplary spectrum, fig. (6.4) considers the unit circle centered at the origin of the complex plane. While for $T = 0$ the circle degenerates to a single point on the real axis, the spectrum is expanded for increasing $T$. Obviously, the elements of the spectrum with the largest real part (here: $\lambda_1 = 1 + \imath 0$) become those with largest magnitude, i.e. they are mapped to the envelope of the spectrum as desired. The evolution of the referential points between $T = 1$

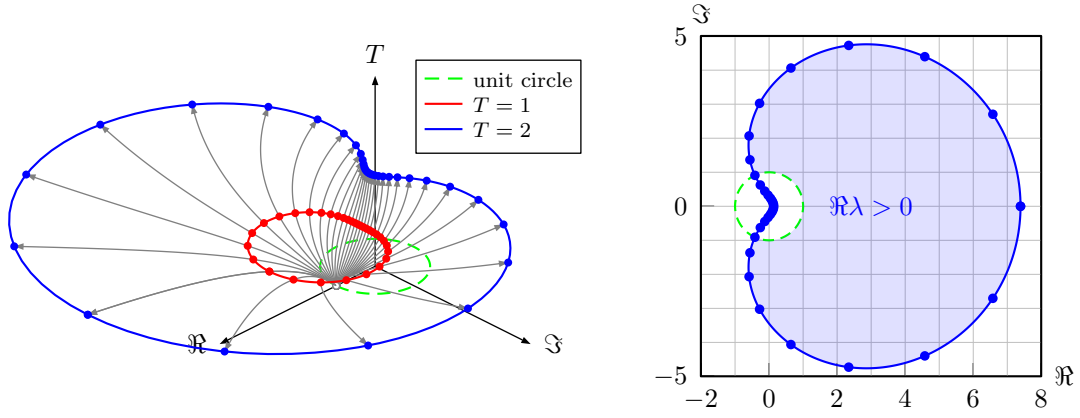


(a) expanding tube

(b) tube section ($T = 2$)

Figure 6.4.: Effect of exponential transformation $\exp(T\lambda)$ on the unit circle for $T \in [0, 2]$. (a): expanding tube with arrows indicating the trajectories of the referential points (equally distributed on the unit circle). (b): tube section for $T = 2$, where the shaded area corresponds to the part of the referential spectrum located in the right complex half-space.

and $T = 2$, corresponding to • and • in fig. (6.4(a)), respectively, indicates another favorable property: as can be seen from fig. (6.4(b)), the referential points within the left complex half-space are shifted closer to the origin as $T$ increases. The part of the spectrum located in the right complex half-space, however, is expanded. This effect helps to alleviate the influence of disadvantageous clustering described by Saad [124] by spreading the eigenvalues; cf. note (6.6).

**Note 6.8** (Choice of transformation parameter $T$)**.** *The above statements may suggest the choice of large values for $T$, irrespective of the underlying system. Besides limitations induced by numerical round-off errors, there is another consideration to bear in mind: in the context of the application within a flow solver, the system under consideration is not linear. Hence, increasing the value of $T$, corresponding to a longer (physical) simulation time, may cause non-linear effects to take over, which is especially the case for unstable leading eigenvalues.*

**Random matrix example** In order to get an idea of the performance of the Arnoldi algorithm, a numerical experiment is conducted employing a matrix with randomly generated eigenvalues. The matrix $\boldsymbol{A}$ is a composition of $N$ $2 \times 2$ normal blocks, i.e.

$$\boldsymbol{A} = \begin{bmatrix} \boldsymbol{A}_1 & & \\ & \ddots & \\ & & \boldsymbol{A}_N \end{bmatrix} \quad \text{with} \quad \boldsymbol{A}_k = \begin{bmatrix} a_k & b_k \\ -b_k & a_k \end{bmatrix} \tag{6.50}$$

with spectrum $\sigma(\boldsymbol{A}) = \{a_k \pm \imath b_k\}_{k=1}^{N}$. Figure (6.5) gathers the results.

While the instances depicted below were selected with regard to their illustrative character, they consi-

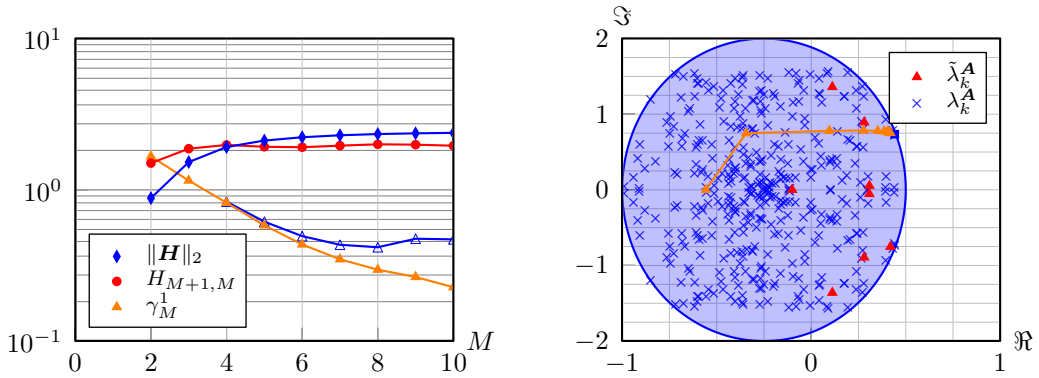


(a) detection of leading eigenvalue (success)

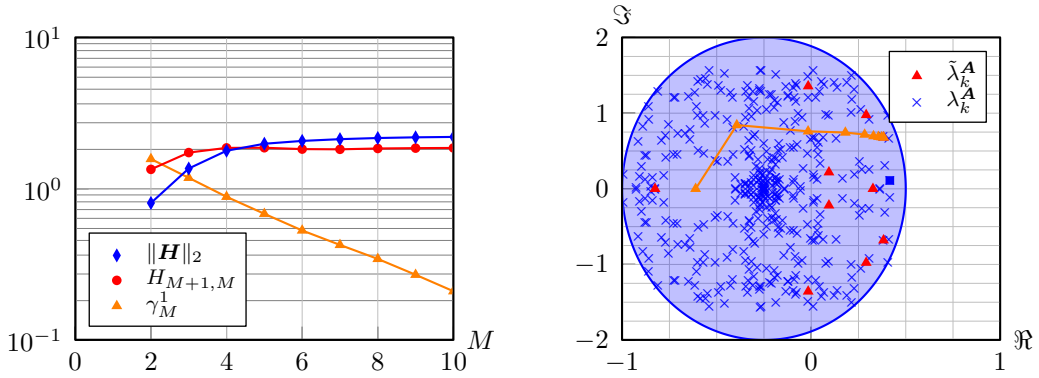


(b) detection of leading eigenvalue (fail)

Figure 6.5.: Illustration of instances of the ARNOLDI method ($M = 10$) applied on exponentially transformed ($T = 2$) matrices from eq. (6.50) for $N = 200$. Left colum: convergence measure from eq. (6.47), spectral norm of HESSENBERG matrix and residual norm $H_{M+1,M} = \|\boldsymbol{r}\|$; cf. alg. (3). Right column: randomly generated spectra, where the eigenvalue of algebraically largest real part is (■).

tute a prototypical set. Therefore, their implications are qualitatively representative for this preliminary assessment. The main observations can be summarized as follows:

1. Contrary to the conjecture of Albert et al. [4], the norm of the residual is not a suitable measure for the convergence of an approximated eigenvalue $\tilde{\lambda}_k^{\boldsymbol{A}}$ in general. To see this, consider the left column in fig. (6.5). As the number of iterations $M$ increases, the norm of the residual $\|\boldsymbol{r}\| = H_{M+1,M}$ remains virtually constant. In fact, as can be seen from the decomposition in eq. (6.48), there is no obvious reason for the norm of the residual to decrease with an increasing number of iterations $M$, irrespective of the transformation applied to $\boldsymbol{A}$.

2. Despite the fact that the convergence measure $\gamma_M^k$, cf. eq. (6.47), allows for a substantiated assessment of the approximation quality, the leading eigenvalue of $\boldsymbol{H}$ does not necessarily, and, in general, will not approximate the leading eigenvalue of $\boldsymbol{A}$, as can be seen from comparison of figs. (6.5(a)) and (b). If one seeks to employ a number of iterations which is small compared to the matrix size, i.e. if $\frac{M}{N} \ll 1$, our numerical experiments have found this effect to occur. A close inspection of the

right panel in fig. (6.5(a)) exhibits that the leading eigenvalue (■) is located within a cluster, which is approximated by $\tilde{\lambda}_1^{\boldsymbol{A}}$. Especially in cases where these clusters are close to the imaginary axis, the interpretation of converged eigenvalues requires great care.

As stated by Saad [127], cf. note (6.6) above, the number of iterations $M$ required for sufficiently accurate extraction of the leading eigenvalue may become prohibitively large. While convergence was obtained in the present numerical experiment, recall that $\frac{M}{N} = 2.5 \times 10^{-2}$, which can be considered too large for the desired application in a numerical flow solver. This result is in accordance with a revisited version of the numerical experiment conducted by Albert et al. [4, fig. 6]. Figure (6.6) depicts the continuous (gray disk) and discrete (gray dots) spectra of the matrix under consideration, where □, ∘ and × correspond to the approximated eigenvalues. For ratios $\frac{M}{N} \ll 1$, large values of $T$ are required to extract the leading eigenvalue. However, note (6.8) has shown that this features numerical difficulties.

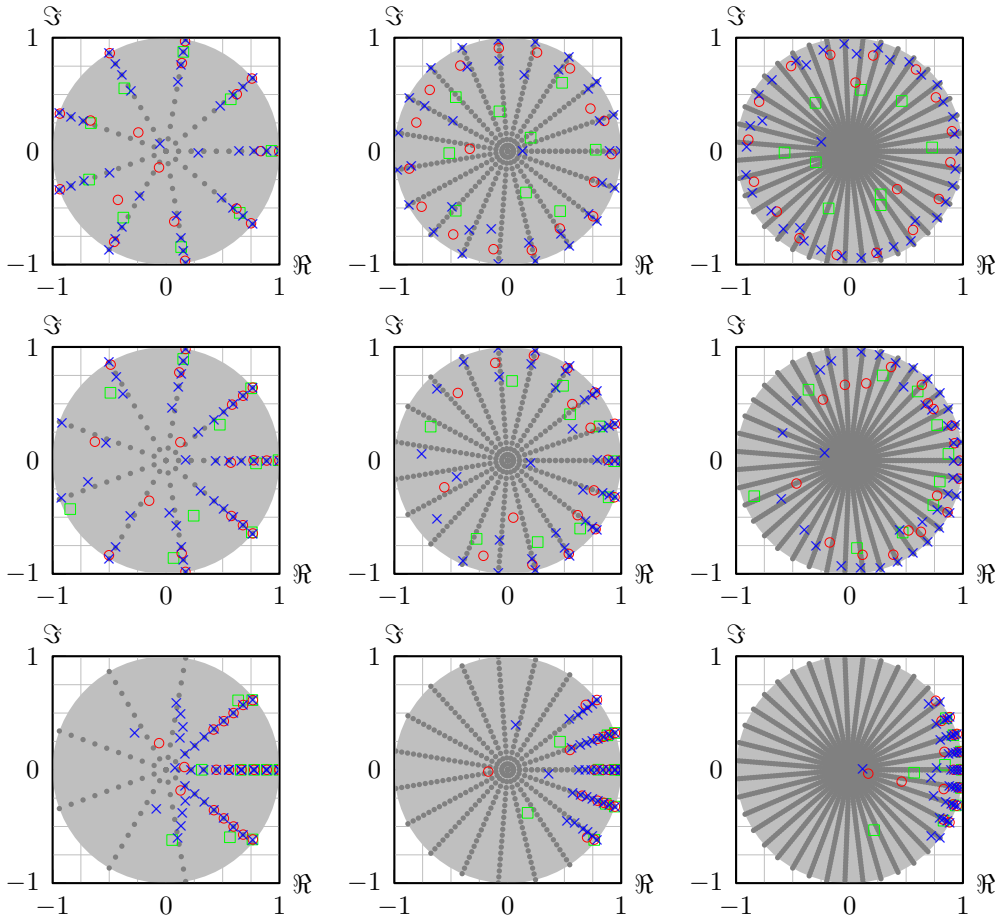


Figure 6.6.: Performance analysis of Arnoldi algorithm from Albert et al. [4] (center row, $T = 1$) revisited (top/bottom row) for varying number of iterations $M$ and evolution times (top row: $T = 10^{-1}$, center row: $T = 1$, bottom row: $T = 5$) with $M = 10$ (□), $M = 20$ (∘) and $M = 40$ (×) iterations for matrix of size $N \in \{100, 400, 1600\}$ (left to right).

Hence, the next subsection introduces an modified version of the Arnoldi algorithm which is implicitly restarted in order to reduce the computational effort in terms of storage.

### 6.3.3. The implicitly restarted Arnoldi method (IRAM)

As stated in note (6.6) above, the convergence behavior of the ARNOLDI method is affected by the choice of the initial vector $\boldsymbol{v}_1$. In cases where achieving convergence by naively increasing the number of iterations $M$ is not feasible, it is advantageous to restart the factorization after a given number of iterations, resorting to an updated initial vector. Since the previous factorization contains an approximation of the desired spectrum, the unwanted elements can be filtered from the orthonormal basis $\boldsymbol{V}$, cf. alg. (3), by means of a $QR$-factorization. Sorensen [132] put forth this idea by introducing an *implicitly restarted* ARNOLDI iteration; cf. alg. (4) for a commented flowchart. The concept can be outlined as follows: Select a number of ARNOLDI iterations $M$ and a number of desired eigenvalues $K < M$. After performing $M$ iterations of the ARNOLDI method (alg. (4: lines 1-13)), an eigendecomposition of $\boldsymbol{H}$ is performed (alg. (4: lines 14-18)), where the $\tilde{\lambda}_k$ are sorted in descending order with respect to their real part. If the convergence measures $\gamma_M^k$ associated to the first $K$ eigenvalues of the HESSENBERG matrix are below the prescribed tolerance $\epsilon$, the algorithm terminates. Otherwise, the last $M - K$ eigenvalues, corresponding to the *undesired* part of the spectrum, are selected as shifts $\{\mu_s\}_{s=1}^{M-K}$. By means of a $QR$-factorization, cf. alg. (4: lines 20-28), the matrix $\boldsymbol{H}$ is modified. After the application of all shifts, the orthonormal basis is rotated accordingly; cf. alg. (4: lines 29-32).

**Note 6.9** (Numerical implementation)**.** *Some comments on the numerical implementation are at order:*

1. *The selection of the shifts $\{\mu_s\}_{s=1}^{M-K}$ may be carried out by any appropriate criterion.*
2. *In order to ensure that real arithmetics can be maintained throughout, Golub and Loan [56] introduced a so-called double-shift startegy, i.e. any complex shift $\mu_s$ is applied together with its conjugate $\mu_s^*$; cf. alg. (4: line 24). Since the number of complex and real eigenvalues of $\boldsymbol{H}$ is not known a priori, the number of applied shifts (including the respective conjugates) is not neccessarily equal to $M - K$. Thus, we introduce the effective number of applied shifts $p$, ensuring that at most $M - K$ shifts are applied.*
3. *The eigendecomposition in alg. (4: line 14) is carried out using the `LAPACK` routine `dgeev`.*
4. *The QR-factorization in alg. (4: lines 20-28) employs the `LAPACK` routine `dgeqrfp`.*

Sorensen [132] suggests an error tolerance of $\epsilon = 10^{-16}$ for the assessment of the eigenpair convergence in terms of $\gamma_M^k$; cf. alg. (4: line 16) and eq. (6.47). Conducting several numerical experiments has shown, however, that such a small tolerance implies a large number of restarts, each corresponding to a full $M$-step ARNOLDI factorization. If one is only interested in a small number of (leading) eigenpairs, say, e.g. $K = 2$, we have found empirically that $\epsilon = 10^{-6}$ is sufficient. However, the tolerance may vary for different applications.

**Algorithm 4:** Implicitly restarted ARNOLDI algorithm; cf. Sorensen [132].

**Data:** matrix $\boldsymbol{B} \in \mathbb{R}^{N \times N}$, initial vector $\boldsymbol{V}_1 \in \mathbb{R}^N$ with $\|\boldsymbol{V}_1\| = 1$, tolerance $\epsilon > 0$, number of ARNOLDI iterations $M \leq N$, number of desired eigenvalues $K < M$, max. number of restarts $N_{\text{restart,max}}$

/* first iteration of ARNOLDI factorization */

$\boldsymbol{r} := \boldsymbol{B}\boldsymbol{v}_1$; $H_{1,1} := \langle \boldsymbol{r}, \boldsymbol{v}_1 \rangle$; $\boldsymbol{r} := \boldsymbol{r} - H_{1,1}\boldsymbol{v}_1$;

$p := M - 1$; $n_{\text{restart}} := 0$;

**while** $n_{\text{restart}} \leq N_{\text{restart,max}}$ **do**

  $n_{\text{restart}} = n_{\text{restart}} + 1$;

  /* extend ARNOLDI factorization */

  **for** $k = M - p + 1, M$ **do**

    $H_{k,k-1} := \|\boldsymbol{r}\|$;

    $\boldsymbol{v}_k := \frac{\boldsymbol{r}}{H_{k,k-1}}$;

    $\boldsymbol{r} := \boldsymbol{B}\boldsymbol{v}_k$;

    **for** $j = 1, k$ **do**

      $H_{j,k} := \langle \boldsymbol{r}, \boldsymbol{v}_j \rangle$;

      $\boldsymbol{r} := \boldsymbol{r} - H_{j,k}\boldsymbol{v}_k$;

    **end**

  **end**

  $\boldsymbol{W}\boldsymbol{\Lambda}_M\boldsymbol{W}^{-1} = \boldsymbol{H}$ with $\Re\tilde{\lambda}_k \geq \Re\tilde{\lambda}_{k+1}$; /* compute eigenvalues/-vectors */

  $\gamma_M^k := \frac{|\langle \boldsymbol{w}_k, \boldsymbol{e}_M \rangle| \|\boldsymbol{r}\|}{\|\boldsymbol{H}\|_2}$; /* evaluate error estimates */

  **if** $\gamma_M^k \leq \epsilon \; \forall \; 1 \leq k \leq K$ **then**

    **done** ; /* convergence of $K$ eigenvalues with largest real part */

  **end**

  $\{\mu_s\}_{s=1}^{M-K} = \{\tilde{\lambda}_k\}_{K+1}^{M}$; $p := 1$; $\boldsymbol{T} := \boldsymbol{I}$; /* get $M - K$ shifts with smallest real part */

  /* apply at most $M - K$ shifts using $QR$-factorization */

  **while** $p < M - K - 1$ **do**

    **if** $\Im\mu_p = 0$ **then**

      $\boldsymbol{Q}\boldsymbol{R} = \boldsymbol{H} - \mu_p\boldsymbol{I}$; $p := p + 1$; /* real (single) shift */

    **else**

      $\boldsymbol{Q}\boldsymbol{R} = (\boldsymbol{H} - \mu_p\boldsymbol{I})(\boldsymbol{H} - \mu_p^*\boldsymbol{I})$; $p := p + 2$; /* complex (double) shift */

    **end**

    $\boldsymbol{T} := \boldsymbol{T}\boldsymbol{Q}$; /* collect rotation */

    $\boldsymbol{H} := \boldsymbol{Q}^{\mathsf{T}}\boldsymbol{H}\boldsymbol{Q}$; /* update HESSENBERG matrix */

  **end**

  $\boldsymbol{V} := \boldsymbol{V}\boldsymbol{T}$; /* apply rotation to ARNOLDI basis */

  $\boldsymbol{r} := \boldsymbol{V}_{M-p+1}H_{M-p+1,M-p} + T_{M,M-p}\boldsymbol{r}$; /* update residual */

  $\boldsymbol{H} := \sum_{i=1}^{M-p}\sum_{j=1}^{M-p} H_{ij}\boldsymbol{e}_i \otimes \boldsymbol{e}_j$; /* extract reduced HESSENBERG matrix */

  $\boldsymbol{V} := [\boldsymbol{v}_k]_{k=1}^{M-p}$; /* extract reduced ARNOLDI basis */

**end**

## 6.4. The numerical algorithm

Finally, the numerical algorithm can be assembled as depicted in fig. (6.7). Let us recall for reading convenience that we seek to approximate the leading eigenvalues of the JACOBIAN of $\boldsymbol{f}$ at the steady state $\boldsymbol{\chi}_0$ from its exponential $\boldsymbol{B}_0(T) := \exp(T\boldsymbol{A}_0)$ with $\boldsymbol{A}_0 := \boldsymbol{J}_{\boldsymbol{f}}(\boldsymbol{\chi}_0)$ and some $T > 0$.

Starting from a steady state provided by the flow solver FS3D, cf. section 3.1, an initial volume-invariant perturbation $\boldsymbol{\zeta}_1 \in \boldsymbol{X}(L_\Sigma, 0)$ is randomly generated and normalized, where the details are given in subsection 6.2.1. From the perturbation $\boldsymbol{\zeta}_k$, the initial conditions $\boldsymbol{\chi}^{\text{ini}}_{k\pm}$ are computed by superposition with the steady state $\boldsymbol{\chi}_0$, transformed according to eq. (6.26) and imposed to the flow solver. After performing $N$ time steps of size $\Delta t$, the evolved states $\boldsymbol{\chi}_\pm$ are transformed to the referential domain; cf. fig. (6.8(b)). The action of $\boldsymbol{B}_0$ on the perturbation $\boldsymbol{\zeta}_k$ is inferred according to eq. (6.12), corresponding to the ARNOLDI algorithm (alg. (3: line 5)). The next perturbation $\boldsymbol{\zeta}_{k+1}$ is computed from its predecessors as in alg. (3: lines 6-9), simultaneously populating the HESSENBERG matrix. Note that the pendant of the residual $\boldsymbol{r}$ in alg. (3) is $\boldsymbol{\zeta}_{k+1}$. Once $M$ iterations are performed, the algorithm terminates.

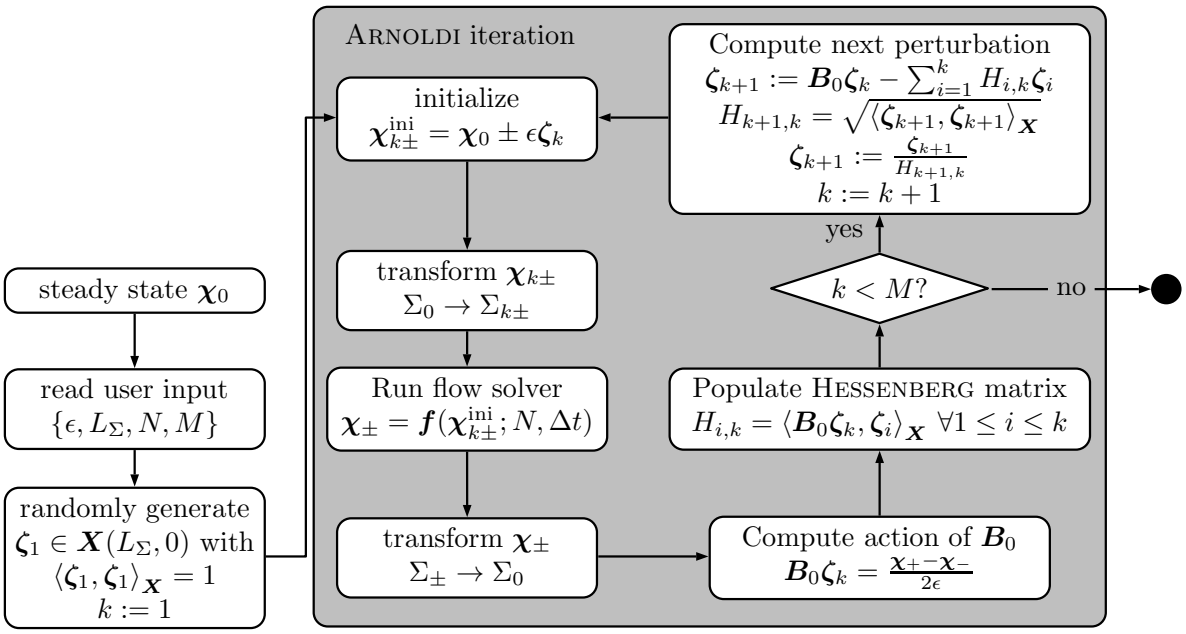


Figure 6.7.: Flowchart of the global linear stability analysis employing the ARNOLDI method of alg. (3), where the transformations from subsection 6.2.2 are shown in fig. (6.8).

Inverting the exponential transformation allows to obtain the approximate eigenvalues of $\boldsymbol{A}_0$ from the HESSENBERG matrix via

$$\tilde{\lambda}_k^{\boldsymbol{A}_0} = \frac{\log \lambda_k^{\boldsymbol{H}}}{N\Delta t}, \tag{6.51}$$

where the associated eigenvectors are computed from eq. (6.44). However, recall that they only provide an approximation to the *eigenspace*, whose basis can be chosen arbitrarily; cf. note (6.7). For ease of notation, the matrix superscript for the approximated eigenvalues is formally omitted henceforth.

To understand the concept of the numerical domain transformation, recall from fig. (6.2) that $\boldsymbol{x}'$ and $\boldsymbol{x}$ denote the coordinates in the referential and evolved system, respectively. The hypersurfaces required

for the transformation, cf. subsection 6.2.2, are obtained from the superposition of the coefficient vectors $\boldsymbol{c}_\Sigma$ belonging to the steady state $\boldsymbol{\chi}_0$ and the perturbtion $\boldsymbol{\zeta}_k$; cf. eq. (2.20). The transformation from the referential to the evolved system requires the velocity of the steady state $\boldsymbol{u}'_0(\boldsymbol{x})$ and the perturbation $\Delta\boldsymbol{u}'(\boldsymbol{x})$ to be given at the nodes of the CARTESIAN grid, denoted by $\boldsymbol{y}$. In order to apply the inverse spatial transformation to obtain $\boldsymbol{x} = \boldsymbol{T}(\boldsymbol{x}') = \boldsymbol{y}$, an interpolation of the velocity $\boldsymbol{u}'(\boldsymbol{y})$ to $\boldsymbol{x}' = \boldsymbol{T}^{-1}(\boldsymbol{y})$ is required. Due to the staggered arrangement of the velocities, cf. again section 3.1, the JACOBIAN of the transformation $\boldsymbol{J_T}$ is computed componentwise for the respective face. While the transformation preserves the solenoidal character of $\boldsymbol{u}$, the interpolation in fig. (6.8(a)) introduces deviations. Hence, a pressure projection is applied the obtain a numerically divergence-free velocity. Transforming the velocity of an evolved to the referential state works in the same way, with the difference that the transformation $\boldsymbol{T}$ is based on the coefficient vector $\boldsymbol{c}_\Sigma$ obtained from the hypersurface extraction given in section 3.2.

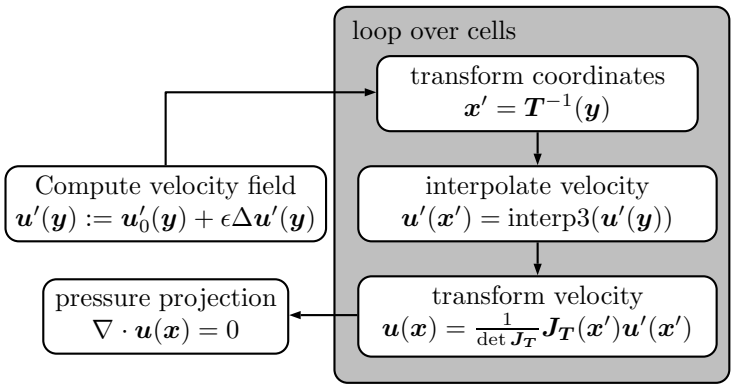


(a) $\Sigma_0 \rightarrow \Sigma_\pm$ (referential to evolved)

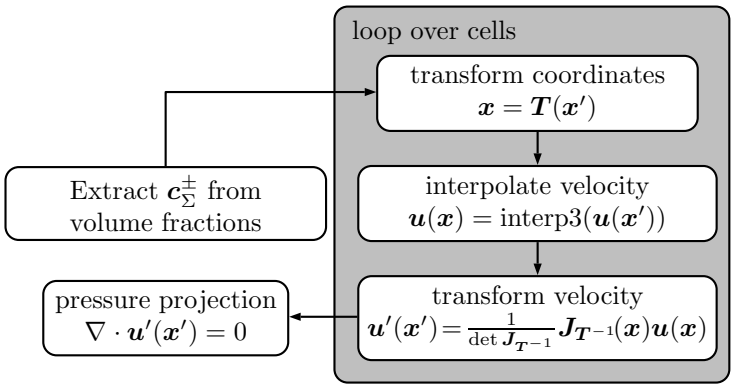


(b) $\Sigma_\pm \rightarrow \Sigma_0$ (evolved to referential)

Figure 6.8.: Transformation of the velocity $\boldsymbol{u}$ as shown in fig. (6.2).

## 6.5. Numerical results

The present section applies the stability algorithm introduced above to two prototypical flows. The first configuration is a stagnant fluid particle in zero gravity, which sustains its spherical shape due to surface tension. The NAVIER-STOKES equations, cf. section 2.1, provide the rationale behind this

choice, since they admit a trivial solution for an initially spherical droplet. If a small perturbation is applied, surface tension restores the spherical shape, where non-vanishing viscosities imply that the amplitude tends to zero for large times. In terms of physics, the present configuration is unconditionally stable, i.e. the spectrum is located entirely in the left complex half-plane. A numerical discretization, however, enriches the spectrum by artificial components, implying that the stability of the physical state is potentially degraded. A candidate prone to introduce eigenvalues with positive real parts is the inaccurate approximation of surface tension forces. The source of these errors is the numerical computation of curvature, as has been shown in chapter 5. The resulting *parasitic* or *spurious currents*, cf. subsection 4.6.6 are a well-known phenomenon in the literature. E.g., Harvie et al. [62] derive a correlation of magnitudes of spurious velocities for a wide range of physical and numerical parameters. Their findings include that, irrespective of refining the spatial or temporal resolution, the magnitudes do not decrease. Hence, the application of stability analysis of this configuration allows separately assessing the stability properties of the underlying discretization. In view of the numerical investigation of highly viscous droplets, cf. section 3.4, the second configuration is a fluid particle freely rising in an ambient fluid due to buoyancy. As shown by the numerical investigation of Albert et al. [5], cf. section 3.4, the paths and shapes of corn oil droplets rising in tap water undergo a transition: while droplets with a diameter $d \leq 2.6\text{mm}$ remain nearly spherical while rising on vertical paths, sidewards migration is observed for $d = 3.2\text{mm}$. The onset of this first path instability was found to be weakly observable for the 2.6mm droplet, where the bifurcation is induced by the accumulation of vorticity, causing the paths to become oblique after forming a bifid wake. The investigation of this transition is the motivation for the choice of the second configuration. Figure (6.9) sketches the numerical setup of the configurations depicted above.

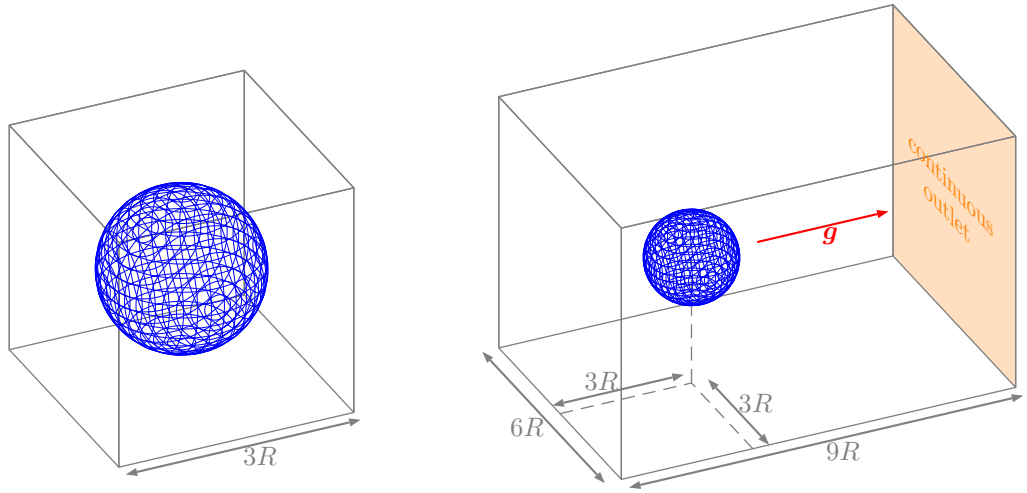


Figure 6.9.: Numerical setup for flow solver for stagnant (left) and buoyant (right) droplets.

### 6.5.1. Stagnant droplet in zero gravity

The algorithm for the linear stability analysis developed above is first applied to stagnant fluid particles in zero gravity. In terms of physical parameters, we consider two sets of pairings for the droplet and ambient material, namely **water/air** and **corn oil/water**. The simulation domain $\Omega$ is a cuboidal box with edge length $3R$, within which a sphere of radius $R$ is initialized using the algorithm presented in

chapter 4. See the left panel in fig. (6.9) for an illustration. In terms of nondimensional numbers, the stagnant viscous droplet of radius $R$ in zero gravity is characterized by the LAPLACE number

$$La = \frac{\sigma \rho R}{\mu^2}, \tag{6.52}$$

which is defined using the material properties of the droplet and can be understood as the ratio of surface tension to viscous dissipation. The LAPLACE number $La$ is varied by the droplet radius $R \in \{2, 4, 6, 10\}$mm. For the material parameters of the systems given above, we obtain $La = \mathcal{O}(10^1)$ and $La = \mathcal{O}(10^5)$, corresponding to the limiting cases of a *weak* and *strong* influence of dissipation. Once again employing the material parameters of the particle, the eigenvalues are normalized by the time scale

$$\tau = \frac{R\mu}{\sigma}. \tag{6.53}$$

The material parameters are

$$\begin{aligned} \rho_{\text{water}} &= 1 \frac{\text{g}}{\text{cm}^3}, \quad \rho_{\text{air}} = 1.1 \times 10^{-3} \frac{\text{g}}{\text{cm}^3}, \quad \rho_{\text{cornoil}} = 0.97 \frac{\text{g}}{\text{cm}^3}, \\ \mu_{\text{water}} &= 10^{-2} \frac{\text{g}}{\text{cm s}}, \quad \mu_{\text{air}} = 1.8 \times 10^{-3} \frac{\text{g}}{\text{cm s}}, \quad \mu_{\text{cornoil}} = 45 \times 10^{-2} \frac{\text{g}}{\text{cm s}}, \\ \sigma_{\text{water/air}} &= 72.86 \frac{\text{g}}{\text{s}^2}, \quad \sigma_{\text{cornoil/water}} = 20.1 \frac{\text{g}}{\text{s}^2}. \end{aligned} \tag{6.54}$$

Table (6.1) gathers the resulting LAPLACE numbers $La$, where note (6.10) provides the remaining algorithm parameters.

**Note 6.10** (Parameter variation)**.** *The flow solver resorts to the following parameters:*

1. *For the purpose of this analysis, the box extension $3R$ was chosen, corresponding to a distance of $R/2$ between the interface $\Sigma$ and the domain boundary. This is justified since the deviations from the initial configuration are expected to be small. Furthermore, numerical tests have shown that further increasing the distance to the boundary does have a significant influence on the obtained spectra. At the entire boundary $\partial\Omega$, symmetry conditions are prescribed; cf. section 3.1.*

2. *The simulation domain was decomposed in $N_\Omega = 64$ cells per spatial direction, corresponding to a resolution of $\frac{2N}{3} = 42\frac{2}{3}$ cells per diameter; cf. section 3.1.*

| ***parameter*** | ***description*** | ***range*** |
|---|---|---|
| $L_\Sigma$ | *order of spherical harmonics (cf. eq. (2.18))* | $\{1, 3\}$ |
| $N$ | *number of time steps (cf. fig. (6.7))* | $\{20, 40, 80, 100\}$ |
| $\epsilon$ | *perturbation magnitude (cf. eq. (6.13))* | $\{5 \times 10^{-4}, 1 \times 10^{-3}\}$ |
| $\alpha_T$ | *transformation domain size (cf. subsection 6.2.2)* | 0.2 |

In all cases, the leading eigenvalue $\tilde{\lambda}_1$ is real and positive, i.e. all the cases are unconditionally unstable. As indicated above, the observed instability is of numerical provenience, i.e. it is caused by some component of the numerical discretization. The difference in magnitude between the configuration corn oil/water (fig. (6.10(d))) and water/air (fig. (6.10(b))) is roughly two orders of magnitude, which is in

Table 6.1.: LAPLACE number $La$ and time scales $\tau$ for stangant droplets ($\frac{\tau_{\text{cornoil/water}}}{\tau_{\text{water/air}}}$=163.11).

| $R$ | | 2mm | 4mm | 6mm | 10mm |
|---|---|---|---|---|---|
| **symbol** | | □ | △ | ◇ | • |
| $La$ | **water/air** | $1.46 \times 10^5$ | $2.91 \times 10^5$ | $4.37 \times 10^5$ | $7.29 \times 10^5$ |
| $\tau$ | | 27.45µs | 54.90µs | 82.35µs | 137.21µs |
| $La$ | **corn oil/water** | $1.82 \times 10^1$ | $3.64 \times 10^1$ | $5.46 \times 10^1$ | $9.10 \times 10^1$ |
| $\tau$ | | 4.47ms | 8.95ms | 13.43ms | 22.39ms |

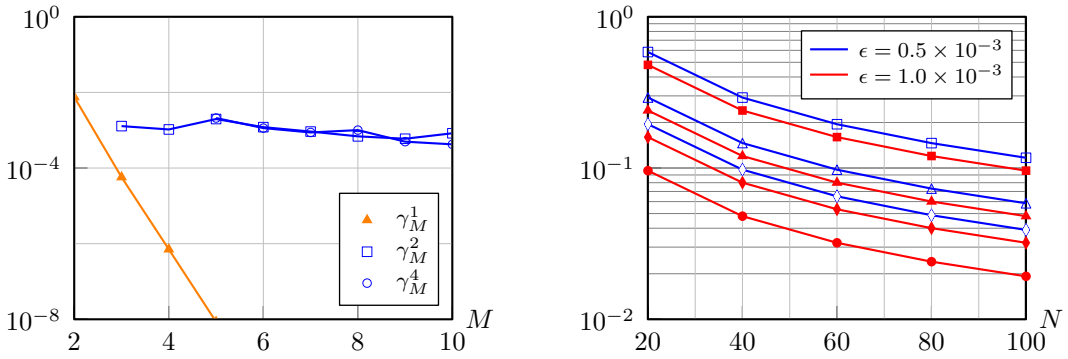


(a) ARNOLDI convergence measure

(b) $\tau\tilde{\lambda}_1$

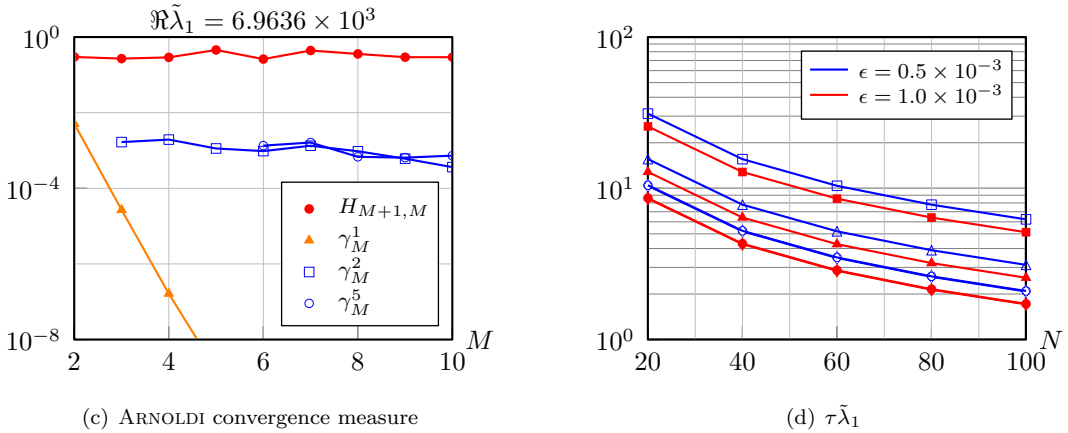


(c) ARNOLDI convergence measure

(d) $\tau\tilde{\lambda}_1$

Figure 6.10.: Leading eigenmodes (right column, nondimensionalized by $\tau$ from eq. (6.53)) and representative convergence measures from eq. (6.47) (left column) for (a)-(b) and water/air and (c)-(d) corn oil/water; cf. tab. (6.1) and note (6.10)

accordance with the ratio of the respective time scales $\tau$; cf. tab. (6.1). Figure (6.11) exhibits the eigenmodes associated to the instability are of parasitic current type, where the spatial structure resembles the volume fraction quality, potentially superposed with the modes induced by the order $L_\Sigma$ of the spherical harmonics expansion; cf. fig. (A.1) for an illustration. Let us note in passing that the spatial patterns observed in fig. (6.11) emerge irrespective of the material pairing or droplet radius, indicating their geometrical provenience, substantiating the findings of Harvie et al. [62]. When comparing the magnitudes of the velocities in the modes, those induced by linear volume fractions are one order of magnitude larger. This is in qualitative accordance with the findings of subsection 4.6.6. While the results for the eigenvectors are robust, the random initial perturbation inherently implies slight differences between the instances. E.g., the bottom row in fig. (6.11) shows a vivid realization of the parasitic currents induced by linear and quadratic volume fractions, which are in very good agreement with the spatial structures of the curvature errors reported in section 5.4. For the first eigenvalue, convergence in the sense of eq. (6.47) is obtained, where $\gamma_M^1$ steeply decreases to $\mathcal{O}(10^{-10})$ for $M = 10$ iterations. The remaining eigenvalues do not exhibit convergence, which is in accordance with the findings from subsection 6.3.2, indicating that only the extraction of the leading eigenvalue is feasible. The fast convergence of $\tilde{\lambda}_1$ is likely to be caused by its isolation within the spectrum, implying that its contribution to the polynomial in eq. (6.48) is dominant, hence indicating the severeness of the numerical influence. However, recall that the normalization employed for the definition of $\gamma_M^k$ involves the spectral norm of $\boldsymbol{H}$, corresponding to the largest singular value. Especially in the presence of isolated eigenvalues with a large real part, this might not be a suitable reference for the remaining spectrum and, hence, tend to underestimate convergence. However, the influence of parasitic currents remains dominant and eliminates the possibility of observing stable modes within a linear analysis. Contrary to intuition, figs. (6.10(b)) and (6.10(d)) show that increasing the perturbation amplitude $\epsilon$ yields lower real parts of the leading eigenvalue. This is explained as follows: the effect of spurious currents is nonlinear, and while the growth is always positive, it decelerates with increasing velocity magnitude. For the same reason, the fact that an increasing number of time steps $N$ yields smaller real parts is in accordance with this conjecture. Note that the convergence analysis in fig. (6.10) shows no difference between linear and quadratic volume fractions in terms of growth rates, while, as discussed above, both the initial conditions and the magnitude of the modes differ. For increasing $La$, cf. tab. (6.1), the magnitude of the leading eigenvalue decreases, which is a direct consequence of the increased radius $R$, and, hence, the decreased curvature, which is causing the spurious currents.

**Note 6.11** (A comment on the numerical algorithm.)**.** *For the stagnant droplets considered here, the $L_1$-norm of the divergence of the velocity field $\mathbf{u}$, cf. eq. (6.26) and fig. (6.8), before the transformation was of order $\mathcal{O}(10^{-12})$, whereas afterwards it was $\mathcal{O}(10^{-6})$.*

*For all cases investigated here, the convergence of the eigenvalues $\tilde{\lambda}_k$ with $k > 1$ could not be accelerated by application of the implicitly restarted* Arnoldi *method introduced in alg. (4). As stated above, this can be explained by the dominant influence of the parasitic currents.*

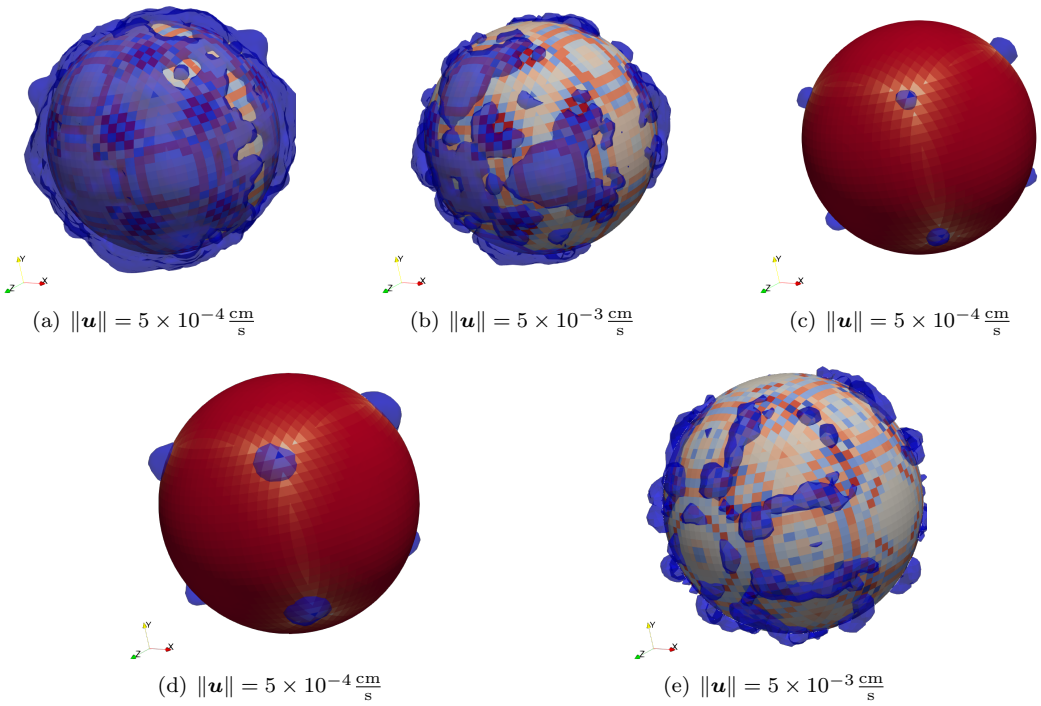

(a) $\|\boldsymbol{u}\| = 5 \times 10^{-4}\,\frac{\text{cm}}{\text{s}}$ (b) $\|\boldsymbol{u}\| = 5 \times 10^{-3}\,\frac{\text{cm}}{\text{s}}$ (c) $\|\boldsymbol{u}\| = 5 \times 10^{-4}\,\frac{\text{cm}}{\text{s}}$

(d) $\|\boldsymbol{u}\| = 5 \times 10^{-4}\,\frac{\text{cm}}{\text{s}}$ (e) $\|\boldsymbol{u}\| = 5 \times 10^{-3}\,\frac{\text{cm}}{\text{s}}$

Figure 6.11.: Iso-surface of velocity norm for 2mm water droplet in air for linear ((a) and (b)) and quadratic volume fractions (c). The colour of the surface corresponds to the curvature error; cf. fig. (5.8).

### 6.5.2. Freely rising fluid particles

Seeking to extend the findings for rising corn oil droplets, of which section 3.4 gave an excerpt, the configuration that shall be considered here is **corn oil/water**; cf. eq. (6.54) for the material properties. The right panel in fig. (6.9) sketches the computational setup, whereas tab. (6.2) gathers the relevant setup parameters.

Table 6.2.: Flow solver parameters; cf.fig. (6.9).

| | | **comment** |
|---|---|---|
| $\Omega$ | $[-3R, 3R] \times [-3R, 3R] \times [-6R, 3R]$ | |
| center position | $\mathbf{0}$ | windowing, cf. note (3.1) |
| resolution $N_{\Omega,i}$ | $128 \times 128 \times 192$ | $\frac{\Delta x}{d} = 42^2/_3$ |
| time step limit | $\frac{3}{4}\Delta t_{\text{vis}}$ | see eq. (3.5) |

Since the transition from steady vertical to oblique rise paths has its onset for droplets of size $\approx$ 3mm, we consider such a configuration. Figure (6.12) plots the terminal rise velocity $U_t := \langle \boldsymbol{u}_{\text{center}}, \boldsymbol{e}_z \rangle$ along with its deviation from the steady state value $U_{t,\infty} = 5.51\,\frac{\text{cm}}{\text{s}}$, which is in very good agreement with the terminal velocities obtained by Albert et al. [5]. Note that the spread of the deviation in fig. (6.12) for $t > 1.5$s is due to the finite precision of the output; cf. section 1.3. Nonetheless, since the deviation is of order $\mathcal{O}(10^{-4})$, the state can be considered stationary.

Figure (6.13) visualizes the axisymmetric flow around the particle in terms of streamlines and iso-surfaces of streamwise vorticity.

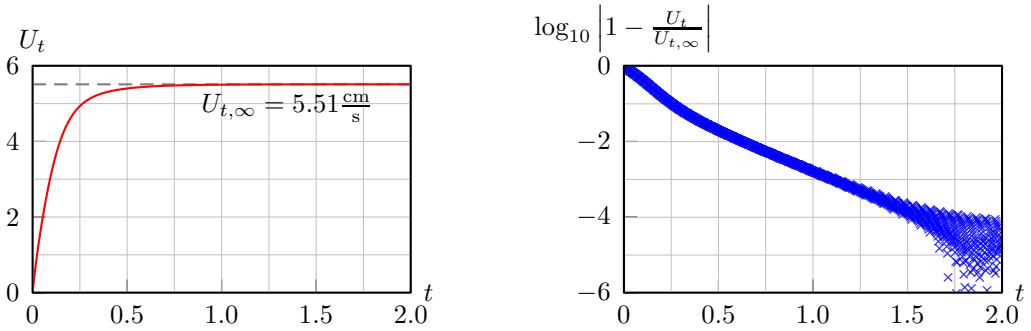


Figure 6.12.: Rise velocity (left) and relative deviation from steady state (right) over time in s for 3mm corn oil droplet rising in water.

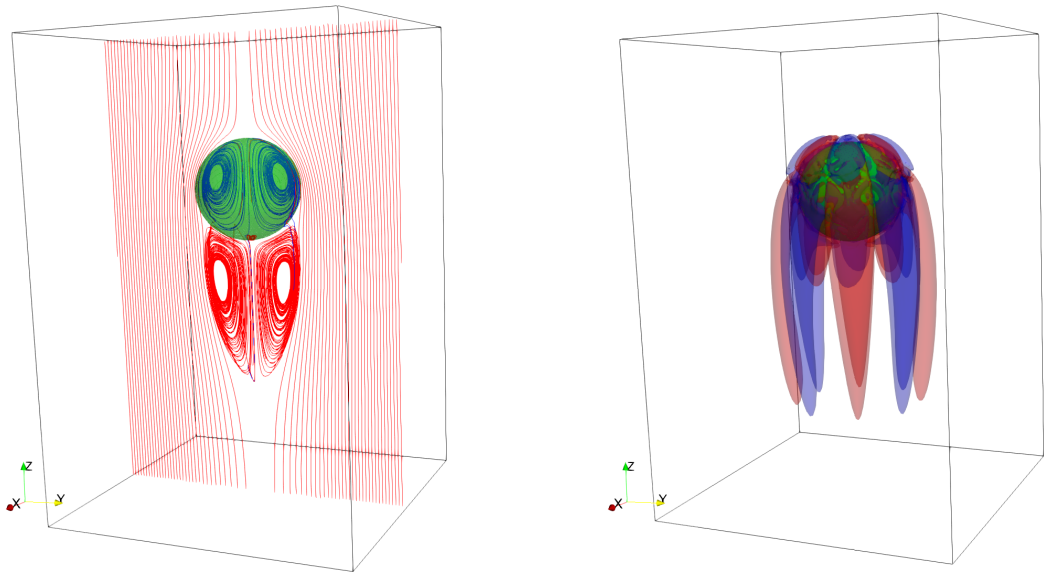

Figure 6.13.: Streamlines (left) and $\pm 7.5 \times 10^{-2}\text{s}^{-1}$ iso-surfaces of streamwise vorticity (right) for 3mm corn oil droplet at steady state, featuring two symmetry planes; cf. fig. (6.15(a)).

**Note 6.12** (Choice of parameters)**.** *For the analysis of buoyant corn oil droplets, the motivation of the choice of parameters is as follows:*

***number of time steps:*** *As described in note (3.1), the flow solver FS3D employs a windowing technique for the simulation of buoyant particles. Compared to the cell size $\Delta x$, the relative displacement of the particle center within one time step $\Delta t$ is $\delta x := \frac{U_t \Delta t}{\Delta x} = \frac{3}{4} \frac{U_t \Delta x}{6 \max(\nu_{\text{cornoil}}, \nu_{\text{water}})} \approx 9.87 \times 10^{-3}$. While the windowing technique was applied for finding the steady state, its influence on the approximated spectrum is undesired. In the most disadvantageous configuration, i.e. starting in the center of a computational cell, it takes the particle center $\frac{1}{2\delta x} = 51$ time steps to leave the cell. Hence, let $N = 20$.*

***order of hypersurface representation:*** *To capture accurately the deformation of the droplet, consider the shape errors of freely rising corn oil droplets of fig. (3.9(b)) in section 3.4. For the diameter of* 3mm *considered here, $L_\Sigma = 8$ is sufficient.*

***size of transformation domain:*** *To account for the deviation from the sphere, the size of the transformation domain is $\alpha_T = 0.5$; cf. subsection 6.2.2.*

***perturbation magnitude:*** *As for the stagnant case, let $\epsilon = 5 \times 10^{-4}$; cf. eq. (6.13).*

***Number of iterations:*** *Motivated from the observations for the stagnant droplet, we choose $M = 10$, since we expect only the leading eigenvalue to converge.*

The findings for the 3mm corn oil droplet are summarized as follows: fig. (6.14) depicts the Arnoldi convergence measure from eq. (6.47). As in the stagnant case, convergence is only obtained for the first approximated eigenvalue $\tilde{\lambda}_1$. While the values of $\gamma_M^2$ and $\gamma_M^5$ decrease for an increasing number of iterations $M$, they do reach values of approximately $10^{-3}$. However, compared to $10^{-14}$ for $\gamma_M^1$, they cannot be considered converged. The leading eigenvalue $\tilde{\lambda}_1 = 1.5401 \times 10^4$ is real and positive, implying

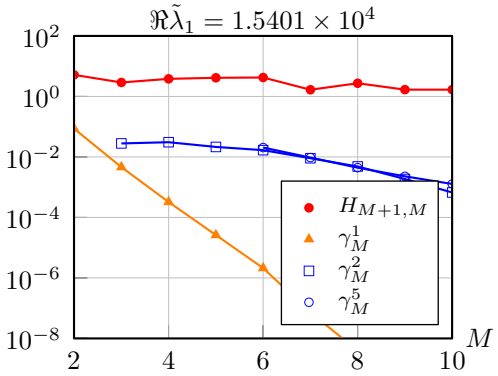


Figure 6.14.: Arnoldi convergence measure for 3mm corn oil droplet over iterations $M$.

that the steady state under consideration is unconditionally unstable. Since we expect a transition from steady vertical rise to steady oblique rise, accompanied by the loss of axisymmetry and formation of a

bifid wake, in principle, this result is in acoordance with the findings of the literature; cf. Albert et al. [5]. The underlying mechanism can be identified from fig. (6.15), which visualizes the iso-surfaces of streamwise vorticity of the steady state and the leading eigenmode. According to Zenit and Magnaudet [159], the aforementioned loss of symmetry in the wake is caused by the accumulation of surface vorticity, whose onset can be seen from fig. (6.15(b)). Along with the small-scale structures near the interface, there a two large sheets of vorticity forming to the right, where two smaller sheets are forming on the top and bottom, respectively. While the steady state streamwise vorticity is of order $10^{-2}\mathrm{s}^{-1}$, the

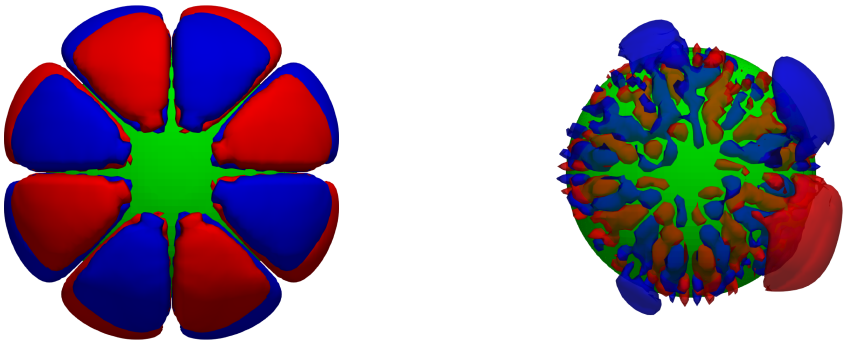

(a) steady state ($\pm 7.5 \times 10^{-2}\mathrm{s}^{-1}$) (b) leading eigenmode ($\pm 25\mathrm{s}^{-1}$)

Figure 6.15.: Iso-surfaces of streamwise vorticity (blue/red) in $\mathrm{s}^{-1}$ over interface (green), where the view is direction of gravity $\boldsymbol{g}$.

leading eigenmode exhibits a magnitude of $25\mathrm{s}^{-1}$ near the interface. In combination with the large magnitude of the eigenvalue, which can be interpreted as a temporal growth rate, the vorticity quickly reaches the critical threshold, causing the loss of axisymmetry. As can be seen from fig. (6.15(b)), the spatial structure of the streamwise vorticity resembles the curvature error patterns obtained for perturbed spheres; cf. fig. (5.18). This observation suggests that the observed eigenmode is a combination of physics and numerical artifacts. However, substantiation or falsification of this conjecture cannot be achieved without the implementation of a different discretization scheme for the surface tension forces. As has been indicated in section 5.5, approaches overcoming the need to compute derivatives of the volume fractions are promising, since they do not introduce spatial structures in the curvature errors.

**Note 6.13** (Variation of the algorithm parameters)**.** *Let us not in passing that the results reported above are robust with respect to variations of the perturbation magnitude $\epsilon$, the number of time steps $N$ (while considering the rationale in note (6.12)) and the size of the transformation domain $\alpha_T$.*

## 6.6. Conclusion

The present chapter has introduced a numerical algorithm for the linear stability analysis of fluid particles, combining the method of Arnoldi [7] with the numerical flow solver FS3D. The main findings are summarized as follows:

1. Subsection 6.3.2 conducted a review of the ARNOLDI method, both in the original and modified form of Sorensen [132]. It was shown that, employing an algorithm-intrinsic convergence measure, the quality of the approximated eigenvalues can be assessed in normalized terms. For the extraction of the leading eigenvalues, i.e. those with the algebraically largest real part, the ARNOLDI method is best combined with an exponential transformation. By doing so, the leading eigenvalue, which was real positive in all cases encountered here, could be extracted with reliable accuracy in terms of the measure introduced in eq. (6.47), i.e. $\gamma_M^1 = \mathcal{O}(10^{-10})$. Besides the leading eigenvalue, within the range of applied iterations $M$, no further eigenvalues exhibited convergence in the sense of sufficiently small $\gamma_M^k$, compared to the leading $\gamma_M^1$.

2. Section 6.2 introduced an algorithm that is capable of performing linear stability analysis for deformable fluid particles. An appropriately designed phase space, along with a divergence-preserving domain transformation, allows performing linear algebra on states with different interface configurations, which in turn enables the application of KRYLOV-type methods for the approximation of eigenvalues. The divergence-preserving domain transformation resorts to spherical coordinates, where the degeneration at the poles was removed by appropriate limit considerations. Furthermore, a decomposition of the simulation domain $\Omega$ into a transformation ($\Omega_{\boldsymbol{T}}$) and identity domain ($\Omega_{\mathbf{1}}$) avoids anisotropy being induced by the CARTESIAN background grid. Hence, it also can be applied to transform general velocity fields to a referential interface configuration, say, e.g., a sphere, which would allow for comparison of flow fields of configurations where the interfaces do not coincide.

3. For stagnant particles in zero gravity, the stability analysis was shown to reproduce the well-known parasitic currents. While previous literature contributions, such as Harvie et al. [62], have addressed this numerical artifact as well, the present algorithm, to the best of our knowledge, for the first time allows quantitatively assessing parasitic currents in terms of growth rates and spatial patterns. The latter, both in magnitude and structure, have been shown to crucially depend on the underlying volume fraction accuracy. In other words, the present algorithm can be employed to numerically quantify the spectral properties of employed discretization schemes, making them accessible to a quantitative comparison.

4. Numerical experiments of buoyant corn oil particles in the transition from steady vertical to oblique rise are conducted. The leading eigenvalue was found to be real positive, corresponding to the instability of the associated steady state. The spatial structure of the associated eigenmode exhibits vorticity accumulation at the interface, which is in accordance with the findings in the literature; cf. Zenit and Magnaudet [159]. However, the influence of curvature computation from height functions remains, despite the high accuracy of the volume fraction computation, implying that a conceptually different scheme for the computation of $\kappa_\Sigma$ is required.

# 7. Summary & Outlook

The subject of chapter 2 was the introduction of the **mathematical model**, where a special focus was put on the analytical computation of curvature from hypersurfaces parametrized in spherical coordinates. The degeneration at the poles was shown to be remediable by combining limit considerations of L'HÔSPITAL-type with an appropriate exploitation of EULER's theorem of differential geometry.

In chapter 3, we have introduced the **numerical method** employed for the integration of the NAVIER-STOKES equations, along with a concept for the extraction of interface information. For fluid particles, the representation in terms of spherical harmonics of order $L_\Sigma$ proved to be suitable for accurately capturing the shape evolution in detail. A principal component analysis further provides an idea of the particle orientation, which can be compared to dynamic quantities such as, e.g., the center velocity. For corn oil droplets freely rising in water, a shift in the time evolution of the aforementioned quantities is observed for increasing diameter, indicating that, due to increased inertia effects, changes in the path are induced by changes in shape.

A novel concept for the numerical computation of **highly accurate volume fractions** was introduced in chapter 4. Application of appropriate divergence theorems and solving a LAPLACE-BELTRAMI equation allows rewriting the volume integrals over implicitly given domains to planar line integrals. Based on differential geometry, a locally tangential second-order approximation of the hypersurface was shown to provide up-to fourth-order accurate volumes for domains bounded by both convex and non-convex hypersurfaces. For spheres, resembling a class of particular interest in both theoretical and numerical regards, an exact computation of volume fractions was derived. The numerical implementation, employing robust topological evaluation of the intersection status of the mesh entities, was applied to a wide range of spatial resolutions on CARTESIAN meshes.

The aforementioned volume fractions were applied within chapter 5 to assess the performance of the height function method with respect to the numerical **computation of curvature**. For sufficiently accurate data, general smooth hypersurfaces were shown to exhibit second-order convergence with spatial resolution in theory. In the case of spheres, the coefficient for the quadratic term in the deviation was derived explicitly, resembling a performance benchmark for this method. While the theoretical second-order convergence is reported throughout the literature, we find that second-order convergence is only obtained for spherical hypersurfaces with quadratic or exact volume fractions, while linear volume fractions do not admit convergence at all. For non-spherical hypersurfaces, first-order convergence is obtained at most, where for the classes investigated here only ellipsoids exhibited convergence. Perturbed spheres were shown to yield divergent curvature estimates, irrespective of the volume fraction quality. As a general result, we have found that volume fraction quality (in the sense of global volume approximation) does not necessarily imply convergence of curvature estimates, where for non-spherical hypersurfaces severe checkerboard patterns are observed.

The original motivation for this thesis, namely the development of an algorithm for the **global linear stability analysis of fluid particles**, was the subject of chapter 6. The concept of Albert et al. [4] was extended from falling films in two spatial dimensions to fluid particles in three spatial dimensions. The mathematical foundations of the algorithm were provided in detail, including a domain transformation, which is required to account for the freely deformable interface. The numerical algorithm employs a modified version of the Arnoldi method, resorting to a rigorous measure for the convergence of the approximated eigenvalues. By means of theoretical considerations, we have substantiated the advantages of applying an exponential transformation for the acceleration of convergence. A numerical assessment of the performance was conducted based on experiments with randomly generated matrices, where the findings include that, beyond the leading eigenvalue, a reliable approximation of the spectrum was not feasible. We have investigated the stability of stagnant (water/air and corn oil/water) and freely rising (corn oil/water) fluid particles, where in both cases we found the leading eigenvalues to be real positive, implying unconditional instability of the respective physical state. For stagnant particles, the instability is caused by parasitic currents, which were quantified in terms of growth rates and spatial patterns. For buoyant corn oil droplets with $d = 3\text{mm}$, the leading eigenvalue was found to be real positive, corresponding to the instability of the associated steady state. The spatial structure of the associated eigenmode exhibits vorticity accumulation at the interface, which causes the loss of axisymmetry in the wake. However, the numerical effect of the curvature errors induced by the height function algorithm remains. This observation once more highlights the necessity for approaches that do not involve derivatives of the volume fractions.

# A. Mathematical supplement

## A.1. Spherical harmonics

The real or *tesseral* spherical harmonics of degree $l$ and order $m$ with $|m| \leq l$ are defined as

$$Y_l^m(\varphi,\theta) = \begin{cases} \sqrt{2}\sqrt{\frac{2l+1}{4\pi}\frac{(l+m)!}{(l-m)!}}P_l^{-m}(\cos\theta)\sin(-m\varphi) & \text{if} \quad m<0 \\ \sqrt{\frac{2l+1}{4\pi}}P_l^m(\cos\theta) & \text{if} \quad m=0 \\ \sqrt{2}\sqrt{\frac{2l+1}{4\pi}\frac{(l-m)!}{(l+m)!}}P_l^m(\cos\theta)\cos m\varphi & \text{if} \quad m>0 \end{cases}, \tag{A.1}$$

where $P_l^m(\cos\theta)$ are the *associated Legendre polynomials*; cf. section A.2. Note that the definition does not include the Condon-Shortley phase. Figure (A.1) provides an illustration. The derivatives with respect to the azimuthal and polar angle read

$$\partial_\varphi Y_l^m(\varphi,\theta) = -m \begin{cases} \sqrt{2}\sqrt{\frac{2l+1}{4\pi}\frac{(l+m)!}{(l-m)!}}P_l^{-m}(\cos\theta)\cos m\varphi & \text{if} \quad m<0 \\ \sqrt{2}\sqrt{\frac{2l+1}{4\pi}\frac{(l-m)!}{(l+m)!}}P_l^m(\cos\theta)\sin m\varphi & \text{if} \quad m\geq 0 \end{cases}, \tag{A.2}$$

$$\partial_\theta Y_l^m(\varphi,\theta) = \frac{Y_l^{m+1}(\varphi,\theta) - (l+m)(l-m+1)Y_l^{m-1}(\varphi,\theta)}{2}. \tag{A.3}$$

For the evaluation of eq. (A.3), it holds that $Y_l^m(\varphi,\theta) \equiv 0$ for $|m| > l$. For an in-depth treatment of spherical harmonics, the reader is referred to the book of Hobson [67]. The integral and convolution of tesseral spherical harmonics are governed by

$$\int_{\mathbb{S}^2} Y_l^m(\varphi,\theta)\,\mathrm{d}o = \begin{cases} 1 & l=m=0 \\ 0 & \text{else} \end{cases} \quad \text{and} \quad \int_{\mathbb{S}^2} Y_l^m(\varphi,\theta)Y_h^n(\varphi,\theta)\,\mathrm{d}o = \delta_{lh}\delta_{nm}. \tag{A.4}$$

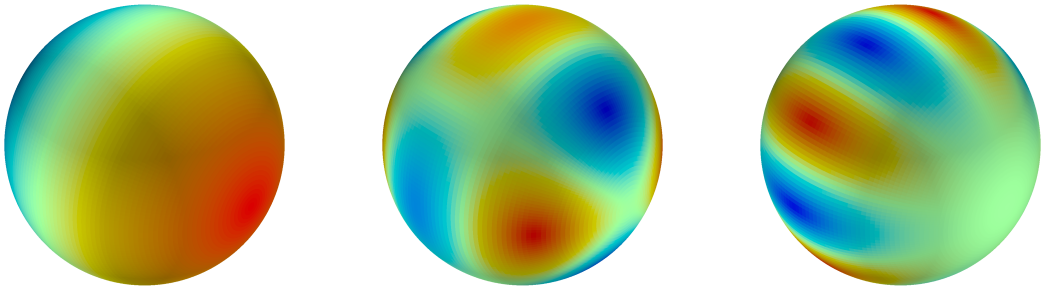

(a) $l=1$, $m=0$ (b) $l=4$, $m=2$ (c) $l=5$, $m=5$

Figure A.1.: Illustration of spherical harmonics.

## A.2. Associated Legendre polynomials

The associated Legendre polynomials are the solution of the canonical solutions of the general Legendre equation, admitting the explicit representation

$$P_l^m(x) = (-1)^m 2^l (1-x^2)^{\frac{m}{2}} \sum_{k=m}^{l} \frac{(k)!}{(k-m)!} x^{k-m} \binom{l}{k} \binom{\frac{l+k-1}{2}}{l}. \tag{A.5}$$

An extensive mathematical treatment is offered, e.g., in the seminal book of Abramowitz and Stegun [1]. See fig. (A.2) for an illustration. Note that substituting $x = \cos\theta$ into eq. (A.5) implies $P_l^m(\cos\theta)|_{\theta\in\{0,\pi\}} = 0$ for $m \neq 0$. For numerical implementation, it is convenient to employ a recursive computation by exploiting

$$\begin{aligned} P_{l+1}^m(x) &= \frac{2l+1}{l-m+1} x P_l^m(x) - \frac{l+m}{l-m+1} P_{l-1}^m(x), \\ P_l^l(x) &= (-1)^l (2l-1)!!(1-x^2)^{\frac{l}{2}}, \\ P_{l+1}^l(x) &= x(2l+1)P_l^l(x). \end{aligned} \tag{A.6}$$

with the double factorial $(n)!! := \prod_{i=0}^{\lceil \frac{n}{2} \rceil + 1} (n-2i)$. Note that, for very high orders, i.e. $l \approx 10^3$, Homes and Featherstone [68] have found that the recursive computation of the $P_l^m(x)$ raises complications. However, since this thesis covers relatively small orders, i.e. $l < 10^2$, the applied algorithms do not employ their findings. From symmetry considerations it follows that

$$P_l^{-m}(x) = (-1)^m \frac{(l-m)!}{(l+m)!} P_l^m(x). \tag{A.7}$$

Within the interval $[-1, 1]$, the associated Legendre polynomials of identical degree $m$ form a normal basis, i.e.

$$\int_{-1}^{1} P_l^m(x) P_k^m(x) \mathrm{d}x = \frac{2(l+m)!}{(2l+1)(l-m)!} \delta_{l,k}. \tag{A.8}$$

For eq. (A.3), we have exploited $\partial_\theta P_l^m(\cos\theta) = \partial_x\theta \; \partial_x P_l^m(x)|_{x=\cos\theta}$ and

$$\sqrt{1-x^2}\partial_x P_l^m(x) = \frac{1}{2}\left[(l+m)(l-m+1)P_l^{m-1}(x) - P_l^{m+1}(x)\right]. \tag{A.9}$$

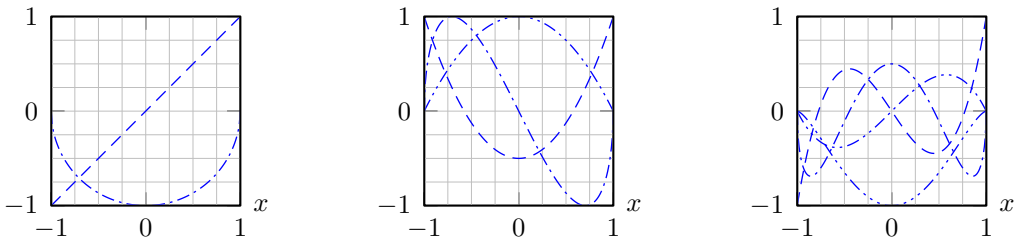


Figure A.2.: Illustration of associated Legendre polynomials $P_l^m(x)$ (scaled to $[-1, 1]$) of different orders $l \in \{1, 2, 3\}$, where the number of dots corresponds to the value of $m$.

## A.3. Basis facts of differential geometry

Prüss and Simonett [111] give a survey on smooth closed hypersurfaces embedded in $\mathbb{R}^N$, including rigorous mathematical statements on the associated operators, fundamental forms and other geometrical properties. The present section heavily draws from their work. Here, however, we only reproduce those results needed within the scope of this work. For further mathematical details, the interested reader is referred to, e.g., the book of Kühnel [79]. Let $\Sigma$ be a hypersurface patch of class $\mathcal{C}^2$ confined by $\mathcal{K} \subset \mathbb{R}^d$ with $d \in \{2, 3\}$, which is given via the zero iso-contour of a level-set $\phi$, i.e.

$$\Sigma = \{\boldsymbol{x} \in \mathcal{K} : \phi(\boldsymbol{x}) = 0\} \qquad \text{with normal} \qquad \boldsymbol{n}_\Sigma := \frac{\nabla\phi}{\|\nabla\phi\|}. \tag{A.10}$$

**Inverse function theorem** For any point $\boldsymbol{x}_0 \in \Sigma$ with outer unit normal $\boldsymbol{n}_\Sigma$, there is a ball $\mathcal{B}_R(\boldsymbol{x}_0) \subset \mathbb{R}^d$ with radius $R$ and a diffeomorphism $\Phi : \mathcal{B}_R(\boldsymbol{x}_0) \mapsto \mathcal{U} \subset \mathbb{R}^d$, such that $\mathcal{U} \ni \Phi(\boldsymbol{x}_0) = \boldsymbol{0}$ and

$$\Phi^{-1}(\mathcal{U} \cap (\mathbb{R}^{d-1} \times \{0\})) = \Phi^{-1}(\mathcal{S}_\Sigma \times \{0\})) = \mathcal{B}_R(\boldsymbol{x}_0) \cap \Sigma. \tag{A.11}$$

The implication of eq. (A.11) is that in the vicinity of $\boldsymbol{x}_0$, i.e. for $\|\boldsymbol{x} - \boldsymbol{x}_0\| \leq R$, the hypersurface can be parametrized as the graph of a function over some (open) parameter set $\mathcal{S}_\Sigma \subset \mathbb{R}^{d-1}$, i.e.

$$\Sigma \cap \mathcal{B}_R(\boldsymbol{x}_0) = \boldsymbol{g}(\mathcal{S}_\Sigma; \boldsymbol{x}_0) \qquad \text{with} \qquad \boldsymbol{g}(\boldsymbol{t}; \boldsymbol{x}_0) := \Phi^{-1}(\boldsymbol{t}, 0) \quad \text{and} \quad \boldsymbol{t} = \sum_{i=1}^{d-1} t_i \boldsymbol{e}_i; \tag{A.12}$$

cf. fig. (A.3) for an illustration. The (covariant) tangent space $T_\Sigma$ attached to $\boldsymbol{x}_0$ is spanned by

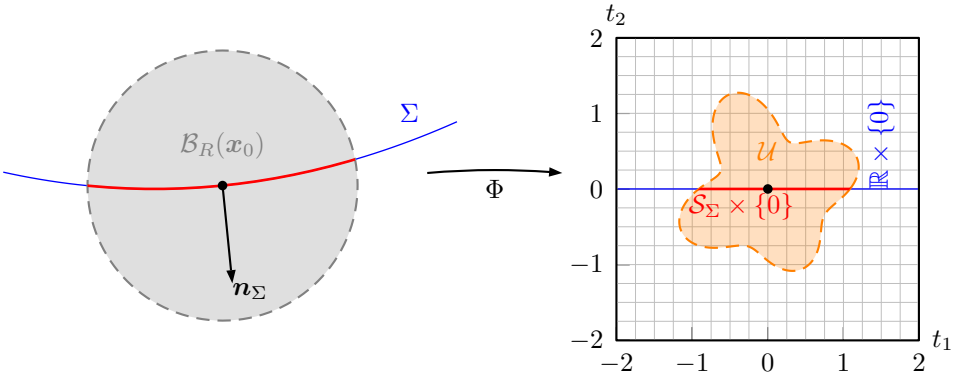


Figure A.3.: Illustration of the implicit function theorem for $\Sigma \subset \mathbb{R}^2$.

$$\boldsymbol{\nu}_i := \frac{\partial \boldsymbol{g}}{\partial t_i}(\boldsymbol{t}; \boldsymbol{x}_0) \qquad \text{for} \qquad 1 \leq i \leq d-1, \tag{A.13}$$

where $\langle \boldsymbol{\nu}_i, \boldsymbol{n}_\Sigma \rangle \equiv 0$, but, in general, $\|\boldsymbol{\nu}_i\| \neq 1$ and $\langle \boldsymbol{\nu}_i, \boldsymbol{\nu}_j \rangle \neq 0$. Analogously, $\boldsymbol{\nu}_{ij}$ denotes the second derivatives. Employing the EINSTEIN summation convention, the *first* and *second fundamental form*, respectively, can be written as

$$\boldsymbol{G}(\boldsymbol{x}_0) := \langle \boldsymbol{\nu}_i, \boldsymbol{\nu}_j \rangle \, \boldsymbol{e}_i \otimes \boldsymbol{e}_j \qquad \text{and} \qquad \boldsymbol{L}(\boldsymbol{x}_0) := \langle \boldsymbol{n}_\Sigma, \boldsymbol{\nu}_{ij} \rangle \, \boldsymbol{e}_i \otimes \boldsymbol{e}_j. \tag{A.14}$$

The eigenvalues $\{\kappa_i\} \subset \mathbb{R}^{d-1}$ of the WEINGARTEN map $\boldsymbol{W}(\boldsymbol{x}_0) := \boldsymbol{G}^{-1}\boldsymbol{L}$, also called *shape matrix* of $\Sigma$, correspond to the principal curvatures of the hypersurface at $\boldsymbol{x}_0$. The associated eigenvectors $\boldsymbol{\tau}_i^0 \in \mathbb{R}^{d-1}$ provide the local directions of principal curvature, whose global pendant is obtained via $\boldsymbol{\tau}_i := \langle \boldsymbol{\tau}_i^0, \boldsymbol{e}_k \rangle \boldsymbol{\nu}_k$ and normalization. Note that $\langle \boldsymbol{\tau}_i, \boldsymbol{\tau}_j \rangle = \delta_{ij}$ as well as $\langle \boldsymbol{\tau}_i, \boldsymbol{n}_\Sigma \rangle = 0$, i.e. $\{\boldsymbol{\tau}_i, \boldsymbol{n}_\Sigma\}(\boldsymbol{x}_0)$ forms an orthonormal system and $T_\Sigma(\boldsymbol{x}_0) = \operatorname{span}(\boldsymbol{\tau}_i)$.

**Surface gradient & surface divergence** Let $f : \Sigma \mapsto \mathbb{R}$ be a continuously differentiable field. Assume for the moment that the full gradient $\nabla f$ exists. Then, the surface gradient can be understood as the projection of $\nabla f$ onto the tangent space $T_\Sigma(\boldsymbol{x}_0)$, i.e.

$$\nabla_\Sigma f = (\boldsymbol{I} - \boldsymbol{n}_\Sigma \otimes \boldsymbol{n}_\Sigma)\, \nabla f = \frac{\mathrm{d}f}{\mathrm{d}\boldsymbol{\tau}_2}\boldsymbol{\tau}_1 + \frac{\mathrm{d}f}{\mathrm{d}\boldsymbol{\tau}_2}\boldsymbol{\tau}_2. \tag{A.15}$$

Note that left multiplication with $\boldsymbol{P}_\Sigma := \boldsymbol{I} - \boldsymbol{n}_\Sigma \otimes \boldsymbol{n}_\Sigma$ corresponds to a projection onto the tangent plane $T_\Sigma(\boldsymbol{x}_0)$. Following Gilbarg and Trudinger [54], the lack of definition of the normal component can be eliminated by an extension of the definition, i.e. $f(\boldsymbol{x} \pm \epsilon \boldsymbol{n}_\Sigma) = f(\boldsymbol{x})$ for $\boldsymbol{x} \in \Sigma$ and $\epsilon \in \mathbb{R}^+$ with $\epsilon \ll 1$. Hence, within a tubular neighborhood of thickness $2\epsilon$, the function value is extended to be constant along a normal deviation from the hypersurface. Throughout this thesis, we assume any function mapping from the hypersurface $\Sigma$ to be extensible in this way. Then, the derivative in normal direction indeed becomes zero, since

$$\frac{\mathrm{d}f}{\mathrm{d}\boldsymbol{n}_\Sigma} = \lim_{\epsilon \to 0} \frac{f(\boldsymbol{x} + \epsilon \boldsymbol{n}_\Sigma) - f(\boldsymbol{x})}{\epsilon} \equiv 0. \tag{A.16}$$

By analogous arguments, one obtains the surface divergence of a vector field $\boldsymbol{f} : \Sigma \mapsto \mathbb{R}^d$ as

$$\operatorname{div}_\Sigma \boldsymbol{f} = \operatorname{tr}\left(\boldsymbol{P}_\Sigma \nabla \boldsymbol{f}\right) = \langle \frac{\mathrm{d}f}{\mathrm{d}\boldsymbol{\tau}_i}, \boldsymbol{\tau}_i \rangle, \tag{A.17}$$

i.e. the surface divergence is the trace of tangential projection of the full gradient. For a differentiable tangential vector field $\boldsymbol{f} : \Sigma \mapsto T_\Sigma$, especially including the case $\boldsymbol{f} = \nabla_\Sigma f$, the (surface) divergence theorem reads

$$\int_\Sigma \operatorname{div}_\Sigma \boldsymbol{f}\, \mathrm{d}o = \int_{\partial\Sigma} \langle \boldsymbol{f}, \boldsymbol{n}_{\partial\Sigma} \rangle\, \mathrm{d}l. \tag{A.18}$$

For application within the variational formulation, note that two scalar functions $f, g : \Sigma \mapsto \mathbb{R}$ fulfill

$$\int_\Sigma g \Delta_\Sigma f\, \mathrm{d}o = \int_{\partial\Sigma} g \langle \nabla_\Sigma f, \boldsymbol{n}_{\partial\Sigma} \rangle \mathrm{d}l - \int_\Sigma \langle \nabla_\Sigma f, \nabla_\Sigma g \rangle \mathrm{d}o, \tag{A.19}$$

where the LAPLACE-BELTRAMI operator is

$$\Delta_\Sigma u = \operatorname{div}_\Sigma \nabla_\Sigma u. \tag{A.20}$$

## A.4. Comparison of polynomials

The first three elements of the coefficient vector $\hat{\boldsymbol{u}}$, where $\hat{u}_{ij}$ corresponds to $t_1^{2i}t_2^{2j}\left(1+\kappa_1^2t_1^2+\kappa_2^2t_2^2\right)^{\frac{1}{2}}$, resulting from the polynomial comparison, cf. subsection 4.4.5, are

$$\begin{aligned}
\hat{u}_{00} = \frac{1}{3465D}\big[&72544885875\kappa_1^{25} + 4193272314000\kappa_1^{24}\kappa_2 - 2577212786610\kappa_1^{23}\kappa_2^2 \\
&- 26658698588694\kappa_1^{22}\kappa_2^3 - 57357128755944\kappa_1^{21}\kappa_2^4 + 336181054285530\kappa_1^{20}\kappa_2^5 \\
&+ 417146275795279 46\kappa_1^{19}\kappa_2^6 + 362007665932049430\kappa_1^{18}\kappa_2^7 \\
&+ 1974693936115434347\kappa_1^{17}\kappa_2^8 + 869021667523373 7542\kappa_1^{16}\kappa_2^9 \\
&+ 1816979830945434622 0\kappa_1^{15}\kappa_2^{10} + 1799723734886964496 4\kappa_1^{14}\kappa_2^{11} \\
&+ 840047126609648999 2\kappa_1^{13}\kappa_2^{12} + 762188062726301126 8\kappa_1^{12}\kappa_2^{13} \\
&+ 187312918569405176 20\kappa_1^{11}\kappa_2^{14} + 200161982487357802 04\kappa_1^{10}\kappa_2^{15} \\
&+ 160849264362714984 25\kappa_1^{9}\kappa_2^{16} + 411198025356501532 4\kappa_1^{8}\kappa_2^{17} \\
&- 981532678914241570 6\kappa_1^{7}\kappa_2^{18} - 678429712802614135 8\kappa_1^{6}\kappa_2^{19} \\
&- 139314003672349782 4\kappa_1^{5}\kappa_2^{20} - 146622851045506110\kappa_1^{4}\kappa_2^{21} \\
&- 12737929185209566\kappa_1^{3}\kappa_2^{22} + 250947833147550\kappa_1^{2}\kappa_2^{23} \\
&+ 7442937203625\kappa_1\kappa_2^{24} + 5318812248750\kappa_2^{25}\big], \qquad \text{(A.21)}
\end{aligned}$$

$$\begin{aligned}
\hat{u}_{10} = \frac{-1}{2130D}\big[&72544885875\kappa_1^{27} + 3830547884625\kappa_1^{26}\kappa_2 - 22099585675860\kappa_1^{25}\kappa_2^2 \\
&+ 64209322185606\kappa_1^{24}\kappa_2^3 - 206549792452944\kappa_1^{23}\kappa_2^4 \\
&+ 1517363124557580\kappa_1^{22}\kappa_2^5 + 3046101870200924 6\kappa_1^{21}\kappa_2^6 \\
&+ 1094469183268449 30\kappa_1^{20}\kappa_2^7 + 815480671742008547\kappa_1^{19}\kappa_2^8 \\
&+ 1495391079214882517\kappa_1^{18}\kappa_2^9 + 4399306375420376470\kappa_1^{17}\kappa_2^{10} \\
&+ 1154016243620987356 4\kappa_1^{16}\kappa_2^{11} + 1587688888105259519 2\kappa_1^{15}\kappa_2^{12} \\
&+ 1575870577498507436 8\kappa_1^{14}\kappa_2^{13} + 9058115615694138220\kappa_1^{13}\kappa_2^{14} \\
&+ 1457712866118151600 4\kappa_1^{12}\kappa_2^{15} + 8744727214400259625\kappa_1^{11}\kappa_2^{16} \\
&+ 2890522443599094029 9\kappa_1^{10}\kappa_2^{17} + 2594680716262097144\kappa_1^{9}\kappa_2^{18} \\
&+ 7186618173791294142\kappa_1^{8}\kappa_2^{19} - 9947751822646978024\kappa_1^{7}\kappa_2^{20} \\
&- 6203435202180262860\kappa_1^{6}\kappa_2^{21} - 8286430563586602 66\kappa_1^{5}\kappa_2^{22} \\
&- 6484442578943175 0\kappa_1^{4}\kappa_2^{23} + 1826532320191425\kappa_1^{3}\kappa_2^{24} \\
&- 63336193160625\kappa_1^{2}\kappa_2^{25} + 26594061243750\kappa_1\kappa_2^{26}\big], \qquad \text{(A.22)}
\end{aligned}$$

$$\begin{aligned}
\hat{u}_{01} = \frac{-1}{2130D}\big[&362724429375\kappa_1^{26}\kappa_2 + 19594917775125\kappa_1^{25}\kappa_2^2 - 86674748460300\kappa_1^{24}\kappa_2^3 \\
&+ 146615450910390\kappa_1^{23}\kappa_2^4 - 1207840768860744\kappa_1^{22}\kappa_2^5 \\
&+ 1119625174876275 6\kappa_1^{21}\kappa_2^6 + 2528969286594900 30\kappa_1^{20}\kappa_2^7 \\
&+ 1200927891952953746\kappa_1^{19}\kappa_2^8 + 7556833261950904455\kappa_1^{18}\kappa_2^9 \\
&+ 1574518587014940409 7\kappa_1^{17}\kappa_2^{10} + 1514729158789350894 2\kappa_1^{16}\kappa_2^{11} \\
&+ 1069338069449824102 0\kappa_1^{15}\kappa_2^{12} + 9860412201147581864\kappa_1^{14}\kappa_2^{13}
\end{aligned}$$

$$
\begin{aligned}
&+ 1807364750734286939 2\kappa_1^{13}\kappa_2^{14} + 1306095021481727546 8\kappa_1^{12}\kappa_2^{15} \\
&+ 2607149107881175642 0\kappa_1^{11}\kappa_2^{16} - 4777045933690144771\kappa_1^{10}\kappa_2^{17} \\
&+ 3674918930866985575\kappa_1^{9}\kappa_2^{18} - 9858935048252420176\kappa_1^{8}\kappa_2^{19} \\
&- 1260715003218935506\kappa_1^{7}\kappa_2^{20} - 727484776891384608\kappa_1^{6}\kappa_2^{21} \\
&- 577234908550047124\kappa_1^{5}\kappa_2^{22} - 81527477422926810\kappa_1^{4}\kappa_2^{23} \\
&- 14557017568197366\kappa_1^{3}\kappa_2^{24} + 319602838556925\kappa_1^{2}\kappa_2^{25} \\
&- 19151124040125\kappa_1\kappa_2^{26} + 5318812248750\kappa_2^{27}\big] ,
\end{aligned} \tag{A.23}
$$

with the common factor

$$
\begin{aligned}
D = {} & 942141375\kappa_1^{28} + 50895890325\kappa_1^{27}\kappa_2 - 224230144725\kappa_1^{26}\kappa_2^{2} \\
&+ 598532006835\kappa_1^{25}\kappa_2^{3} - 2428874075520\kappa_1^{24}\kappa_2^{4} + 16349986503270\kappa_1^{23}\kappa_2^{5} \\
&+ 427125623057490\kappa_1^{22}\kappa_2^{6} + 2231665401399570\kappa_1^{21}\kappa_2^{7} + 14828318817700617\kappa_1^{20}\kappa_2^{8} \\
&+ 44864797857680423\kappa_1^{19}\kappa_2^{9} + 119751294597828609\kappa_1^{18}\kappa_2^{10} + 214219532483111305\kappa_1^{17}\kappa_2^{11} \\
&+ 237484900845042006\kappa_1^{16}\kappa_2^{12} + 227521098241347780\kappa_1^{15}\kappa_2^{13} + 193178681355432300\kappa_1^{14}\kappa_2^{14} \\
&+ 273867280881223980\kappa_1^{13}\kappa_2^{15} + 191980286687434545\kappa_1^{12}\kappa_2^{16} + 37360016234307739 5\kappa_1^{11}\kappa_2^{17} \\
&+ 26654117097834493\kappa_1^{10}\kappa_2^{18} + 94462186400242197\kappa_1^{9}\kappa_2^{19} - 112459641067919644\kappa_1^{8}\kappa_2^{20} \\
&- 58932688180872330\kappa_1^{7}\kappa_2^{21} - 30317166816236766\kappa_1^{6}\kappa_2^{22} - 10190296532147550\kappa_1^{5}\kappa_2^{23} \\
&- 1260751770087705\kappa_1^{4}\kappa_2^{24} - 183530830884975\kappa_1^{3}\kappa_2^{25} + 4003879094775\kappa_1^{2}\kappa_2^{26} \\
&- 164509592625\kappa_1\kappa_2^{27} + 69075483750\kappa_2^{28}.
\end{aligned} \tag{A.24}
$$

# B. Supplementary figures

## Curvature computation

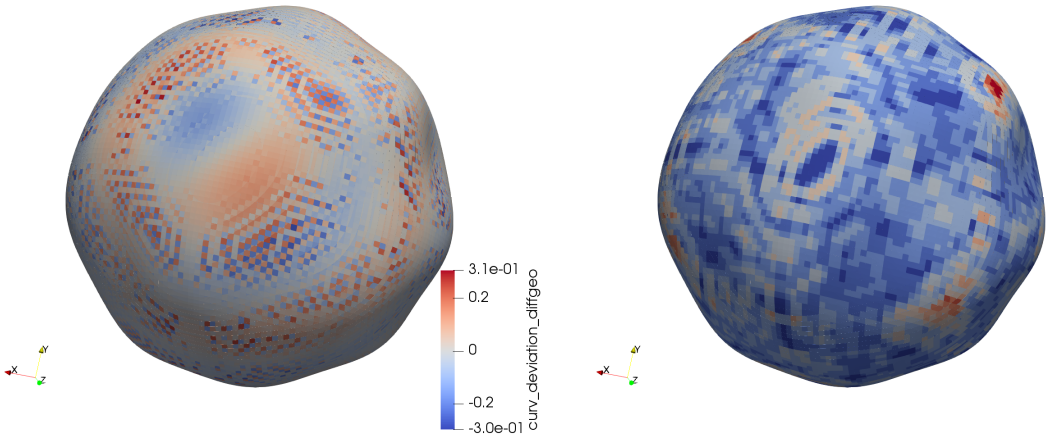


Figure B.1.: Gradient of $n_{\mathcal{S},\Sigma}$ for perturbed sphere ($L_\Sigma = 9$, $\hat{\sigma}^2 = 10^{-4}$, $R_0 = \frac{4}{5}$) centered in $[-1,1]^3$, corresponding to fig. (5.18).

# Index

# References


[1] Milton Abramowitz and Irene Stegun. *Handbook of Mathematical Functions*. Dover Publications, 1965.

[2] James Ahrens, Berk Geveci, and Charles Law. *ParaView: An End-User Tool for Large Data Visualization*. Elsevier, 2005. ISBN 978-0123875822.

[3] Christoph Albert, Henning Raach, and Dieter Bothe. Influence of surface tension models on the hydrodynamics of wavy laminar falling films in volume of fluid-simulations. *International Journal of Multiphase Flow*, 43:66–71, 2012.

[4] Christoph Albert, Dieter Bothe, and Asei Tezuka. Global linear stability analysis of falling films with in- and outlet. *Journal of Fluid Mechanics*, 745:444–486, 2014.

[5] Christoph Albert, Johannes Kromer, A. M. Robertson, and Dieter Bothe. Dynamic behaviour of buoyant high viscosity droplets rising in a quiescent liquid. *Journal of Fluid Mechanics*, 778: 485–533, 2015.

[6] E. Anderson, Z. Bai, C. Bischof, S. Blackford, J. Demmel, J. Dongarra, J. Du Croz, A. Greenbaum, S. Hammarling, A. McKenney, and D. Sorensen. *LAPACK Users' Guide*. Society for Industrial and Applied Mathematics, Philadelphia, PA, third edition, 1999. ISBN 0-89871-447-8 (paperback).

[7] W. E. Arnoldi. The principle of minimized iterations in the solution of the matrix eigenvalue problem. *Quaterly of Applied Mathematics*, 9:17–29, 1951. doi: https://doi.org/10.1090/qam/42792.

[8] Steven Flynn Ashby. Chebycode: a FORTRAN implementation of Manteuffel's adaptive Chebyshev algorithm. Technical report, University of Illinois at Urbana-Champaign, 1985.

[9] Utkarsh Ayachit. *The ParaView Guide: A Parallel Visualization Application*. Kitware, 2015.

[10] Zhaojun Bai. Progress in the numerical solution of the nonsymmetric eigenvalue problem. *Numerical Linear Algebra with Applications*, 2(3):219–234, 1995.

[11] Georges Balmino. Gravitational potential harmonics from the shape of an homogeneous body. *Celestial Mechanics and Dynamical Astronomy*, 60:331–364, 1994.

[12] J. Thomas Beale. The initial value problem for the Navier-Stokes equations with a free surface. *Communications on Pure and Applied Mathematics*, 34:359–392, 1981.

[13] Mohammed Bellalij, Yousef Saad, and Hassane Sadok. On the convergence of the arnoldi process for eigenvalue problems. Technical Report UMSI-2007-12, Minnesota Supercomputer Institute, University of Minnesota, 2007. URL `https://www-users.cs.umn.edu/~saad/PDF/umsi-2007-12.pdf`.

[14] Mohammed Bellalij, Youcef Saad, and Hassane Sadok. Further analysis of the arnoldi process for eigenvalue problems. *SIAM Journal on Numerical Analysis*, 48(2):393–407, 2010. ISSN 00361429. URL `http://www.jstor.org/stable/41062642`.

[15] Maria Bennani and Thierry Braconnier. Stopping criteria for eigensolvers. Technical Report TR/PA/94/22, CERFACS, 1994.

[16] Jiri Blazek. *Computational Fluid Dynamics: Principles and Applications*. Butterworth-Heinemann, third edition edition, 2015. ISBN 978-0-08-099995-1.

[17] Simone Bná, Manservisi Sandro, Ruben Scardovelli, Philip Yecko, and Stéphane Zaleski. Numerical integration of implicit functions for the initialization of the VOF function. *Computers & Fluids*, 113:42–52, 2015.

[18] Simone Bná, Manservisi Sandro, Ruben Scardovelli, Philip Yecko, and Stéphane Zaleski. Vofi – a library to initialize the volume fraction scalar field. *Computer Physics Communications*, 200, 11 2015. doi: 10.1016/j.cpc.2015.10.026.

[19] David N. Bock. On the Navier-Stokes equations in noncylindrical coordinates. *Journal of Differential Equations*, 25:151–162, 1977.

[20] Simon Bogner, Ulrich Rüde, and Jens Harting. Curvature estimation from a volume-of-fluid indicator function for the simulation of surface tensionand wetting with a free-surface lattice boltzmann method. *Physical Review E*, 93:043302, 04 2016. doi: 10.1103/PhysRevE.93.043302.

[21] G. Bornia, A. Cervone, S. Manservisi, R. Scardovelli, and S. Zaleski. On the properties and limitations of the height function method in two-dimensional cartesian geometry. *Journal of Computational Physics*, 230:851–862, 2011.

[22] G. E. P. Box and Mervin E. Muller. A note on the generation of random normal deviates. *Ann. Math. Statist.*, 29(2):610–611, 06 1958. doi: 10.1214/aoms/1177706645. URL `https://doi.org/10.1214/aoms/1177706645`.

[23] J. U. Brackbill, D. B. Kothe, and C. Zemach. A continuum method for modeling surface tension. *Journal of Computational Physics*, 100:335–354, 1992.

[24] J.C. Cano-Lozano, P. Bohorquez, and C. Martínez-Bazán. Wake instability of a fixed axisymmetric bubble of realistic shape. *International Journal of Multiphase Flow*, 51:11–21, 2013.

[25] José Carlos Cano-Lozano, Carlos Martínez-Bazán, Jacques Magnaudet, and Joel Tchoufag. Paths and wakes of deformable nearly-spheroidal rising bubbles close to the transition to path instability. *Physical Review Fluids*, 1(5):053604, 2016. doi: 10.1103/PhysRevFluids.1.053604.

[26] José Carlos Cano-Lozano, Joel Tchoufag, Jacques Magnaudet, and Carlos Martínez-Bazán. A global stability approach to wake and path instabilities of nearly oblate spheroidal rising bubbles. *Physics of Fluids*, 28:014102, 2016. doi: 10.1063/1.4939703.

[27] Amanda H.L.M. Charin, Paulo L.C. Lage, Luiz Fernando L.R. Silva, Željko Tuković, and Hrvoje Jasak. On the dynamic behavior of rising droplets. *International Journal of Multiphase Flow*, 110:

165–178, 2019. doi: https://doi.org/10.1016/j.ijmultiphaseflow.2018.09.005. URL http://www.sciencedirect.com/science/article/pii/S0301932218300429.

[28] Wen-Long Cheng, Wei-Wei Zhang, Hua Chen, and Lei Hu. Spray cooling and flash evaporation cooling: The current development and application. *Renewable and Sustainable Energy Reviews*, 55: 614–628, 2016.

[29] S. Chiba. Global stability analysis of incompressible viscous flow. *Journal of the Japanese Society for Computational Fluid Dynamics (in japanese)*, 7:20–48, 1998.

[30] A. Chorin. Numerical solution of the navier-stokes equation. *Mathematics of Computation*, 22: 745–762, 1968.

[31] Alexandre Joel Chorin. Curvature and solidification. *Journal of Computational Physics*, 57(3):472 – 490, 1985.

[32] R. Clift, J. R. Grace, and M. E. Weber. *Bubbles, Drops and Particles*. ACADEMIC Press New York, 1978.

[33] M. Clint and Alan Jennings. The evaluation of eigenvalues and eigenvectors of real symmetric matrices by simultaneous iteration. *Computer Journal*, 13(1):76–80, 1970.

[34] M. Crouzeix, P. Philippe, and Miloud Sadkane. The Davidson method. *SIAM Journal of Scientific Computing*, 15(1):62–76, 1994.

[35] Sharen J. Cummins, Marianne M. Francois, and Douglas B. Kothe. Estimating curvature from volume fractions. *Computers & Structures*, 83:425–434, 2005.

[36] Ernest R. Davidson. The iterative calculation of a few of the lowest eigenvalues and corresponding eigenvectors of large real-symmetric matrices. *Journal of Computational Physics*, 17(1):87–94, 1975.

[37] Antoine Wilhelmus Gerardus de Vries. *Path and wake of a Rising Bubble*. PhD thesis, University of Twente, Enschede, February 2001. URL http://doc.utwente.nl/37637/.

[38] Fabian Denner. *Balanced-Force Two-Phase Flow Modelling on Unstructured and Adaptive Meshes*. PhD thesis, Imperial College London, 2013.

[39] Fabian Denner and Berend G. M. van Wachem. Fully-coupled balanced-force vof framework for arbitrary meshes with least-squares curvature evaluation from volume fractions. *Numerical Heat Transfer, Part B*, 65:218–255, 2014.

[40] W. S. Edwards, L. S. Tuckerman, R. A. Friesner, and D. C. Sorensen. Krylov methods for the incompressible navier-stokes equations. *Journal of Computational Physics*, 110(1):82–102, 1994.

[41] Kjetil Elligsen and Frederic Risso. On the rise of an ellipsoidal bubble in water: oscillatory paths and liquid-induced velocity. *Journal of Fluid Mechanics*, 440:235–268, 2001.

[42] Lars E. Eriksson and Arthur Rizzi. Computer-aided analysis of the convergence to steady state of discrete approximations to the euler equations. *Journal of Computational Physics*, 57(1):90–128, 1985.

[43] Fabien Evrard, Fabian Denner, and Berend van Wachem. Estimation of curvature from volume fractions using parabolic reconstruction on two-dimensional unstructured meshes. *Journal of Computational Physics*, 351:271–294, 2017.

[44] Fabien Evrard, Fabian Denner, and Berend Wachem. Surface reconstruction from discrete indicator functions. *IEEE Transactions on Visualization and Computer Graphics*, 25:1629–1635, 03 2019. doi: 10.1109/TVCG.2018.2809751.

[45] Anja Fath and Dieter Bothe. Direct numerical simulations of thermocapillary migration of a droplet attached to a solid wall. *International Journal of Multiphase Flow*, 77:209–221, 2015.

[46] S. A. Shahzadeh Fazeli, Nahid Emad, and Zifan Liu. A key to choose subspace size in implicitly restarted Arnoldi method. *Numerical Algorithms*, 70:407–426, 2015. doi: doi:10.1007/s11075-014-9954-5.

[47] Stefan Fleckenstein and Dieter Bothe. Simplified modeling of the influence of surfactants on the rise of bubbles in vof-simulations. *Chemical Engineering Science*, 102:514–523, 2013.

[48] C. Focke and D. Bothe. Direct numerical simulation of binary off-center collisions of shear thinning droplets at high weber numbers. *Physics of Fluids*, 24:073105–1, 2012.

[49] Christian Focke and Dieter Bothe. Direkte numerische Simulation binärer Kollisionen scherverdünnender Tropfen. *Chemie Ingenieur Technik*, 84:121–126, 2012.

[50] Marianne M. Francois and Blair K. Swartz. Interface curvature via volume fractions, heights, and mean values on nonuniform rectangular grids. *Journal of Computational Physics*, 229(3):527–540, 2010.

[51] Marianne M. Francois, Sharen J. Cummins, Edward D. Dendy, Douglas B. Kothe, James M. Sicilian, and Matthew W. Williams. A balanced-force algorithm for continuous and sharp interfacial surface tension models within a volume tracking framework. *Journal of Computational Physics*, 213:141–173, 2006.

[52] Mathis Fricke, Johannes Kromer, and Dieter Bothe. Error estimates for curvature computation from height functions in vof methods. (unpublished).

[53] D. Gerlach, G. Tomar, G. Biswas, and F. Durst. Comparison of volume-of-fluid methods for surface tension-dominant two-phase flows. *International Journal of Heat and Mass Transfer*, 49(3):740–754, 2006. doi: https://doi.org/10.1016/j.ijheatmasstransfer.2005.07.045. URL `http://www.sciencedirect.com/science/article/pii/S0017931005005314`.

[54] David Gilbarg and Neil S. Trudinger. *Elliptic Partial Differential Equations of Second Order*. Classics in Mathematics. Springer Berlin, 2001.

[55] Irina Ginzburg and G. Wittum. Two-phase flows on interface refined grid modelled with vof, staggered finite volumes, and spline interpolants. *Journal of Computational Physics*, 166:302–335, 01 2001.

[56] Gene H. Golub and Charles F. Van Loan. *Matrix Computations (3rd Ed.)*. Johns Hopkins University Press, Baltimore, MD, USA, 1996. ISBN 0-8018-5414-8.

[57] Francesco Gomez, R. Gomez, and Vassilis Theofilis. On three-dimensional global linear instability analysis of flows with standard aerodynamics codes. *Aerospace Science and Technology*, 32(1): 223–234, 2014.

[58] Francesco Gomez, Jose Miguel Perez, Hugh M. Blackburn, and Vassilis Theofilis. On the use of matrix-free shift-invert strategies for global flow instability analysis. *Aerospace Science and Technology*, 44:69–76, 2015.

[59] Zhenyi Guo, David F. Fletcher, and Brian S. Haynes. Implementation of a height function method to alleviate spurious currents in cfd modelling of annular flow in microchannels. *Applied Mathematical Modelling*, 39:4665–4686, 2015.

[60] Thomas Hahn. Cuba–a library for multidimensional numerical integration. *Computer Physics Communications*, 168:75–95, 2005.

[61] F. H. Harlow and J. E. Welch. Numerical calculation of time-dependent viscous incompressible flow of fluid with free surface. *Physics of Fluids*, 8:2182–2189, December 1965. doi: 10.1063/1.1761178.

[62] D. J. E. Harvie, M. R. Davidson, and M. Rudman. An analysis of parasitic current generation in vof simulations. *Applied Mathematical Modelling*, 30(10):1056–1066, 2006.

[63] John Helmsen and Phillip Colella. Non-convex profile evolution in two dimensions using volume of fluids. Technical Report LBNL-40693, Lawrence Livermore National Laboratory, 1997.

[64] C. W. Hirt and B. D. Nichols. Volume of fluid (vof) method for the dynamics of free boundaries. *Journal of Computational Physics*, 39:201–225, 1981.

[65] Diem Ho. Tchebychev acceleration technique for large scale nonsymmetric matrices. *Numerische Mathematik*, 56:721–734, 1989.

[66] Diem Ho, Francoise Chatelin, and Maria Bennani. Arnoldi-Tchebyshev procedure for large scale nonsymmetric matrices. *Mathematical Modelling and Numerical Analysis*, 24(1):53–65, 1990.

[67] Ernest William Hobson. *The theory of spherical and ellipsoidal harmonics*. Cambridge University Press, 1931.

[68] S. A. Homes and W. E. Featherstone. A unified approach to the clenshaw summation and the recursive computation of very high degree and order normalised associated legendre functions. *Journal of Geodesy*, 76:279–299, 2002.

[69] Robert Hooke and T. A. Jeeves. *Direct Search* solution of numerical and statistical problems. *Journal of the ACM*, 8(2):212–229, April 1961. doi: 10.1145/321062.321069. URL `http://doi.acm.org/10.1145/321062.321069`.

[70] M. Horowitz and C.H. K. Williamson. The effect of reynolds number on the dynamics and wakes of freely rising and falling spheres. *Journal of Fluid Mechanics*, 651:251–294, 2010.

[71] Kei Ito, Tomoaki Kunugi, Shuji Ohno, Hideki Kamide, and Hiroyuki Ohshima. A high-precision calculation method for interface normal and curvature on an unstructured grid. *Journal of Computational Physics*, 273:38–53, 2014.

[72] Christopher B. Ivey and Parviz Moin. Accurate interface normal and curvature estimates on three-dimensional unstructured non-convex polyhedral meshes. *Journal of Computational Physics*, 300: 365–386, 2015.

[73] Zhongxiao Jia. A refined iterative algorithm based on the block ARNOLDI process for large unsymmetric eigenproblems. *Linear Algebra and its Applications*, 270:171–189, 1998.

[74] Bevan Jones, Arnaud Malan, and Niran Ilangakoon. The initialisation of volume fractions for unstructured grids using implicit surface definitions. *Computers & Fluids*, 179:194 – 205, 2019. ISSN 0045-7930. doi: https://doi.org/10.1016/j.compfluid.2018.10.021. URL `http://www.sciencedirect.com/science/article/pii/S0045793018308338`.

[75] Bruno B. M. Kassar, Joao N. E. Carneiro, and Angela O. Nieckele. Curvature computation in volume-of-fluid method based on point-cloud sampling. *Computer Physics Communications*, 222: 189–208, 2018.

[76] Shigeo Kida, Michio Yamada, and Kohji Ohkitani. Route to chaos in a navier-stokes flow. In Masayasu Mimura and Takaaki Nishida, editors, *Recent Topics in Nonlinear PDE IV*, volume 160 of *North-Holland Mathematics Studies*, pages 31–47. North-Holland, 1989. doi: https://doi.org/10.1016/S0304-0208(08)70505-X.

[77] M. N. Kooper, H. A. van der Vorst, S. Poedts, and J. P. Goedbloed. Application of the implicitly updated ARNOLDI method with a complex shift-and-invert strategy in MagnetHydroDynamics. *Journal of Computational Physics*, 118(2):320–328, 1995.

[78] Johannes Kromer and Dieter Bothe. Highly accurate computation of volume fractions using differential geometry. *Journal of Computational Physics*, 396:761–784, 2019.

[79] Wolfgang Kühnel. *Differential geometry. Curves-Surfaces-Manifolds*, volume 2. American Mathematical Society, 2005.

[80] R. Lehoucq, D. Sorensen, and C. Yang. *ARPACK Users' Guide*. Society for Industrial and Applied Mathematics, 1998. doi: 10.1137/1.9780898719628. URL `https://epubs.siam.org/doi/abs/10.1137/1.9780898719628`.

[81] R. B. Lehoucq and J. A. Scott. An evaluation of software for computing eigenvalues of sparse nonsymmetric matrices. Technical Report 96712, Center for Research on Parallel Computation (CRPC), Rice University, 1996.

[82] Randall J. LeVeque. *Finite Volume Methods for Hyperbolic Problems*. Cambridge Texts in Applied Mathematics. Cambridge University Press, 2002. doi: 10.1017/CBO9780511791253.

[83] Muyuan Liu and Dieter Bothe. Numerical study of head-on droplet collisions at high weber numbers. *Journal of Fluid Mechanics*, 789:785–805, 2016. ISSN 0022-1120. URL `http://tubiblio.ulb.tu-darmstadt.de/78012/`.

[84] Muyuan Liu and Dieter Bothe. Toward the predictive simulation of bouncing versus coalescence in binary droplet collisions. *Acta Mechanica*, 230(2):623–644, 2019.

[85] J. Lopez and J. Hernandez. On reducing interface curvature computation errors in the height function technique. *Journal of Computational Physics*, 229:4855–4868, 2010.

[86] Joaquin Lopez, Claudio Zanzi, Pablo Gomez, Rosendo Zamora, Felix Faura, and Julio Hernandez. An improved height function technique for computing interface curvature from volume fractions. *Computer Methods in Applied Mechanics and Engineering*, 198:2555–2564, 2009.

[87] Knud Lunde and Richard Perkins. Shape oscillations of rising bubbles. *Applied Scientific Research*, 58:387–408, 1998.

[88] Chen Ma and Dieter Bothe. Direct numerical simulation of thermocapillary flow based on the volume of fluid method. *International Journal of Multiphase Flow*, 37(9):1045–1058, 2011.

[89] J. Magnaudet and I. Eames. The motion of high-reynolds-number bubbles in inhomogeneous flows. *Annual Review of Fluid Mechanics*, 32(1):659–708, 2000.

[90] Jacques Magnaudet and Guillaume Mougin. Wake instability of a fixed spheroidal bubble. *Journal of Fluid Mechanics*, 572:311–337, 2007.

[91] Thomas Albert Manteuffel. The Tchebyshev iteration for nonsymmetric linear systems. *Numerische Mathematik*, 28:307–327, 1977.

[92] Thomas Albert Manteuffel. Adaptive procedure for estimating parameters for the nonsymmetric Tchebyshev iteration. *Numerische Mathematik*, 31:183–208, 1978.

[93] Karl Meerbergen and Dirk Roose. Matrix transformations for computing rightmost eigenvalues of large sparse non-symmetric eigenvalue problems. *Journal of Numerical Analysis*, 16:297–346, 1996.

[94] Chohong Min and Frederic Gibou. Geometric integration over irregular domains with application to level-set methods. *Journal of Computational Physics*, 226:1432–1443, 2007.

[95] Guillaume Mougin and Jacques Magnaudet. Path instability of a rising bubble. *Physical Review Letters*, 88:014502, 2001.

[96] Björn Müller, Florian Kummer, and Martin Oberlack. Highly accurate surface and volume integration on implicit domains by means of moment-fitting. *International Journal for Numerical Methods in Engineering*, 96:512–528, 2013.

[97] Ramesh Natarajan. An arnoldi-based iterative scheme for nonsymmetric matrix pencils arising in finite element stability problems. *Journal of Computational Physics*, 100:128–142, 1992.

[98] Narinder Nayar and James M. Ortega. Computation of selected eigenvalues of generalized eigenvalue problems. *Journal of Computational Physics*, 108:8–14, 1993.

[99] Akira Nishida and Yoshio Oyanagi. Evaluation of acceleration techniques for the resarted Arnoldi method. Technical report, Kyoto University, Department of Information Science, 1997. URL `http://hdl.handle.net/2433/61103`.

[100] Takaaki Nishida, Yoshiaki Teramoto, and Hideaki Yoshihara. Hopf bifurcation in viscous incompressible flow down an inclined plane. *Journal of Mathematical Fluid Mechanics*, 7:29–71, 2005.

[101] Mark Owkes and Olivier Desjardins. A mesh-decoupled height function method for computing interface curvature. *Journal of Computational Physics*, 281:285–300, 2015.

[102] B. N. Parlett. The software scene in the extraction of eigenvalues from sparse matrices. *SIAM Journal on Scientific and Statistical Computing*, 5(3):590–604, 1984. doi: 10.1137/0905042. URL `http://dx.doi.org/10.1137/0905042`.

[103] H. V. Patel, J. A. M. Kuipers, and E. A. J. F. Peters. Computing interface curvature from volume fractions: A hybrid approach. *Computers & Fluids*, 161:74–88, 2018.

[104] H. V. Patel, A. Panda, J. A. M. Kuipers, and E. A. J. F. Peters. Computing interface curvature from volume fractions: A machine learning approach. *Computers & Fluids*, page 104263, 2019. ISSN 0045-7930. doi: https://doi.org/10.1016/j.compfluid.2019.104263. URL `http://www.sciencedirect.com/science/article/pii/S0045793019302282`.

[105] M. Pick, J. Picha, and V. Vyskocil. *Theory of the Earth's Gravity Field*. Elsevier. Pub. Co., 1973.

[106] Mark B. Pinsky, Alexander P. Khain, and Zev Levin. The role of the inertia of cloud drops in the evolution of the spectra during drop growth by diffusion. *Quarterly Journal of the Royal Meteorological Society*, 125(554):553–581, 1999.

[107] Thomas Pohl. *High Performance Simulation of Free Surface Flows Using the Lattice Boltzmann Method*. PhD thesis, Universität Erlangen-Nürnberg, 2008.

[108] J.Y. Poo and N. Ashgriz. A computational method for determining curvatures. *Journal of Computational Physics*, 84(2):483 – 491, 1989. ISSN 0021-9991. doi: https://doi.org/10.1016/0021-9991(89)90245-3. URL `http://www.sciencedirect.com/science/article/pii/0021999189902453`.

[109] Stephane Popinet. An accurate adaptive solver for surface-tension-driven interfacial flows. *Journal of Computational Physics*, 228(16):5838–5866, 2009.

[110] Stephane Popinet. Numerical models of surface tension. *Annual Review of Fluid Mechanics*, 50:49–75, 2018.

[111] Jan Prüss and Gieri Simonett. On the manifold of closed hypersurfaces in $\mathbb{R}^N$. *Discrete and continuous dynamical systems*, 33(11&12):5407–5428, 2013.

[112] Jan Prüss and Gieri Simonett. *Moving Interfaces and Quasilinear Parabolic Evolution Equations*. Springer, 2016. ISBN 978-3-319-27698-4.

[113] Yinghe Qi, Jiacai Lu, Ruben Scardovelli, Stephane Zaleski, and Gretar Tryggvason. Computing curvature for volume of fluid methods using machine learning. *Journal of Computational Physics*, 377:155–161, 2019.

[114] M. Raessi, J. Mostaghimi, and M. Bussmann. Advecting normal vectors: A new method for calculating interface normals and curvatures when modeling two-phase flows. *Journal of Computational Physics*, 226(1):774–797, 2007.

[115] Mashetti Ravibabu and Arindama Singh. A new variant of Arnoldi method for approximation of eigenpairs. *Journal of Computational and Applied Mathematics*, 344:424–437, 2018.

[116] Yuriko Renardy and Michael Renardy. Prost: A parabolic reconstruction of surface tension for the volume-of-fluid method. *Journal of Computational Physics*, 183:400–421, 2002.

[117] Yuriko Renardy, Vittorio Cristini, and J. Li. Drop fragment distributions under shear with inertia. *International Journal of Multiphase Flow*, 28(7):1125–1147, 2002.

[118] Yuriko Renardy, Michael Renardy, and Vittorio Cristini. A new volume-of-fluid formulation for surfactants and simulations of drop deformation under shear at a low viscosity ratio. *European Journal of Mechanics - B/Fluids*, 21(1):49–59, 2002.

[119] William J. Rider and Douglas B. Kothe. Reconstructing volume trackiing. *Journal of Computational Physics*, 141:112–152, 1998.

[120] Martin Rieber. *Numerische Simulation der Dynamik freier Grenzflächen in Zweiphasenströmungen.* PhD thesis, Universität Stuttgart, 2004.

[121] Carlos Rodríguez-Abreu and Ana Pena. Nano-droplet systems by surfactant self-assembly and applications in the pharmaceutical industry. *Current topics in medicinal chemistry*, 14, 01 2014. doi: 10.2174/1568026614666140118221658.

[122] Axel Ruhe. *The two-sided arnoldi algorithm for nonsymmetric eigenvalue problems*, pages 104–120. Springer Berlin Heidelberg, Berlin, Heidelberg, 1983. ISBN 978-3-540-39447-1. doi: 10.1007/BFb0062097. URL `http://dx.doi.org/10.1007/BFb0062097`.

[123] Youcef Saad. Variations on Arnoldi's method for computing eigenelements of large unsymmetric matrices. *Linear Algebra and its Applications*, 34:269–295, 1980.

[124] Youcef Saad. Chebyshev acceleration techniques for solving nonsymmetric eigenvalue problems. *Mathematics of Computation*, 42(166):567–588, 1984.

[125] Yousef Saad. Krylov subspace methods for solving large unsymmetric linear systems. *Mathematics of Computation*, 1981.

[126] Yousef Saad. Analysis of augmented krylov subspace methods. *SIAM Journal on Matrix Analysis and Applications*, 18(2):435–449, 1997.

[127] Yousef Saad. *Numerical Methods for Large Eigenvalue Problems: Revised Edition.* Society for Industrial and Applied Mathematic, 2011. URL `https://www-users.cs.umn.edu/~saad/eig_book_2ndEd.pdf`.

[128] Miloud Sadkane. A block Arnoldi-Chebyshev method for computing the leading eigenpairs of large sparse unsymmetric matrices. *Numerische Mathematik*, 64:181–193, 1993.

[129] Jennifer A. Scott. An ARNOLDI code for computing selected eigenvalues of sparse real unsymmetric matrices. *ACM Transactions on Mathematical Software*, 21(4):432–475, December 1995.

[130] John C. Slattery. *Advanced Transport Phenomena.* Cambridge Series in Chemical Engineering. Cambridge University Press, 1999. doi: 10.1017/CBO9780511800238.

[131] Peter Smereka. The numerical approximation of a delta function with application to level set methods. *Journal of Computational Physics*, 211:77–90, 2006.

[132] D. C. Sorensen. Implicit application of polynomial filters in a $k$-step arnoldi method. *SIAM Journal on Matrix Analysis and Applications*, 13(1):357–385, January 1992.

[133] G. Strang. On the construction and comparison of difference schemes. *SIAM Journal of Numerical Analysis*, 5:506–517, 1968.

[134] Severin Strobl, Arno Formella, and Thorsten Pöschel. Exact calculation of the overlap volume of spheres and mesh elements. *Journal of Computational Physics*, 311:158–172, 2016.

[135] Mark Sussman. A second order coupled level set and volume-of-fluid method for computing growth and collapse of vapor bubbles. *Journal of Computational Physics*, 187:110–136, 2003.

[136] Mark Sussman and Mitsuhiro Ohta. Improvements for calculating two-phase bubble and drop motion using an adaptive sharp interface method. *Fluid Dynamics & Materials Processing*, 3: 21–36, 01 2007.

[137] Joel Tchoufag, Jacques Magnaudet, and D. Fabre. Linear stability and sensitivity of the flow past a fixed oblate spheroidal bubble. *Physics of Fluids*, 25:05410, 2013. doi: 10.1063/1.4804552.

[138] Joel Tchoufag, David Fabre, and Jacques Magnaudet. Global linear stability analysis of the wake and path of buoyancy-driven disks and thin cylinders. *Journal of Fluid Mechanics*, 740:278–311, 2014.

[139] Joel Tchoufag, Jacques Magnaudet, and David Fabre. Linear instability of the path of a freely rising spheroidal bubble. *Journal of Fluid Mechanics*, 751:R4, 2014. doi: 10.1017/jfm.2014.340.

[140] Asei Tezuka and Kojiro Suzuki. Three-dimensional global linear stability analysis of flow around a spheroid. *AIAA Journal*, 44:1697–1708, 2006.

[141] Vassilios Theofilis. Advances in global linear instability analysis of nonparallel and three-dimensional flows. *Progress in Aerospace Sciences*, 39:249–315, 2003.

[142] Vassilios Theofilis. Global linear instability. *Annual Review of Fluid Mechanics*, 43:319–352, 2011.

[143] M.D. Torrey, L.D. Cloutman, R.C. Mjolsness, and C.W. Hirt. NASA-VOF2D: a computer program for incompressible flows with free surfaces. Technical Report LA-10612-MS, Los Alamos National Lab., 1985.

[144] Manoj Kumar Tripathi, Kirti Chandra Sahu, and Rama Govindarajan. Dynamics of an initially spherical bubble rising in quiescent liquid. *nature Communications*, 6:6268, 2015.

[145] G. Tryggvason, B. Bunner, O. Ebrat, and W. Tauber. Computations of multiphase flows by a finite difference/frot tracking method. i. multi-fluid flows. Lecture Notes, 1998.

[146] Lorenzo Valdettaro, Michel Rieutord, Thierry Braconnier, and Valérie Frayssséd. Convergence and round-off errors in a two-dimensional eigenvalue problem using spectral methods and Arnoldi-Chebyshev algorithm. *Journal of Computational and Applied Mathematics*, 205(1):382–393, 2007.

[147] H .K. Versteeg and W. Malalasekera. *An introduction to computational fluid dynamics: the finite volume method*. Pearson Education, 2007.

[148] Herbert Voß. *PSTricks: Grafik mit PostScript für TEXund LATEX*, volume 5. Lehmanns, 2008. ISBN 9783865412805.

[149] Andre Weiner and Dieter Bothe. Advanced subgrid-scale modeling for convection-dominated species transport at fluid interfaces with applicaton to rising bubbles. *Journal of Computational Physics*, (347):261–289, 2017. URL `http://tubiblio.ulb.tu-darmstadt.de/92742/`.

[150] Xin Wen. High order numerical methods to a type of delta function integrals. *Journal of Computational Physics*, 226:1952–1967, 2007.

[151] Xin Wen. High order numerical methods to twodimensional delta function integrals in level set methods. *Journal of Computational Physics*, 228:4273–4290, 2009.

[152] Xin Wen. High order numerical methods to three dimensional delta function integrals in level set methods. *SIAM Journal of Scientific Computing*, 32:1288–1309, 2010.

[153] E. P. Wigner. *On the Matrices Which Reduce the Kronecker Products of Representations of S. R. Groups*, pages 608–654. Springer Berlin Heidelberg, Berlin, Heidelberg, 1993. ISBN 978-3-662-02781-3. doi: 10.1007/978-3-662-02781-3_42. URL `https://doi.org/10.1007/978-3-662-02781-3_42`.

[154] M. W. Williams, D. B. Kothe, and E. G. Puckett. Accuracy and convergence of continuum surface-tension models. In Wei Shyy and Ranga Narayanan, editors, *Fluid Dynamics at Interfaces*, chapter Multiphase systems, pages 294–305. Cambridge University Press, 1. edition, 1999.

[155] Franz-Erich Wolter and Seamus T. Tuohy. Curvature computations for degenerate surface patches. *Computer Aided Geometric Design*, 9:241–270, 1992.

[156] Hsuan-Chung Wu, Huey-Jiuan Lin, Yung-Chi Kuo, and Weng-Sing Hwang. Simulation of droplet ejection for a piezoelectric inkjet printing device. *Materials Transactions*, 45:893–899, 03 2004. doi: 10.2320/matertrans.45.893.

[157] Binze Yang and Andrea Prosperetti. Linear stability of the flow past a spheroidal bubble. *Journal of Fluid Mechanics*, 582:53–78, 2007.

[158] D. L. Youngs. An interface tracking method for a 3d eulerian hydrodynamics code. Technical Report 44/92/35, AWRE, 1984.

[159] Roberto Zenit and Jacques Magnaudet. Path instability of rising spheroidal air bubbles: A shape-controlled process. *Physics of Fluids*, 20:061702, 2008.

[160] Roberto Zenit and Jacques Magnaudet. Measurements of the streamwise vorticity in the wake of an oscillating bubble. *International Journal of Multiphase Flow*, 35:195–203, 2009.

[161] W. Zhou and J. Dusek. Marginal stability curve of a deformable bubble. *International Journal of Multiphase Flow*, 89:218–227, 2017.